Force-detected spectroscopy of single molecules on insulators

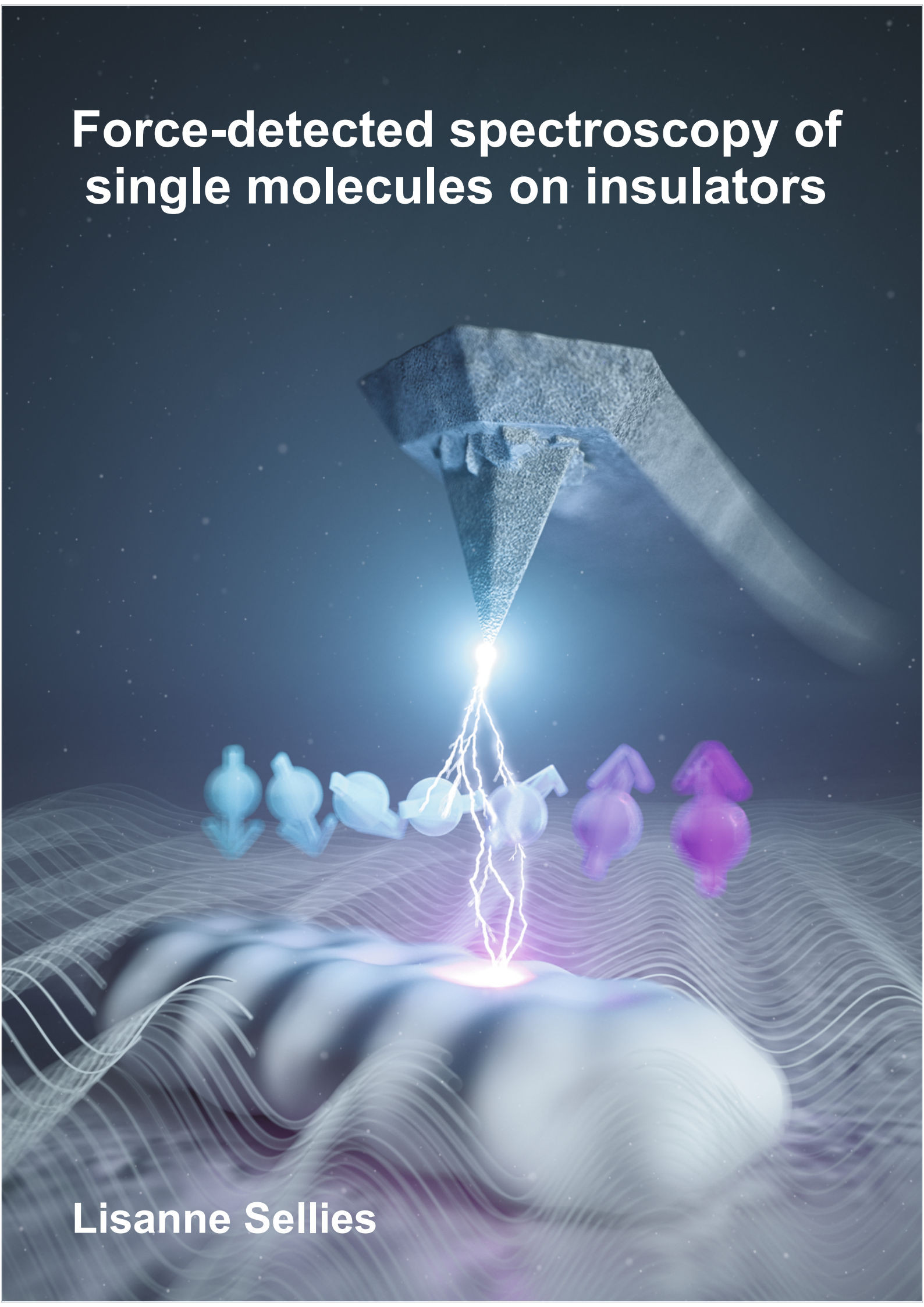

Lisanne Sellies

Everything, including our own bodies, is built up from atoms and molecules. Understanding their properties is thus crucial for all natural and life sciences as well as for countless applications in engineering. Using an atomic force microscope (AFM), atoms and molecules can be imaged with atomic-scale spatial resolution. Since AFM is based on scanning a physical probe, the tip, across the surface, this tip can also be used to interfere with the sample. For instance, electrons can be steered between the tip and the single molecule under investigation. Molecules can thereby be brought to non-equilibrium states, which play a crucial role in many natural phenomena.

Studying such non-equilibrium states with AFM is the topic of this thesis. Two novel methods based on AFM were developed that allow accessing a wide range of properties of non-equilibrium electronic states, of which most were not accessible so far in combination with AFM.

First, we introduce an excited-state spectroscopy method that allows extracting the energy levels of ground and excited states for different net charges on the molecule. Thereby, excitation energies can be quantified that are difficult to access otherwise. Furthermore, the molecule can be prepared in specific excited states and the subsequent transitions can be controlled, potentially applicable to induce and study chemical reactions.

Second, we demonstrate - for the first time - that electron spin resonance spectroscopy (ESR) signals of single molecules can be measured using AFM. Our method, called ESR-AFM, is based on driving spin transitions between non-equilibrium triplet substates. By combining the spatial resolution of AFM with the isotope sensitivity of ESR, we can locally identify molecules only differing in their isotopic configuration. Moreover, we can coherently manipulate the electron spins of pentacene over tens of microseconds. The high energy resolution of ESR-AFM and the long spin coherence observed represent a leap forward for local studies in the fields of quantum computing and quantum sensing.

Cover: Artistic illustration of the integration of electron spin resonance in atomic force microscopy. The white structure at the bottom represents a single pentacene molecule, the arrows its spin quantum state and the wavy lines the radio-frequency magnetic field needed for the electron spin resonance, which is detected by the tip of the atomic force microscope.

Universität Regensburg
Institut für Experimentelle und Angewandte Physik
Research Group Prof. Dr. Jascha Repp

Force-detected spectroscopy of single molecules on insulators

DISSERTATION ZUR ERLANGUNG DES DOKTORGRADES
DER NATURWISSENSCHAFTEN (DR. RER. NAT.)
DER FAKULTÄT FÜR PHYSIK

DER UNIVERSITÄT REGENSBURG

vorgelegt von
Lisanne Sellies
aus Zwolle (Niederlande)

Im Jahr 2024

Das Promotionsgesuch wurde am 17. 04. 2024 eingereicht.
Die Arbeit wurde angeleitet von Prof. Dr. Jascha Repp.

Prüfungsausschuss:
Vorsitzender: Prof. Dr. Rupert Huber
1. Gutachter: Prof. Dr. Jascha Repp
2. Gutachter: Prof. Dr. Andrea Donarini
Weitere Prüferin: Prof. Dr. Isabella Gierz

Contents

1. Introduction

Everything, including our own bodies, is built up from atoms and molecules. That is why an exact understanding of the properties of these building blocks is crucial for all natural and life sciences as well as for countless applications in engineering. Excitingly, forty years ago two microscopic techniques were introduced[1,2] that allow imaging atoms and molecules with atomic-scale spatial resolution. Both of these techniques belong to the family of scanning probe microscopy (SPM); they rely on scanning a surface using a physical probe, an atomically sharp tip. They differ in the detected signal: the tunneling current in scanning tunneling microscopy (STM) and the force in atomic force microscopy (AFM). STM provides thereby access to the electronic structure of the surface, including the density of molecular orbitals[3]. AFM, on the other hand, allows for instance resolving the structure of single molecules with atomic-scale spatial resolution[4].

Thus, these microscopic techniques are powerful due to their atomic-scale imaging capabilities. On top, in contrast to most other microscopic techniques, the usage of a physical probe, the tip, offers the possibility to interfere with the sample. Already shortly after the development of SPM, it was shown that single atoms can be moved around, allowing to built atomic-scale structures at will[5,6], and thereby to study atomic-scale physical phenomena in real-space[7]. Furthermore, chemical reactions can be induced by the tip[8,9], thereby forming molecules that were elusive so far[10,11]. Next to imaging and manipulation, a range of spectroscopic methods have been developed. For instance, scanning tunneling spectroscopy (STS) provides access to the energies of different orbitals of single molecules[3], while Kelvin probe force spectroscopy (KPFS) allows detection of atoms and molecules in states with different net charge[12,13].

Typically, single molecules are studied in their ground state with STM and AFM. However, many phenomena in nature are governed by non-equilibrium properties[14], so it is crucial to study also non-equilibrium states. Different methods based on STM have been developed to access such states, for example the combination of STM with luminescence[15–17]. However, since STM is based on electron tunneling, the molecule under investigation can only be partly electronically decoupled from the required conductive substrate (by using a thin insulating film). In other words, electrons can tunnel between the molecule and metal substrate, which will bring the molecule typically rapidly back to its ground state. To study non-equilibrium states, a full electronic decoupling of the molecule from the underlying surface is desirable, which can be achieved by using bulk insulators or insulating films with a thickness that fully suppresses electron tunneling[18]. Since STM cannot be used on such surfaces, AFM is the method of choice.

The aim of this thesis is to develop two novel AFM spectroscopic methods that allow accessing a wide range of properties of non-equilibrium electronic states, of which most were not accessible so far. These methods exploit the combination of AFM detection with single-electron tunneling between a conductive AFM tip and the individual molecules adsorbed on an insulating surface[19]. This combination has been instrumental to several pioneering

works. In particular, Fatayer et al. managed to access the energies of a few low-lying electronic states[20], while Peng et al. could measure the lifetime of the first excited triplet state[21]. Building on these developments, we propose two novel methods: one to access a large number of electronic excited states, and another to study the spin properties of the first excited triplet state, as follows.

In Chapter 3, an excited-state spectroscopy method will be introduced that allows extracting the energy levels of ground and excited states for different net charges on the molecule. It thereby complements other scanning probe microscopy experiments and guides their interpretation, as we will demonstrate for recent STM-induced luminescence experiments. Furthermore, our method allows preparing a molecule in a specific excited state, and controlling subsequent transitions. This will be used in the context of this thesis to guide the interpretation of the observed spectroscopic features. In general, our method can be used to guide, understand and engineer tip-induced chemical reactions as well as phosphorescence and fluorescence of individual molecules.

In Chapter 4, we demonstrate - for the first time - that electron spin resonance spectroscopy (ESR) signals can be measured using AFM. Specifically, we drive and detect spin transitions between non-equilibrium triplet states of single molecules. The resulting ESR spectra exhibit sub-nanoelectronvolt spectral resolution, which allows us to distinguish molecules only differing in their isotopic configuration. Moreover, because of the minimally invasive nature of this method, which we name ESR-AFM, we could demonstrate coherent manipulation of the electron spins of pentacene over tens of microseconds. ESR-AFM combines such single-molecule ESR measurements with the possibility to image the molecule and its environment with atomic-scale spatial resolution. We can, for instance, visualize the interplay of the ESR selection rules and the molecular orientation at atomic scales. We foresee that ESR-AFM could for instance be used for fundamental quantum-sensing experiments.

2. Theoretical background

Part of the presentation of the theory in this chapter is part of a manuscript that is under review or has been published in ref. [22]. Some of the figures in this chapter are reprinted and modified with permission from Springer Nature (2023).

2.1. Energy states in individual molecules

In the context of this thesis, two methods were developed to study electronically excited states of single molecules. Whereas in most steady-state STM studies a single-particle description is sufficient for a basic understanding of the data, here, the many-body pictures are required in many cases (e.g. to understand which states are energetically accessible). Therefore, in the following the low-lying states of a generic system of a molecule with a closed-shell ground state are introduced. This means that in the ground state all electrons are paired up, filling the orbitals up to the highest occupied molecular orbital (HOMO). Such a state is the singlet ground state S_0, where singlet indicates that the spin quantum number is zero. Figure 2.1 shows this S_0 state together with the corresponding low-lying electronic states, including the occupation of the frontier orbitals (HOMO and lowest unoccupied molecular orbital (LUMO)) for every state. Typically, the lowest-lying excited states are formed by exciting one of the electrons from the HOMO to the LUMO (note that we consider here a molecule without degeneracies of the frontier orbitals). Thereby, either the first excited triplet state T_1 or the first excited singlet state S_1 is formed, which are separated by the exchange interaction of the two unpaired electrons. In contrast to the singlet states, the triplet state has a spin quantum number of 1. This gives rise to three triplet substates differing in their spin magnetic quantum number (the triplet substates are discussed in detail in Section 2.4.1). For some molecules, a second excited triplet state T_2 (not shown here) may be located energetically between T_1 and S_1. Such a state might have two electrons in the HOMO and one electron in each the LUMO and the HOMO-1 (ref. [23]).

Note that many of the states are expected to have a multi-reference character, which means that more than one electronic configuration (a certain occupation of orbitals) is significantly contributing to the many-body state[23–25]. For example, the above-described T_2 state is expected to strongly interact via pair-hopping with another neutral excited triplet state, which has one electron in each the HOMO and the LUMO+1. Pair-hopping is the simultaneous hopping of two electrons between different orbitals[26,27]. The smaller the energy difference between the electronic configurations, the larger their admixture is[25].

Upon removing or adding one electron, the doublet ground states D_0^+ and D_0^- of the charged molecule are formed, respectively. Here, doublet indicates that the molecule has one unpaired electron spin, thus a spin quantum number of 1/2. Throughout this thesis we refer to the orbital electronic levels according to the neutral molecule's states (instead of

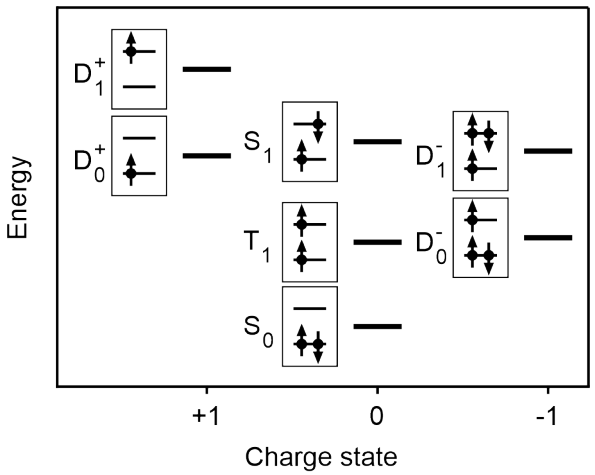

Figure 2.1.: Many-body energy diagram of the electronic states of a prototypical molecule with a closed-shell ground state. The small diagrams depict the electronic configuration, that is, the occupation of the HOMO (bottom) and LUMO (top). The depicted spin configurations represent only one exemplary case. These small diagrams are not drawn quantitatively. Whereas this diagram is drawn for a prototypical molecule, the relative energetic alignment of the states (black solid lines) are in Chapter 3 typically drawn quantitatively. They depend on the specific molecule, work function of the surface and the applied gate voltage (see for more details Chapter 3).

calling for instance the highest occupied molecular orbital in D_0^+ a singly occupied molecular orbital (SOMO)). The corresponding lowest-lying excited states are the first excited doublet states D_1^+ and D_1^-, depicted in this thesis with one electron being excited from the HOMO to the LUMO. Depending on the molecule under study, D_1^+ and D_1^-, may instead involve an excitation from the HOMO-1 to HOMO or from LUMO to LUMO+1, respectively. In any case, D_1^+ and $D_1^-$are characterized by an exciton in the molecule that carries a net charge, also called trion.

2.2. Scanning Tunneling Microscopy

Although AFM is the main technique used in the context of this thesis, the AFM spectroscopic methods developed, strongly rely on concepts from STM, which will be introduced here.

In 1982, Binnig and Rohrer developed the STM[1]. STM relies on bringing an atomically sharp conductive tip in close proximity (on the ångström scale) to a conducting surface. Upon applying a voltage between tip and sample, called bias voltage V_B, electrons can tunnel between the tip and the surface. This is visualized in Figure 2.2a.

The tunneling of an electron through a potential barrier is a quantum-mechanical effect. The electron is described by a wavefunction $\phi(z)$, which satisfies the Schrödinger equation[28]

$$-\frac{\hbar^2}{2m}\frac{\partial^2}{\partial z^2}\phi(z) + V(z)\phi(z) = E_n\phi(z), \tag{2.1}$$

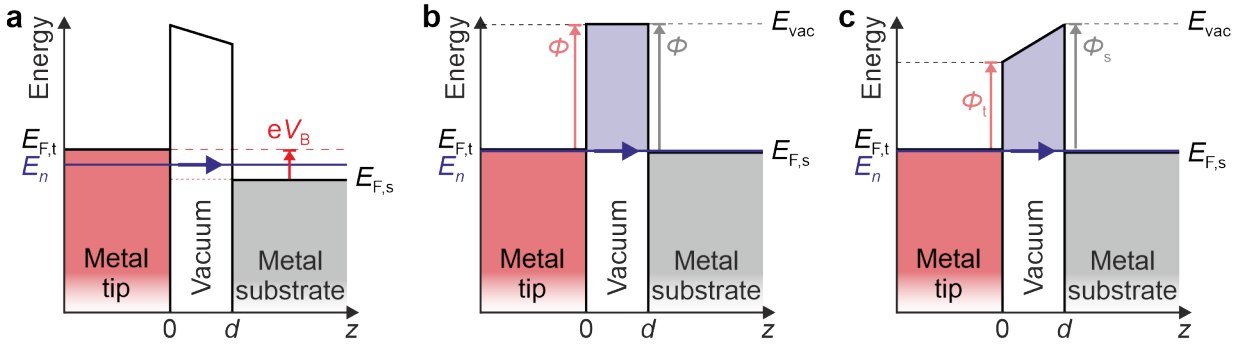

Figure 2.2.: One-dimensional metal-vacuum-metal tunneling junctions. **a**, Schematic to illustrate electron tunneling from a metal substrate to a metal tip. Due to the Pauli exclusion principle[30], electron tunneling can only occur from occupied to unoccupied states. Upon applying a positive bias voltage V_B to the metal substrate, the Fermi level of the sample ($E_{F,s}$) shifts below the one of the tip ($E_{F,t}$) (vice versa for a negative bias voltage). Therefore, at $T = 0$ K, tunneling occurs in the energy range between the two Fermi levels, also called bias voltage window (indicated by eV_B). This tunneling is schematically illustrated for an electron with an energy E_n ($E_{F,s} < E_n < E_{F,t}$). The tunneling probability scales exponentially with the tip-sample distance d, see Equation (2.3). **b**, Electron tunneling through a square barrier for a very small applied positive bias voltage to the sample. Here, the work functions of the sample and tip are assumed to be the same (Φ). The tunneling barrier is indicate by the purple shaded area. The tunneling probability through a square barrier is given by Equation (2.3). **b**, Electron tunneling through a trapezoidal barrier for a very small applied positive bias voltage to the sample. Here, the work functions of the sample Φ_s and tip Φ_t are different. The tunneling probability through a trapezoidal barrier (purple shaded area) is given by Equation (2.6). These schematics are based on figures from ref. [28, 29].

with $\hbar$ the reduced Planck's constant, m the electron mass, z the position, V the potential and E_n the energy of the tunneling electron. Here, the time-independent Schrödinger equation is used since the potential is typically not time-dependent[29] and, for simplicity, only one dimension is considered.

The simplest case of a tunneling barrier is a square barrier, as is illustrated in Figure 2.2b. One possible solution of the Schrödinger equation inside this square barrier, where $V(z) = E_{vac} > E_n$ with E_{vac} the vacuum energy, is given by an exponentially decaying wave function[29]:

$$\phi(z) = \phi(0)\exp(-\kappa z) \text{ with } \kappa = \frac{1}{\hbar}\sqrt{2m(E_{vac} - E_n)}, \tag{2.2}$$

where $\phi(0)$ is the wavefunction at the incident edge of the barrier. The probability to find the electron at the other edge of the square barrier with width d is approximately proportional to the square of this wavefunction at this other edge: $|\phi(d)|^2$. The tunneling probability T is, therefore, approximately given by[28,29]

$$T = \frac{|\phi(d)|^2}{|\phi(0)|^2} \approx \exp(-2d\kappa) = \exp(-\frac{2d}{\hbar}\sqrt{2m(E_{vac} - E_n)}) \approx \exp(-\frac{2d}{\hbar}\sqrt{2m\Phi}), \tag{2.3}$$

where the last approximation follows from the definition of the work function Φ as the energy required to remove an electron from the metal: $\Phi = E_{vac} - E_F \approx E_{vac} - E_n$, where

E_F is the Fermi level of the metal. In other words, the applied bias voltage V_B is assumed to be small compared to Φ, such that E_n lies always close to E_F (see Figure 2.2b). Note that the same approximate expression for the tunneling probability can be obtained from the general solution of the Schrödinger equation inside and outside of the barrier (see for the derivation ref. [29]).

It follows from Equation (2.3) that the tunneling probability depends exponentially on the tip-sample distance (the barrier width d). To be more specific, the tunneling probability decays typically one order of magnitude per 1 Å increase in tunneling distance, assuming a (typical) work function of around 5 eV (ref. [28]).

The tunneling barrier deviates in most cases from a simple square barrier. Often, it can be assumed as having a constant slope, as illustrated in Figure 2.2c. Since the Schrödinger equation cannot be solved analytically in this case, instead the semi-classical Wentzel-Kramers-Brilliouin (WKB) approximation can be used. For a potential barrier that depends on z, the local decay constant inside the vacuum barrier (Equation (2.2)) is given by[28]

$$\kappa(z) = \frac{1}{\hbar}\sqrt{2m(V(z) - E_n)}. \tag{2.4}$$

The WKB approximation assumes that the potential V is slowly varying with z (ref. [31]). The total decay of the wavefunction due to the slowly varying potential can be derived from integrating over the local decay constant $\kappa(z)$ in the region of the potential (0 to d) (ref. [29]). The tunneling probability results then as[28]

$$T \approx \exp\left(-2\int_0^d \kappa(z)dz\right) = \exp\left(-\frac{2\sqrt{2m}}{\hbar}\int_0^d \sqrt{V(z) - E_n}dz\right). \tag{2.5}$$

Assuming the trapezoidal barrier shown in Figure 2.2b, $V(z)$ is given by $E_n + \Phi_s - \frac{z}{d}(\Phi_s - \Phi_t)$. Inserting this into Equation (2.5) gives

$$T \approx \exp\left(-\frac{2\sqrt{2m}}{\hbar}\int_0^d \sqrt{\Phi_s - \frac{z}{d}(\Phi_s - \Phi_t)}dz\right) = \exp\left(-2\frac{2\sqrt{2m}}{3\hbar}\frac{\Phi_s^{\frac{3}{2}} - \Phi_t^{\frac{3}{2}}}{\Phi_s - \Phi_t}d\right). \tag{2.6}$$

To take an STM image, the tunneling current can be measured while the tip is scanned over the surface at a constant height (alternatively, the height of the tip can be recorded, while scanning the tip at a constant tunneling current - kept constant using a feedback loop). The spatial contrast observed in STM can typically be understood from the approximation Tersoff and Hamann[32,33] made when applying Bardeen's model of tunneling[34] to describe tunneling in an STM. Before the invention of the STM, Bardeen derived a formula for the tunneling between two metals separated by an oxide layer[34]. It follows from Bardeen's model that tunneling between a sample and an STM tip depends on the wavefunctions of both the sample and the tip[34]. Since the exact wavefunctions of the tip are in general not known, Tersoff and Hamann modeled the tip using an s-wavefunction[32]. They could derive that for small voltages and temperatures the tunneling current is proportional to the density of the sample wavefunctions ($|\phi_s|^2$) at the position of the center of curvature

of the tip ($\boldsymbol{r}_0$)[29,32]:

$$I \propto \sum_n |\phi_{n,\mathrm{s}}(\boldsymbol{r}_0)|^2 \delta(E_{n,\mathrm{s}} - E_{\mathrm{F,t}}) = \rho_{\mathrm{s}}(E_{\mathrm{F,t}}, \boldsymbol{r}_0). \tag{2.7}$$

The Dirac delta function indicates that for small voltages tunneling occurs between the Fermi level of the tip $E_{F,\mathrm{t}}$ and sample wavefunctions with the same energy $E_{n,\mathrm{s}}$ (because of energy conservation). The equality follows from the definition of the local density of states[29]. Thus, the spatial STM contrast can be interpreted as the local density of states of the sample at the position of the center of curvature of the tip ($\rho_{\mathrm{s}}(E_{\mathrm{F,t}}, \boldsymbol{r}_0)$)[29].

In the experiments throughout this thesis, typically larger bias voltages (a few volts) are applied. The Tersoff-Hamann model can be straightforwardly extended to the case of finite bias voltages if the density of states of the tip and the tunneling probability can be approximated to be constant over the energy interval of interest[28]. The tunneling current then follows from integrating over the bias voltage window, as[28]

$$I \propto \int_0^{eV_{\mathrm{B}}} \rho_{\mathrm{s}}(E_{F,\mathrm{t}} + \epsilon, \boldsymbol{r}_0) d\epsilon. \tag{2.8}$$

The methods developed in the context of this thesis rely on tunneling between the tip and individual orbitals of single molecules. If the sample consists of a single molecule, the tunneling current will be proportional to the density of its molecular orbitals (see Equations (2.7) and (2.8)). This still holds if the molecules are deposited on a surface, provided that the molecular orbitals are decoupled from the metallic surface by using a thin insulating film. Indeed, Repp et al. managed to image the intrinsic molecular orbital densities of single pentacene molecules by depositing them on a thin insulating film (2 monolayers (ML) of NaCl) grown on a metal substrate[3].

If we consider competing tunneling pathways into different molecular levels, the relative tunneling rates will not only depend on their spatial orbital densities, but also on their energy (and on their multiplicity, see Section 3.4). This is exemplified for tunneling between the tip and the HOMO and LUMO of a single molecule in Figure 2.3. According to Equations (2.5) and (2.6), the tunneling probability will depend on the area between the vacuum barrier and the energy at which the tunneling occurs. The single-particle pictures, shown in Figure 2.3a and c, indicate a smaller tunneling barrier for tunneling in or out of the LUMO (purple area) than for tunneling in or out of the HOMO (purple plus light blue area).

Based on this barrier-height argument, the arrows of competing tunneling processes in the many-body diagrams are drawn qualitatively with different relative thicknesses throughout this thesis. For the tip side of the tunneling barrier, the following rule applies: for electron tunneling processes from the tip to the molecule (that is, when the molecule gets charged more negatively, e.g. $\mathrm{D}_0^+ \rightarrow \mathrm{S}_0$, $\mathrm{S}_0 \rightarrow \mathrm{D}_0^-$), the tunneling barrier is the smallest for (energetically allowed) processes with a final state having the highest energy (see Figure 2.3a and b), whereas upon tunneling an electron from the molecule to the tip (that is, when the molecule gets charged more positively, e.g. $\mathrm{D}_0^- \rightarrow \mathrm{S}_0$ $\mathrm{S}_0 \rightarrow \mathrm{D}_0^+$), the barrier is the smallest for processes with the final state having the lowest energy in the many-body energy diagram (see Figure 2.3c and d). Note that, this simple rule applies only to tunneling through a vacuum barrier[35], as considered here.

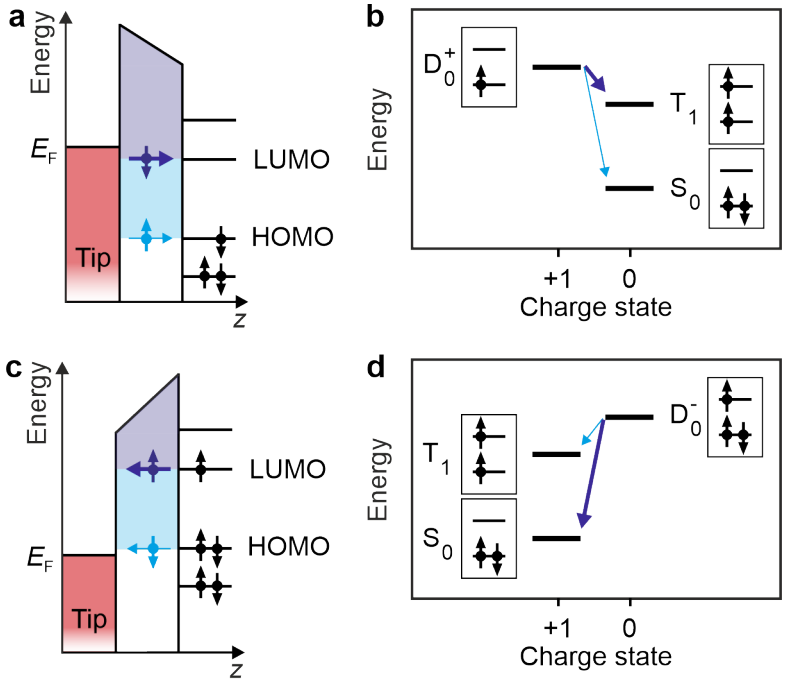

Figure 2.3.: Relative tunneling rates to/from different molecular levels. **a**, **c**, Single-particle pictures showing the tunneling barrier for tunneling to or from the HOMO (light blue) and LUMO (dark blue), respectively. The vacuum-tunneling barriers are indicated by the colored areas. From these single-particle pictures it is apparent that tunneling in or out of the LUMO has a lower tunneling barrier than tunneling in or out of the HOMO. **b**, **d**, Many-body energy diagrams for the processes indicated in **a**, **c**, respectively. The two transitions are highlighted in light and dark blue, with their relative rates indicated qualitatively by the thicknesses of the arrows.

2.3. Atomic Force Microscopy

The main technique used in this thesis is AFM. The AFM was developed a few years after the invention of the STM, by Binnig, Gerber and Quate[2]. Instead of detecting the tunneling current, the force between the tip and the sample is detected in AFM. The major advantage of detecting the force is that this renders AFM much wider applicable than STM. It, for instance, allows imaging insulating surfaces with atomic-scale spatial resolution[36–38].

The AFM can be operated in different modes. In the so called static AFM mode, the force is detected by mounting the tip to a cantilever and measuring the bending of the cantilever. In principle, a cantilever with a spring constant k that is as small as possible is desired, since it gives the largest displacement z for the small tip-sample forces being detected (from Hooke's law: $F_{\mathrm{ts}} = -kz$)[29]. However, to obtain atomic-scale spatial resolution, the tip has to be scanned close to the surface, risking that the tip jumps into contact with the surface. This jump-to-contact will occur if the spring constant with which the tip-sample interaction can be described (see Section 2.3.1) is larger than the one of the cantilever itself[38,39].

To circumvent this issue, the AFM can be operated in a dynamic mode, where the cantilever is driven to oscillate at or close to its resonance frequency. In this case, jump-to-contact will be prevented if the product of the oscillation amplitude and spring constant

of the cantilever (the restoring force) is larger than the tip-sample force[38,40,41]. In other words, even for soft cantilevers, jump-to-contact can be prevented by using large oscillation amplitudes. To measure the topography of a surface, typically either the amplitude or frequency of the oscillation is kept constant via a feedback loop[42]. The sensitivity of dynamic AFM improves with increasing quality factors[43] (Q-factor = Energy stored in the oscillator/Energy dissipated in one radian of the oscillation cycle)[29]. However, in case of amplitude-modulated AFM[44], the bandwidth, and thus the scanning speeds that can be employed, reduces with increasing Q-factors[43]. Therefore, frequency-modulated (FM)-AFM[43] is typically the method of choice for ultra-high vacuum (UHV) conditions, conditions under which high quality factors can be obtained.

2.3.1. Frequency-modulated atomic force microscopy

FM-AFM relies on driving a cantilever at its resonance frequency while keeping its amplitude constant. The frequency shift due to the tip-sample interaction (Δf) is measured[43], which is the difference between the resonance frequency (f) and the eigenfrequency of the cantilever (f_0): $\Delta f = f - f_0$.

Since the AFM cantilever movement can be described as a driven and damped oscillator, the eigenfrequency of the cantilever can be assumed to correspond to the one of a harmonic oscillator[29]:

$$f_0 = \frac{1}{2\pi}\sqrt{\frac{k}{m}}, \tag{2.9}$$

where m is the effective mass of the cantilever and k the spring constant of the cantilever.

The resonance frequency deviates from the eigenfrequency of the cantilever because of the tip-sample interaction. Importantly, although a constant tip-sample force will change the bending of the cantilever (as used in the static AFM mode), it will not change the resonance frequency of the cantilever. The resonance frequency is determined by the spring constant, as for the eigenfrequency, see Equation (2.9). The tip-sample interaction can also be described as a spring constant k_{ts}, which adds to the spring constant of the cantilever[29,43]. According to the general expression for a spring constant (from Hooke's law)[29], k_{ts} can be written as

$$k_{\mathrm{ts}} = -\left\langle \frac{\partial F_{\mathrm{ts}}}{\partial z} \right\rangle_w \approx -\left. \frac{\partial F_{\mathrm{ts}}}{\partial z} \right|_{z=0}. \tag{2.10}$$

Here, the extension of the spring is in the z direction, due to the vertical orientation of the tip-sample junction. The spring constant is the average over a cantilever oscillation period, weighted by the sinusoidal movement of the cantilever. In other words, the spring constant is a convolution of a semispherical weight function w with the tip-sample force gradient[38]. Therefore, any linear components of the tip-sample force gradient around $z = 0$ give a zero contribution to the spring constant. Neglecting any square or higher order components around $z = 0$, the weighted average can be approximated as the single value at $z = 0$ giving the effective spring constant k_{ts} (see approximation in Equation (2.10)). This approximation holds for small cantilever oscillation amplitudes compared to the equilibrium tip-sample distance[40], as used in the context of this thesis. By adding k_{ts} to the spring

constant of the cantilever k, the resonance frequency can be expressed as

$$f = \frac{1}{2\pi}\sqrt{\frac{k+k_{\mathrm{ts}}}{m}} = f_0\sqrt{1+\frac{k_{\mathrm{ts}}}{k}} \approx f_0\left(1+\frac{k_{\mathrm{ts}}}{2k}\right) \tag{2.11}$$

where for the last step the approximation $\sqrt{1+x} \approx 1+\frac{1}{2}x$ is used, which holds since $|k_{\mathrm{ts}}| \ll k$ (k_{ts} is typically below 10 N/m (ref. [29, 45]) and for our cantilever $k \approx 1.8$ kN/m (ref. [46])). The frequency shift follows then from Equations (2.9) to (2.11), as

$$\Delta f = f - f_0 \approx -\frac{f_0}{2k}\left.\frac{\partial F_{\mathrm{ts}}}{\partial z}\right|_{z=0}. \tag{2.12}$$

The measured frequency shift in FM-AFM is thus proportional to the derivative of the tip-sample force.

2.3.2. High-resolution AFM on molecules

Although the implementation of FM-AFM enabled already in 1995 atomic-scale spatial resolution on a variety of surfaces[47,48], the complete chemical structure of an individual molecule was not imaged until 2009 (ref. [4]). The main challenge that had to be overcome to image individual molecules with atomic-scale spatial resolution was the reactivity of the tip apex. Such imaging typically requires tip-sample distances at which the attractive interaction between the foremost tip atom and the atoms to be imaged is maximized[49]; a distance at which the molecule is typically picked up or displaced using a metal tip apex. This challenge was overcome by functionalizing the tip apex, for example with a CO molecule[4], which adsorbs with its carbon atom toward the metal tip[50]. Using such a well-defined and inert tip-apex, single molecules can be imaged with intramolecular resolution (see for example the image of pentacene in Figure 4.7a (inset)).

The intramolecular resolution is attributed to the Pauli repulsion between the electrons in the molecule and the tip[4,51]. The Pauli repulsion is a result of the Pauli exclusion principle that no two electrons may occupy the same quantum state simultaneously[30]. The Pauli repulsion becomes substantial when regions of high electron density overlap. Since the electron density is concentrated at the atomic positions and bonds (more at the C-C than C-H bonds), these positions and bonds can be revealed at sufficiently small tip-sample distances ($d \approx 5$ Å)[4], where the Pauli repulsion force is large. To increase the sensitivity to these short-range forces, the cantilever oscillation amplitude needs to be on the order of the range of these forces[38]. Therefore, typically amplitudes around 0.5 Å are chosen[4,49]. To prevent jump-to-contact at these small tip-sample distances and cantilever oscillation amplitudes, a cantilever with a spring constant that is at least a few hundred N/m is required[38]. The qPlus sensor[52] used in the context of this work (see for more details Section 3.2.1) fulfills this requirement, having a spring constant of around 1.8 kN/m (ref. [46]).

2.3.3. Detection of single-electron charges

The novel AFM methods developed in the context of this thesis rely on the sensitivity of AFM to single-electron charges. This section introduces the principles underlying the AFM detection of single atoms and molecules in states with different net charge.

The first experiments in which the net charge of single atoms and molecules on a surface could be changed and detected were not performed with AFM, but with STM[53–55]. Key to these measurements was the decoupling of the atoms and molecules from the required conductive substrate by a thin insulating film (2-5 ML)[53,56]. Typically, atoms and molecules on such thin insulators will always revert back to their ground electronic state by electron tunneling to/from the underlying conductive surface. However, in some cases, two states with different electronic charge can have similar energies, and can both be stable on a thin insulating film, as discussed in the next section.

2.3.3.1. Relaxation energy and charge bistability

Molecules and atoms can be stabilized in electronic states with different net charge on thin insulating films because of the structural relaxations of the nuclei (of the molecule or atom and substrate) upon changing the net charge of the molecule or atom, as will be explained in this section.

To this end, the energies of the two involved charge states are considered as a function of the structural relaxations. To not have to consider the multidimensional space of all nuclear coordinates, the energy states are plotted along generalized nuclear coordinates. The energy of the two states along these coordinates have minima representing the respective relaxed situation, from where the energy increases approximately quadratically[57], as illustrated in Figure 2.4a. The two minima are displaced with respect to each other. The vertical displacement reflects the difference in energy of the electronic states, while the horizontal displacement represents the relaxation upon electron transfer. This relaxation can be understood by considering the charging of an atom or molecule on, for instance, a NaCl film. Upon negatively charging such an adsorbate, the Na^+ ions will move slightly upwards and Cl^- ions slightly downwards[53,54]. Although the atoms inside a charged molecule will also slightly rearrange, the largest effect is due to the surface atoms because of their net charges[58,59]. In case of dielectric surfaces, the relaxation of the ions is large if the static dielectric constant is substantially larger than the optical one (the ionic polarization only contributes to the static dielectric constant; at optical frequencies the ions cannot follow the frequency of an electric field anymore)[54,57,60].

Importantly, during the addition or removal of an electron to/from an atom or molecule, the nuclei are considered to be stationary (Born-Oppenheimer approximation). Thus, any transitions between the two parabolas are vertical transitions[62,67]; their probability is proportional to the square of the overlap integral between the vibrational wavefunctions of the two states (Franck-Condon factor)[63,68], see Figure 2.4a.

Subsequently, the nuclei will relax from the vibrational excited states to the vibrational ground state of this charge state. The resulting change in energy is called the relaxation energy, see Figure 2.4a. Similarly, to return to the original charge state, a vertical transition will bring the system into vibrational excited states, after which the system will return to the vibrational ground state.

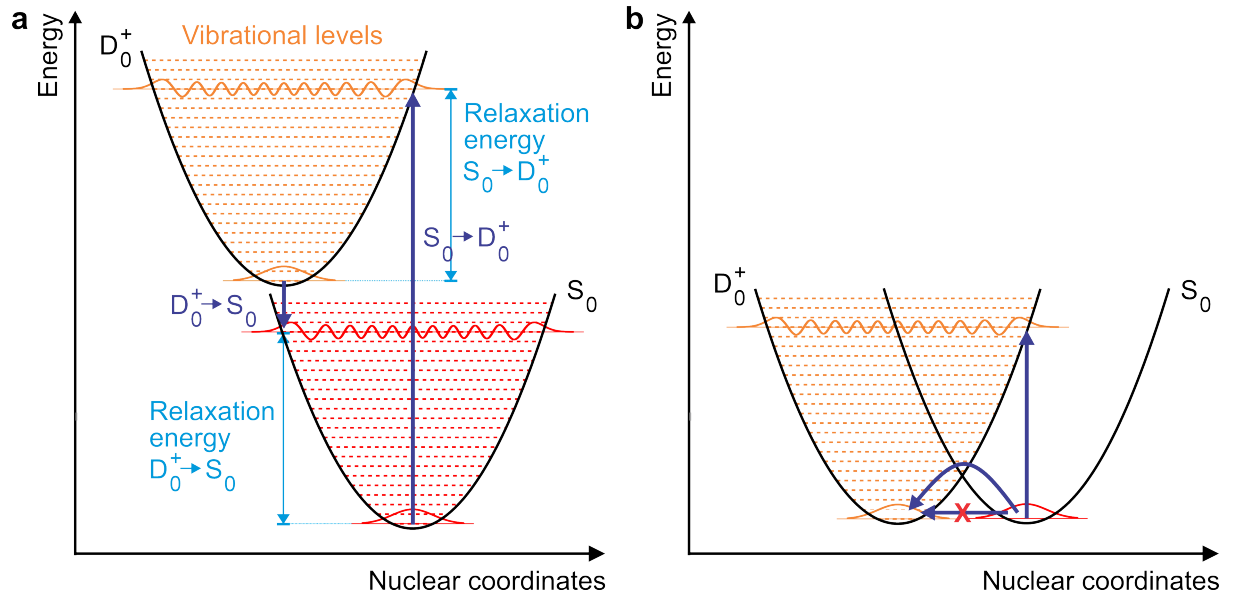

Figure 2.4.: Schematic illustrating the relaxation energy and the charge bistability. **a**, The energy of the two charge states can be approximated to depend quadratically on the nuclear coordinates of the atom or molecule and the surface; the charge states are thus both represented by a parabola[57]. Because of the Franck-Condon principle[61], the charge transitions are vertical transitions[62], their probability depending on the wave function overlap of the ground and excited states[63]. As an example, it is assumed that only the vibrational state with the largest wavefunction overlap is populated; in practice a range of vibrational levels can be populated (see Figure 2.5). After this excitation, the nuclei will reorganize to bring the system in the lowest vibrational level of the populated electronic state. The resulting change in energy is called the relaxation energy. Similarly, upon tunneling an electron back into the atom or molecule, a higher vibrational state of the ground electronic state will be populated, and the atom or molecule will return back to the corresponding vibrational ground state. This schematic is drawn for the D_0^+-S_0 transition, but can analogously be drawn for other transitions. This schematic is based on figures from ref. [57, 58, 64]. **b**, If the energy difference of the two electronic states is small, two charge states can be bistable on a thin insulating film. Similarly as in **a**, because of the strong electron-phonon coupling, the two states have their energy minimum at significantly different nuclear coordinates. Therefore, there is a vanishing overlap of the vibrational ground states (red and orange Gaussians) of two electronic states of different charge such that zero-phonon transitions are blocked (crossed-out arrow). Consequently, if the states are (close to) degenerate, the atom or molecule becomes charge bistable around zero bias voltage. The barrier between the two states can be overcome thermally (bend arrow) or by applying a sufficiently large bias voltage. In the latter case, vertical transitions, such as the one shown by the vertical arrow, become possible. Note that it is also possible to tunnel through the barrier, the probability of which depends on the nuclear wavefunction overlap between the initial and final states[65,66].

Large relaxation energies can lead to a charge bistability of the adsorbed atoms and molecules. At first glance one might assume that it is sufficient that the energy barrier between the two charge states is larger than the available thermal energy. However, the requirement to the energy barrier is much stricter, as can be understood from considering the Arrhenius equation, describing the temperature dependence of reaction rates, which is given by[69]

$$k = A \cdot \exp\left(\frac{-\Delta E}{k_{\mathrm{B}} T}\right) \tag{2.13}$$

with A the frequency factor, ΔE the energy barrier, k_{B} Boltzmann's constant and T the temperature. The rate constant k for a change in net charge of the molecule can be calculated assuming that the frequency factor is roughly equal to a vibrational frequency[69]. Using the frequency of the longitudinal optical phonon of bulk NaCl[70–72], the molecule will be stable in one of its charge states on the timescale of an hour if the barrier to states with a different net charge, ΔE, is approximately larger than 40 times the available thermal energy. For instance, at helium temperatures ΔE should be approximately larger than 14 meV.

This energy barrier is classically given by $\Delta E = \frac{1}{4\lambda}(\lambda - \Delta E^0)^2$, with λ the relaxation energy and ΔE^0 the energy difference between the two electronic states[57,65]. Thus, the larger the relaxation energy compared to the energy difference of the two charge states, the more likely it is that the atom or molecule will be bistable in these charge states. The energy difference ΔE^0 depends on the work function of the surface, the ionization and affinity energies of the atom or molecule and the electronic relaxations in the ionic film, metal substrate and tip[53,54,58,73].

This bistability on thin insulating films is schematically illustrated in Figure 2.4b. Because of the strong electron-phonon coupling, (vertical) transitions between the ground vibrational states are blocked (see horizontal arrow in Figure 2.4b). If the available thermal energy (of the phonons and substrate electrons) is smaller than the barrier, it cannot be overcome thermally (bend arrow in Figure 2.4b). Furthermore, around 0 V, the electrons have not enough energy to open up vertical transitions to higher-lying excited states (see vertical arrow in Figure 2.4b). Although tunneling through the barrier should also be considered, its rate will depend on the (in this case very small) wavefunction overlap between the initial and final states[65,66]. Note that in principle any combinations of these mechanisms can lead to a transition between the two charge states.

2.3.3.2. Broadening of the charge transitions

The charge transitions described in the previous section typically show a considerable broadening. This broadening is a result of the large number of vibrational excited states of the final electronic state that can be accessed, as schematically illustrated in Figure 2.5. For a single phonon mode, electronic transitions will occur for a number of energies separated by $\hbar\omega$ (harmonic approximation)[70]. Each of these transitions is broadened because of the finite lifetime of these states. Depending on the ratio between $\hbar\omega$ and the lifetime-induced broadening, individual peaks can be observed, or only a broadening[15,74]. Additional broadening can result if the electron does not couple to a single phonon mode, but to a band of phonon modes[70]. In case of adsorbates on NaCl, a Gaussian broadening of charge transitions was observed[3,70].

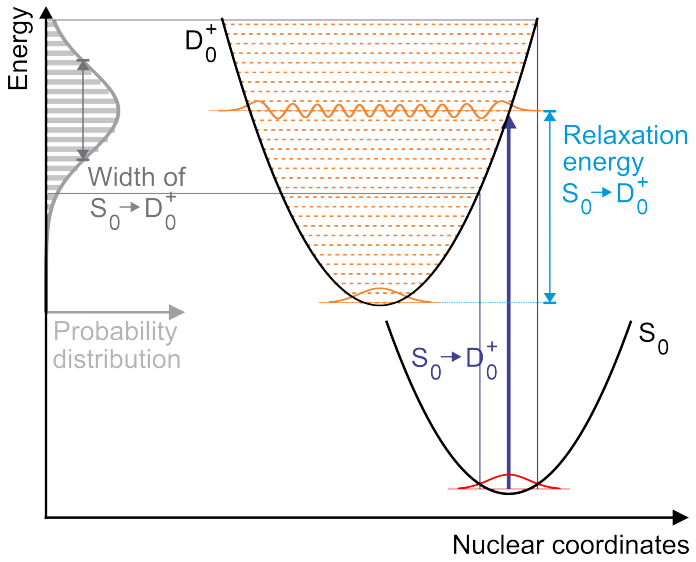

Figure 2.5.: Schematic illustrating the broadening of charge transitions. Schematic illustration of the broadening mechanism for the vertical $S_0 \rightarrow D_0^+$ transition depicted in Figure 2.4a. The probability of the vertical charge transitions depends on the wavefunction overlap of the ground and excited states[67]. These Franck-Condon factors (horizontal gray bars) become large for a range of higher-lying vibrational states (the wave function, for which the overlap with the ground-state wavefunction is largest, is shown exemplarily). Outside this range, the Franck-Condon factors are very small. Negligible overlap is present between the vibrational ground state of S_0 and the lowest-lying vibrational levels of D_0^+. Although there is an overlap with higher-lying vibrational states (above the top gray line), the overlap integral is small, since their wavefunctions are rapidly oscillating in the region of nuclear coordinates where the vibrational ground state is non-zero[63]. The vibrational levels for one phonon mode are schematically indicated (using the harmonic approximation). Since there are multiple phonon modes that can be excited, a Gaussian lineshape results (indicated at the left in gray). This schematic is based on a figure from ref. [53].

This is visualized in Figure 2.5 by the projection of the vibrational ground state of the initial electronic state (having a Gaussian shape) onto the slope of the parabola of the final electronic state. This projection can be justified by the fact that the Franck-Condon factors are dominated by the overlap with the maxima of the vibrational excited state wavefunctions, which are for the excited vibrational states localized around the edge of the parabola[63]. The overlap integral at other nuclear coordinates is small due to the rapid oscillations of the vibrational excited state wavefunctions[63]. The width of the resulting Gaussian-broadened signal depends on the relaxation energy[70]. According to Figure 2.5, a larger relaxation energy implies that the slope of the parabola on which the vibrational ground state is projected is larger, giving a larger width of the transition.

2.3.3.3. Charge detection with AFM

Next to STM, different charge states can also be detected with AFM. The advantage of AFM is that the surface can be insulating, allowing the stabilization of multiple charge states of, for instance, single molecules[75]. The presence of such single-electron charges will change the resonance frequency of the cantilever, by changing the electrostatic force gradient between the tip and sample[76]. Since the tip-sample junction can be modeled as a

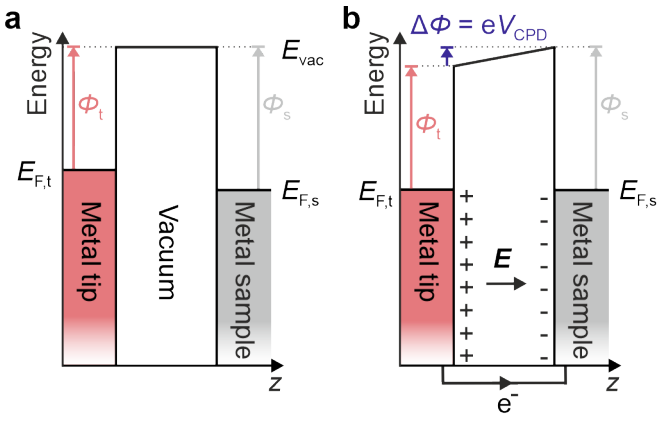

Figure 2.6.: Schematic illustrating the contact potential difference. **a**, If no electrical contact is present between tip and sample, their vacuum levels are aligned (E_{vac}), but their Fermi levels are generally not (E_F, where t and s indicate tip and sample). The latter arises from a difference in work functions of the tip and the sample. **b**, If the tip and sample are brought into electrical contact, electrons will flow from the lower work function electrode (tip) to the higher work function electrode (sample), aligning their Fermi levels. Charges will built up on the surfaces of the tip and sample, and thus an electric field exists in the tip-sample junction. The electrons will flow until the potential drop V_{CPD} because of the electric field equals the difference in work functions $\frac{1}{e}(\Phi_s - \Phi_t)$. This schematic is based on a figure from ref. [29]. Note that in the experiments throughout this thesis the tip and sample are in electrical contact and a (typically non-zero) bias voltage is applied to the sample.

capacitor with a distance dependent capacitance $C(z)$, the electrostatic force is given by[29]

$$F_{el} = -\frac{1}{2}\frac{\partial C(z)}{\partial z}\Delta V^2 \tag{2.14}$$

where the potential difference ΔV is given by the applied sample voltage V_{DC} corrected for the voltage of local contact potential difference V_{CPD}, as

$$\Delta V = V_{DC} - V_{CPD}. \tag{2.15}$$

The local contact potential difference arises from the difference in work functions Φ of the tip and sample: $V_{CPD} = \frac{1}{e}(\Phi_s - \Phi_t)$, as illustrated in Figure 2.6. The electrostatic force shifts the frequency of the cantilever according to Equations (2.12) and (2.14) by

$$\Delta f \approx \frac{f_0}{4k}\left.\frac{\partial^2 C(z)}{\partial z^2}\right|_{z=0}\Delta V^2. \tag{2.16}$$

Typically, measurements of charges on a surface with FM-AFM are performed by sweeping the applied sample voltage while recording the frequency shift, called Kelvin probe force spectroscopy (KPFS). According to Equation (2.16), a negative parabola will result, as schematically shown in Figure 2.7. Surface charges will vertically and horizontally shift this parabola[12].

A horizontal shift indicates a change in the local contact potential difference[76], since charges locally modify the work function of the surface. This can be explained by the fact that the charge of an adsorbate together with its image charge[77] in the substrate gives

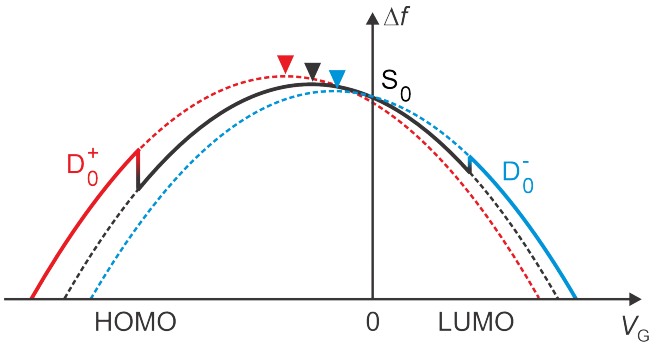

Figure 2.7.: KPFS parabolas for three states differing in their net charge. As an example, a molecule (e.g. pentacene/NaCl(>20 ML)/Ag(111)) is taken with S_0 as its ground state (black parabola). Upon reducing the applied gate voltage V_G, at some voltage an electron tunnels out of the HOMO ($S_0 \rightarrow D_0^+$ transition), charging the molecule positively (red parabola). Analogously, for positive gate voltage at some voltage an electron tunnels into the LUMO ($S_0 \rightarrow D_0^-$ transition), negatively charging the molecule (blue parabola). The three parabolas are shifted both vertically as well as horizontally. Their maxima are indicated by the triangles, the voltage at which these maxima occur corresponds to V_{CPD}. The size of these shifts depends on the molecule, the lateral and vertical tip position, the cantilever oscillation amplitude and the tip apex used. The solid line indicates the electronic state of the molecule for the different gate voltages. This schematic is based on a figure from ref. [18].

rise to a dipole moment, whose direction depends on the charge state of the adsorbate[12,78]. For example, for a positively charged adsorbate this dipole moment is oriented from the surface to the vacuum[78]. The resulting electrostatic field eases the removal of an electron and thereby decreases the work function of the sample and thus V_{CPD} (ref. [12, 78, 79]). Although the size of the horizontal shift depends on the tip termination, its direction was found to be determined by the charge state of the adsorbate[76].

The vertical shift of the KPFS parabola is mainly due to the interaction of the localized surface charge with the localized tip charges[76]. For instance, surface dipoles will be present in the tip due to its shape, arising from the Smoluchowksi effect[76,80]. Furthermore, the charge on the surface will also induce an image charge in the tip[12,76,81,82]. Not only the size but also the direction of the vertical shift can vary depending on the tip termination[18,76].

FM-AFM measurements of single charges were initially performed for localized states on an insulating surface[83–85] and different quantum dots[86–88]. In 2009, Gross et al. demonstrated the AFM detection of individual charged atoms[12], which was quickly extended to molecules[13]. This was followed by the measurement of charged atoms and molecules on thick insulating films[18,19,75,89–91], typically NaCl with a thickness of more than 20 ML. Steurer et al. experimentally confirmed that charge states were stabilized for more than 24 h on such thick NaCl films[18].

This inhibition of electron tunneling through the film allows the stabilization of multiple charge states. A voltage can be applied between the tip and the underlying metal substrate to control the alignment of the molecular levels with respect to the Fermi level of the tip, and thereby steer single-electron tunneling between the tip and the molecule (see next section for more details). In case of thin films, the applied voltage was called a bias voltage (V_B) since it drives a net current across the junction. In case of thick films, the applied

voltage is instead called a gate voltage (V_G). However, technically V_B and V_G are the same and both refer to the voltage applied to the substrate with respect to the tip.

Upon varying the gate voltage while measuring the frequency shift, at some gate voltages a sudden step in the frequency shift was observed[18,85]. This indicates that an electron tunneled to/from the molecule from/to the conductive tip[18,83,85]. In other words, the dependence of the frequency shift on the voltage is now described by the KPFS parabola corresponding to another charge state (shifted both vertically and horizontally), see Figure 2.7. Thus, by tuning the gate voltage, the charge state of adsorbates on insulating films can be changed, which can be observed in the frequency shift. At which gate voltage such tunneling events occur will be described in more detail in Section 2.3.3.5, after introducing the concept of voltage drop and possible tunneling pathways (on thin and thick insulating films) in the next section.

2.3.3.4. Voltage drop and tunneling for thin and thick insulating films

To quantitatively determine the energy at which single molecules change their charge state, it is important to take into account that part of the applied sample voltage will drop in an insulating film, reducing the voltage between tip and molecule. Such a voltage drop was first observed for a layer of upright standing molecules[92], before its effects on molecules adsorbed on insulating films were investigated[93]. In both cases, it was observed that the bias voltage was not only shifting the molecular levels with respect to the Fermi level of the tip, but also with respect to the Fermi level of the metal substrate.

On thin (2-5 ML) insulating films, such a shift of the molecular levels with respect to the Fermi level of the metal substrate can lead to the opening of additional substrate tunneling pathways, in particular, if at zero bias voltage the molecular levels are close to the Fermi level[93]. Figure 2.8a demonstrates the effect of the applied bias voltage in a double-barrier tunneling junction with a thin insulating film. The largest part of the voltage drops in the vacuum between the tip and the molecule. It opens thereby tip-molecule tunneling pathways (e.g. the dark blue arrow in Figure 2.8a). Such tip-molecule tunneling events are typically followed by tip-substrate tunneling events (e.g. the red arrow in Figure 2.8a), to bring the molecule back to the state(s) lowest in energy. Because of the voltage drop in the thin insulating film, the molecular levels also shift with respect to the metal substrate. The fraction of the voltage dropping in the vacuum we call the lever arm α (ref. [94]). Consequently, the voltage dropping in the thin insulating film is $(1-\alpha)V_B$, and is the amount by which the molecular levels shift with respect to the Fermi level of the metal substrate.

As introduced in Section 2.1, we will typically use a many-body energy diagram for the description of the states and their relative energy alignment. Such a diagram for the tunneling event in Figure 2.8a is shown in Figure 2.8b, including only the two relevant states. Since the substrate tunneling will always bring the molecule back to the state(s) lowest in energy, we choose the Fermi level of the metal surface as the reference energy in the many-body diagram for thin films. As indicated in orange in Figure 2.8a and b, the applied bias voltage shifts the energy levels with respect to the Fermi level of the surface by $-q(1-\alpha)V_B$, with q the net charge of the molecule. Tip-molecule tunneling channels open by the application of V_B, having a vertical component of up to qV_B in the many-body diagram. For example, the tunneling of an electron into the LUMO ($S_0 \rightarrow D_0^-$ transition)

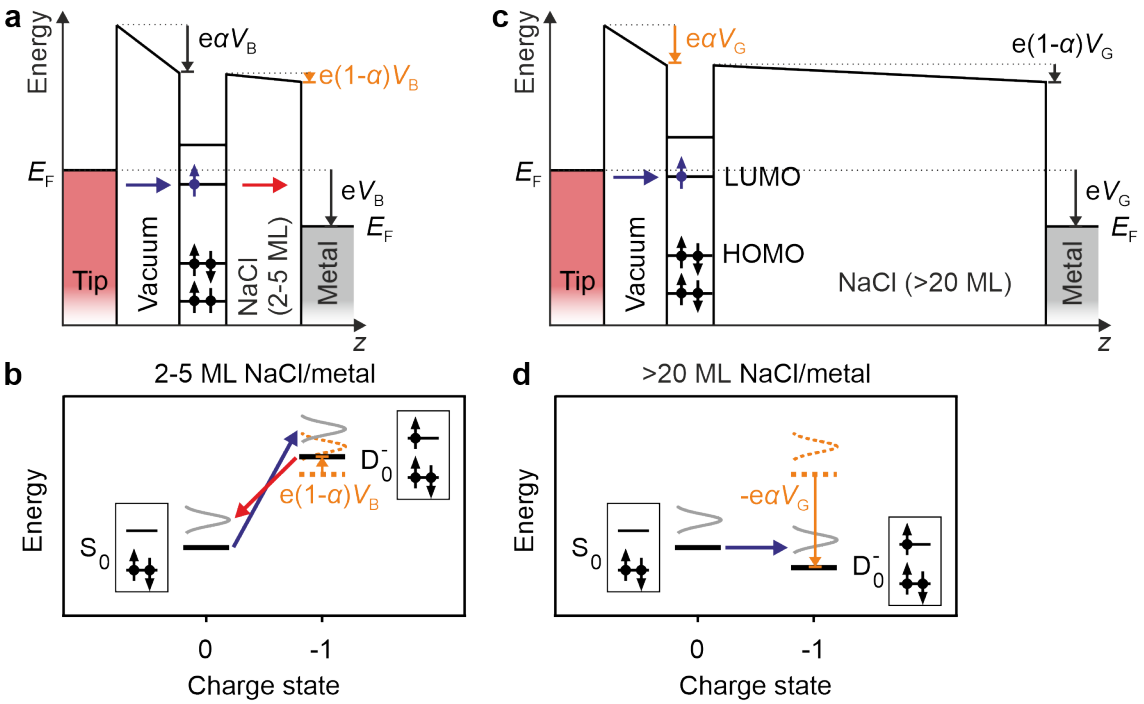

Figure 2.8.: Schematic illustrating the voltage drop in thin and thick insulating films. **a**, **c**, Schematic of the double-barrier tunneling junction for thin (2-5 ML) NaCl (**a**) and thick (>20 ML) NaCl (**c**). An applied voltage V_i (V_i is the bias V_B (**a**) or gate V_G (**c**) voltage) shifts the molecular levels with respect to the Fermi level of the tip and substrate. A part of V_i, i.e., $(1-\alpha)V_i$, drops in the NaCl film, and the remainder, i.e., αV_i, drops in the vacuum between tip and molecule. In the situation displayed, the applied voltage enables tunneling of an electron from the tip to the LUMO (dark blue arrow). On thin films (**a**), the molecule will be quickly brought back to its ground state (here S_0) by substrate-molecule tunneling (red arrow). To simplify these illustration, it implies that at $V_B = 0$ (**a**) and $V_G = 0$ (**c**) there is no electric field in the junction - without loss of generality for other situations. **b**, **d**, Many-body energy diagrams displaying the same tunneling processes as in **a**, **c**, respectively. The reference energy for the many-body energy diagram on thin and thick films is chosen to be the Fermi level of the metal substrate and tip, respectively. The shifts of the energy levels due to applied sample voltage are indicated in orange, they are due to the shifts in the molecular levels with respect to the Fermi energy of the reference electrode (indicated in orange in **a**, **c**). Note that the molecular levels shift upwards (downwards) with respect to the Fermi level of the substrate (tip), explaining the difference in sign of the shifts in the energy levels. In the many-body diagram on thin films (**b**), V_B allows tip-molecule tunneling events that increase the energy by maximally eV_B (dark blue arrow), tip-substrate tunneling events correspond to a transition going downward in the many-body diagram (red arrow). In the many-body diagram on thick films (**d**), tip-sample tunneling events correspond to transitions that go downward in the many-body diagram (dark blue arrow). The rotated Gaussians in the many-body energy diagrams (gray) indicate the nuclear component of the transition rate (see Section 2.3.3.5); the offset between the Gaussians' maxima and energy levels visualizes the relaxation energy, see Figure 2.5. The charge transitions start at a vibrational ground state (black lines) and end in an excited vibrational state with an energy within the indicated Gaussians, after which the system relaxes to the vibrational ground state of the newly populated electronic state.

is indicated by the dark blue arrow in Figure 2.8b. The possible tunneling events between the molecule and metal substrate are indicated by downward transitions in the many-body diagram (e.g. the red arrow in Figure 2.8b). Typically, substrate tunneling will bring the molecule quickly to the state(s) lowest in energy in the many-body diagram.

The rotated Gaussians in these many-body diagrams (gray) indicate the broadening of the transitions due to electron-phonon coupling[70], as explained in Section 2.3.3.2. The charge transitions start from a vibrational ground state and end in an excited vibrational state with an energy within the indicated Gaussians (see for more details Section 2.3.3.5). Subsequently, the system will quickly relax to the vibrational ground state of the newly populated electronic state. The offset between the Gaussians' maxima and these ground states visualizes the relaxation energy (see Section 2.3.3.1).

Figure 2.8c shows the double-barrier tunneling junction for thick (>20 ML) insulating films. As indicated in the previous section, such films suppress tunneling between the molecule and the underlying metal substrate. Figure 2.8d shows how the gate voltage controls the alignment of the molecular levels with respect to the Fermi level of the tip and thereby steers single-electron tunneling between the tip and the molecule. The shift of the molecular levels with respect to the tip is given by αV_{G}.

Since on thick (>20 ML) insulating films only tunneling between molecule and tip is possible, we choose in the many-body description the Fermi level of the tip as the reference energy for electron tunneling. A tip-sample tunneling event is therefore indicated by an arrow going downwards in the many-body diagram (e.g. dark blue arrow in Figure 2.8d). The gate voltage steers such tip-sample tunneling events by shifting the states by $q\alpha V_{\mathrm{G}}$ with q being the net charge of the molecule, thus shifting the positive (+) and negative (−) charge states in opposite directions.

2.3.3.5. Charging hysteresis

As indicated in Section 2.3.3.3, single atoms and molecules on thick insulating films can be brought to states with different net charge by changing the gate voltage. Figure 2.9a shows measured Δf signals versus the applied gate voltage for a pentacene molecule on >20 ML NaCl/Ag(111). Two steps in Δf are observed in opposite directions, indicating that an electron tunneled out of the molecule and back into the molecule. Importantly, this second step is occurring at a different voltage than the first one[85], because of the relaxation of the molecule and the underlying surface (see Section 2.3.3.1)[18,58]. In other words, a hysteresis is observed in the Δf signal[19,84,85]. This hysteresis becomes smaller upon reducing the tip-sample distance[85], and is even observed to disappear for small distances (see yellow curve in Figure 2.9a).

Next to the tip-sample distance, the observed width of the hysteresis depends on other experimental parameters, such as the change of the gate voltage per unit time, and on the properties of the studied molecule and surface (e.g. relaxation energy and electron-phonon broadening). In the following, the origin of the observed hysteresis as well as its dependence on the tip-sample distance will be discussed.

Considering the tunneling of one electron (in or out of the molecule), the probability that the electron tunneled in a certain time interval will depend on the rate of the tunneling process k_{tun}. k_{tun} has an electronic k_{el} and nuclear k_{nuc} component: $k_{\mathrm{tun}} = k_{\mathrm{el}} \cdot k_{\mathrm{nuc}}$. The electronic contribution was discussed in Section 2.2 and is exponentially dependent on the

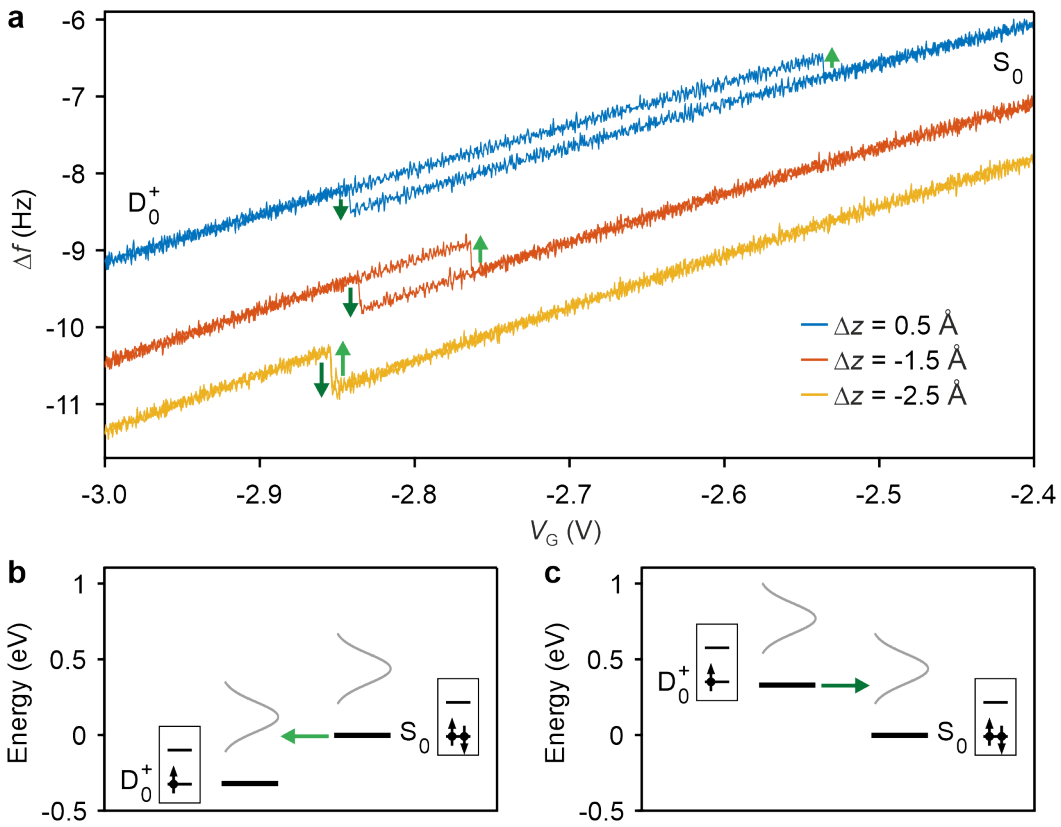

Figure 2.9.: Charging hysteresis observed in KPFS. a, KPFS curves measured above a pentacene molecule adsorbed on NaCl(>20 ML)/Ag(111) (oscillation amplitude $A = 1$ Å, Δz is given with respect to the setpoint $\Delta f = -1.285$ Hz at $V = 0$ V, $A = 3$ Å, negative values indicate a smaller tip-sample distance). The curves were measured by sweeping the gate voltage from −2.4 to −3.0 V and back in a time interval of 20 s. Upon sweeping the voltage to −3.0 V, an upwards step is observed (light green arrow), which is attributed to $S_0 \rightarrow D_0^+$ (see **b**). When sweeping the voltage back to −2.4 V, a downward step is observed (dark green arrow), which is attributed to $D_0^+ \rightarrow S_0$ (see **c**). The hysteresis is observed to reduce in width (and even collapses) for smaller tip-sample distances. **b**, **c**, Many-body energy diagrams displaying the tunneling processes that cause the upwards and downwards steps in **a**, respectively. At the tip-sample distances typically used throughout this thesis, tunneling occurs into an excited vibrational state with an energy within the drawn Gaussians (corresponding to the nuclear component of the transition rate).

tip-sample distance. The nuclear contribution (Franck-Condon overlap) is strongly voltage dependent; as discussed in Section 2.3.3.2.

In Figure 2.9b and c, this nuclear component of the tunneling rate is plotted in the many-body diagram of pentacene. Since this tunneling rate is very small around the charging degeneracy point (the gate voltage at which the two states have the same energy), for pentacene typically no charging steps are observed around this gate voltage for typically used tip-sample distances of around 9 Å. This blocking of tunneling events due to the very small Franck-Condon overlap is called the Franck-Condon blockade[95]. In contrast, if a gate voltage is applied for which the D_0^+ state is substantially below the S_0 state, the tunneling rate and thus tunneling probability is large, such that it is likely that a charging event occurs in the short time interval during which this gate voltage is applied (during the gate voltage sweep to measure a KPFS curve). Similarly, upon reversing the gate voltage, the

tunneling probability is sufficiently large (to make tunneling likely to occur) for an applied gate voltage for which the S_0 state is substantially below D_0^+ (see Figure 2.9c).

If the tip-sample distance is reduced, k_{el} and hence the tunneling rates will (exponentially) increase. The resulting increase in tunneling probability will make tunneling likely around a gate voltage closer to the charging degeneracy point. This results in a hysteresis with a smaller width. The width is further reduced by the varying tip-molecule voltage during a cantilever period, due to the modulation of the lever arm (see Section 2.3.3.4). At close tip-sample heights, the tunneling probability will not only be sufficiently large (to make tunneling likely to occur) at the bottom turnaround point of the cantilever movement, but also at different phases during the cantilever period (assuming small cantilever oscillation amplitudes). In other words, tunneling can occur at a small range of tip-molecule voltages for a given applied gate voltage, further reducing the width of the hysteresis.

The voltage drop in the salt also causes the observed shift of the center of the hysteresis to higher absolute voltages when reducing the tip-sample distance[85] (see Figure 2.9a). This can be explained by a larger fraction of the voltage that will drop into the NaCl film for a smaller tip-sample distance (the lever arm α is smaller), requiring a higher gate voltage for tunneling.

2.4. Electron Spin Resonance

In the context of this thesis, a method is developed to measure Electron Spin Resonance (ESR) signals of single molecules with AFM. ESR is a spectroscopic method that relies on driving transitions between states that differ in their spin configuration, as first experimentally demonstrated in 1945 by Zavoisky[96]. Typically, molecules with one unpaired electron are studied, having an electron-spin quantum number of 1/2. Upon applying a magnetic field $\boldsymbol{B}$, the two spin states with magnetic quantum numbers $m_s = -1/2$ and $m_s = 1/2$ split up in energy because of the Zeeman interaction (see Figure 2.10). The Hamiltonian $\boldsymbol{\mathcal{H}}_Z$ for this interaction is given by[97]

$$\boldsymbol{\mathcal{H}}_Z = g_e \mu_B \boldsymbol{S} \cdot \boldsymbol{B} \tag{2.17}$$

where g_e is the electron g-factor, μ_B the Bohr magneton and $\boldsymbol{S}$ the electron spin operator with electron-spin quantum number S (ref. [97]) (note that Equation (2.17) is only valid when the spin-orbit interaction is weak compared to the Zeeman interaction). Transitions between different spin states can be driven by an electromagnetic field with a frequency that matches the energy difference between the states. Typically, the required frequencies lie in the radio-frequency (RF) regime. By recording the absorption of the RF field versus the RF frequency, an ESR spectrum can be measured.

ESR spectra can provide access to the electronic g-factors and thereby the electronic spin distribution[98]. The coupling of the electron spins to the nuclear spins can also be detected, allowing further structural elucidation. Furthermore, ESR can provide access to the environment of the unpaired electrons and can gives insights into chemical reactions (e.g. their rates and the detection of short-lived intermediates)[98]. Next to organic radicals, ESR has been widely applied to transition metals (e.g. catalysts), biologically relevant systems, defects in solids, metals and semiconductors[97,99].

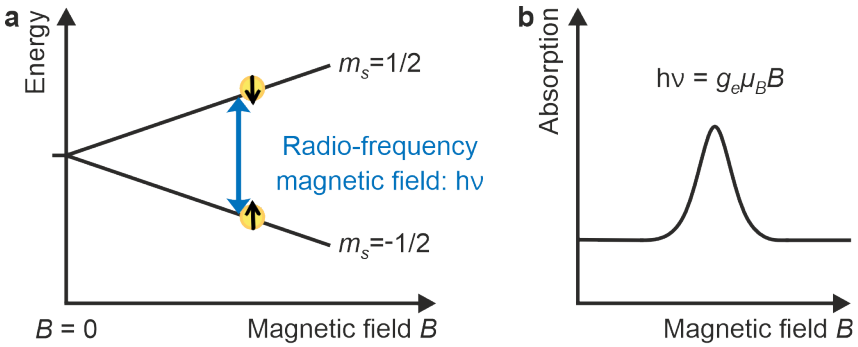

Figure 2.10.: Basic principles of ESR. a, Effect of a magnetic field on a spin with $S = 1/2$. At zero magnetic field the two spin states are degenerate. Upon applying a magnetic field B, the two spin states split up in energy because of the Zeeman interaction. Using a radio-frequency magnetic field that matches in energy with the energy splitting between the states, transitions can be driven between the two spin states. **b**, An ESR spectrum is measured by sweeping the magnetic field at a fixed RF frequency (or vice versa). If the resonance condition is met (the Zeeman energy, $g_e\mu_B B$, equals the energy of the RF, $h\nu$), the RF will be absorbed by the spin system. For illustration purposes, the spectrum in **b** is schematically shown as an absorption signal. In contrast to that, in most experiments amplitude modulation is employed to improve the signal-to-noise ratio, providing a signal proportional to the derivative of absorption as a function of field[97].

2.4.1. Zero-field triplet state ESR

Next to molecules with a non-zero spin in their ground state, ESR can also be applied to molecules that can (temporarily) be brought to a state with a non-zero spin. Most commonly, the molecule is excited to its first excited triplet state. Such triplet state ESR at zero magnetic field is implemented in AFM in the context of this thesis, and therefore the triplet substates are discussed in more detail in this section.

Hutchison et al. were the first to detect an ESR spectrum of a molecule in its triplet state[100]. In the presence of a magnetic field, the three triplet substates split because of the Zeeman interaction (Equation (2.17)). The eigenstates of this Hamiltonian are in the basis of magnetic quantum numbers $m_S = -1$, 0 and +1:

$$\mathrm{T}_{-1} = |{\downarrow\downarrow}\rangle, \mathrm{T}_0 = \frac{|{\uparrow\downarrow}\rangle + |{\downarrow\uparrow}\rangle}{\sqrt{2}} \text{ and } \mathrm{T}_{+1} = |{\uparrow\uparrow}\rangle. \tag{2.18}$$

Hutchison et al. found that even at zero-magnetic field, the triplet substates are split in energy[100]. This so called zero-field splitting is mainly due to the magnetic dipole-dipole interaction between the two electron spins. It may also have contributions from spin-orbit interaction[101]. The dipole-dipole interaction is described by the Hamiltonian[102]

$$\mathcal{H}_{\text{d-d}} = \boldsymbol{S}\mathbf{D}\boldsymbol{S} = -\frac{\mu_0\gamma_e^2\hbar^2}{4\pi r^3}(3(\boldsymbol{S}_1\cdot\hat{\boldsymbol{r}})(\boldsymbol{S}_2\cdot\hat{\boldsymbol{r}}) - \boldsymbol{S}_1\cdot\boldsymbol{S}_2) \tag{2.19}$$

with the two spins $\boldsymbol{S}_1$ and $\boldsymbol{S}_2$ at a distance r in a relative direction $\hat{\boldsymbol{r}} = \boldsymbol{r}/r$, $\mathbf{D}$ the dipole-dipole-interaction tensor, μ_0 the magnetic constant, γ_e the electron gyromagnetic ratio, $\hbar$ the reduced Planck constant and $\boldsymbol{r}$ the vector connecting the two spins. Notably, the

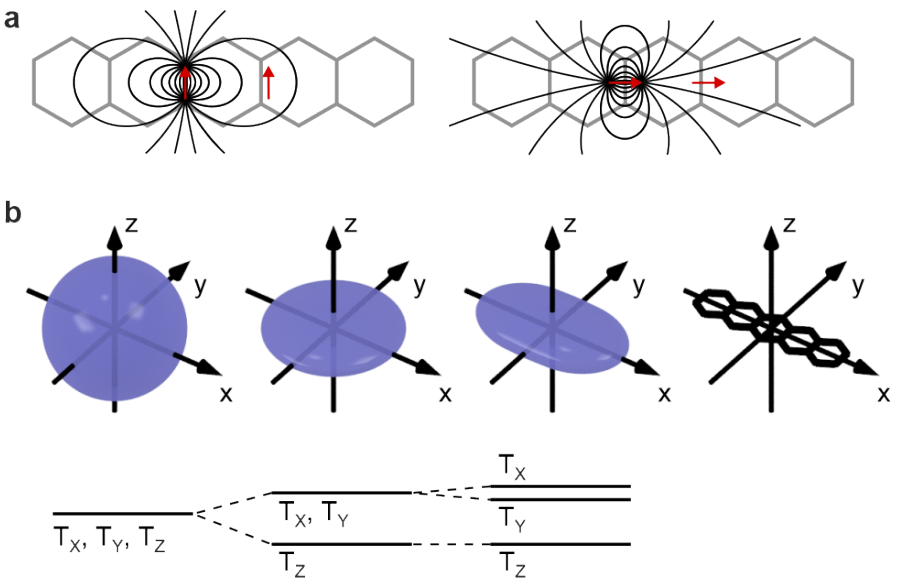

Figure 2.11.: Explanation of the zero-field splitting. **a**, Schematic illustration of the anisotropic nature of the magnetic dipole-dipole interaction (black field lines) between the two spins (red arrows) constituting the triplet state, as shown for the case of pentacene (gray molecular skeleton). **b**, For a spherical density distribution of the two electrons, the three triplet substates T_X, T_Y and T_Z are degenerate. However, for an oblate density, the probability distribution of the electrons' mutual distance differs in the different spatial directions. In this case, because of the anisotropy of the dipole-dipole interaction, the alignment of the spins with respect to the spatial directions matters and T_Z splits off in energy. For a probability distribution that differs in all three dimensions, the degeneracy of all three substates (T_X, T_Y and T_Z) is lifted. The x, y and z directions refer to the axes of **D** as explained in Section 2.4.1, and depicted here for pentacene[103].

magnetic dipole-dipole interaction is highly anisotropic, that is, for given spin orientations, it strongly differs and even changes sign for different relative positions of the two spins (see Figure 2.11a). The spatial positions of the electron spins are given by the orbital densities of the two electrons, the confinement of which is for a typical molecule very different along the three molecular axes. This is shown in Figure 2.11b for the example of pentacene. The anisotropy of the dipole-dipole interaction together with the non-uniformity of the orbital densities gives rise to an energy difference in the range of microelectronvolts for the spins pointing in different real-space dimensions. This zero-field splitting is thus a fingerprint of the orbital densities and thereby the molecular species.

At zero magnetic field, the corresponding eigenstates are no longer T_{-1}, T_0 and T_{+1} but T_X, T_Y and T_Z. The latter eigenstates expressed in the basis of the former read

$$T_X = \frac{T_{-1} - T_{+1}}{\sqrt{2}}, T_Y = \frac{(T_{-1} + T_{+1})i}{\sqrt{2}} \text{ and } T_Z = T_0, \tag{2.20}$$

whereas expressed as the states of the two individual spins $|m_{s1}m_{s2}\rangle$, they are

$$T_X = \frac{|\downarrow\downarrow\rangle - |\uparrow\uparrow\rangle}{\sqrt{2}}, T_Y = \frac{i(|\downarrow\downarrow\rangle + |\uparrow\uparrow\rangle)}{\sqrt{2}} \text{ and } T_Z = \frac{|\uparrow\downarrow\rangle + |\downarrow\uparrow\rangle}{\sqrt{2}}. \tag{2.21}$$

Further, they have the property that the expectation value of the total spin $\langle \mathrm{T}_i|\mathbf{S}|\mathrm{T}_i\rangle$ vanishes for all three substates $\mathrm{T}_{i=\mathrm{X,Y,Z}}$, whereas $\left\langle \mathrm{T}_i\middle|\mathbf{S}_j^2\middle|\mathrm{T}_i\right\rangle = 1 - \delta_{ij}$, with $\delta_{ij} = 0$ for $i \neq j$ and 1 for $i = j$. The x, y and z axes of the triplet substates are chosen along the axes of $\mathbf{D}$, where the z axis is defined as the axis of maximum attractive or repulsive dipolar coupling, and thus the axis along which the electron density is the most or the least confined[104,105]. The example where the electron density is the most confined along the z axis is shown in Figure 2.11. To understand why the $\mathrm{T_Z}$ substate is the lowest in energy in this case, it is important to realize that the unpaired spins in the $\mathrm{T_Z}$ substate are pointing in the x-y plane and analogously for the $\mathrm{T_Y}$ and $\mathrm{T_X}$ substates (this follows directly from the above stated expectation values). For an electron density that is the most confined along the z axis, the spins in $\mathrm{T_Z}$ can interact (overall) attractively, while those in $\mathrm{T_X}$ and $\mathrm{T_Y}$ interact (overall) repulsively (due to the anisotropy of the dipolar interaction, see Figure 2.11a). Therefore, the energy of $\mathrm{T_Z}$ is the lowest. In general, due to the definition of the axes of $\mathbf{D}$ the largest energy difference exists between $\mathrm{T_X}$ and $\mathrm{T_Z}$, and the smallest between $\mathrm{T_X}$ and $\mathrm{T_Y}$ (ref. [104]).

Since the expectation value of the total spin vanishes, the triplet substates are relatively insensitive to external perturbations; an external magnetic field affects the system and energies only to the second order. The effect of a small magnetic field on the zero-field triplet substates can be appreciated from writing the spin Hamiltonian for the zero-field splitting (Equation (2.19)) and an external magnetic field $\boldsymbol{B}$ (Equation (2.17))

$$\boldsymbol{\mathcal{H}} = \boldsymbol{S}\mathbf{D}\boldsymbol{S} + g_e\mu_B\boldsymbol{S}\cdot\boldsymbol{B}, \tag{2.22}$$

explicitly in the basis of the zero-field split substates $\mathrm{T_X}$, $\mathrm{T_Y}$ and $\mathrm{T_Z}$:[102]

$$\boldsymbol{\mathcal{H}} = \begin{pmatrix} \epsilon_\mathrm{X} & -ig_\mathrm{e}\mu_\mathrm{B}B_\mathrm{Z} & ig_\mathrm{e}\mu_\mathrm{B}B_\mathrm{Y} \\ ig_\mathrm{e}\mu_\mathrm{B}B_\mathrm{Z} & \epsilon_\mathrm{Y} & -ig_\mathrm{e}\mu_\mathrm{B}B_\mathrm{X} \\ -ig_\mathrm{e}\mu_\mathrm{B}B_\mathrm{Y} & ig_\mathrm{e}\mu_\mathrm{B}B_\mathrm{X} & \epsilon_\mathrm{Z} \end{pmatrix}. \tag{2.23}$$

Here, ϵ_X, ϵ_Y and ϵ_Z are the zero-field energies of $\mathrm{T_X}$, $\mathrm{T_Y}$ and $\mathrm{T_Z}$, respectively. With increasing external magnetic field, the eigenstates will gradually change and asymptotically become the states T_{-1}, T_0 and T_{+1} in the limit of large magnetic fields (for example see Figure 2.12).

2.4.2. Hyperfine interaction

The most important source of chemical information in ESR spectra is due to the coupling of nuclei with non-zero spin to the electron spins[97,106], such as ^{1}H and ^{13}C. The Hamiltonian of this so called hyperfine interaction (HFI) is given by[103,107]

$$\boldsymbol{\mathcal{H}}_\mathrm{HFI} = \sum_i \boldsymbol{S}_i\cdot\mathbf{A}^i\cdot\boldsymbol{I}_i \tag{2.24}$$

with $\mathbf{A}^i$ the hyperfine interaction tensor of nucleus i and $\boldsymbol{I}_i$ the nuclear spin operator of nucleus i.

Here, we will discuss the effect of the hyperfine interaction on zero-field triplet state ESR spectra, as will be measured in the context of this thesis. First, an explanation will be given

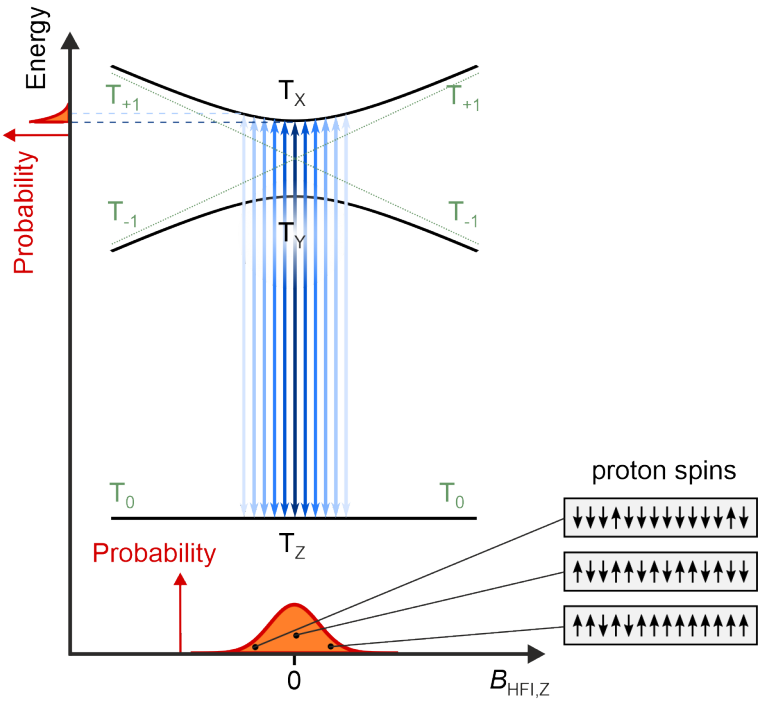

Figure 2.12.: Explanation of the asymmetric lineshape. Schematic to explain the asymmetric lineshape of the ESR-AFM signals due to the hyperfine interaction, for the example of the T_X-T_Z transition of pentacene-h_{14}. The hyperfine interaction can be described as an effective magnetic field $\boldsymbol{B}_{\mathrm{HFI}}$ created by the nuclei acting on the electron spins. Owing to the random orientation of the 14 proton nuclear spins in pentacene-h_{14} (right), $\boldsymbol{B}_{\mathrm{HFI}}$ will fluctuate around zero-field and its probability distribution for the z component is depicted (orange, bottom). Note that the z component has in this case the largest influence on the lineshape, as explained in the Section 2.4.2. The T_X and T_Y substates show a hyperbolic energy dependence (top) as a function of a magnetic field in the z direction, $B_{\mathrm{HFI,Z}}$. Weighting the different transition frequencies (blue double-headed arrows) with the probability distribution of $B_{\mathrm{HFI,Z}}$ gives rise to the asymmetric lineshape as schematically illustrated for the T_X-T_Z transition by the projection onto the energy axis (orange, top left).

along the schematic shown in Figure 2.12. The hyperfine interaction can be described as an effective magnetic field $\boldsymbol{B}_{\mathrm{HFI}}$ created by the nuclei with non-zero spin acting on the electron spins. Every spin can either contribute a positive or negative value to $\boldsymbol{B}_{\mathrm{HFI}}$ depending on its orientation. Assuming a random orientation of a large number of nuclear spins at a given point in time, which act together at random, the probability distribution of $\boldsymbol{B}_{\mathrm{HFI}}$ has its maximum around zero and falls off toward larger absolute values, as is shown at the bottom of Figure 2.12.

To understand how this magnetic field distribution affects the zero-field split ESR signals, it is important to understand how the energies of the triplet substates change as a function of magnetic field. As explained in the previous section, at zero magnetic field, the T_X, T_Y and T_Z substates are split in energy only by the zero-field splitting, while at finite magnetic fields, the Zeeman interaction further splits the substates (see Equation (2.23)). If the splitting due to the Zeeman interaction dominates the zero-field splitting, the triplet substates are given by T_0, T_{+1} and T_{-1}. In the intermediate regime, for a magnetic field

along the z direction, the T_X and T_Y substates show a hyperbolic energy dependence as a function of magnetic field, as depicted in Figure 2.12 (analogously for the other directions).

Knowing this triplet-state energy dependence, the effect of a $\boldsymbol{B}_{\mathrm{HFI}}$ distribution on the zero-field ESR spectra can be graphically understood. For example, upon driving a transition between T_X and T_Z in the presence of a $\boldsymbol{B}_{\mathrm{HFI}}$ with a (Gaussian) probability distribution in the z direction, a signal will be observed at the transitions frequencies indicated by the blue arrows in Figure 2.12. Weighting the different transition frequencies with the probability distribution of $B_{\mathrm{HFI,Z}}$ results in an asymmetric lineshape as schematically illustrated by the projection onto the energy axis (Figure 2.12: top left).

Note that so far we only considered the $\boldsymbol{B}_{\mathrm{HFI}}$ component in the z direction, $B_{\mathrm{HFI,Z}}$. Figure 2.12 demonstrates that the curvature around $B_{\mathrm{HFI}} = 0$ of the hyperbolic avoided crossing is responsible for the asymmetric broadening. This curvature is inversely proportional to the energy difference of the respective pair of substates. As, per definition, the T_X-T_Y transition has the smallest energy splitting of all possible pairs[104] (see Section 2.4.1), the broadening is typically dominated by their avoided crossing occurring along the z component of $\boldsymbol{B}_{\mathrm{HFI}}$ (ref. [103])). For example, for pentacene the energy difference is larger by roughly one order of magnitude in the other two directions.

So far, it was implicitly assumed that all the nuclear spins couple with a similar strength to the electron spins. In reality, the coupling is largely dependent on the nuclear isotope and its location in the molecule. To understand how the hyperfine interaction depends on these factors, we will look at the two different contributions to the hyperfine coupling: the dipole-dipole interaction between the electron and nuclear spins and the Fermi-contact interaction, which is proportional to the electron spin density at the nucleus[106]. Both of these terms depend on the nuclear isotope since they are proportional to g_n, the g-factor of the nucleus[106]. In first approximation, the Fermi-contact term for unpaired electrons in π orbitals of planar aromatic molecules, studied in the context of this thesis, vanishes for both the aromatic ^{13}C and ^{1}H nuclei, since they lie at the nodal x-y plane of the π orbitals[106]. However, the unpaired electrons polarize the electrons in the inner-shell s atomic orbitals of the carbons and the σ bonds, creating a finite spin polarization at the ^{13}C and ^{1}H nuclei[106]. The second term of the hyperfine interaction, the dipole-dipole interaction, is anisotropic and scales with $1/r^3$ with r the distance between the unpaired electron and the nucleus (see Equation (2.19)). The dipole-dipole interaction term depends thus strongly on the relative orientations of the nuclear and electron spins and their distance.

To take these different contributions to the hyperfine interaction into account, we use that for planar aromatic molecules the hyperfine interaction tensor $\mathbf{A}^i$ is in good approximation proportional to the spin density at the carbon atom ρ_j, where the ^{13}C nucleus i is, or to which the ^{1}H nucleus i is bound: $\mathbf{A}^i = \rho_j \mathbf{Q}^i$, with $\mathbf{Q}^i$ the hyperfine interaction tensor of nucleus i if $\rho_j = 1$ (ref. [106–108]). Since $\boldsymbol{\mathcal{H}}_{\mathrm{HFI}}$ (Equation (2.24)) is small compared to $\boldsymbol{\mathcal{H}}_{\mathrm{d.d.}}$ (Equation (2.19)), it can be treated by perturbation theory to derive a formula for the shifts of the zero-field split energy levels due to the hyperfine interaction[103,109]. The first order perturbation term vanishes, since in zero-magnetic field the expectation value of $\boldsymbol{S}_i$ is zero for the zero-field triplet substates (see Section 2.4.1). The hyperfine interaction thus contributes only to second order to the zero-field ESR spectra. Assuming as above a molecule for which T_X and T_Y are close together in energy compared to T_Z, the leading

terms of the shifts of the energy levels follow as[103,107,109]

$$\Delta E_x = \frac{\left(\sum_i m_i \rho_i Q^i_{zz}\right)^2}{E_x - E_y},\ \Delta E_y = \frac{\left(\sum_i m_i \rho_i Q^i_{zz}\right)^2}{E_y - E_x} \text{ and } \Delta E_z \approx 0. \tag{2.25}$$

Here, the sum runs over the nuclear spins in the molecule, which are presented here in their usual basis quantized along the molecular z axis[107]. m_i is the magnetic quantum number of nucleus i. For example, for a nuclear spin with a nuclear-spin quantum number $I = 1/2$, $m_I = 1/2$ (spin up) or $-1/2$ (spin down). These formulas mathematically express how the hyperfine coupling of a certain number of nuclear spins gives rise to the observed ESR-AFM lineshapes. For example, the broadening of the T_X-T_Z transition results from ΔE_x, since $\Delta E_z \approx 0$. This formula predicts similarly as derived above that the ESR-AFM signals for a large number of (similar) nuclear spins have an abrupt onset with a decaying tail. For example, for a nuclear spin with $I = 1/2$, there is a large probability of having roughly equally many spins in the $m_I = 1/2$ and $-1/2$ states, and a small probability of finding most of the nuclear spins in the same state[107] (see also bottom of Figure 2.12).

3. Controlled single-electron transfer enables time-resolved excited-state spectroscopy of individual molecules

The results presented in this chapter have been obtained and interpreted in collaboration with Jakob Eckrich, Andrea Donarini, Leo Gross and Jascha Repp. Most of the text and figures are based on those in a manuscript that is currently under review.

3.1. Introduction

The combination of scanning-probe microscopy with an increasing number of spectroscopic techniques provides spectacular insights into the properties of individual molecules at their intrinsic atomic scale. Examples of such pioneering single-molecule studies with atomic-scale local information encompass structure determination[4], orbital density imaging[3], ultrafast spectroscopy at an approximately 100 fs timescale[110] and electron-spin resonance[22,111]. In particular, the integration of optical spectroscopy into local-probe microscopy such as Raman[112] and electro-[15–17] and photo-induced[113–116] luminescence has recently provided breathtaking atomic-scale insights into light-matter interaction: theoretical concepts can now be tested and visualized directly in real-space providing an understanding of the fundamental processes in light emission from organic materials[117]. Examples of such processes are the dipole-dipole coupling[118,119] and energy transfer[16,120] between individual molecules.

Despite its very direct access to well-defined single-molecule model systems, the unambiguous assignment of observations to specific electronic quantum transitions is not always straightforward. One issue is that in scanning tunneling spectroscopy (STS) a tip-to-molecule tunneling event is typically followed by a quick molecule-to-substrate tunneling event, and the two events are not detected separately. In other words, the molecule typically reverts to its ground state. However, in some cases, a second electron can tunnel into the molecule starting from a transient charge state. The discrimination of such multiple charging effects from the population of an energetically higher-lying excited state is, therefore, usually difficult[35,121]. For example, in STS a feature at a higher bias voltage than required for tunneling into the LUMO might be associated to either electron attachment into the LUMO+1 or to tunneling of a second electron into the LUMO starting from a transient charge state. Next to the ambiguity related to the assignment, many charge transitions are typically not observable, since the molecule typically quickly reverts back to its ground state. It is, therefore, often hard to access states that require multiple tip-molecule tunneling events (see Figure 3.1).

Detecting and identifying some of the states that can be formed after multiple tunneling events was made possible by the above-mentioned combination between luminescence and

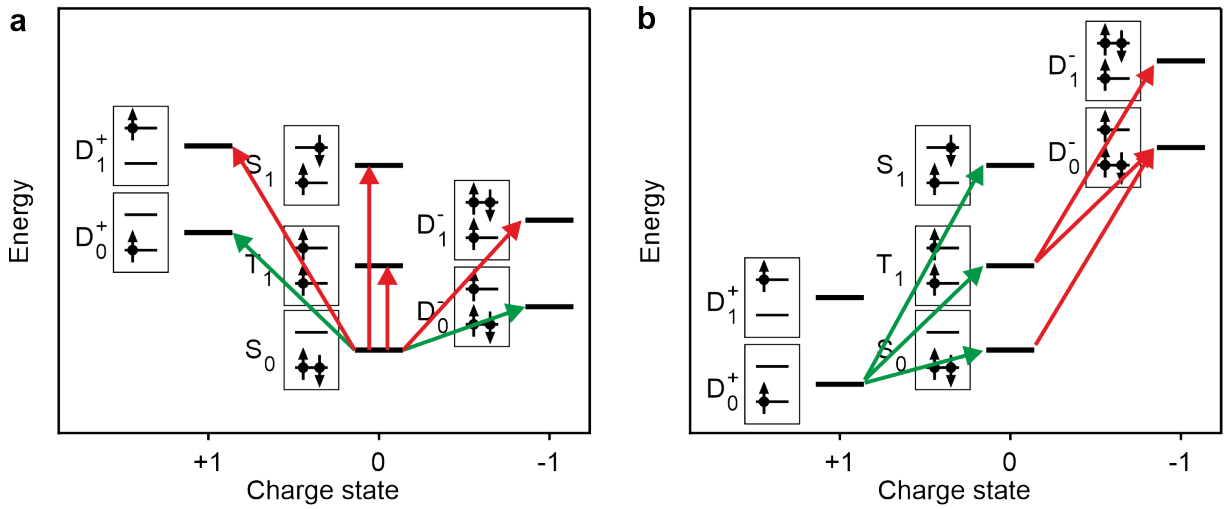

Figure 3.1.: Typically observable transitions in STS. Many-body energy diagrams (see Section 2.1) for two different hypothetical molecules with a different ground state: S_0 (**a**) and D_0^+ (**b**). The green arrows show the typically observed transitions in STS, while the red arrows show transitions that are typically not observed. Note that the states typically have a multi-reference character, meaning that (small) components of other states are mixed in; this could allow additional transitions, which are neglected here because of their typically low probability. **a**, If the ground state is S_0, from the shown states only D_0^+ and D_0^- can be accessed directly via a single-electron tunneling event. The other states can only be accessed indirectly, typically via other states and often requiring multiple tunneling events[122,123], which makes it challenging to access their energies. **b**, If the ground state is D_0^+, transitions to S_0, T_1 and S_1 are possible via single-electron tunneling processes; the other drawn states can only be reached via a transient neutral state. Although such two-electron tunneling processes are typically much less likely (since typically a quick molecule-substrate tunneling brings the molecule back in the D_0^+ state), they can in principle also occur and can be hard to distinguish from a single-electron tunneling processes.

scanning tunneling microscopy[15,121], called STM-induced luminescence (STML). In STML, the molecule is brought to an excited state by electron tunneling and decays via the emission of a photon, which is collected in the far field[117]. The applications of STML are continuously expanding and include next to the above-mentioned study of energy transfer[16,120] and coherent intermolecular dipole-dipole coupling[118,119], also the study of excitons in charged molecules[17,123], photon cascades[122], chemical reactions[124,125] and the sensing of the atomic environment[126,127].

Still, studying the individual electronic transitions separately with STML remains out of reach, since several electronic transitions lead to one spectral feature. That is why the interpretation of these spectral features in STML is also not always straightforward. For example, the assignment of an STML signal as phosphorescence or trion-related fluorescence is contradictory in recent literature[128,129]. To access the energies of such transitions, we introduce a new single-molecule AFM spectroscopy that relies on the shuttling and detection of single electrons.

Already in 1990, single electrons were detected with AFM[82]. The direct observation of their tunneling between the tip of an AFM and a surface was demonstrated in 2001 (ref. [130]). This led to the development of a single-electron spectroscopy with AFM[85], as well as approaches to image the populated localized states[131,132].

Gross et al. enabled the extension of these concepts to single atoms and molecules. In 2009, they demonstrated the detection of single-electron charges on single atoms[4]. Key to this achievement was the use of a smaller cantilever oscillation amplitude, to increase the sensitivity to the short-range chemical forces[38] and thereby allowing atomic-scale spatial resolution. Ten years later, single-electron AFM spectroscopy on single molecules was demonstrated[20,58].

Next to the single-molecule sensitivity, this spectroscopic method introduced by Fatayer et al. dealt with the stochastic nature of the single-electron tunneling processes by the usage of a pump-probe pulse sequence[58]. To access different electronic states of single molecules, they were deposited on thick insulating films[19]. A gate voltage was applied between the tip and the underlying metal surface, to steer single-electron tunneling processes between the tip and the molecule. First, the molecule was initialize in a specific state, e.g. D_0^+ (or another ground state with a different net charge) by applying a suitable pump gate voltage. Subsequently, a probe gate voltage was set, and it was determined if at this voltage an electron tunnels from (or to) the tip into (or out of) the molecule within a specified time interval. Such tunneling events will change the net charge of the molecule and would thus result in a detectable change in the frequency of the cantilever oscillation[12,83] (see Section 2.3.3). The tunneling probability for these stochastic processes can be determined by repeating this multiple times, and determining for each repetition the timing of a possible tunneling event. Upon varying the voltage, the tunneling probability can be measured as a function of voltage. Thereby, the energies of multiple excited states can be accessed[20], and the reorganization energies of single molecules on insulating films can be determined[58].

Although this novel method offers access to quantities inaccessible to conventional STS, a spectroscopic characterization of the broader low-energy spectrum of molecules remained out of reach for the following reasons. First, the method is essentially limited to the study of single-electron tunneling processes, restricting the number of excited states that can be accessed. To be more specific, similar processes can be observed as in STS (see Figure 3.1). Second, only the energies of available states can be accessed, the nature of the accessed states is unknown (e.g. singlet, triplet). Further, extremely long measurement times are required to energetically map one or two transitions, making it too time-consuming to allow varying a wide-range of parameters to obtain additional insights (such as the tip position). Finally, the tip is subject to stringent requirements; it is, therefore, not unlikely that different tip apexes are required to cover the desired range of voltages[20].

Here, we introduce a new type of single-molecule excited-state spectroscopy with AFM that overcomes these issues, and thereby allows probing many quantum transitions of different types individually, including radiative, non-radiative and redox transitions, in which the charge state changes. It relies on an AFM pump-probe voltage pulse technique introduced by Peng et al.[21], which was used to determine the triplet-state lifetime of a single pentacene molecule (see e.g. Figure 4.4). Building on these developments, we introduce an electronic pump-probe tunneling spectroscopy based on AFM.

Similar as in the existing AFM spectroscopy method from Fatayer et al.[20,58], our pump-probe voltage pulse sequence initializes the molecule in a certain state (e.g. D_0^+) by a voltage pulse, after which the voltage is changed to bring the molecule to different possible states (e.g. T_1 or S_0). In contrast to the existing AFM spectroscopy method, this second voltage, called sweep voltage, is only applied for a very short duration (typically a few microseconds). The populated states for a certain sweep voltage are then read-out during an additional

read-out interval (see for more details Section 3.3). This approach has multiple advantages. First of all, it allows us to discriminate between states with a different lifetime, guiding their assignment. Second, next to single-electron tunneling processes, our method also allows detecting and assigning multiple-electron tunneling processes, allowing access to a wide-range of transitions and states (for example a two electron-tunneling process such as $D_0^+ \rightarrow T_1 \rightarrow D_0^-$, see Figure 3.1b). Combined with the short time-scale of a pump-probe cycle and the less stringent tip requirements, the full low-energy spectrum of single molecules can be mapped out.

As a proof of principle, our method is applied to the well-studied pentacene molecule. The resulting spectroscopic data can be fitted to yield various energy differences, reorganization energies as well as the broadening associated with the charge transitions. We demonstrate the power of this spectroscopy by applying it to perylenetetracarboxylic dianhydride (PTCDA), thereby shedding light on the interpretation of recent STML experiments on PTCDA[128,129].

3.2. Experimental

3.2.1. Atomic force/scanning tunneling microscope

Experiments were carried out with a home-built combined AFM/STM, as schematically shown in Figure 3.2. The scan-head of the SPM (as described in more detail in ref. [133, 134]) is attached with springs to a liquid-helium bath cryostat, which is surrounded by a liquid-nitrogen bath cryostat, see for more details ref. [133, 135]. These cryostats are mounted on a vacuum chamber called SPM chamber. Two additional vacuum chambers are present that are interconnected via gate valves.

Samples (e.g. single crystals) are mounted onto button heaters on sample holders (see e.g. Figure 4.1b) and are introduced into ultrahigh vacuum (UHV) via the chamber called load-lock. This chamber is pumped with a diaphragm and turbomolecular pump and can reach pressures below 10^{-8} mbar. From the load-lock samples can be transferred into the preparation chamber using the transfer arm, where they can be grabbed with the manipulator. The manipulator is electrically contacted to allow annealing of the samples via the button heater. The preparation chamber is used for sample preparation (see next section), and is equipped with among others a leak-valve for sputtering gas, a sputter gun, a NaCl salt evaporator, a mask for NaCl evaporation and a quartz crystal microbalance. Using the manipulator, a sample can be transferred into the SPM scan head. Since the SPM head is connected to the liquid-helium bath cryostat, the sample can be cooled down to 8 K (the operation temperature used in the context of this thesis). Such low temperatures are crucial for single-molecule investigations, since it prevents diffusion of the molecules under study as well as diffusion of undesired molecular/atomic contaminations. Contaminations were minimized by the use of ultrahigh vacuum (UHV) (base pressure, $p < 10^{-10}$ mbar), generated by a combination of the cryo-pumping effect of the cryostat, a non-evaporable getter pump attached to the SPM chamber and a titanium sublimation pump and ion-getter pump at the bottom of the preparation chamber.

The microscope was equipped with a qPlus sensor[52] (for the used sensor: resonance frequency, $f_0 = 30.0$ kHz; quality factor, $Q \approx 1.9 \times 10^4$) and operated in frequency-modulation

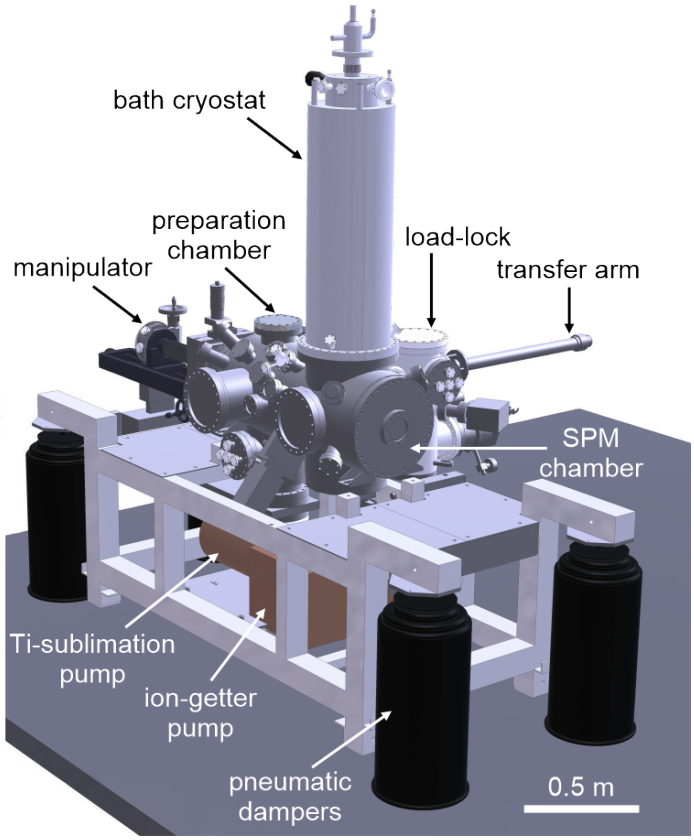

Figure 3.2.: Schematic overview of the home-built AFM/STM system. The system consists of three vacuum chambers (load-lock, preparation chamber and SPM chamber). The scan-head of the SPM (not shown) is located in the SPM chamber, and cooled via the liquid helium bath cryostat. Image adapted from ref. [133] with permission.

mode for AFM measurements (see Section 2.3.1). The qPlus sensor is based on a quartz tuning fork[52]. To one of the prongs of this fork a conductive Pt-Ir tip was glued, while the other prong was fixed on a substrate. More details of the used sensor design and mounting can be found in ref. [134]. A major advantage of a qPlus sensor is that it can stably operate at the optimal oscillation amplitude, which corresponds to the decay length of the chemical forces: around 1 Å (ref. [38]). The stable operation (without jump-to contact, see Section 2.3) at these small amplitudes is made possible due to the high stiffness of the sensor, with a typical spring constant of around 1.8 kN/m (ref. [46]). Since the qPlus sensor is made out of a piezo-electric material, quartz, its bending can be easily detected by collecting the strain-induced surfaces charges[46].

3.2.2. Sample and tip preparation

As a sample substrate, a Ag(111) single crystal was used. The surface of this sample was cleaned by repeated sputtering and annealing cycles. The sputtering was performed with neon ions: the preparation chamber was filled with $5 \cdot 10^{-5}$ mbar neon gas and the neon atoms were ionized and accelerated toward the sample, such that the ions have a kinetic energy of 1 keV. This resulted in a current of around 10 µA at the sample surface. The sample was sputtered in three cycles of approximately 30 minutes. In between the

cycles, the crystal was heated to 600 °C for a few seconds using Joule heating of the button heater on which the crystal was mounted. After the third sputtering cycle, the sample was annealed to 580 °C and held at the maximum temperature for two minutes, after which the temperature was slowly reduced.

Subsequently, a NaCl film with a thickness of more than 20 ML was grown on half of the sample, while the sample was held at a temperature of 80 °C. NaCl was evaporated from a tantalum crucible by Joule heating, and the deposited amount was monitored using a calibrated quartz crystal microbalance. The other half of the sample was covered by a metal sheet, which was mounted to a movable rod in the preparation chamber. In addition, a sub-ML coverage of NaCl was deposited on the entire surface at a sample temperature of approximately 35 °C, to grow 2 ML NaCl islands also on the other half of the sample that is used for tip preparation. The measured molecules (pentacene-h_{14} and PTCDA-h_8 (Sigma-Aldrich)) were deposited in-situ onto the sample ($T \approx 8$ K) inside the scan head. To this end, a silicon wafer was loaded with molecules under ambient conditions, after which it was brought into UHV before a small shutter covering small holes (diameter ≈ 1 cm) in the radiation shields that surround the scan-head. To degas the silicon wafer, it was heated to 150 °C (by Joule heating) before opening the shutter. After the shutter was opened, the wafer was further heated to 650 °C.

The tip was prepared by indentation into the remaining Ag(111) surface, presumably covering the tip apex with Ag. This indentation was repeated until the absolute value of the Δf signal was smaller than 5 Hz at a setpoint of $V_B = 0.5$ V, $I = 4$ pA. Subsequently, a constant-current STM image of the HOMO of pentacene on the 2 ML NaCl films was taken at $V_B = -2.4$ V. If the image contrast was similar as reported in ref. [3], the tip was transferred to the >20 ML NaCl film[75]. Otherwise, the indentation was repeated until these two requirements were fulfilled. To approach the tip on >20 ML NaCl, Δf feedback was used, the cantilever oscillation amplitude was regulated at 6 Å (12 Å peak-to-peak) and a gate voltage of −4 V was applied. These parameters were chosen to enhance the sensitivity to the long-range electrostatic force.

3.2.3. Voltage pulses

Figure 3.3 shows a schematic overview of the electronic circuit used for the sample voltage pulse generation. The voltage pulses were generated by an arbitrary waveform generator (AWG) (Pulse Streamer 8/2, Swabian Instruments), amplified by a factor of −10 using an inverting amplifier based on an operational amplifier (OpAmp) [a] and combined with the Direct-Current (DC) voltage using an adder based on an another OpAmp [b]. Since the adder also inverts the signal, an inverter based on a third OpAmp [c] was employed to invert the polarity of the DC voltage, while the sample voltage pulses were inverted during their amplification ([a]). The combined voltage signal was fed to the microscope head by a semi-rigid coaxial high-frequency cable (SC-033/50-AuSS-SS, Coax Japan Co. Ltd.) and applied to the metal substrate as a gate voltage V_G. Note that the high frequency components of the pulses of V_G lead to spikes in the AFM signal because of the capacitive coupling between the sample and the electrodes of the qPlus sensor, which can lead to an undesired excitation or damping of the cantilever. To suppress these spikes, we applied the same pulses with opposite polarity and adjustable magnitude to an electrode that capacitively couples to the sensor. To generate these canceling pulses, the AC voltage pulse signal was split

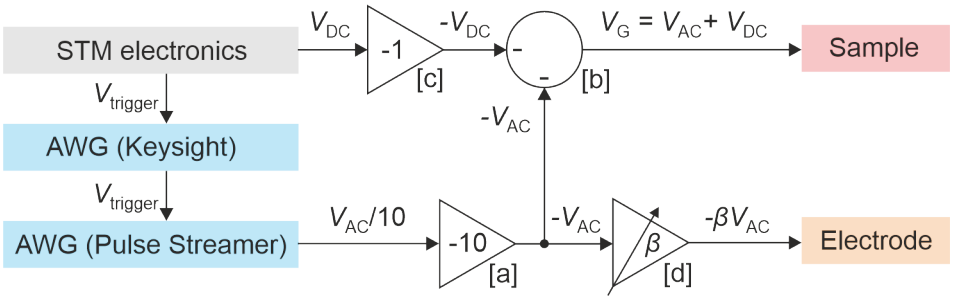

Figure 3.3.: Schematic overview of the electronic circuit for the sample voltage pulse generation. The sample voltage pulses (AC) were generated using an AWG (Pulse Streamer). This AWG was triggered using a signal from the STM electronics that was synchronized with the cantilever oscillation. This trigger signal was conditioned using another AWG (Keysight) to reduce cross-talk in the Pulse Streamer. The AC voltage pulses were tenfold amplified using an inverting amplifier [a], added together with the DC voltage generated by the STM electronics using an inverting adder [b] and applied as V_G to the sample. Since this adder inverts the polarity of the voltage, the DC voltage was inverted before entering adder [b] using an inverter [c]. The AC voltage pulses were fed in parallel to another amplifier [d] with a variable amplification factor β and applied to an electrode that capacitively couples to the sensor. This non-inverting amplifier contains an RC-network to fine tune the shape of the pulses.

before the adder ([b]), and fed in parallel through a non-inverting amplifier with a tunable amplification factor using a variable feedback resistor [d]. The magnitude of the pulses was set such that the observed spikes in the AFM signal were minimized. Importantly, the delay of the canceling pulses was tuned to match the one of the sample voltage pulses by varying the cable length (by using cables with different lengths) used to fed the canceling pulses into the microscope. Furthermore, a correction for slightly different shapes of the sample voltage pulses and canceling pulses was implemented. This difference in shape is largely attributed to the different cables used to fed the pulses into the microscope. To this end, an RC network with variable resistors and capacitors was built into the feedback of the OpAmp for the cancelling pulses ([d]) in order to fine tune the shape of the canceling pulses for an optimal cancellation.

The amplifiers, adders and inverters that we used were based on evaluation boards from Analog Devices, Inc. The inverter [c] was based on an ADA4523-1ARMZ evaluation board, while the adder [b] and amplifiers [a] and [d] were based on ADA4870 evaluation boards, modified for the above-described purposes. Reflections and resonances in the gate-voltage circuitry were avoided by impedance matching, absorptive cabling, and limiting the bandwidth of the external circuit to approximately 50 MHz (because of the ADA4870 amplifier). Experimental tests showed no indication of severe waveform distortions.

The sample voltage pulses were synchronized with the cantilever oscillation period, typically such that they started at the bottom turnaround point (closest to the sample). This synchronization was done with respect to the phase-locked loop of the AFM (see e.g. ref. [29] for more information on the phase-locked loop), which provides a 2 µs-long signal for every oscillation period. Before feeding this signal into the AWG (Pulse streamer) to trigger the output of the sample voltage pulses, its length was reduced from 2 µs to 5 ns via another AWG (Keysight 33600A Series). This minimizes the undesired coupling of this signal into the output of the Pulse Streamer.

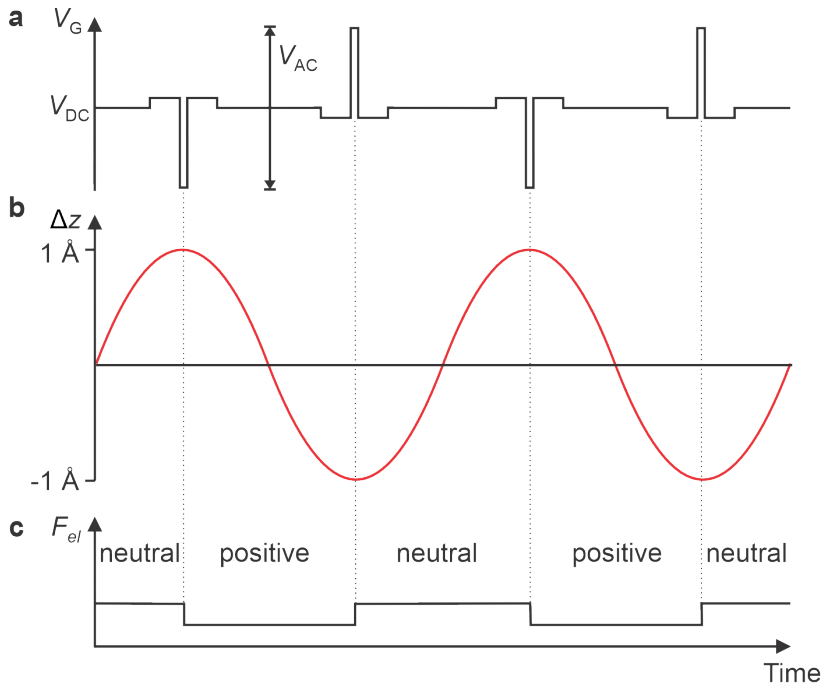

Figure 3.4.: Schematic of the AC-STM voltage pulses and the resulting electrostatic force. **a**, **b**, The voltage pulses used for AC-STM are shown in **a**, including their compensation pulses (see Section 3.2.4 for more details). A DC voltage V_{DC} is applied that is chosen to be close to the charge-degeneracy point (see Section 3.2.4), AC voltage pulses are given to charge and discharge the molecule. These pulses were synchronized with the cantilever movement, as displayed in **b**. Note that in practice the typical pulse duration (100 ns) is much shorter than the cantilever oscillation period (33.4 µs). **c**, The pulses cause a change in the charge state of the molecule (by the transfer of an electron between tip and molecule), resulting in a change in electrostatic force between tip and substrate. As an example, the charge states for the S_0 to D_0^+ transition are shown. The electrostatic force for the positively charged molecule is typically less attractive than for the neutral molecule (a less negative Δf signal is typically observed, see Section 2.3.3.3). A less attractive force during the inward compared to the outward cantilever movement causes a (positive) damping of the cantilever. Here, during every pulse a tunneling event occurred. In reality the parameters were chosen such that the pulse at the top turnaround point does not always cause a tunneling event. The magnitude of the measured signal will then strongly depend on the spatially varying probability of these tunneling events, allowing us to take maps of the orbital density. Note that the modulation of the electrostatic force due to the cantilever movement is neglected in this schematic. This schematic is based on a figure from ref. [89].

3.2.4. AC-STM

The electronic charge transitions, and thereby the orbital densities[136], can be mapped on thick insulating films by controlled shuttling of single electrons[89]. The resulting images are called alternating-charging (AC)-STM images[89]. In the context of excited-state spectroscopy, AC-STM images were used to confirm the expected charge state of the molecule at a certain gate voltage[137] (see Section 3.4.3), to determine the tip position at which the measurements were performed (see Section 3.3.1), and for lateral creep correction (see Section 3.3.1). This section explains in detail how to record AC-STM images.

In AC-STM single electrons are shuttled between the tip and the molecule, thereby changing the charge state of the molecule. If the gate voltage is chosen within the observed hysteresis of a charge transition (see Figure 2.9a), two charge states are bistable. Using voltage pulses with a voltage exceeding the relaxation energy (see Sections 2.3.3.1 and 3.8), the molecule can be switched between these two charge states. Such voltage pulses were synchronized with the bottom and top turnaround point of the cantilever oscillation (see previous section and Figure 3.4a and b). A tip-sample distance was chosen during which the voltage pulse at the bottom turnaround point is always efficiently setting a certain charge state, (almost) independent of the lateral tip position[138]. Using a cantilever oscillation amplitude of 1 Å (2 Å peak to peak)[138], the tunneling rate during the voltage pulse at the top turnaround point is approximately 100 times smaller. This tunneling will, therefore, only happen at those spatial positions where the orbital overlap between tip and molecule is large and this tunneling process is efficient. If an electron tunneled at the top turnaround point, the charge state of the molecule is different during the outward and inward movement of the cantilever (since the electron always tunnels back at the bottom turnaround point). Thus, the electrostatic force between the tip and sample is different during the outward and inward movement (see Figure 3.4c), which generates a detectable damping or excitation of the cantilever oscillation. Since the tunneling probability during the pulse at the top turnaround point of the cantilever movement depends on the electron density in the orbital to/from which is tunneled, this density can be imaged by measuring the damping/excitation signal at different spatial positions (in constant-height mode). The tip-sample height was chosen sufficiently close to get a large signal-to-noise ratio of the detected signal, but not too close to prevent saturation of the signal. This saturation is a consequence of the fact that maximally one electron can tunnel during the pulse. To be more exact, if the tip-sample distance is too small, an electron can always tunnel at the top turnaround point, even at positions where the orbital density is very small, which leads to a saturation of the signal. The tip-sample height was, therefore, typically chosen to be 2 to 3 Å smaller than the tip-sample height used for the excited-state measurements (see Section 3.3.1).

Note that this tip-sample distance is so small that the charging hysteresis is typically collapsed (see Figure 2.9). Around the bottom turnaround point of the cantilever movement, tunneling processes can then also occur spontaneously, instead of only being steered by the voltage pulses. To prevent undesired effects from such spontaneous tunneling processes, the DC gate voltage was typically chosen such that it was approximately 50 mV lower in magnitude than the voltage of the charge degeneracy point (for $0 \rightarrow 1^+$ and $0 \rightarrow 1^-$, in case of $1^+ \rightarrow 0$ and $1^- \rightarrow 0$ a voltage 50 mV higher in magnitude was chosen). This ensures that the only spontaneous tunneling process is the one that should anyhow always occur because of the pulse at the bottom turnaround point. Thus, the choice of this voltage minimizes the artifacts that are due to spontaneous tunneling processes.

Importantly, since during the pulses a different voltage is applied, the Δf is different because of electrostatic forces, which could lead to an additional undesired excitation/damping of the cantilever motion. To circumvent this, the AC-STM pulses were designed such that they do not have any frequency components at the cantilever frequency[138]. Therefore, compensation pulses were added to each pulse, such that the time integral over each main pulse and its compensation pulses was zero, see Figure 3.4a. Their magnitude was reduced by a factor 8 compared to the main pulse to prevent any tunneling events induced by the compensation pulses[138]. Assuming that the frequency shift is linear with

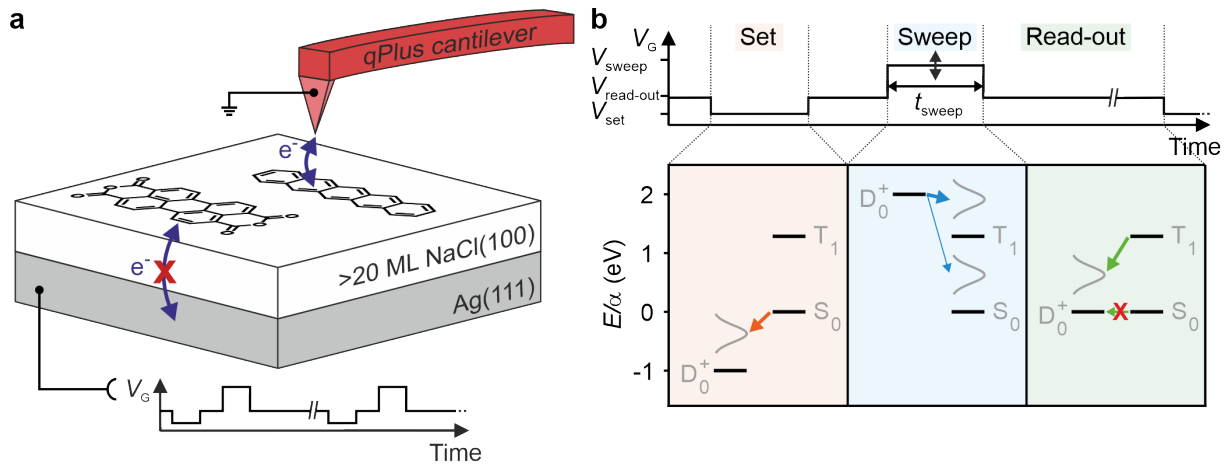

Figure 3.5.: Experimental set-up and pulse sequence. **a**, Sketch of the experimental set-up. Molecules (pentacene and PTCDA) were deposited on a >20 ML thick NaCl film that prevents tunneling to the underlying Ag(111) substrate. A pump-probe voltage-pulse sequence was applied to steer single-electron tunneling between the tip of a qPlus[52] cantilever and the molecule. **b**, A typical pump-probe voltage-pulse sequence is displayed together with the many-body energy diagrams that show the possible transitions during the different phases of the pulse sequence (only three states are shown for simplicity). Thicker arrows indicate dominating transitions (see Figure 2.3). The molecule is initialized in a specific state (here D_0^+) by the set pulse with voltage V_{set}, followed by a sweep pulse with variable time t_{sweep} and voltage V_{sweep}. At the end of the sweep pulse, the states are mapped onto two different charge states using a read-out voltage $V_{\text{read-out}}$, which is adjusted such that two different charge states are degenerate. The finite relaxation energies render the molecule bistable in these two charge states, see Figure 2.4. The different charge states can be discriminated by AFM. As explained in Sections 2.3.3.4 and 2.3.3.5, transitions occur from a vibrational ground state (black lines) to an excited vibrational state with an energy within the indicated Gaussians (gray), after which the system relaxes to the vibrational ground state of the newly populated state. α denotes the lever arm, as explained in Section 2.3.3.4.

voltage, such compensation pulses would be sufficient to suppress any undesired frequency components of short voltage pulses. In reality, there is a quadratic dependence of Δf on voltage. In general, this quadratic component can be minimized by applying the pulses with a frequency matching twice the cantilever frequency. Since the quadratic component is being minimized, the two pulses during a cantilever period may have different polarities, as is the case for the pulses used in AC-STM (see Figure 3.4a).

3.3. Excitation and read-out scheme

A schematic of the experimental setup is shown in Figure 3.5a. Pentacene and PTCDA molecules were deposited on thick NaCl films (>20 ML) on Ag(111), where the NaCl electrically isolates the molecules from the underlying metal[18]. Voltage pulses were applied as a gate voltage to the Ag(111) substrate. The gate voltage V_{G} controls the alignment of the molecular electronic states with respect to the Fermi level of the tip, and steers single-electron tunneling between the tip and the molecule, used for mapping out the electronic transitions.

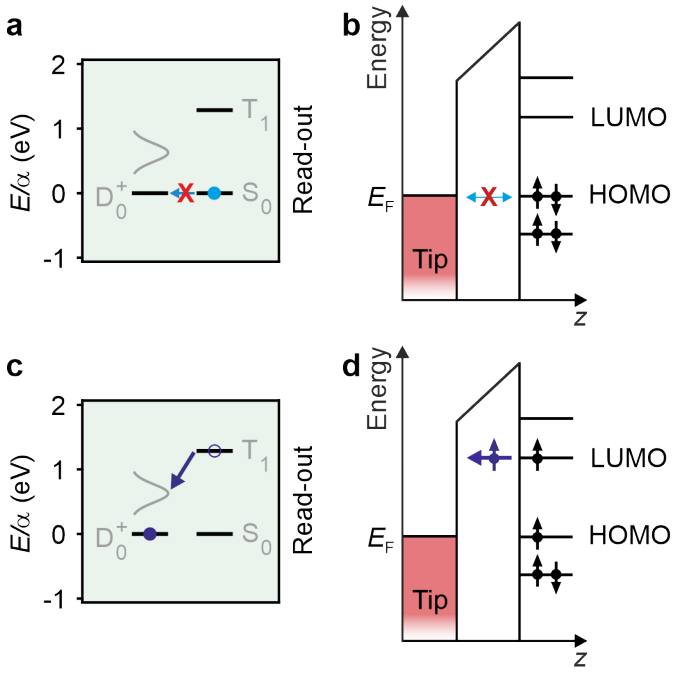

Figure 3.6.: Discrimination of S_0 and T_1 by mapping on two different charge states. **a**, **c**, Many-body energy diagrams for the read-out phase with a read-out voltage corresponding to the D_0^+-S_0 degeneracy point. If the molecule was in the S_0 state (**a**), it will stay in S_0 at the read-out voltage; a transition to D_0^+ is blocked since - roughly speaking - the relaxation energy would need to be overcome (see Section 2.3.3.1). If the molecule was instead in the T_1 state (**c**), an electron will tunnel out of the LUMO forming D_0^+ (see **d**). **b**, **d**, Single-particle pictures corresponding to the processes indicated in **a**, **c**, respectively. If the molecule was in S_0 (two electrons in the HOMO, none in the LUMO), electron tunneling is blocked (**b**). In contrast, if the molecule was in the T_1 state (one electron in the HOMO and one in the LUMO, with parallel spins), an electron can tunnel out of the LUMO (**d**). Note that tunneling in or out of the HOMO of the molecule in the T_1 state at this voltage is energetically not allowed (in that case D_0^- or D_1^+ would be formed, which is energetically not possible according to the read-out many-body diagram in Figure 3.8b).

To acquire an excited-state spectrum, we repeatedly apply a pulse sequence to the gate voltage, controlling cycles of driven tunneling events and charge-state detection. In each sequence, we first bring the molecule with a set pulse to a defined state, for example the D_0^+ state (see Figure 3.5d). Subsequently, a sweep pulse with a variable voltage V_{sweep} is applied, bringing the molecule via one or more tunneling events to a variety of possible states. Finally, a read-out voltage is applied that corresponds to the charge-degeneracy point[18] between S_0 and one of the singly charged ground states, that is, D_0^+ or D_0^- (see Section 2.3.3.1). The populated states at the end of the sweep pulse are thereby mapped onto the two degenerate charge states (see Figure 3.5b)[21], which can be read out by means of the electrostatic force acting on the tip[12], see Sections 2.3.3.3 and 2.3.3.5. Interconversion between these two states by single-electron tunneling to/from the tip is prevented close to their degeneracy point by the vanishing overlap between their vibrational ground states due to the large electron-phonon coupling present. In other words, roughly speaking the relaxation energy needs to be overcome to change the net charge (see for a more detailed discussion Section 2.3.3.1 and Figure 3.6a).

Next to differentiating electronic states with different net charge, this read-out scheme also allows differentiating certain electronic states that correspond to the same charge state. Specifically, long-lived excited states (with a lifetime comparable or longer than t_{sweep}) can be distinguished from the ground state and any short-lived excited states that decayed to the ground state during t_{sweep}. For example, S_0 and T_1 can be distinguished by projecting them onto different charge states, such as S_0 and D_0^+, respectively[21,22], as is depicted in Figure 3.6. At a read-out voltage corresponding to the S_0-D_0^+ degeneracy point, the molecule will stay in S_0 if it was in S_0 at the end of the sweep pulse, see Figure 3.6a and b. In contrast, if the molecule was in T_1, an electron can tunnel out of the LUMO of the molecule, which brings the molecule into D_0^+, see Figure 3.6c and d.

In general, all the resulting states after each sweep pulse are mapped onto the two different charge states being degenerate at the read-out voltage. Upon repeating this voltage pulse sequence 8 times per second, typically for 80 seconds, the populations in these two charge states can be determined. A part of such a measured data trace for pentacene is shown in Figure 3.7a. It is important to realize that the read-out interval (125 ms) is long compared to the voltage pulse duration (typically less than 100 µs). The resulting Δf signal is thus predominantly determined by the read-out phase, and is analyzed as described in Section 3.3.2. Excited-state spectra were measured by sweeping V_{sweep} and recording for every voltage a Δf data trace, from which the population in the charge state was extracted. The further V_{sweep} differs from V_{set}, the more transitions become possible, allowing us to infer the transitions during the sweep pulse and in turn the energetic alignment of the low-lying electronic states.

3.3.1. Experimental parameters for excited-state spectroscopy

The excited-state spectroscopy measurements were performed with the pulse sequence presented in the previous section. This section discusses the choice of cantilever oscillation amplitude, lateral tip position, tip-sample height, sweep-pulse durations, set-pulse parameters and the parameters for creep correction.

A cantilever oscillation amplitude of 1 Å (2 Å peak-to-peak) was chosen to optimize the signal-to-noise ratio for charge-state detection[38]. The oscillation amplitude modulates the tip height and thereby induces variations in the tunneling rate and slight variations in the lever arm of the gate voltage. To minimize these effects, the voltage pulses were synchronized with the cantilever oscillation period (see Section 3.2.4), such that they started 2 µs before the turn-around point at minimal tip-sample distance. Furthermore, the sweep pulses were chosen to be short, such that the entire sweep pulse occurs around the point of minimal tip-sample distance. If this was not possible, full cantilever-period pulses were chosen. The resulting minor influence of the cantilever's oscillation amplitude on the excited-state spectroscopy data was neglected in the modeling (see Section 3.5) and, hence, in the fitting.

The lateral tip position was chosen by taking an AC-STM image (see Section 3.2.4) of the $S_0 \rightarrow D_0^+$ transition (HOMO) and placing the tip on one of the brightest lobes of the HOMO, see for example tip position I in Figure 3.11.

The tip height was iteratively set such that a decay constant of approximately 1.5 µs for the $D_0^+ \rightarrow S_0$ transition was obtained. To this end, this decay was measured using a

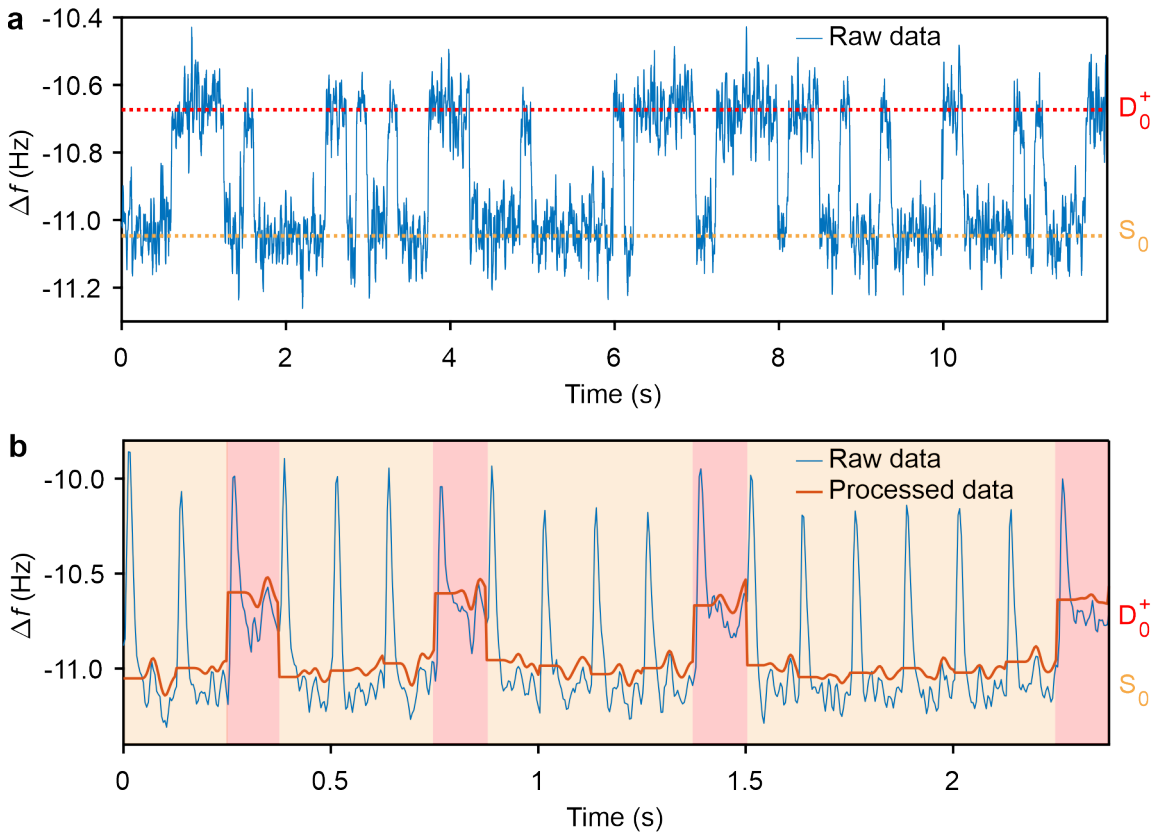

Figure 3.7.: Raw and processed Δf data traces. **a**, **b**, Two data traces measured for a pentacene molecule using the pump-probe voltage pulse sequence displayed in Figure 3.5b. The measured data without processing is shown in case of **a**. Note that the duration of the set and sweep pulses is negligible against the duration of the read-out interval (125 ms). The two extracted frequency shifts of the read-out states, D_0^+ and S_0, are indicated by the red and yellow lines, respectively. In case of **b** the raw and processed data are displayed (note the displayed time scale is here shorter than in **a**). In this case, spikes were present at the beginning of every pump-probe cycle (peaking at around −10.0 Hz), which were removed in the processed data (these spikes were not present in the raw data shown in **a**, since shorter sweep voltage pulses were used in that case (**a**, $t_{\text{sweep}} = 0.7\,\mu\text{s}$ and **b**, 7 µs). The processed data was low-passed per read-out interval to facilitate read-out. The read-out charge states are indicated by the red and yellow shading. To keep track of the creep, the frequency shift of the neutral state was compared to the one of the first dataset and the processed dataset was shifted by the difference.

voltage pulse sequence similar to the one used for the excited-state spectroscopy, except that the sweep voltage was fixed to $V_{\text{read-out}} + 1\,\text{V}$ and t_{sweep} was swept. In general, the tip-sample height should be chosen such that it fulfills the following two requirements. The tip-sample height should be sufficiently large to minimize tunneling events between the two bistable states during the read-out phase of the pulse sequence, which gives a lower limit to the tip-sample height. An upper limit to the tip-sample height is given by the requirement that the tunneling rates should be much faster than the slowest triplet decay rate. Typically, these two requirements restrict the possible tip-sample heights to a small range (less than 2 Å) around the relatively large tip-sample height used (estimated to be 9 Å, see Section 3.5).

The shortest sweep-pulse duration was then chosen such that at the largest V_{sweep} used, the read-out fraction in the D_0^+ state was around 0.10. This allows the detection of the transition(s) at largest V_{sweep}. In contrast, a longer sweep-pulse duration is crucial for the observation of transitions with a slower rate. The longest pulse duration was, therefore, typically set such that the fraction in the D_0^+ state was close to zero at a voltage of 1 V above the voltage corresponding to the degeneracy of the D_0^+ and S_0 states. Two or three additional sweep-pulse durations were chosen in between the determined shortest and longest pulse duration, to improve the reliability of the fitting.

To initialize in the D_0^+ state, the set-pulse voltage and duration were chosen such that it reliably brings the molecule in this state. We chose, therefore, a set pulse with a voltage that exceeds the relaxation energy (see Section 2.3.3.1) of the $S_0 \rightarrow D_0^+$ transition, having a duration that is much longer than the decay constant of this transition. Specifically, a set-pulse voltage was chosen that is 1 V lower than the D_0^+-S_0 degeneracy point, having a duration of 33.4 µs (one cantilever period). In case of initialization in T_1 and S_0 (see Section 3.4.2), the set pulse sequence consists of two parts, where the first part is the same as for initializing in D_0^+, and the second part is described in Section 3.4.2.

The measurements were performed in constant-height mode. To correct for vertical piezo creep, the tip-sample distance was typically reset every 15 minutes by shortly turning on the Δf-feedback. Lateral creep was corrected every hour by taking an AC-STM image (see Section 3.2.4) and cross-correlating it with an AC-STM image taken at the beginning of the measurement.

3.3.2. Data analysis

The data acquisition and on-the-fly analysis were performed with Matlab. For data analysis, the data must contain information on the timing of the pump-probe intervals. The AWG was, therefore, programmed to output trigger pulses synchronized with the pump-probe voltage pulses. These trigger pulses were fed into the control electronics of the microscope, and could therefore be recorded simultaneously with the measured Δf data trace.

To analyze such Δf traces (see Figure 3.7a), first the frequency shifts of the two charge states were extracted from a data trace measured at the beginning of a voltage sweep. This dataset was measured using voltage pulse parameters for which it was approximately equally likely to find the molecule in the two different charge states during the read-out phase. The frequency shifts of these two charge states were extracted from the two largest maxima of a kernel density estimation of the data trace (a probability density estimation using a kernel with a normal distribution for smoothening), see for example the lines in Figure 3.7a.

Subsequently, the data traces for different V_{sweep} were measured and analyzed. The frequency shifts of the charged and neutral states were determined for each dataset individually via a kernel density estimate. In case only one charge state was observed, the frequency shift of the other charge state was extrapolated from the frequency shifts determined from the first dataset under the assumption that the difference in Δf for the two charge states is approximately constant. Note that the remaining effect of the capacitive coupling described in Section 3.2.3 as well as the excitation of the cantilever due to the

few µs sweep voltage pulses can cause spikes at the beginning of every read-out period, as shown in Figure 3.7b. In contrast to AC-STM it was not necessary to restrict the used voltage pulses to those that prevent cantilever excitation/damping (e.g. only use full period pulses), because of the low (8 times per second) repetition rate. The resulting spikes were simply removed from the data trace by setting the datapoints around these spikes equal to the average frequency shift over the rest of the corresponding read-out phase, see Figure 3.7b. After removing the spikes, every read-out interval was low-passed and it was determined if the averaged frequency shift during this interval was above or below the value centered between the frequency shifts of the two charge states. Counting the number of read-out intervals for which the frequency shift was above this value (see Figure 3.7b red background) and dividing it by the total number of intervals gives the read-out fraction in the charge state. For the metal tips we have employed, the D_0^+ and D_0^- states always had a less negative frequency shift compared to S_0 (at the respective read-out voltage).

3.3.3. Statistical uncertainty

The uncertainty on the determined read-out fraction in the charge state is dominated by the statistical uncertainty. Because of the two possible outcomes (charged or neutral), the statistics of a binomial distribution apply[21]. The standard deviation (s.d.) on the counts in a charged state N_c is, therefore, given by

$$\sigma_{Nc} = \sqrt{\frac{N_0 N_c}{N_c + N_0}}, \tag{3.1}$$

with N_0 the counts in the neutral state. In addition, the discrete nature of N_c should be accounted for. That Equation (3.1) does not correctly account for the discreteness contributing to the uncertainty margins is most obvious for the examples, in which either N_0 or N_c is zero, for which Equation (3.1) provides a vanishing uncertainty. This discreteness is accounted for by raising the error bars by one ($\sigma_{Nc} + 1$) (ref. [21]). The error bars on the measured fractions in the charged state are then given by

$$\Delta_c = \frac{\sigma_{Nc} + 1}{N_c + N_0}. \tag{3.2}$$

If not indicated otherwise, every data point in the excited-state spectra corresponds to 640 pump–probe cycles and the error bars were derived from the s.d. according to this equation.

3.4. Excited-state spectroscopy on pentacene

Figure 3.8a shows the results of an excited-state spectroscopy measurement for a single pentacene molecule, recorded using the pulse sequence described in Section 3.3 with read-out at the D_0^+-S_0 degeneracy. Here, the set pulse prepares the molecule in D_0^+ (see Figure 3.8b). For V_{sweep} voltages close to $V_{read\text{-}out}$, the molecule remains in D_0^+ because of the Franck-Condon blockade[70,95] (see Section 2.3.3.1); hence at the end of each cycle, the state is read-out as D_0^+. Upon increasing V_{sweep} and thereby passing certain threshold voltages, labeled as (1, 2, ...), various transitions open or close. To facilitate the understanding, schematic many-body diagrams in Figure 3.8e show the possible transitions when passing

the corresponding V_{sweep} threshold voltages (see for the definition of the many-body states Section 2.1 and for their shifts with the gate voltage Section 2.3.3.4).

Upon V_{sweep} passing (1), a first tunneling channel opens and an electron can tunnel from the tip into the HOMO resulting in S_0, see Figure 3.8e. At (2) the electron can tunnel into the LUMO forming T_1. Importantly, this T_1 state has a lifetime of tens of microseconds[21] and is mapped onto D_0^+ during the read-out interval, while the population in S_0 remains in S_0 (see Figure 3.6 and Figure 3.8e)[21]. Note that more than 80% of the population was read-out in the D_0^+ state, indicating that most of the population ended up in the T_1 state. This larger rate of tunneling into the T_1 state than into the S_0 state can be explained by a difference in tunneling barrier (see Figure 2.3), multiplicity, spin-state overlap and the (position dependent) different spatial overlap between the tip and LUMO and HOMO, respectively. The difference in multiplicity and spin-state overlap gives rise to a ratio of tunneling of 3 to 2 for $D_0^+ \rightarrow T_1$ and $D_0^+ \rightarrow S_0$, respectively. This ratio results from considering the possible transitions starting with both spin configurations of D_0^+ (up and down) and ending in the spin configurations of the T_1 (see Equation (2.21)) and S_0 states.

In general, the assignment of features in the read-out signal to certain molecular transitions can be achieved by analyzing the temporal evolution of the many-body states populations as follows. The transition rates associated to the tunneling of electrons between tip and molecule can be controlled by the tip-sample distance and are chosen to be in the range of a fraction of a microsecond to a few microseconds. In contrast, the triplet-to-singlet transition occurs on a considerably longer timescale of tens of microseconds[21], whereas optically allowed transitions are typically much faster than the chosen rate of charge transitions[139]. By varying the duration of the sweep pulse t_{sweep}, the temporal evolution of the populations can be extracted, providing insight into the transition rates. For example, the fast and slow population decay with increasing t_{sweep} in the spectra between (1) and (2) and between (2) and (3), respectively, strongly supports the assignment of the first and second feature in Figure 3.8 to the $D_0^+ \rightarrow S_0$ and the $D_0^+ \rightarrow T_1$ transitions, respectively.

The assignment of other features in the spectra at increased sweep voltages follows the procedure as outlined above, namely by considering which transitions sequentially open and which time dependence is associated to it. If several transition pathways are available, their competition must be considered. This analysis suggests that at (3) in Figure 3.8a two new transitions could potentially become accessible.

One of them is the $D_0^+ \rightarrow S_1$ transition. S_1 will immediately decay to the singlet ground state S_0 (see schematic 3A). Since this decay is within one multiplicity and therefore spin allowed, it can safely be assumed to be instantaneous on the time scale of the experiment[139,140]. The opening of the $D_0^+ \rightarrow S_1 \rightarrow S_0$ pathway will reduce the population in T_1, since it competes with the $D_0^+ \rightarrow T_1$ pathway, also starting at D_0^+ (see Figure 3.8e). The ratio of these two pathways is governed by the difference in tunneling barrier, multiplicity and spin-state overlap. The multiplicity and spin-state overlap give a 1 to 3 ratio for the rates of $D_0^+ \rightarrow S_1$ and $D_0^+ \rightarrow T_1$, respectively[141] (note that this is different from the 2 to 3 ratio for $D_0^+ \rightarrow S_0$ and $D_0^+ \rightarrow T_1$, due to the different wavefunctions of S_0 and S_1).

The other new pathway that could open starts with the $T_1 \rightarrow D_0^-$ transition, which is then followed by a $D_0^- \rightarrow S_0$ transition, effectively quenching the T_1 population, see schematic 3B. As will be clarified in Section 3.4.2, with the help of an additional experiment, the results of which are shown in Figure 3.12, we recognized that both of these processes

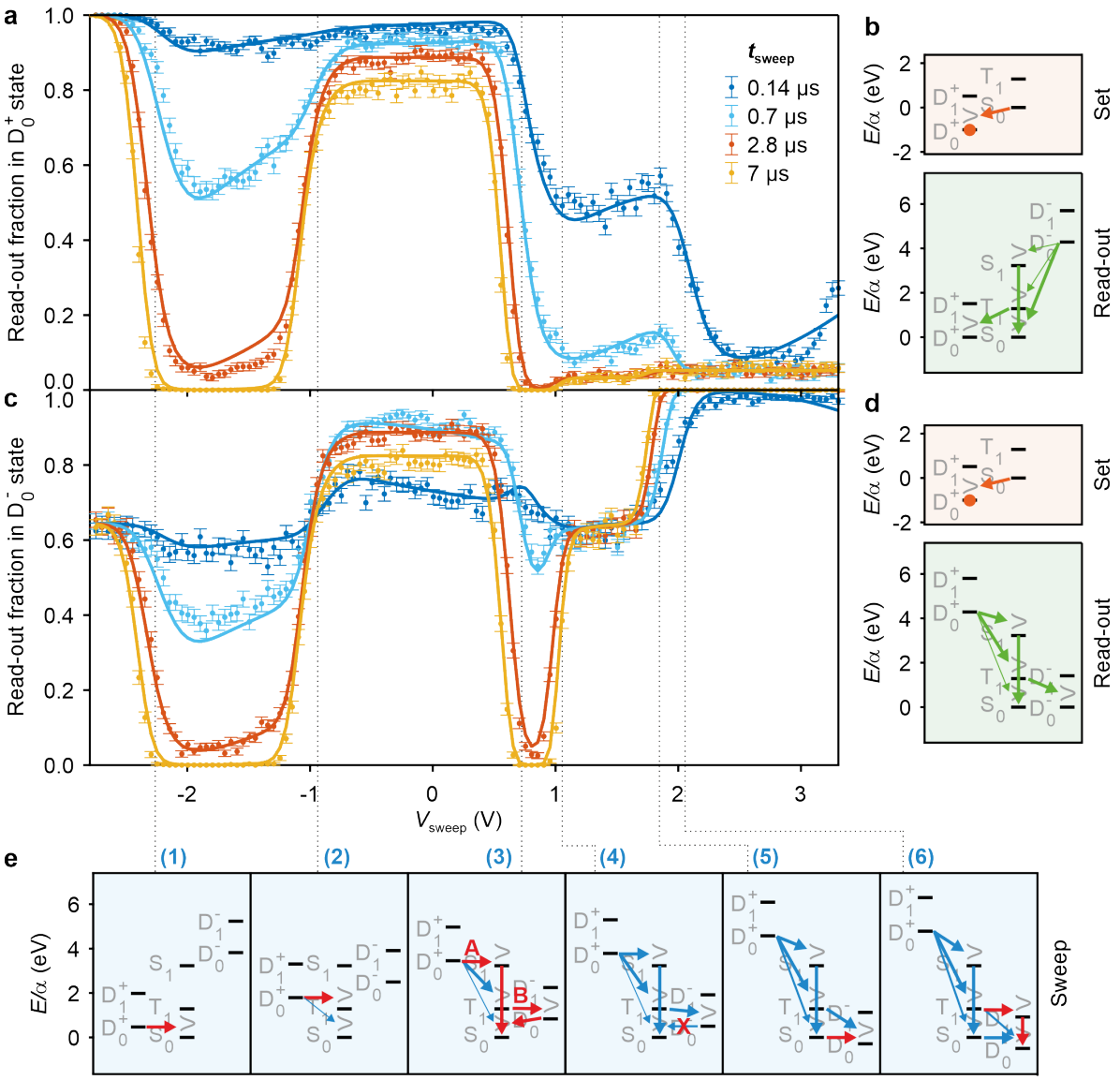

Figure 3.8.: Excited-state spectroscopy of pentacene, initialized in the cationic charge state. **a**, **c**, Plot of the read-out fraction (the normalized population during the read-out phase) in the D_0^+ and D_0^- states, respectively, as a function of the gate voltage V_{sweep} applied during the sweep pulse. Measurements were performed with a voltage pulse sequence similar to Figure 3.5b ($V_{set} = -3.795\,V$), using a read-out voltage at the D_0^+-S_0 ($V_{read\text{-}out} = -2.795\,V$) and S_0-D_0^- ($V_{read\text{-}out} = 1.416\,V$) degeneracies for **a** and **c**, respectively. Four different t_{sweep} were used, as indicated. Solid lines represent fits to the data (see Sections 3.5 and 3.6). **b**, **d**, Many-body energy diagrams of the transitions taking place during the set pulse and at the beginning of the read-out phase for the spectra shown in **a** and **c**, respectively. The state resulting from the set pulse is indicated by a dot. **e**, Many-body energy diagrams at the sweep voltages indicated by the dotted lines (note that these voltages were chosen as a guide to the eye, the fitted threshold voltages are listed in Table 3.1). The process(es) that cause the change in the read-out fraction around the indicated voltage are represented by red arrows (opening of a transition) and crosses (closing of a transition). At (3) two new transitions open, as indicated with A and B, and referred to as (3A) and (3B). The opening of a certain transition (horizontal red arrows) may also enable a cascade of further transitions (downward red arrows in (3) and (6)). The relative thicknesses of the different arrows connecting two charge states roughly indicates the ratio of the rates governed by the different tunneling barriers (see Figure 2.3).

contribute to the features observed at (3). Similarly, the feature observed at (6) at a higher sweep voltage could either stem from accessing a transition from D_0^+ to a short lived excited neutral state, or accessing a transition from T_1 to an excited negative charge state. We find from the experiment shown in Figure 3.12 that the feature at (6) relates to accessing a $T_1 \rightarrow D_1^-$ transition.

At $V_{\mathrm{sweep}} = 3.2\,\mathrm{V}$ for $t_{\mathrm{sweep}} = 0.14\,\mu\mathrm{s}$ we observe another feature, indicating that a transition opens or closes. We tentatively assign the feature to a $D_0^+ \rightarrow T_1 \rightarrow Q_1^-$ pathway (see Figure 3.9a), where Q_1^- is a negatively charged quadruplet state with presumably one electron in the HOMO, one in the LUMO and one in a higher-lying orbital, such as the LUMO+1. This is supported by the fact that this feature is also observed when the molecule is initialized in T_1 and S_0 (see Figure 3.12) and scales with the initial T_1 population (see Figure 3.13). In contrast to D_0^-, Q_1^- cannot directly decay into the S_0 state, as this would require the simultaneous tunneling of multiple electrons, see Figure 3.9b. Instead Q_1^- could decay into D_0^-, either directly (although being spin forbidden, orange pathway in Figure 3.9b), or via an excited doubly charged triplet state (blue pathway in Figure 3.9b). The assignment of the observed feature at $V_{\mathrm{sweep}} = 3.2\,\mathrm{V}$ to $T_1 \rightarrow Q_1^-$ assumes that the rate of populating Q_1^- is faster than its decay. In contrast to D_0^-, Q_1^- will likely be fully read-out as D_0^+, since the pathways $Q_1^- \rightarrow S_0$ and $Q_1^- \rightarrow S_1$ are not possible via a single-electron tunneling process (see Figure 3.9c).

Note that around the same voltage at which we observe this feature also another charging step is observed in a KPFS spectrum (not shown), which we assume to originate from a $D_0^- \rightarrow S_0^{-2}$ transition (see the approximate energetic alignment in Figure 3.9b). We do, however, assume that the population of this state cannot be observed in the spectrum, since S_0^{-2} will convert to D_0^- (possibly via the short-lived D_1^-), and thus likely behave identical to the D_0^- population, see Figure 3.9d. Following this argumentation, we tentatively assign the feature at 3.2 V to $D_0^+ \rightarrow T_1 \rightarrow Q_1^-$. Since this assignment is tentative and is not considered any further, we did not include this transition in the rate equations (Section 3.5).

There are two additional very small steps at (4) and (5) visible in Figure 3.8a for the longer durations of the sweep pulse. These features appear at a V_{sweep} relatively close to the S_0-D_0^- charge-degeneracy point at 1.42 V, suggesting that these features might relate to transitions between states with neutral and negative charge. As will become clear in the following, the visibility of such charge transitions in the signal is low, if read out at the charge degeneracy of a different pair of charge states (for this case at the neutral-positive charge degeneracy). Instead, the visibility is large, if transitions between two charge states are read out at the charge degeneracy corresponding to these two states (for this case at the neutral-negative charge degeneracy). Therefore, we repeated the experiments with a different read-out voltage, mapping the states onto the D_0^- and S_0 state instead of the D_0^+ and S_0 state. The resulting spectra shown in Figure 3.8c exhibit pronounced steps at (4) and (5).

To understand these steps at (4) and (5), it is easiest to analyze the spectrum in Figure 3.8c starting at large positive voltages (from right to left). At the right end of the spectrum, V_{sweep} is far beyond the negative-neutral charge degeneracy point at 1.42 V such that every state decays to D_0^- at long t_{sweep}, resulting in a read-out fraction in D_0^- of 1 (Figure 3.8c). We recall that the molecule is still initialized in D_0^+, such that for large V_{sweep} it may cascade via the neutral S_0 and T_1 toward D_0^-. However, at a V_{sweep} below (5) but above (4), the cascade via S_0 becomes blocked, since S_0 will not decay into D_0^-, explaining

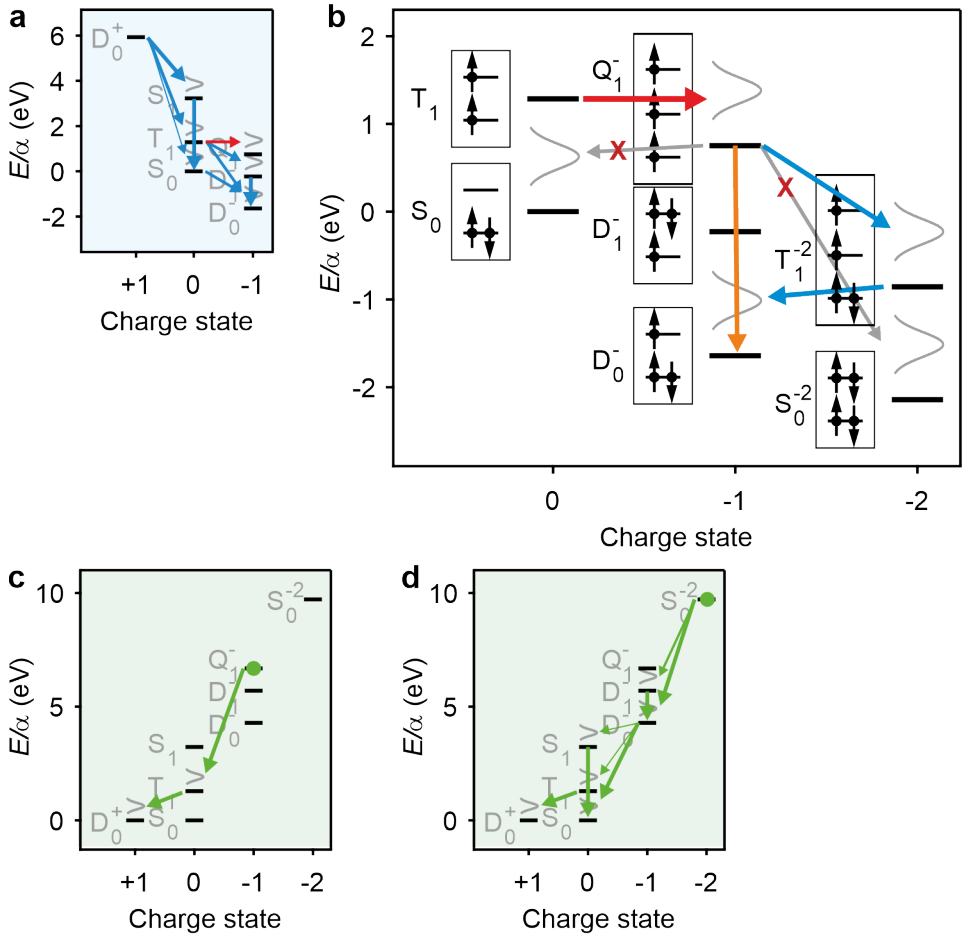

Figure 3.9.: Hypothesized origin of the feature around 3.2 V in excited-state spectroscopy of pentacene. **a**, Many-body energy diagram of the hypothesized transition pathway opening at 3.2 V: $T_1 \rightarrow Q_1^-$ as indicated by the red horizontal arrow. **b**, Many-body energy diagram of the relevant states. Whereas the insets with two levels indicate the occupation of HOMO and LUMO, the ones showing three levels include also the LUMO+1. Q_1^- is assumed to have a significant contribution of a state with one electron in the HOMO, one in the LUMO and one in a higher-lying orbital such as the LUMO+1. The hypothesized transition pathway that opens at 3.2 V is $T_1 \rightarrow Q_1^-$ (red arrow). Q_1^- cannot decay into S_0 or S_0^{-2} via a single-electron tunneling event (gray arrows) (also not in S_1^{-2} if energetically accessible, not shown). Q_1^- could decay to an excited doubly charged triplet state T_1^{-2} (blue arrow), assuming it has a significant contribution of a state with two electrons in the HOMO, one in the LUMO and one in the LUMO+1. This T_1^{-2} could then decay into D_0^-. Alternatively, Q_1^- could directly decay into D_0^- (orange arrow), despite being spin forbidden. Assuming that the rate of populating Q_1^- (red arrow) is faster than the rate of its decay (orange and blue arrows), a detectable population in Q_1^- could be present for short t_{sweep}. Note that the energy difference between S_0^{-2} and T_1^{-2} is unknown, and is for simplicity assumed to be the same as for S_1 and T_1 (in any case, it is very likely that T_1^{-2} is energetically below Q_1^- at a gate voltage of 3.2 V). **c**, **d**, Many-body energy diagrams of the transitions taking place at the beginning of the read-out phase assuming the initial population is in Q_1^- (**c**) or S_0^{-2} (**d**). Note that the transitions $Q_1^- \rightarrow S_0$ and $Q_1^- \rightarrow S_1$ in **c** are not possible via a single-electron tunneling process. The remaining population in Q_1^- will thus likely be fully read out as D_0^+ (other possible pathways via excited triplet states will likely also be read-out as D_0^+). In case of **d**, $S_0^{-2} \rightarrow Q_1^-$ is not possible via a single-electron tunneling process. Thus, S_0^{-2} will likely be read-out in the same way as D_0^- (mainly as S_0).

the decrease in the read-out fraction (in D_0^-) in the direction of decreasing V_{sweep} at (5) in Figure 3.8c. Decreasing V_{sweep} further to below (4), D_0^- (after its population from T_1) can decay into S_0 such that all the population can transfer into S_0, explaining the additional decrease in the read-out in D_0^- in the direction of decreasing V_{sweep} at (4).

As mentioned above, the transitions assigned to (4) and (5) are also those that cause the small steps at the voltages associated to (4) and (5) in Figure 3.8a. However, in Figure 3.8a the population in the D_0^- state at the end of the sweep pulse is read-out at the positive-neutral charge degeneracy, causing only a small fraction of D_0^- to be read-out as D_0^+. Analogously, at the left end of the spectrum in Figure 3.8c, transitions between states with positive and neutral charge are read out at the negative-neutral charge degeneracy, explaining the reduction in read-out signal from Figure 3.8a to Figure 3.8c below the voltage of feature (1). In both cases, the magnitude of the read-out signal depends on the rates of the competing pathways that are indicated by the thickness of the arrows in the read-out diagrams in Figure 3.8b and d.

There are two approaches to further substantiate the above interpretation of the data shown in Figure 3.8. First, data can be taken at different tip positions above the molecule, as will be shown in the next section. Second, as already indicated above, we can adapt the set pulse to initialize the population in the neutral state, partly in S_0 and partly in T_1, as will be demonstrated in Section 3.4.2.

3.4.1. Varying the lateral tip position

To further scrutinize the interpretation of the data shown in Figure 3.8a and c, we performed experiments at three different lateral tip positions above the molecule. The results for three t_{sweep} are displayed in Figure 3.10a, b and c. The spectra were taken at the positions indicated in the AC-STM images[89] of the HOMO and LUMO densities shown in Figure 3.11a and b. These images show that upon moving at constant height from position I to III, the tunneling rates to the HOMO and LUMO are both reduced. This explains the increase of the fraction in D_0^+ during the read-out in Figure 3.10a from position I to III between voltages associated to (1) and (2) and above (3): with a decreasing tunneling probability from position I to III, a larger fraction remains in the initialized D_0^+ state. However, the fraction that is read-out between voltages corresponding to (2) and (3) seems much less affected by the lateral tip position, as can be seen in Figure 3.10b and c. This supports our assignment that the plateau between voltages of (2) and (3) is governed by two competing tunneling rates, namely those corresponding to the $D_0^+ \rightarrow S_0$ and the $D_0^+ \rightarrow T_1$ transitions. Interestingly, for the long t_{sweep} used in Figure 3.10c, the fraction that is read-out in the D_0^+ state at these voltages is - within uncertainty margins - the same for the three different tip positions. For such long t_{sweep} all population will end up at the end of the sweep pulse (with a sweep voltage corresponding to the plateau between (2) and (3)) in either the S_0 or T_1 state. Thus, the competing tunneling rates into these two states are apparently suppressed to a similar extent by changing the tip position from I to III.

Figure 3.10b shows two additional peaks in the data: one just below the voltage corresponding to (3) and another between the voltages corresponding to (5) and (6). A similar peak is observed in data measured on PTCDA (at (9) in Figure 3.20). We assign it to accessing an excited triplet state, which will be explained in Section 3.10. As the first small peak for pentacene in Figure 3.10b is located in proximity to the V_{sweep} where the

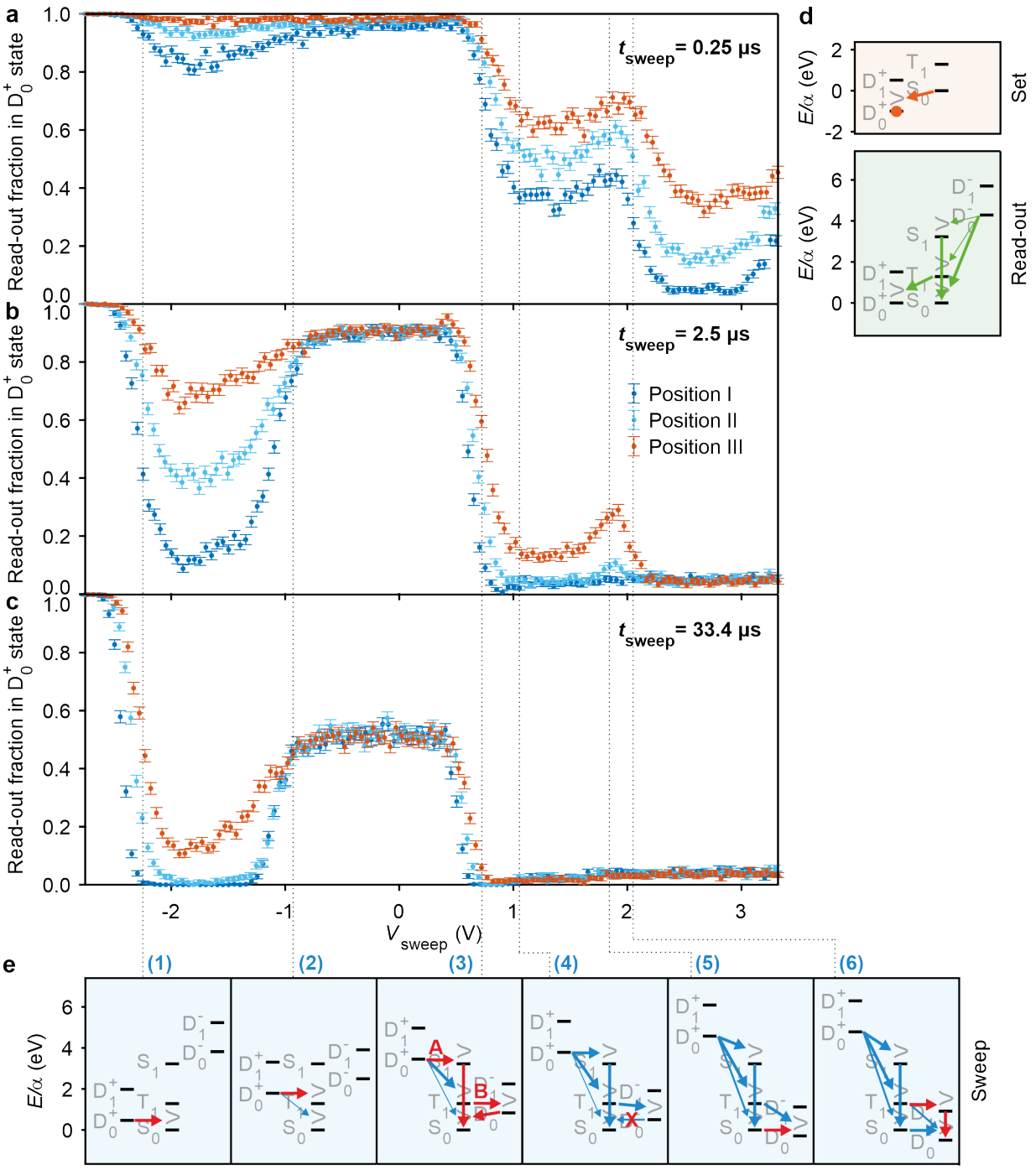

Figure 3.10.: Excited-state spectroscopy of pentacene at different lateral tip positions. **a-c**, Measured read-out fraction in the D_0^+ state versus the applied gate voltage during the sweep pulse V_{sweep}, for three different tip positions and for three different sweep-pulse durations. Measurements were performed above the same individual molecule as in Figures 3.8 and 3.12 with a voltage pulse sequence similar to Figure 3.5b, using a set pulse to initialize the molecule in D_0^+ ($V_{\text{set}} = -3.8\,\text{V}$) and read-out at the D_0^+-S_0 degeneracy ($V_{\text{read-out}} = -2.8\,\text{V}$). **d**, Many-body energy diagrams of the transitions taking place during the set pulse and at the beginning of the read-out phase for the spectra shown in **a-c**. **e**, Many-body energy diagrams of the transitions taking place at the sweep voltages indicated by the dotted lines. The arrows, crosses and dots are analogous to Figure 3.8e. Panel **b** shows two additional features at 0.4 and 1.7 V, respectively, which are not indicated in **e** but described in Section 3.4.1.

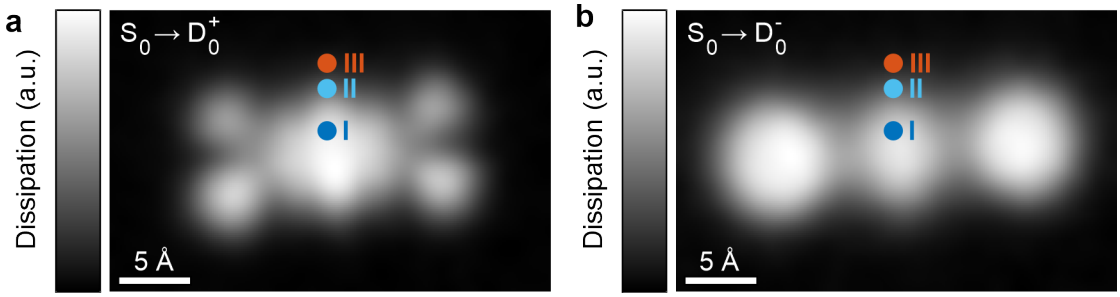

Figure 3.11.: Lateral tip positions used for the excited-state spectroscopy of pentacene in Figure 3.10. **a**, **b**, AC-STM images[89] of the same pentacene as in Figure 3.10a to c indicating the three positions where the spectra shown in Figure 3.10a to c were measured (oscillation amplitude $A = 1\,\text{Å}$). **a**, $S_0 \rightarrow D_0^+$ (HOMO): $\Delta z = -2.6\,\text{Å}$, $V_G = -2.9\,\text{V}$, $V_{a.c.} = 1.2\,\text{V}$ peak-to-peak (V_{pp}). **b**, $S_0 \rightarrow D_0^-$ (LUMO): $\Delta z = -2.0\,\text{Å}$, $V_G = 1.43\,\text{V}$, $V_{a.c.} = 1.2\,V_{pp}$). The tip-height offset Δz is given with respect to the setpoint $\Delta f = -1.443\,\text{Hz}$ at $V = 0\,\text{V}$, $A = 3\,\text{Å}$.

$D_0^+ \rightarrow S_1$ transition becomes accessible (3), it is assigned to a transition to T_2, because of the experimental evidence that a higher-lying triplet state lies close to the S_1 state of pentacene[142,143].

We note that this $D_0^+ \rightarrow T_2$ transition might (partially) also proceed via S_1 followed by intersystem crossing to T_2, hence as $D_0^+ \rightarrow S_1 \rightarrow T_2$. The likelihood of such an intersystem crossing pathway competing with a direct decay of S_1 to S_0 was found to be strongly dependent on the exact energy level alignment of S_1 and T_2, which depends on the environment[142,143]. For two different lattices sites of pentacene in a p-terphenyl host crystal an intersystem crossing yield of 0.5% was found, while for the two other lattice sites a yield of 60% was found[144]. It was determined that for the two lattice sites with the large intersystem crossing rate, T_2 has a slightly lower energy than S_1, while for the two other lattice sites T_2 has a slightly higher energy[142]. This could explain the large difference in intersystem crossing rates: if T_2 is energetically below S_1, rapid intersystem crossing to T_2 could be possible, while if it is energetically above S_1, this process is blocked at low temperatures.

The feature in Figure 3.10b at 1.7 V we assign to accessing a transition to a higher-lying triplet excited state, here called T_3, at which one electron occupies the HOMO and another a higher-lying unoccupied orbital. Interestingly, these peaks only show up at spatial positions laterally displaced from the HOMO and LUMO density maxima, indicating that higher-lying orbitals with a different spatial distribution are involved, which is consistent with the assignment as a transition to a higher-lying excited triplet state (see Section 3.10).

From the AC-STM images in Figure 3.11, it appears that for other lateral tip positions the ratio of tunneling into the HOMO and LUMO can be significantly changed. However, no tip positions could be found were such a clear change was observed. This can be explained by the fact that these images were taken at a tip-sample distance 2.0 and 2.6 Å smaller than used for the excited-state spectroscopy measurements, such as those shown in Figure 3.10a to c. Therefore, the dependence of tunneling rates on the lateral tip position is less pronounced than in the AC-STM images.

3.4.2. Different initialization

The second approach to further substantiate the interpretation of the data shown in Figure 3.8 is to initialize the molecule in the neutral state, partly in the S_0 state and partly in the T_1 state, instead of initialization in the positive charge state. This different starting configuration modifies the weight of the different pathways and eliminates pathways that start at D_0^+. It can thereby aid the assignment of spectral features to specific electronic transitions.

To initialize the population partly in S_0 and partly in T_1, the set pulse is replaced by a set pulse sequence consisting of two pulses: a pulse to bring the molecule to D_0^+ and another pulse to subsequently bring the molecule in the T_1 state. For the second pulse, a voltage of $V_{\text{read-out}} + 2.5\,\text{V}$ was chosen for pentacene (here, $-0.3\,\text{V}$). This pulse sequence has the same effect as the set and sweep pulse for the data at $-0.3\,\text{V}$ in Figure 3.8 and thus allows the population of T_1 and S_0. The duration of the second pulse determines the ratio of the populations of the T_1 and S_0 states, since the T_1 state will decay during this pulse to the S_0 state according to its molecule-specific lifetime[21]. At the end of a 33.4 µs long second pulse of the set pulse sequence with $V_{\text{set}} = -0.3\,\text{V}$, the T_1 and S_0 population was 0.51 ± 0.01 and 0.49 ± 0.01, respectively.

The results are shown in Figure 3.12a and c. In Figure 3.12a around $V_{\text{sweep}} = 0\,\text{V}$, the initialized population in the T_1 state will stay in T_1 during the sweep pulse (except for the slow direct decay into S_0) and will be detected as D_0^+ during the read-out. Upon increasing V_{sweep}, two downward steps are observed for the shortest t_{sweep}, at (3B) and (6). At the same V_{sweep} steps are present in Figure 3.8a. Since processes that start at D_0^+ are excluded in Figure 3.12, the observation of these steps in Figure 3.12a indicates that the T_1 state is involved, supporting the assignment of $T_1 \rightarrow D_0^-$ to (3B) and $T_1 \rightarrow D_1^-$ to (6). Note, however, that the relative step sizes at (3) are quite different for Figure 3.8a and Figure 3.12a (for the shortest t_{sweep} the signal drops by roughly 2/5 and 1/4 of its preceding value, respectively). This indicates that the step in Figure 3.8 cannot stem from $T_1 \rightarrow D_0^-$ alone but must contain another contribution (which we assigned to $D_0^+ \rightarrow S_1$ (3B)), not contributing in Figure 3.12a.

For small enough V_{sweep}, T_1 can decay into D_0^+, giving rise to feature (8). This experiment also allows accessing the $S_0 \rightarrow D_0^+$ transition (7) at voltages more negative than the positive-neutral charging hysteresis at around $-2.8\,\text{V}$. These transitions are not accessible, when initializing the molecule in D_0^+.

3.4.2.1. Controlling the initial population in the triplet state

The initial preparation of the molecule in the neutral state further allows us to vary the initial population of the triplet state by slightly modifying the set pulse sequence. As described in the previous section, the initial population in T_1 is determined by the length of the second pulse of the set pulse sequence. Here, pulse durations of 33.4 and 100.1 µs were chosen to populate the T_1 state with a 52% and 24% probability, respectively. The resulting spectra are shown in Figure 3.13. Figure 3.13a shows that the steps at (3B) and (6) scale with the initial T_1 population, lending further support that (3B) and (6) involve the T_1 state. Figure 3.13b shows a similar scaling in the voltage region between (7) and (5). This confirms that the T_1 state is also involved in (1), (4) and (8). In contrast, the

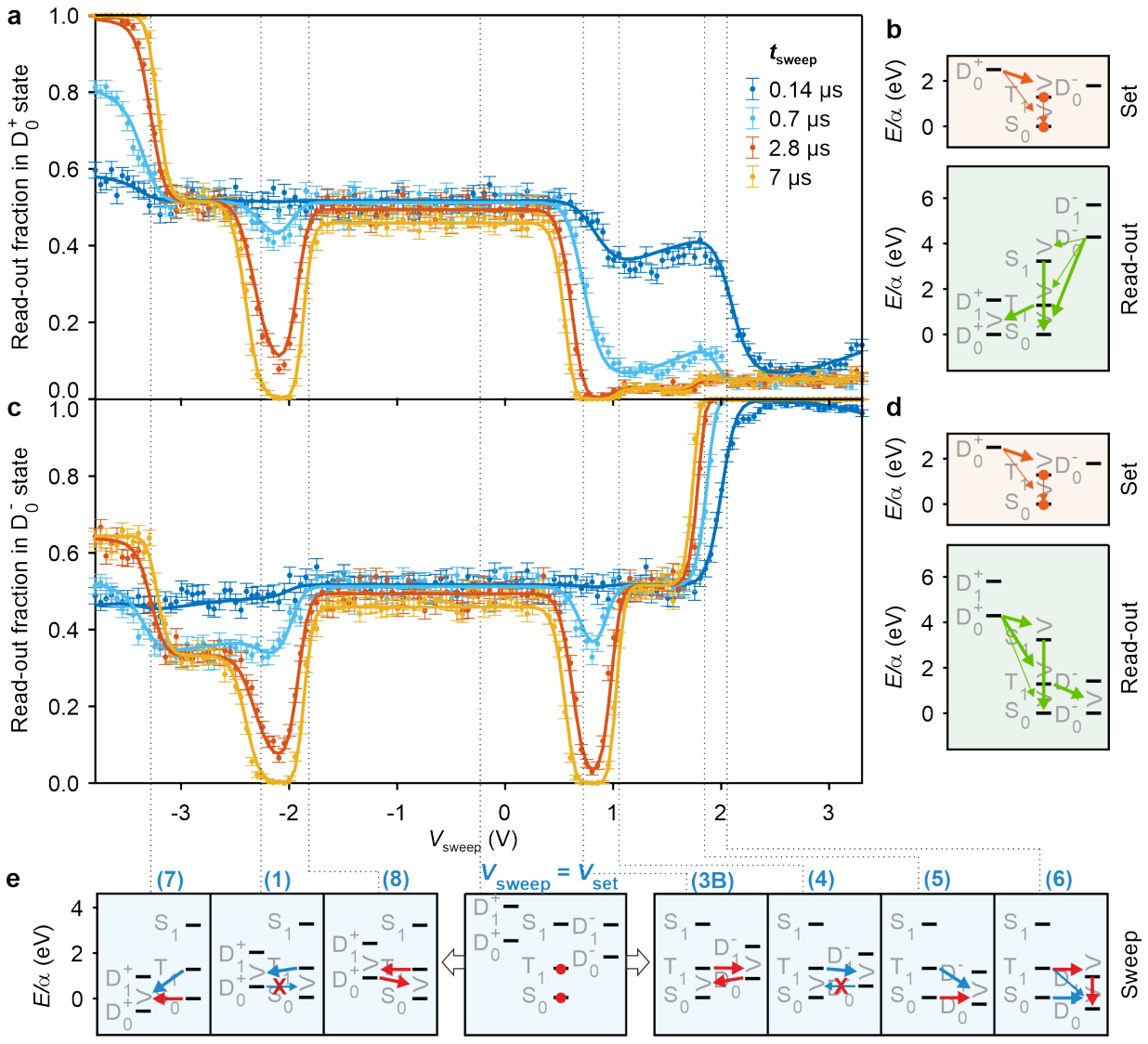

Figure 3.12.: Excited-state spectroscopy of pentacene, initialized in the neutral charge state. **a**, **c**, Plot of the measured read-out fraction in the D_0^+ and D_0^- states, respectively, as a function of V_{sweep}. Measurements were performed with a voltage pulse sequence similar to Figure 3.5b. A set pulse sequence was used to initialize the molecule in S_0 or T_1, with approximately equal populations (see Section 3.4.2). The read-out was at the D_0^+-S_0 ($V_{read\text{-}out} = -2.795\,V$) or S_0-D_0^- ($V_{read\text{-}out} = 1.416\,V$) degeneracies for **a** and **c**, respectively. Four different t_{sweep} were used, as indicated. Solid lines represent fits to the data (see Section 3.6). **b**, **d**, Many-body energy diagrams of the transitions taking place during the second pulse of the set pulse sequence (see Section 3.4.2) and at the beginning of the read-out phase for the spectra shown in **a** and **c**, respectively. **e**, Many-body energy diagrams of the assigned transitions happening at the sweep voltages indicated by the dotted lines. The transitions that correspond to those present in Figure 3.8 are indicated with the same number. The arrows, crosses and dots are analogous to Figure 3.8e. Note that if the sweep voltage is close to the set voltage (between (8) and (3B)) the population remains in the T_1 and S_0 state (see diagram at $V_{sweep} = V_{set}$). Only upon reducing or increasing V_{sweep} outside this range different transition channels open and/or close as indicated.

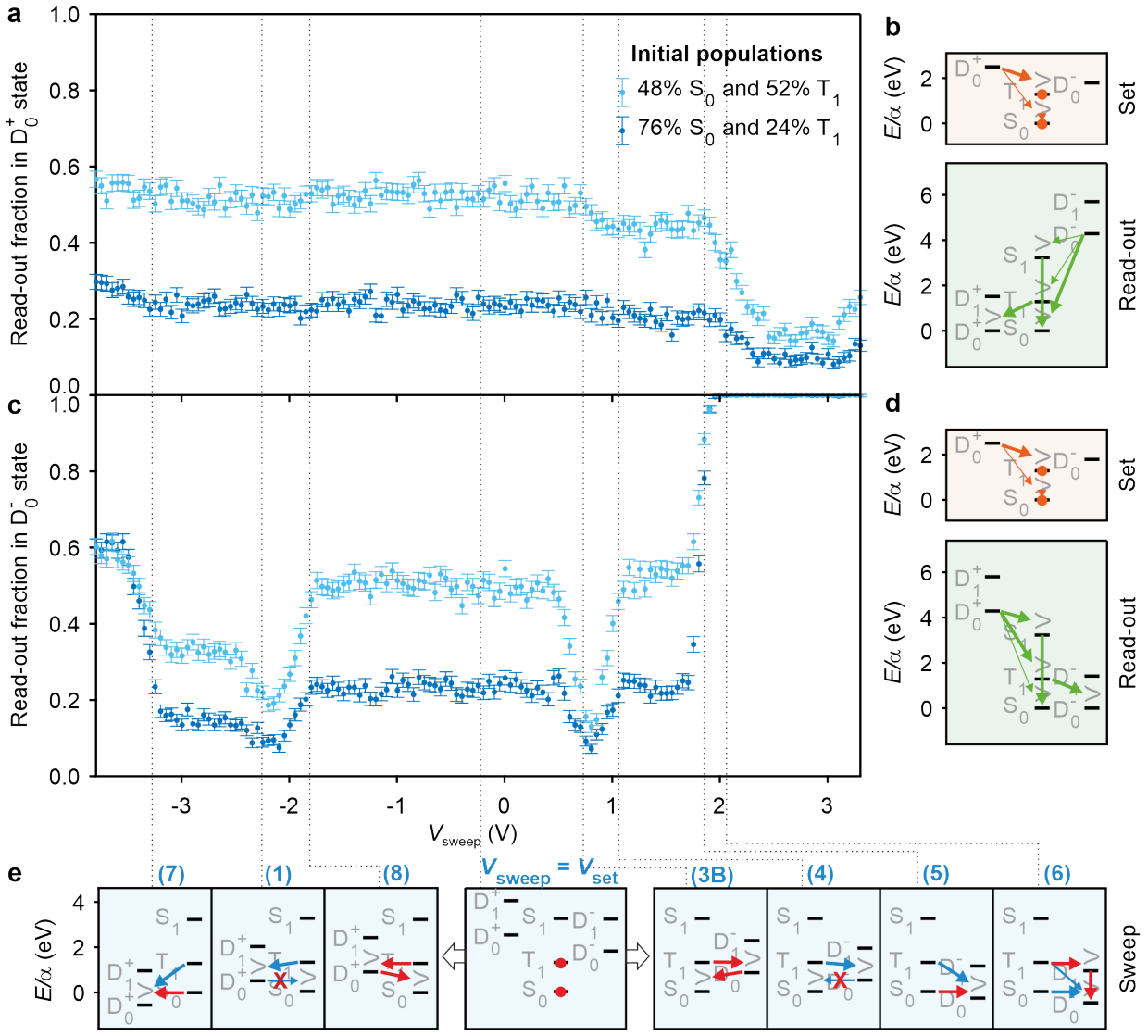

Figure 3.13.: Excited-state spectroscopy of pentacene, initialized in the neutral charge state with different S_0 and T_1 populations. **a**, **c**, Plot of the measured read-out fraction in the D_0^+ and D_0^- states, respectively, versus V_{sweep}. Measurements were performed with a voltage pulse sequence similar to Figure 3.5b. Two different set pulse sequences were used to initialize the molecule with different initial populations in S_0 and T_1, as indicated (see Section 3.4.2.1). The read-out was at the D_0^+-S_0 ($V_{\text{read-out}} = -2.795\,\text{V}$) and S_0-D_0^- ($V_{\text{read-out}} = 1.416\,\text{V}$) degeneracy for **a** and **c**, respectively. A t_{sweep} of 0.14 µs for **a** and 2.8 µs for **c** was used. **b**, **d**, Many-body energy diagrams of the transitions taking place during the set and at the beginning of the read-out phase for the spectra shown in **a** and **c**, respectively. **e**, Many-body energy diagrams of the transitions taking place at the sweep voltages indicated by the dotted lines. The arrows, crosses and dots are analogous to Figure 3.8e. Note that if the sweep voltage is close to the set voltage (between (8) and (3B)), the population remains in the T_1 and S_0 state (see diagram at $V_{\text{sweep}} = V_{\text{set}}$). Only upon reducing or increasing V_{sweep} outside this range different transition channels open and/or close as indicated.

high and low voltage regions are not affected by the ratio of T_1 and S_0 population at the beginning of the sweep pulse. This confirms the interpretation that at these high and low voltages, all the initial population will end up in a single charge state (D_0^- at (5) and D_0^+ at (7)). Therefore, it is not affected by changing the initial T_1 population.

3.4.3. Assessment of the assignment

This section critically reviews the assignment of the transitions as explained in the previous sections and provides a general strategy, how the different transitions can be assigned, for example, in a future study of other molecules.

As a first step, KPFS provides the voltages at which the molecule changes its charge state (see Section 2.3.3.3 and Figure 2.9), corresponding to a transition between the two ground states of different charge. Which charge-state transition is observed can be confirmed by the AC-STM images (see Figure 3.11 for pentacene), which reflect the orbital densities of the respective molecular orbital being tunneled into or out of. $D_0^+ \rightarrow S_0$ and $S_0 \rightarrow D_0^-$ are associated to tunneling into the HOMO and the LUMO respectively, the densities of which are observed in AC-STM, allowing us to identify the positive-neutral and neutral-negative degeneracies. Note that for this assignment, AC-STM images of two sequential transitions are required to be able to distinguish the tunneling of the first and the second electron in or out of a certain orbital.

Transition (1) is the first transition which occurs upon increasing V_{sweep} from the positive-neutral degeneracy and can therefore be assigned to the $D_0^+ \rightarrow S_0$ transition. The assignment of (2) to accessing $D_0^+ \rightarrow T_1$ is confirmed by the fact that the accessed state is long-lived and decays with a triple-exponential decay (see ref. [21] and Figure 4.4).

Based on this assignment the molecule can be prepared in T_1, and the value of the plateau between (8) and (3B) in Figure 3.12 reflects the relative T_1 population. The first transitions that will open upon decreasing or increasing V_{sweep} are those to the cationic and anionic ground states, that is, forming D_0^+ or D_0^-, respectively. Thus, (8) and (3B) can be assigned to $T_1 \rightarrow D_0^+$ and $T_1 \rightarrow D_0^-$, respectively. Assuming similar relaxation energies for the different transitions, the T_1-S_0 energy difference can be derived from $D_0^+ \rightarrow S_0$ and $D_0^+ \rightarrow T_1$ (see Section 3.8). Using this energy difference and the voltage of the $T_1 \rightarrow D_0^-$ transition, the voltage for accessing the $S_0 \rightarrow D_0^-$ transition (5) can be estimated precisely enough to confirm the assignment of the feature corresponding to (5).

Furthermore, the reorganization energy (sum of the relaxation energies) can be obtained from the difference between the $D_0^+ \rightarrow T_1$ and $T_1 \rightarrow D_0^+$ transition energies (see Section 3.8). Assuming similar reorganization energies, the $S_0 \rightarrow D_0^+$ (7) and $D_0^- \rightarrow S_0$ (4) transition voltages can be estimated from the known $D_0^+ \rightarrow S_0$ and $S_0 \rightarrow D_0^-$ transition voltages, respectively, to assign the respective features.

The energy of the $S_1 \rightarrow S_0$ transition is well known from luminescence experiments and can therefore be assigned from literature values. Preferentially, values from experiments in similar sample setups (environments) should be used, as the energy level alignment depends on the environment of the molecule. The $S_1 \rightarrow S_0$ transition of pentacene has been measured as 2.26 eV (ref. [145]) for a single molecule on 4 ML of NaCl on Ag(100), using a Ag covered tip apex, and we use this value for comparison here. Using an estimate

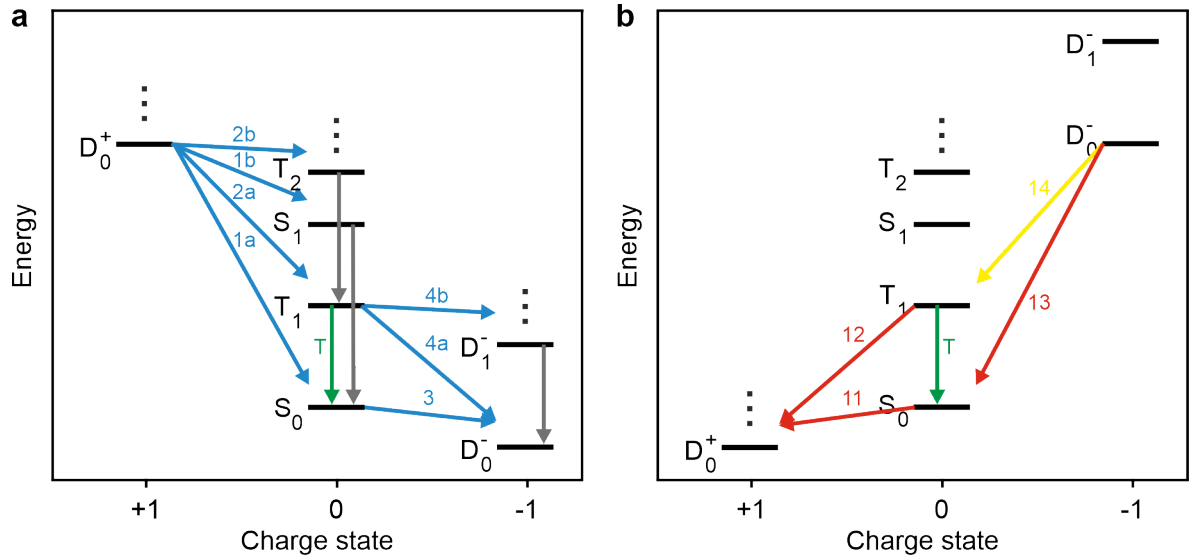

Figure 3.14.: Definition of the transitions and their rates. Many-body diagrams at the largest positive (**a**) and largest negative (**b**) gate voltage used, indicating the labels of the transitions by numbers attached to the arrows. The corresponding rates are indexed according to these labels. Blue (red) arrows are used to indicate an electron tunneling process from the tip (molecule) to the molecule (tip), while the gray arrows indicate the immediate decay processes from a higher-lying excited state to the lowest state of the same multiplicity and charge. The green arrow indicates the $T_1 \rightarrow S_0$ decay. Transition 14 is indicated in yellow, since this transition is not taken into account in the final rate equations that describe the populations during the sweep pulse, for reasons explained in Section 3.5. For similar reasons transitions from D_0^- to S_1 or T_2 during the sweep pulse are also not included.

of the lever arm (we typically find values around $\alpha = 0.7$, see Section 3.7), the $D_0^+ \rightarrow S_1$ transition (3A) can be assigned.

This leaves the assignment of the $T_1 \rightarrow D_1^-$ transition (6). For a preparation of the molecule in T_1, the $T_1 \rightarrow D_1^-$ transition is the second transition toward more positive sweep voltage, following the $T_1 \rightarrow D_0^-$ transition, being the first.

3.5. Rate equations and fitting procedure

Having assigned the transitions in Figures 3.8 and 3.12, the relative energies of the electronic states can be derived by fitting these four sets of data. To this end, we formulated a set of differential rate equations that describe the time-dependent populations of the different states, S_0, T_1, S_1, T_2, D_0^+, D_0^-, and D_1^-, during the sweep period. In the following, we use the italicized labels of the states to describe their populations. The transition rates between these states are used as visualized in Figure 3.14, serving as a definition of the corresponding indices. We assume that the relaxation between states of the same charge and the same multiplicity is fast compared to all other time scales of the experiment. Hence, for the rate equations we assume these relaxations to be immediate. Therefore, a transition into S_1 has the same effect as a transition into S_0, for example. Most rates depend on the applied voltage and the tunneling conditions, as described further below. The resulting set

of differential equations reads

$$\frac{\mathrm{d}}{\mathrm{d}t}D_0^+(t) = -(k_{1\mathrm{a}} + k_{1\mathrm{b}} + k_{2\mathrm{a}} + k_{2\mathrm{b}})D_0^+(t) + k_{12}T_1(t) + k_{11}S_0(t), \tag{3.3}$$

$$\frac{\mathrm{d}}{\mathrm{d}t}T_1(t) = -(k_{4\mathrm{a}} + k_{4\mathrm{b}} + k_{12} + k_{\mathrm{T}})T_1(t) + (k_{2\mathrm{a}} + k_{2\mathrm{b}})D_0^+(t) + k_{14}D_0^-(t), \tag{3.4}$$

$$\frac{\mathrm{d}}{\mathrm{d}t}S_0(t) = -(k_3 + k_{11})S_0(t) + (k_{1\mathrm{a}} + k_{1\mathrm{b}})D_0^+(t) + k_{\mathrm{T}}T_1(t) + k_{13}D_0^-(t), \tag{3.5}$$

$$\frac{\mathrm{d}}{\mathrm{d}t}D_0^-(t) = -(k_{13} + k_{14})D_0^-(t) + (k_{4\mathrm{a}} + k_{4\mathrm{b}})T_1(t) + k_3S_0(t). \tag{3.6}$$

For the differential equations, rates $k_{1\mathrm{a}}$ and $k_{1\mathrm{b}}$ have the same effect. The same holds true for the pair $k_{2\mathrm{a}}$ and $k_{2\mathrm{b}}$, as well as the pair $k_{4\mathrm{a}}$ and $k_{4\mathrm{b}}$. These pairs are therefore combined to the rates $k_1 = k_{1\mathrm{a}} + k_{1\mathrm{b}}$, $k_2 = k_{2\mathrm{a}} + k_{2\mathrm{b}}$ and $k_4 = k_{4\mathrm{a}} + k_{4\mathrm{b}}$, respectively, leading to the slightly simplified version

$$\frac{\mathrm{d}}{\mathrm{d}t}D_0^+(t) = -(k_1 + k_2)D_0^+(t) + k_{12}T_1(t) + k_{11}S_0(t), \tag{3.7}$$

$$\frac{\mathrm{d}}{\mathrm{d}t}T_1(t) = -(k_4 + k_{12} + k_{\mathrm{T}})T_1(t) + k_2D_0^+(t) + k_{14}D_0^-(t), \tag{3.8}$$

$$\frac{\mathrm{d}}{\mathrm{d}t}S_0(t) = -(k_3 + k_{11})S_0(t) + k_1D_0^+(t) + k_{\mathrm{T}}T_1(t) + k_{13}D_0^-(t), \tag{3.9}$$

$$\frac{\mathrm{d}}{\mathrm{d}t}D_0^-(t) = -(k_{13} + k_{14})D_0^-(t) + k_4T_1(t) + k_3S_0(t). \tag{3.10}$$

This last step of combining rates $k_{i\mathrm{a}}$ and $k_{i\mathrm{b}}$ of transitions to states of the same charge and the same multiplicity, illustrates that it is very easy to include further higher-lying states at a later stage. Conversely, some transitions never occur in the actual experiments. Transition 14, for example, does not occur during the sweep pulse, since the experiments did not include initialization in D_0^-. Occupation of D_0^- can therefore only occur for voltages, for which D_0^- is energetically below T_1, such that transition 14 is energetically not accessible during the sweep pulse.

Before discussing the rate equations further below, we will first consider in general which transitions can occur during our pump-probe pulse sequence. Since for every transition only one electron is tunneling, not all transitions will occur. For example, the transition from D_0^+ to a neutral excited triplet state, which has two electrons in the HOMO and one electron in each LUMO and HOMO-1 (ref. [23]) would require concerted tunneling of more than one electron. Such a process is very unlikely and therefore expected to be invisible here. However, as indicated in Section 2.1, many of the states are expected to have multi-reference character[23–25]. For example, the excited triplet state described above is expected to strongly interact via pair-hopping with another neutral excited triplet state, which has one electron in each the HOMO and the LUMO+1. This latter state will be accessible from D_0^+ by tunneling of a single electron. Likewise, the neutral excited singlet state having two electrons in the LUMO and none in the HOMO is expected to have a non-zero contribution of a configuration with two electrons in the HOMO and none in the LUMO. If such multi-reference character is present, it is enough that one contributing

many-body state is accessible to be observed in our experiment. Nevertheless, we cannot rule out that some excited states might be invisible in the spectra.

The above set of rate equations can be written in a compact form by bringing the time-dependent populations in vector form as $\boldsymbol{P} = (D_0^+, T_1, S_0, D_0^-)$, such that

$$\frac{\mathrm{d}}{\mathrm{d}t}\boldsymbol{P}(t) = \mathbf{K}\boldsymbol{P}(t) \tag{3.11}$$

with

$$\mathbf{K} = \begin{bmatrix} -(k_1+k_2) & k_{12} & k_{11} & 0 \\ k_2 & -(k_4+k_{12}+k_\mathrm{T}) & 0 & k_{14} \\ k_1 & k_\mathrm{T} & -(k_3+k_{11}) & k_{13} \\ 0 & k_4 & k_3 & -(k_{13}+k_{14}) \end{bmatrix} \tag{3.12}$$

having the solution

$$\boldsymbol{P}(t_\mathrm{sweep}) = \exp(\mathbf{K}t_\mathrm{sweep})\boldsymbol{P}(t=0). \tag{3.13}$$

This solution has been used to calculate the final populations numerically and fit the data. The initial populations $\boldsymbol{P}(t=0)$ are those present at the beginning of the sweep pulse, that is, after preparing the molecule with the set pulse (sequence). In case of the data shown in Figure 3.8, the set pulse brings the molecule to D_0^+, such that it was assumed that the molecule was always in D_0^+ at the start of the sweep pulse, hence $\boldsymbol{P}(t=0) = (1,0,0,0)$. In contrast, in case of the data of Figure 3.12, the molecule was brought to either S_0 or T_1 by a set pulse sequence. In this case, it was assumed that the molecule was in one of these two states, and the initial fraction in T_1 was used as a fitting parameter (note that this parameter is directly reflected in the value of the plateau between voltages of (8) and (3B), such that there is little ambiguity in fitting this parameter).

Fitting the data numerically, as described above, is relatively slow. To systematically scrutinize the fitting procedure in many fit runs under varying conditions, approximate analytical solutions of the above differential equations were used. However, the final fit was performed numerically.

All rates except for k_T (and except for the immediate transitions, see above) involve a tunneling event between tip and molecule. Whether a given tunneling process is possible, depends on the applied voltage. Tunneling of an electron into the molecule becomes possible above a certain threshold voltage, while tunneling of an electron from the molecule into the tip becomes possible below a threshold voltage. The phonon-broadened states are observed in conventional STS as Gaussian peaks in the differential conductance[70] (see Figure 2.5), corresponding to an onset of the tunneling rate with voltage as an error function[58], which is also used here for the fitting. Finally, the tunneling probability is also a function of applied voltage, as the latter affects the effective barrier height for tunneling. As the spectra acquired here typically cover a range of several volts, the effective barrier height can vary considerably. To include this effect in the fits, the WKB approximation of tunneling through a trapezoidal barrier is used, as explained in Section 2.2. According to Equation (2.6), the tunneling rates k_i take the form:

$$k_i = k_{i0}\exp\left(-2\frac{2\sqrt{2m}}{3\hbar}\frac{\varphi_m^{\frac{3}{2}} - \varphi_t^{\frac{3}{2}}}{\varphi_m - \varphi_t}d\right)\left(1+\mathrm{erf}\left(\pm\frac{V_\mathrm{G}-V_i}{w_i}\right)\right)/2. \tag{3.14}$$

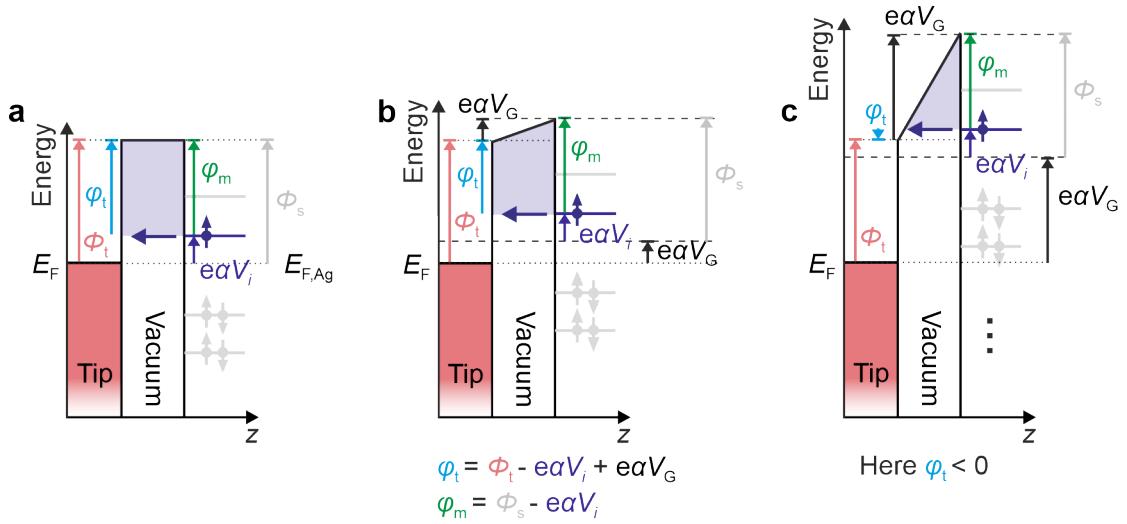

Figure 3.15.: Barrier height. Schematic illustration to deduce the tip-sided φ_t and molecule-sided φ_m flank of the tip-molecule tunneling barrier for a given transition with threshold voltage V_i. **a**, Taking the lever arm into account, tunneling processes occur at an energy $e\alpha V_i$ above the Fermi level of the tip E_F in absence of gating. Hence, at $V_G = 0$, φ_m and φ_t are given by subtracting $e\alpha V_i$ from the work function of the NaCl/Ag(111) substrate Φ_s and tip Φ_t, respectively. **b**, For $V_G \neq 0$, the molecular states will shift with respect to E_F by $e\alpha V_G$ (see also Figure 2.8a). φ_m is not affected by the gate voltage, remaining $\varphi_m = \Phi_s - e\alpha V_i$. In contrast, φ_t changes by $e\alpha V_G$, such that we deduce $\varphi_t = \Phi_t - e\alpha V_i + e\alpha V_G$. **c**, For large negative gate voltages, φ_t can become negative, as illustrated, such that instead of the trapezoidal barrier a triangular barrier of reduced width has to be considered, see Equation (3.15).

with the electron mass m, the reduced Planck constant $\hbar$, the tunneling distance d, the applied gate voltage V_G, the molecule-sided barrier height $\varphi_m = \Phi_s - \alpha V_i$, and the tip-sided barrier height $\phi_t = \Phi_t - \alpha(V_i - V_G)$, with the lever arm α and the work functions of the sample Φ_s and tip Φ_t (see Figure 3.15b). k_{i0}, V_i, and w_i are the three fit parameters for every transition i, describing the reference rate, the voltage threshold and the width of the phonon-broadened states, respectively. The full width at half maximum (FWHM) can be derived from the w_i values by multiplication with $2\sqrt{\ln(2)}$. On the sample side of the junction, a derivation of the tunneling probability based on the specific molecular orbitals would be more appropriate, but this would require an a-priori assignment of molecular orbitals to each transition. The WKB approximation as presented above works without such presumptions and was therefore preferred. Differences in tunneling rate of other origins that do not depend on voltage, as e.g. the multiplicity of the states, their individual spin-state overlap (see Section 3.4) and the lateral dependence of wave-function overlaps are accounted for by different k_{i0}, which serve as fitting parameters. For tunneling into the molecule and out of the molecule the sign in front of the argument of the error function (erf) is positive and negative, respectively.

For large negative voltages V_G, the tip-sided barrier height $\varphi_t = \Phi_t - \alpha(V_i - V_G)$ can become negative (see Figure 3.15c)[146]. In this situation the above equation takes a different

form[147], i.e.,

$$k_i = k_{i0} \exp\left(-2\frac{2\sqrt{2m}}{3\hbar}\frac{\varphi_m^{\frac{3}{2}}}{\varphi_m - \varphi_t}d\right)\left(1 + \mathrm{erf}\left(\pm\frac{V_\mathrm{G} - V_i}{w_i}\right)\right)/2. \tag{3.15}$$

The lever arm α, the work functions Φ_s and Φ_t and the tunneling distance d were not used as fit parameters. α was set by gauging the S_1-S_0 energy difference of pentacene against literature values as described in Section 3.7. The work functions of tip and sample were both set to 4 eV. The tunneling distance d was found empirically to yield a good fit for $d = 9$ Å.

At first glance, the fixed choices for these quantities might seem arbitrary and therefore require a discussion. First of all, the values are reasonable estimates: The substrate Ag(111) has a work function of 4.74 eV (ref. [148]) and it is known that NaCl reduces the work function by roughly 1 eV (ref. [149, 150]). KPFS data directly reveal the work function difference between tip and sample, which we measured to be small compared to 4 eV (see local contact potential difference in Table 3.1). The experimental tunneling distance d was estimated from the experimentally known difference between the tip height used in the excited-state spectra and the tip height required for bond-resolved imaging with a CO-functionalized tip. Bond-resolved images were used that were recorded using a CO-functionalized tip for which also the decay from D_0^+ into S_0 was measured (the tip used for the measurements shown in Figure 4.21). This decay rate was compared to the one measured at the tip-sample height used for the excited-state spectroscopy measurements (see Section 3.3.1). Finally, the tunneling distance for the bond-resolved images was estimated by comparison to density-functional calculations from ref. [4]. In this estimation, it was assumed that the CO molecule itself is part of the barrier, because CO molecules on the surface are imaged as a depression using a metal tip[50]. Using these considerations, a value of approximately 9 Å was derived, which matches the one found empirically to yield a good fit.

In Equations (3.14) and (3.15) one could simply omit the exponential term describing the tunneling probability, while the error function would still provide a reasonable fit to the step-like features in the spectra yielding the desired parameters, namely a set of V_i. The exponential term is included to obtain the explicit voltage dependence of the tunneling probability, which expresses itself in the slight voltage dependent populations between the step-like features, see for example Figure 3.20. Including voltage dependence of the tunneling probability improves the fit considerably. However, the precise choice of barrier height and width (within reasonable bounds) is much less important for the quality of the fit. Likewise, it is unimportant for the fit, whether the barrier is slightly larger at its left flank than at the right, or the other way around. Therefore, we set the work functions to reasonable values, neglect the difference in work functions between tip and sample, and set the tunneling-barrier width such that the voltage-dependent populations between the step-like features in the spectra are reproduced well.

Yet, a difference in work function of tip and sample, i.e. a non-zero contact potential difference (CPD), has another effect. A non-zero CPD will result in an electric field in the junction even at zero gate voltage, equivalent to a constant offset of the applied gate voltage. The voltage of contact potential difference V_CPD can be accessed by KPFS. This offset in the gate voltage resulting from a non-zero CPD is omitted in the equations for simplicity,

since it does not affect the energy differences that we derive (because such differences are always acquired with one individual tip). The effect of a non-zero CPD should be taken into account when considering the absolute energies, at which the transitions happen. To this end, the V_{CPD} values for the tips used, with respect to the NaCl(>20 ML)/Ag(111) surface, are provided in Table 3.1. Note that even with applied V_{CPD}, the electric field is not nullified everywhere in the junction, as the field is inhomogeneous[76]. However, also this effect from the inhomogeneous field contribution is canceled in the energy differences considered here.

Despite the triplet decay being a triple-exponential decay, it is treated in the fit as a single-exponential decay with rate k_{T} as a fitting parameter for simplicity. The rate k_{T} is low (corresponding to a long-lived T_1) compared to all the considered tunneling rates k_i at the parameters of the experiment. Therefore, all sweep times used in the experiments were relatively short compared to the triplet decay. In this limited sweep-time range, the triplet decay is very well approximated by a single-exponential decay.

In principle, during the read-out period similar cascades of transitions as described for the sweep pulse will occur, just at a different gate voltage, the read-out voltage. However, since the read-out time is much longer than the involved tunneling rates, it can be assumed that the molecule will always return to the ground state of one of the two charge states that are brought in degeneracy by the read-out voltage. Thus, the read-out populations represent the equilibrium limit and the fraction that is read-out in the charge state can then be expressed in terms of the populations at the end of the sweep period. For the read-out at the D_0^+-S_0 degeneracy this is

$$D^+_{0,\text{read-out}} = D_0^+ + T_1 + f_{-\to+} D_0^-. \tag{3.16}$$

$D^+_{0,\text{read-out}}$, the read-out fraction in the D_0^+ state, is a sum of the populations in D_0^+ and T_1 as well as a fraction $f_{-\to+}$ of the population in D_0^-. Here, it is assumed that all the population in T_1 at the end of the sweep pulse will end up as D_0^+ during the read-out, since k_{T} is negligible against k_{12} at the tip height used. $f_{-\to+}$ is used as a fitting parameter; it is given by the ratio of rates k_{14} and k_{13}, where k_{14} and k_{13} also include the tunneling processes into the accessible higher-lying triplet and singlet states, respectively. Since tunneling into S_0 (k_{13}) has the lowest tunneling barrier (see Figure 2.3), $f_{-\to+}$ is small. We indeed obtained from the fitting that $f_{-\to+}$ lies in the range of 0.03 to 0.05 for pentacene.

Analogously, for the read-out at the S_0-D_0^- degeneracy

$$D^-_{0,\text{read-out}} = D_0^- + T_1 + f_{+\to-} D_0^+ \tag{3.17}$$

with $f_{+\to-}$ the fraction of the population in D_0^+ that is read-out at D_0^-. This fraction is given by the ratio of rates k_1 and k_2 (including the rates into the accessible higher-lying excited singlet and triplet states). $f_{+\to-}$ is also used as fitting parameter and is found to lie in the range of 0.5 to 0.65 for pentacene. This is much larger than the values found for $f_{+\to-}$, since the tunneling barrier is in this case lowest for the highest-lying states (see Figure 2.3).

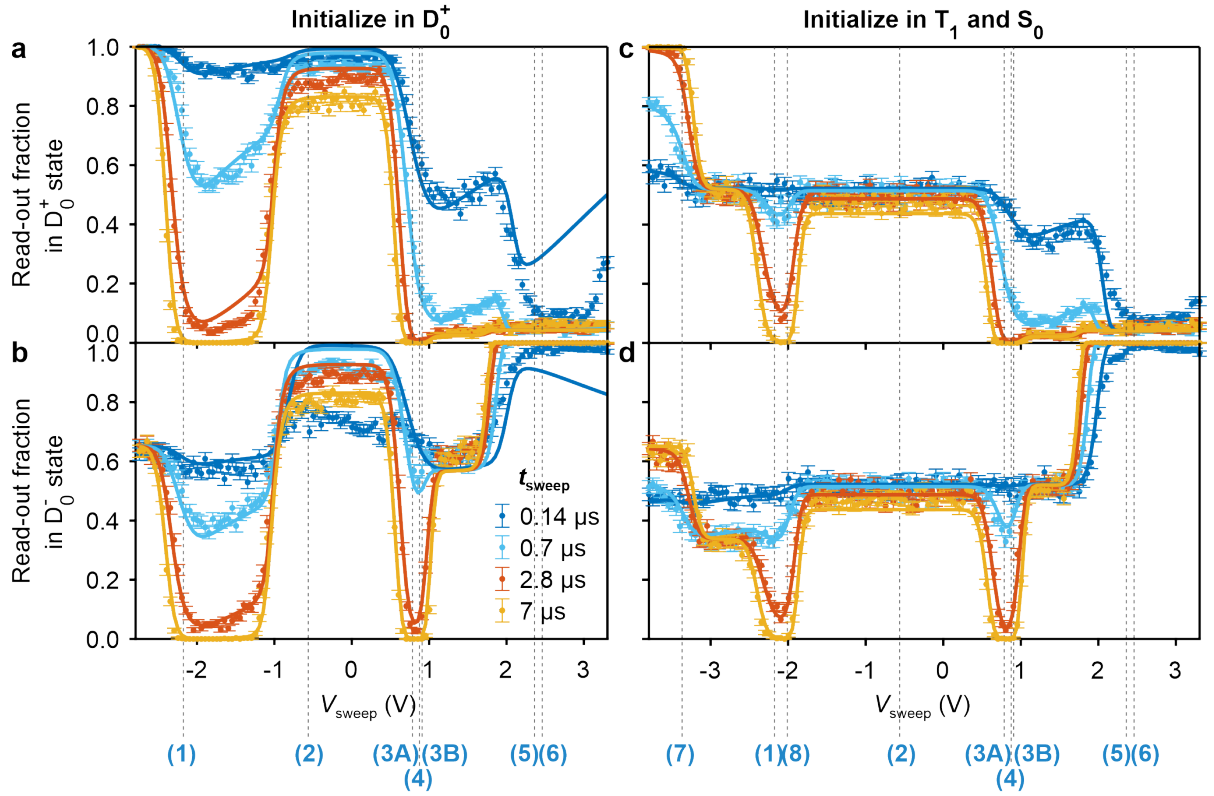

Figure 3.16.: Intermediate result of fitting of the excited-state spectroscopy data of pentacene. The data displayed is the same as in Figures 3.8 and 3.12 for **a**, **b** and **c**, **d**, respectively. The data was fitted using the transitions that were assigned as explained in Section 3.4; the solid lines represent the fits to the data. The fitted voltages of these transitions are indicated by the dotted lines and numbered analogously to Figures 3.8 and 3.12. Three substantial discrepancies are observed between the fit and the data, as elaborated in Section 3.6. These discrepancies point toward other transitions that are taking place during the sweep time, which need to be taken into account to improve the fit.

3.6. Fitting of the pentacene data

The pentacene datasets (Figures 3.8 and 3.12) were fitted simultaneously, including different t_{sweep}, using the equations described in Section 3.5, taking into account the assigned transitions. Importantly, an initial guess should be made for the voltages at which the transitions occur. We estimated these initial parameters based on the experimental data, given the assignment of the transitions, as discussed in the Section 3.4.

Figure 3.16 shows the resulting fits (solid lines) of the pentacene data using one common set of fitting parameters for all data. Although the fit resembles the data overall very well, there are a few pronounced deviations between the fitted curves and the measured data points. These deviations are neither surprising nor alarming, since not all possible low-energy transitions have been accounted for. However, since such deviations can also influence the voltage at which the transitions of interest are fitted, we added an additional transition to improve the fit. To this end, we first identify the largest deviations, namely,

I. around (6) for the initialization in D_0^+ for short t_{sweep} (dark blue graph in Figure 3.16a and b),

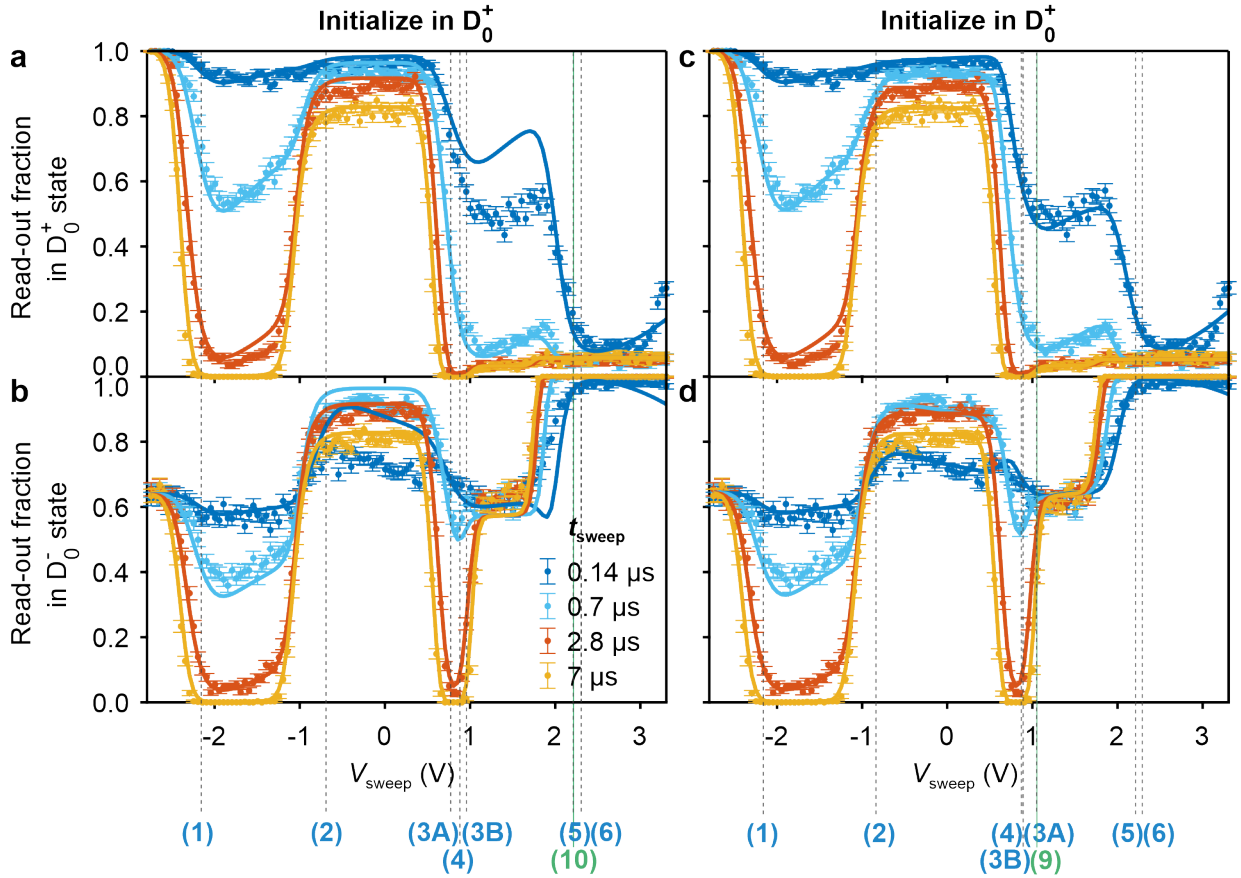

Figure 3.17.: Intermediate and final result of fitting the excited-state spectroscopy data of pentacene. The experimental data displayed is the same as in Figures 3.8 and 3.16a and b. This data (including the spectra with initialization in T_1 and S_0) was fitted using the transitions that were assigned as explained in Section 3.4, and used in Figure 3.16, but including one additional transition (green): $D_0^+ \rightarrow S_2$ (10) in case of **a**, **b** and $D_0^+ \rightarrow T_2$ (9) in case of **c**, **d**. The fitted voltages of the transitions are indicated by the dotted lines and numbered analogously to Figure 3.8. Clear discrepancies between the fit and data exist for **a**, **b**, which are not present for **c**, **d**. Therefore, a $D_0^+ \rightarrow T_2$ transition (9) was included in the final fits.

II. between (2) and (3A) most pronounced for short t_{sweep} (especially the dark blue graph in Figure 3.16b) for initialization in D_0^+ and read-out at the S_0-D_0^- hysteresis, and

III. the plateau after (3B) for initialization in D_0^+ and read-out at the S_0-D_0^- hysteresis, similarly pronounced for all t_{sweep} (Figure 3.16b).

In comparison, the fit resembles the data for initialization in S_0 and T_1 (Figure 3.16c and d) very well. This indicates that the deviations of the fit for initialization in D_0^+ can likely be solved by adding one or more transitions that start in D_0^+. As a first trial, we added the $D_0^+ \rightarrow S_2$ transition, which is expected to improve at least deviation I. As can be seen in the resulting fit in Figure 3.17a and b, adding this transition considerably improved the fit with respect to deviations I and III, but did not remove deviation II. Moreover, it introduced some new deviations. As a second trial, we added a $D_0^+ \rightarrow T_2$ transition instead of the aforementioned $D_0^+ \rightarrow S_2$ transition, which results in the fit shown in Figure 3.17c and d. Since this fit resembles the data very well, we concluded that the assignment as a $D_0^+ \rightarrow T_2$ transition is correct. Interestingly, at a different lateral tip position (see Figure 3.10b), we

	Pentacene 1	**Pentacene 2**	**Pentacene 3**	**Pentacene 4**
Transition voltage (V)				
$D_0^+ \rightarrow S_0$	-2.16 ± 0.05	-2.02 ± 0.05	-2.05 ± 0.05	-1.70 ± 0.05
$D_0^+ \rightarrow T_1$	-0.84 ± 0.05	-0.75 ± 0.05	-0.70 ± 0.05	-0.56 ± 0.05
$D_0^+ \rightarrow S_1$	1.05 ± 0.06	1.17 ± 0.05	1.30 ± 0.11	1.29 ± 0.07
$D_0^+ \rightarrow T_2$	1.05 ± 0.07	1.13 ± 0.06	1.35 ± 0.10	1.16 ± 0.07
$T_1 \rightarrow D_0^-$	0.89 ± 0.05	1.05 ± 0.05	0.92 ± 0.05	1.08 ± 0.05
$T_1 \rightarrow D_1^-$	2.29 ± 0.05	2.48 ± 0.05	2.37 ± 0.05	2.36 ± 0.10
$D_0^- \rightarrow S_0$	0.87 ± 0.05	-	0.90 ± 0.20	-
$S_0 \rightarrow D_0^-$	2.21 ± 0.05	-	2.25 ± 0.05	-
$T_1 \rightarrow D_0^+$	-2.01 ± 0.05	-1.97 ± 0.13	-1.90 ± 0.05	-1.60 ± 0.09
$S_0 \rightarrow D_0^+$	-3.37 ± 0.05	-3.32 ± 0.05	-3.34 ± 0.07	-2.92 ± 0.05
Other				
T_1 decay rate (μs^{-1})	0.017 ± 0.001	0.015 ± 0.001	0.027 ± 0.002	0.020 ± 0.003
$f_{-\rightarrow+}$	0.052 ± 0.003	0.030 ± 0.006	0.049 ± 0.006	0.055 ± 0.006
$f_{+\rightarrow-}$	0.644 ± 0.004	-	0.526 ± 0.008	-
Initial T_1 population	0.518 ± 0.002	0.514 ± 0.005	0.514 ± 0.004	0.510 ± 0.006
Lever arm α	0.70 ± 0.02	0.71 ± 0.02	0.67 ± 0.03	0.76 ± 0.03
V_{CPD} (V)	-0.47 ± 0.01	-0.42 ± 0.02	-0.46 ± 0.02	-0.57 ± 0.05

Table 3.1.: Fitting results for four pentacene molecules. The error bars are given by the uncertainty on the fit, with a minimal error bar on the transition voltages set to 0.05 V. The voltages of local contact potential difference (V_{CPD}) were determined as the maximum of a KPFS parabola measured above the molecule (see Section 2.3.3.3). The lever arm was determined as discussed in Section 3.7.

also found a signature of such a $D_0^+ \rightarrow T_2$ transition - around the corresponding threshold voltage.

We reiterate that this additional $D_0^+ \rightarrow T_2$ transition was only included to improve the fitting of the main transitions. Further, we fitted the data using a minimal number of transitions, but more transitions could be present that coincide with other transitions and are therefore not clearly visible. For instance, additionally including a $D_0^+ \rightarrow T_3$ transition as well as a $D_0^+ \rightarrow S_2$ transition in the fit for pentacene around the voltage where the $D_0^+ \rightarrow T_3$ transition is observed at a different spatial location (see Figure 3.10) fits the data similarly well.

The final fits are also indicated by the solid lines in the plots of Figures 3.8 and 3.12. In general, the fit resembles the data very well which supports our interpretation of the processes mentioned in Section 3.4. Table 3.1 lists the resulting fitting values for this fit (listed as pentacene 1). The fitted voltages at which the transitions occur are displayed for every transition, with error bars given by the uncertainty provided by the fitting algorithm. In addition, we manually estimated the error bar on the fit of a well-resolved transition (without any close-lying transitions) by varying the parameters, and find an uncertainty of ± 0.05 V, which was set as a lower limit of the uncertainties. Table 3.1 also lists the other fitting parameters as well as the local contact potential difference for the used tip. From the determined transition voltages and reorganization energies (see Table 3.2) one can also infer the values of electron affinity and ionization potential.

To account for potential influences of the environment (e.g. presence of nearby step edges), as well as the possible influence of the metallic tip and its workfunction, the measurements were repeated for three other pentacene molecules, all measured with another metallic tip apex. The data measured for these pentacene molecules were similarly fitted including the $D_0^+ \rightarrow T_2$ transition. The resulting values are also listed in Table 3.1. Note that for two of these pentacene molecules, spectra were only measured for read-out at the D_0^+-S_0 degeneracy, not for read-out at the S_0-D_0^- degeneracy. In these cases, the transitions $D_0^- \rightarrow S_0$ and $S_0 \rightarrow D_0^-$ only had a small influence on the spectra and could not be reliably fitted. For the fitting to converge, the fitting parameters of these transitions had to be fixed, and they were fixed to the parameters obtained for pentacene molecule 1, correcting for the overall shifts of all transition voltages for these two molecules by comparing the transition voltages of the $D_0^+ \rightarrow S_0$ transition.

The uncertainty on the fit of some of the transitions is much larger than on the others, which we attribute to the presence of multiple transitions around the same voltage. Another complication is that in some cases the fit could compensate a too large width of a transition by using a larger rate. Since the widths of all the transitions that do not show this behavior are similar and around 0.20 V for pentacene (FWHM 0.33 V), we set a slightly larger upper limit for all widths w_i of 0.25 V. To understand if such an upper limit might affect the corresponding threshold voltages, we varied the upper limit by 0.05 V. While this did affect some fitted threshold voltages, these shifts were within the uncertainty margins and hence insignificant.

The provided values of pulse durations correspond to the ones set at the driving electronics. However, the wiring between the AWG and the sample acts as a low-pass filter, effectively shortening the pulse durations by a fixed amount. Correspondingly, we found that the fit is improved if we subtract 40 ns from all pulse durations for the fit; 40 ns seems in reasonable agreement with the expected settling time of the circuit.

3.7. Determination of the lever arm

From the fitted transition voltages (see Table 3.1), a many-body energy diagram of pentacene can be derived. To this end, the transition voltages have to be rescaled to energies taking into account the partial voltage drop across NaCl, i.e., the lever arm[58,93,94] α (see Section 2.3.3.4). This voltage drop could be estimated from modeling the tip-sample geometry as shown in literature[58], but such simulations are subject to large uncertainty margins due to the uncertainty on the tip-NaCl distance, the tip radius and the local thickness of the NaCl film[58].

Instead, we calibrate our energies using the S_1-S_0 energy difference determined as 2.26 eV by STML for pentacene on NaCl(4 ML)/Ag(100) (ref. [145]). We believe that this value of the S_1-S_0 energy difference is the most reliable to be taken as a reference value, due to the similarity in the environment of the molecule (i.e. NaCl as a surface, presence of a Ag tip). Since the lever arm α also affects the effective barrier heights (see Section 3.5), it was set iteratively for the pentacene datasets such that the S_1-S_0 energy difference was derived as 2.26 eV. We, thereby, estimate a voltage drop of 30% in the NaCl film for the data shown in Figures 3.8 and 3.12, corresponding to a lever arm α of 0.70.

	Pentacene 1	Pentacene 2	Pentacene 3	Pentacene 4	Average
Energy difference (eV)					
T_1-S_0	0.93 ± 0.06	0.90 ± 0.06	0.91 ± 0.06	0.86 ± 0.06	0.90 ± 0.06
S_1-S_0	2.26 ± 0.09	2.26 ± 0.09	2.26 ± 0.12	2.26 ± 0.10	2.26 ± 0.05
D_1^--D_0^-	0.99 ± 0.06	1.01 ± 0.06	0.98 ± 0.06	0.97 ± 0.09	0.99 ± 0.04
T_2-S_0	2.26 ± 0.09	2.23 ± 0.09	2.29 ± 0.12	2.17 ± 0.10	2.24 ± 0.12
Reorganization energy (eV)					
D_0^+-S_0	0.85 ± 0.06	0.92 ± 0.06	0.87 ± 0.07	0.92 ± 0.06	0.89 ± 0.07
D_0^+-T_1	0.83 ± 0.06	0.86 ± 0.10	0.81 ± 0.06	0.78 ± 0.08	0.82 ± 0.07
S_0-D_0^-	0.95 ± 0.06	-	0.91 ± 0.15	-	0.93 ± 0.06

Table 3.2.: Derived energies for pentacene. Energy differences and reorganization energies determined for different transitions for four pentacene molecules. The uncertainties were determined as described in Section 3.8.

The uncertainty of this estimated voltage drop arises from the uncertainty on the fitting of the S_1-S_0 energy difference, as well as the uncertainty on the comparison of the S_1-S_0 energy differences in slightly different environments. For instance, the different thicknesses of the NaCl layer, and thus a different proximity of the metal underneath the NaCl can cause shifts on the order of at least tens of meV (ref. [151]). Furthermore, the difference in electric field in the tip-sample junction for the STML measurements compared to our spectroscopic measurements of the $D_0^+ \rightarrow S_0$ and $D_0^+ \rightarrow S_1$ transitions will cause a slight deviation between our determined value and the 2.26 eV obtained with STML. A change in electric field during the STML measurements on pentacene caused a Stark shift of the S_1-S_0 transition of less than 10 meV/V (ref. [145]). We estimated the uncertainty due to differences in the environment including the applied electric field to be 50 meV. Taking the sources of uncertainty on the lever arm together, we estimate that the resulting uncertainty of the lever arm is ± 0.02. Note that the uncertainty obtained this way is only one third of the uncertainty on the lever arm that was obtained from modeling the tip-sample geometry[58], indicating that our approach gives a more reliable estimate of the lever arm.

Since the lever arm depends on the local thickness of the salt, it was determined individually for every pentacene molecule that was measured. Similar level arms were obtained ranging from 0.67 to 0.76, as listed in Table 3.1.

3.8. Energy differences, reorganization energies, rates and line widths

The many-body energy diagram can be derived from the fitted transition voltages (see Table 3.1). To derive energy differences, we take the difference between two processes starting at the same state and ending in the two states of interest (e.g. $D_0^+ \rightarrow S_0$ and $D_0^+ \rightarrow T_1$ for the T_1-S_0 energy difference), rescaling the result by the lever arm (Section 3.7). The results for the four pentacene molecules are listed in Table 3.2. The uncertainty margins for the individual molecules were derived from the uncertainties of the transition voltages and

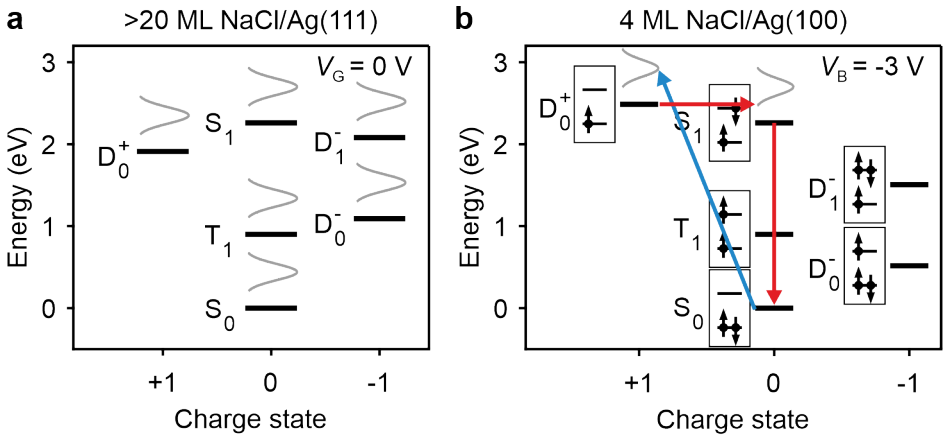

Figure 3.18.: Many-body energy diagrams of pentacene. **a**, The energy diagram was obtained from fitting of excited-state spectroscopy measurements for four individual pentacene molecules, and is drawn for $V_G = 0$ V. As in Figure 3.5b, the rotated Gaussians (gray) indicate the broadening of the transitions due to electron-phonon coupling, although they are not a property of the state, but of the transition being made. Here all relaxation energies and widths are set to their averaged values derived from fitting the experimental data. The relaxation energies are set to half of the reorganization energies. **b**, Many-body energy diagram of pentacene extrapolated to thin films (see Section 3.9.1 for details) showing the pathway that leads to the STML signal with 2.26 eV photon energy[145]. This many-body energy diagram is drawn with respect to the chemical potential of the substrate for an applied bias voltage V_B of -3 V. That way, tunneling events to or from the substrate result in transitions that lower the energy. By tip-molecule tunneling, charge transitions that increase the energy by maximally eV_B become possible, such as the $S_0 \rightarrow D_0^+$ transition (involving molecule-tip tunneling, blue arrow) shown here. On thin films the molecule will revert back to its ground state (here S_0) by molecule-substrate tunneling. One possible pathway is via S_1 (red). Here, the bias voltage also shifts (gates) the charged states with $-q(1-\alpha)V_B$, as explained in Section 2.3.3.4, which is taken into consideration in the level alignment displayed.

the uncertainty on the lever arm (see Table 3.1). The uncertainties on the averaged values were determined from the standard deviation on the four individual values, taking the uncertainty on the comparison between the fitted S_1-S_0 energy difference and the literature value[145] (see Section 3.7) into account. We find a T_1-S_0 energy difference of (0.90 ± 0.06) eV and a D_1^--D_0^- energy difference of (0.99 ± 0.04) eV (see for the many-body diagram Figure 3.18). The obtained T_1-S_0 energy difference of pentacene matches within uncertainty margins the value determined for pentacene in a tetracene crystal (0.86 ± 0.03) eV (ref. [152]), despite the difference of environments.

Deriving energy differences as described above is subject to the implicit assumption that the relaxation energies[58] of the two involved transitions are similar. Because these transitions occur between the same charge states (e.g. from positive to neutral), this assumption seems reasonable. Moreover, the validity of this assumption can be scrutinized experimentally by extracting the reorganization energies and the line widths from our spectroscopic data.

The reorganization energies are given by the difference of energies, at which two opposing charge transitions occur, for example (1) and (7) for $D_0^+ \leftrightarrow S_0$. From the fitting of the four pentacene datasets, the reorganization energies of $D_0^+ \leftrightarrow S_0$, $D_0^+ \leftrightarrow T_1$ and

$S_0 \leftrightarrow D_0^-$ were derived as (0.89 ± 0.07) eV, (0.82 ± 0.07) eV and (0.93 ± 0.06) eV, respectively (see Table 3.2). The uncertainty margins were derived analogously as for the energy differences (see above). The $S_0 \leftrightarrow D_0^-$ value matches the value of (0.9 ± 0.1) eV as obtained from density-functional theory calculations[59]. The similar reorganization energies for the three different transitions found here, strongly support the assumption that the relaxation energies are similar for the transitions under consideration.

Further support for the validity of this assumption can be derived from the similar widths of the different transitions. These widths arise from the same strong electron-phonon coupling that is also the cause of the large relaxation energies[70] (see Section 2.3.3.2). We find similar widths for the transitions that are involved in our derivation of the energy differences, in the range of 0.15 to 0.18 eV (FWHM 0.24 to 0.30 eV), lending further support that the relaxation energies are similar.

The assumption of similar relaxation energies is also justified by the similar confinement of the orbitals involved in the transitions considered here for pentacene (for most transitions, the HOMO and LUMO). However, if - for other molecules - the orbital confinement greatly differs for different states, different relaxation energies should be considered. In such cases the relaxation energies for injecting and removing an electron into and out of one given orbital is still expected to be approximately the same. The relaxation energies can, therefore, be estimated from the reorganization energy, being the sum of these two relaxation energies. As mentioned above, the relaxation energies and the widths of the involved transitions scale in a well-defined manner[70] and provide another way to separately extract relaxation energies for such cases.

The reorganization energies of the short-lived excited states cannot be accessed since transitions from such a state into another state are not observed. The corresponding relaxation energies for pentacene displayed in Figure 3.18 are shown as half of the mean values of the reorganization energies listed above.

The relative rates (not listed) can be interpreted semi-quantitatively. While the fitted threshold voltages vary only slightly when adding more possible transitions to the fitting procedure, the fitted rates show a much larger dependence. Similarly, the relative rates depend strongly on the tip position, reflecting different orbital density distributions. The latter can aid the assignment of features to certain transitions.

The relative rate constants are also reflected in the $f_{+\rightarrow-}$ and $f_{-\rightarrow+}$ parameters, as well as the initial T_1 population listed in Table 3.1. For instance, the initial T_1 population (after the used set pulse sequence to initialize in T_1 and S_0) is determined by the ratio of $D_0^+ \rightarrow T_1$ and $D_0^+ \rightarrow S_0$ as well as the triplet decay rate. The fitted initial T_1 populations are almost equal within their error margins for the four pentacene molecules. A slightly larger spread is found for $f_{+\rightarrow-}$ and $f_{-\rightarrow+}$, which we mainly attribute to the larger number of transitions involved.

3.9. Using AFM excited-state spectroscopy to interpret STM experiments

While our excited-state spectroscopy requires measuring on insulating NaCl films of sufficient thickness to prevent tunneling to the substrate, our results can be extrapolated to

experiments performed on thin (few monolayer) films of NaCl, guiding the interpretation of these experiments. Such an extrapolation can be made guided by the general considerations that are listed in this section.

The voltage applied to the substrate drops also for thin films partially between molecule and substrate, which has to be taken into account. Furthermore, not only tunneling between the tip and the molecule is possible, but also between the molecule and the metal substrate beneath the thin film. This substrate tunneling will always bring the molecule back to the state(s) lowest in energy. It is therefore more convenient to choose the Fermi level of the sample as the reference energy in the many-body diagram for thin films. Section 2.3.3.4 discusses the differences between the many-body energy diagrams drawn for thick and thin films in more detail, including the effect of the lever arm.

When extrapolating from thick to thin films, in addition, the increased screening due to polarization of the metal substrate has to be considered. This may slightly affect excitation energies (e.g. T_1-S_0 and D_1^--D_0^- energy differences). For example, a shift of a few tens of meV was observed for the S_1-S_0 energy difference of zinc phthalocyanine from 2 to 5 ML of NaCl, see ref. [151]. Similarly, the possible difference in electric field present in the tip-sample junction by e.g. differences in the applied voltage can also cause slight shifts in the excitation energies via the Stark effect. For example, a shift of less than 10 meV/V was observed for the S_1-S_0 STML of pentacene on 4 ML NaCl/Ag(100) (ref. [145]) and 30 meV/V for the D_1^--D_0^- STML of PTCDA attached to a Ag tip[127]. Since these shifts are smaller than the uncertainty margins on our derived energy differences, these effects were neglected.

There are three effects that change the relative energy of the different charge states. First, the screening due to polarization of the metal substrate will reduce the energies of the positively and negatively charged states with respect to the neutral ones. In other words, upon reducing the thickness of a thin NaCl film, a reduction of the energy difference between $S_0 \rightarrow D_0^+$ and $S_0 \rightarrow D_0^-$ was observed[3,153,154]. Although this reduction was also partially attributed to the different lever arms, the effect due to polarization was found to be on the order of 0.2 eV from 2 to 4 ML of NaCl (ref. [153]).

Second, changes in the work function would also affect the level alignment. Although the work function changes strongly upon the addition of NaCl to a metal surface (around 1 eV (ref. [149, 150])) because of the formation of an interfacial dipole under the thin film[153], within uncertainty margins the same work function was found comparing 2 and 3 ML of NaCl on Ag(111) (ref. [153]) (and also comparing 1, 2 and 3 ML on Ag(100) (ref. [150])). We, therefore, expect that the work function does not change much from 3 to more than 20 ML of NaCl on Ag(111).

Third, in case of comparing two single molecule measurements, further variations between different individual molecules caused by other variations in their environment should be taken into account. For instance, Table 3.1 shows that for four different pentacene molecules measured with four different microtips, the voltage at which the D_0^+-S_0 charge degeneracy was observed varied by up to 0.45 V. Note that a part of these variations can also be attributed to the different V_{CPD} of the different tips. The tip will also contribute to screening effects as mentioned above, which will then depend on the tip shape.

3.9.1. Demonstrating the extrapolation to thin films for pentacene

As a demonstration of the extrapolation of our results from thick to thin insulating films, the many-body energy diagram for pentacene on 4 ML NaCl/Ag(100) is determined to comprehend how the molecule cycles through different states to yield the observed STML signal at 2.26 eV (ref. [145]).

First, the lever arm was estimated from the STS measured for the same pentacene molecule as for which the STML signal was observed[145]. Around −2.9 V a signal was observed that was assigned to the $S_0 \rightarrow D_0^+$ transition, while around 1.45 V a signal was observed that was assigned to the $S_0 \rightarrow D_0^-$ transition. Comparing this difference in voltage to the energetic difference that we determined with our method yields a lever arm α of 0.89. Note that the observed reduction of this difference for pentacene on 4 ML NaCl versus >20 ML NaCl could also be partly due to screening from the polarization of the metal substrate. Since the effect due to screening on 4 ML NaCl is expected to be small, and since we cannot disentangle these two effects for this molecule from the existing data, it was neglected here.

Second, the effects that can shift the alignment of the ground (and excited) states of different charge (see previous section) were taken into account by comparing our energy of the observed $S_0 \rightarrow D_0^+$ and $S_0 \rightarrow D_0^-$ transitions versus the energy derived from the above mentioned STS using the estimated lever arm α of 0.89. This comparison yields a required shift of $q{\cdot}0.25$ eV, with q the net charge of D_0^+, D_0^- and D_1^-, for extrapolation from >20 ML NaCl/Ag(111) to 4 ML NaCl/Ag(100). Note that one of the three effects that causes this shift is the difference in work function. Indeed, a difference in work function is expected for the two different surfaces, since different Ag faces are compared. In case of the pristine surfaces, a work function of 4.74 eV for Ag(111) (ref. [148]) and 4.64 eV for Ag(100) (ref. [155]) were reported. This difference in work function is in the right direction, and can explain part of the observed shift by 0.25 eV.

Figure 3.18b shows the resulting many-body energy diagram on 4 ML NaCl/Ag(100) taking the derived lever arm and shift of the energy levels into account. This diagram is drawn at a bias voltage of −3 V, at which the STML signal was observed. At this voltage, a tip-sample tunneling event allows accessing states that are up to 3 eV higher in energy, in this case the D_0^+ state (blue arrow in Figure 3.18b). From D_0^+, a substrate tunneling event can bring the molecule back into one of the neutral states, among which the S_1 state. Energetically, this process is just opened at this bias voltage. From there, the short-lived S_1 state can decay under the emission of a photon back into S_0. This extrapolated many-body energy diagram thus confirms the assignment of S_1-S_0 to the observed STML signal at 2.26 eV.

3.10. Excited-state spectroscopy on PTCDA

To demonstrate the wider applicability of our developed spectroscopic method, we chose a system that is controversial in the literature. Specifically, the same STML signal measured for PTCDA on thin NaCl films has been interpreted differently, on the one side, as phosphorescence of the neutral molecule[128] and, on the other side, as fluorescence of the

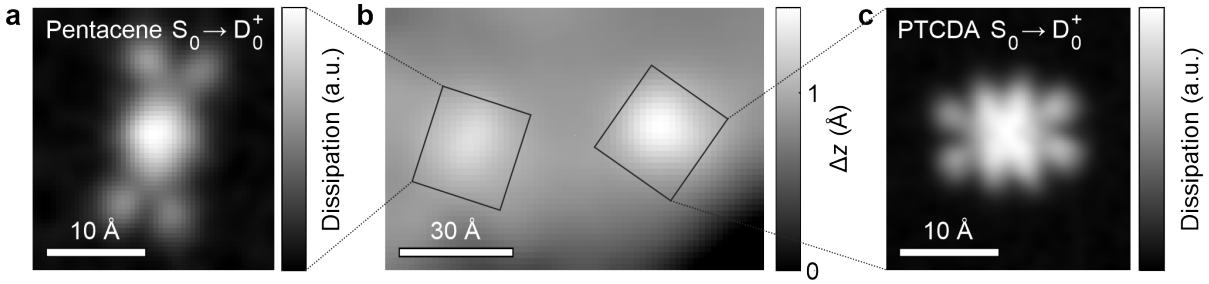

Figure 3.19.: AFM images. **b**, AFM topography image of the NaCl-covered surface with the pentacene and PTCDA molecules for which excited-state spectroscopy data was measured (setpoint $\Delta f = -1.65\,\mathrm{Hz}$ at $V = 0\,\mathrm{V}$, $A = 3\,\mathrm{Å}$). In the lower-right corner of the image a descending NaCl step edge is seen. The corresponding excited-state spectroscopy data is presented for the PTCDA molecule in Figures 3.20 and 3.22. The resulting fitting parameters for pentacene and PTCDA are listed in Table 3.1 (as pentacene 2) and Table 3.3, respectively. **a**, **c**, AC-STM images[89] of the $S_0 \rightarrow D_0^+$ transition (HOMO) of the two molecules in **b** ($A = 1\,\mathrm{Å}$, pentacene (**a**): $\Delta z = -3.0\,\mathrm{Å}$, $V_\mathrm{G} = -2.90\,\mathrm{V}$, $V_\mathrm{a.c.} = 1.2\,V_\mathrm{pp}$, and PTCDA (**c**): $\Delta z = -2.3\,\mathrm{Å}$, $V_\mathrm{G} = -4.55\,\mathrm{V}$, $V_\mathrm{a.c.} = 1.2\,V_\mathrm{pp}$). Δz is given with respect to the setpoint $\Delta f = -1.75\,\mathrm{Hz}$ at $V = 0\,\mathrm{V}$, $A = 3\,\mathrm{Å}$.

anion[129], corresponding to the $T_1 \rightarrow S_0$ (ref. [128]) and $D_1^- \rightarrow D_0^-$ (ref. [129])) transitions, respectively.

To shed some light on these experiments, we measured excited-state spectra for PTCDA, which we co-deposited on the same sample as used for pentacene. Images of the PTCDA molecule on which we performed our measurements are shown in Figure 3.19. Figure 3.20 shows the resulting excited-state spectra for read-out of the signal at the D_0^+-S_0 degeneracy. Although the data with a set pulse sequence that brings the molecule to the S_0 or T_1 state (Figure 3.20c) has a very similar qualitative appearance as the corresponding pentacene data (Figure 3.12a), the data for initializing the molecule in the D_0^+ state (Figure 3.20a) shows substantial differences with respect to the corresponding pentacene data (Figure 3.8a).

The first difference is that there are two downward steps present at thresholds (3B) and (3A) in Figure 3.20a, instead of a single step. From comparing to the data shown in Figure 3.20c, for which transitions starting at D_0^+ are excluded, the step at (3B) can be assigned as the quenching of T_1 via D_0^-, while the step at (3A) is caused by a transition starting at D_0^+ and is assigned to $D_0^+ \rightarrow S_1$. In other words, the same transitions happen for PTCDA as for pentacene, but in contrast to pentacene, (3A) and (3B) are well separated in voltage for PTCDA.

The second striking difference is that another step is visible at (9). Interestingly, this step is upwards, indicating that the population in D_0^+ is increased. No such step is appreciable in the data for initialization in the neutral states (Figure 3.20), indicating that a transition starting at D_0^+ is involved. The upward step suggests that a long-lived state is accessed. We hypothesize that an excited triplet state T_2 is populated, in which one electron is present in the HOMO and the other in a state higher in energy than the LUMO, that is a higher-lying unoccupied orbital (T_2 may also entail further contributions of other configurations). This state is expected to decay to the T_1 state with a fast decay rate because this transition is spin conserving[140] (see Figure 3.21a).

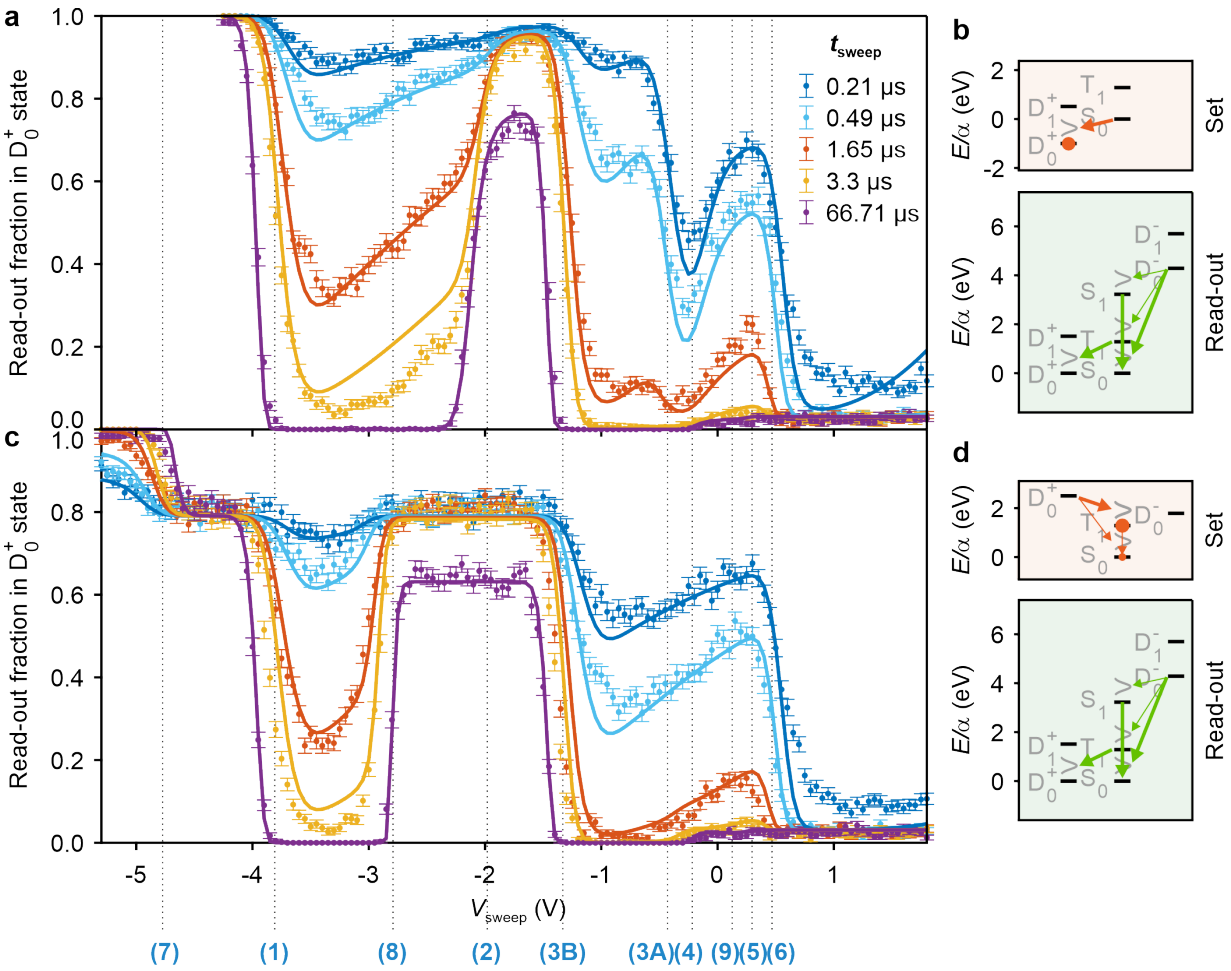

Figure 3.20.: Excited-state spectroscopy of PTCDA. a, **c**, Plot of the measured read-out fraction in the D_0^+ state versus the applied gate voltage during the sweep pulse V_{sweep}. Measurements were performed with a voltage pulse sequence similar to Figure 3.5b. A set pulse (sequence) was used to initialize the molecule in case of **a** in the cationic state D_0^+ ($V_{set} = -5.30\,V$) and in case of **c** in the neutral charge state with 20% in S_0 and 80% in T_1 (the second pulse of the set phase is at $-1.8\,V$ with $t_{set} = 33.4\,\mu s$, see Section 3.4.2). The read-out was at the D_0^+-S_0 degeneracy ($V_{read\text{-}out} = -4.30\,V$). Five different t_{sweep} were used, as indicated. Solid lines represent fits to the data (see Section 3.11). The transition voltages are indicated by dotted lines with numbers indicating the assigned level alignment (see Figures 3.8, 3.12 and 3.21 for the many-body energy diagrams). **b**, **d**, Many-body energy diagrams of the transitions taking place during the set pulse and at the beginning of the read-out phase for the spectra shown in **a** and **c**, respectively. These diagrams are not quantitative and for illustration purposes only.

With our spectroscopic method we can test this hypothesis experimentally. To this end, we performed two experiments, similar to those in Figures 3.12 and 3.20b, but once using a set pulse sequence that prepares the molecule in the state under investigation (that we propose to be T_2), and once using a set pulse with a voltage that is just too low to allow a transition into this state. The results are shown in Figure 3.21. Interestingly, upon populating this state, the read-out fraction in the charge state has increased, especially in the voltage ranges where the read-out population directly reflects the T_1 population (below (1) and between (8) and (3B)). The related state seems, thus, to behave identical to the T_1

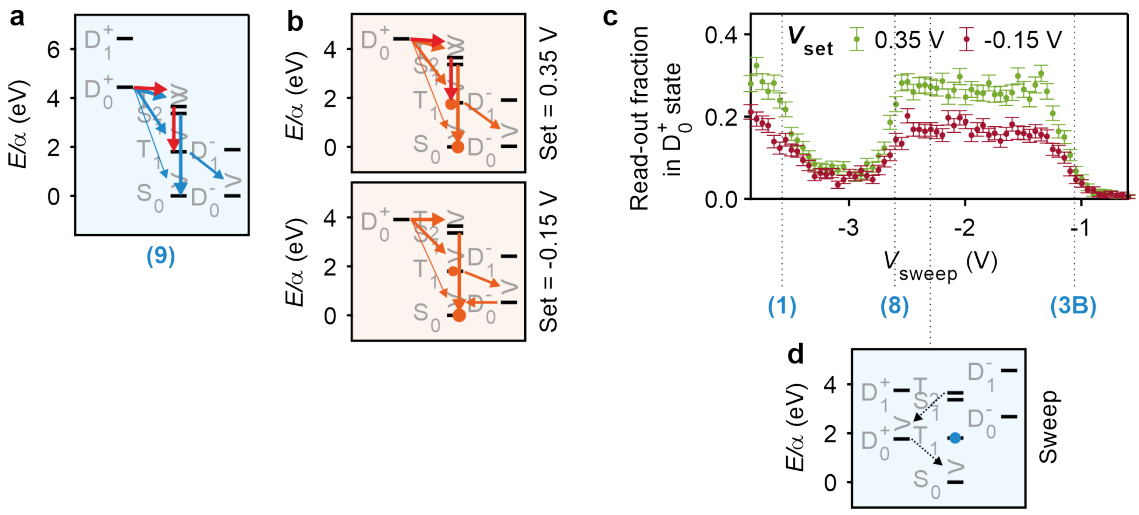

Figure 3.21.: Excited-state spectroscopy to assess the origin of feature (9). **a**, Many-body energy diagram of the assumed transition pathway opening at (9). **b**, To experimentally test this hypothesized transition to T_2, excited-state spectroscopy was performed with a modified set pulse sequence. The first set pulse initializes the molecule in D_0^+. Two different voltages of the second set pulse were used that allow or not allow the proposed $D_0^+ \rightarrow T_2$ transition, as is illustrated by the many-body energy diagrams corresponding to these two voltages. The arrows and dots are analogous to Figure 3.8e. **c**, Resulting plot of the measured read-out fraction in the D_0^+ state versus V_{sweep} for the two different set voltages used. This data was measured using a duration of the second set pulse t_{set} of 0.74 µs and a sweep pulse duration t_{sweep} of 2.96 µs. **d**, Many-body energy diagram at the voltage indicated by the dotted line in **c**, showing that if the T_2 population decayed to T_1, it will stay in T_1 at this voltage. In case a part of the population would still be populating T_2 at the end of the set pulse sequence, it would decay via D_0^+ to S_0 at this voltage (dotted arrows), causing a reduction in read-out fraction in D_0^+, which is not observed in **c**.

state, except that it is populated at higher voltages. If instead a long-lived neutral excited state would be populated, which does not decay to T_1 on the timescale of the sweep pulse (a few microseconds), the resulting signal in Figure 3.21c is expected to clearly deviate around the voltage for which the many-body diagram of Figure 3.21d is drawn. If the state decayed to T_1, this population would stay in T_1 at this voltage (neglecting the much longer decay time of T_1 to S_0), as shown in Figure 3.21d. If the populated state itself was long-lived, the population in this state would decay back to D_0^+ at this voltage, and from there to S_0 (see dotted arrows in Figure 3.21d). In other words, the green curve in Figure 3.21c would then be even lower than the red curve in a small range above (8), which is not observed in Figure 3.21c. (This range is given by the reorganization energy; close to (3B) the green curve is expected to be higher than the red curve, since the pathway $T_2 \rightarrow D_0^+ \rightarrow T_1$ is opened). We, therefore, assign feature (9) to the population of a higher excited triplet state that directly decays to the T_1 state (with a faster rate than the tunneling rates in our experiment).

The assignment of the other transitions is analogous as for pentacene (see Section 3.4); they can also be similarly assessed as for pentacene (see Section 3.4.3).

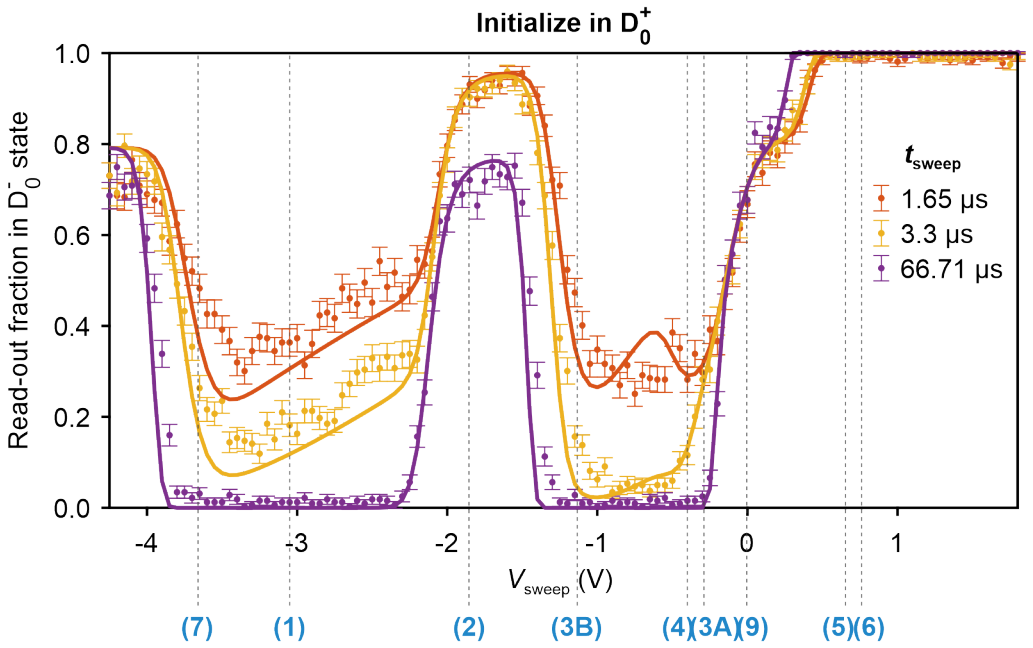

Figure 3.22.: Excited-state spectroscopy of PTCDA, read-out at the S_0-D_0^- degeneracy. Excited-state spectroscopy for the same individual PTCDA molecule as the one of the spectra shown in Figure 3.20. Measurements were performed with a voltage pulse sequence similar to Figure 3.5b, with a set pulse to initialize the molecule in D_0^+ ($V_{set} = -5.30\,V$) and read-out at the S_0-D_0^- degeneracy ($V_{read\text{-}out} = 0.058\,V$). The voltage-pulse sequence was repeated 4 times per second for 80 seconds. Every data point corresponds thus to 320 pump-probe cycles. The data was fitted using the transitions that were assigned as explained in Section 3.10, the solid lines represent the fits to the data. The fitted voltages of these transitions are indicated by the dotted lines and numbered analogously to Figures 3.8, 3.12 and 3.21.

3.11. Fitting of the PTCDA data

The data for PTCDA was fitted analogously to the data of pentacene (see Section 3.6). Next to the data shown in Figure 3.20, a dataset was included with initialization in D_0^+ and read-out at the S_0-D_0^- hysteresis, as shown in Figure 3.22. In case of PTCDA, the $D_0^+ \rightarrow T_2$ transition was included in the fitting from the beginning, since this transition was already assigned, as described in the previous section. The upper limit for the fitted widths was set to $w_i = 0.20\,V$ for PTCDA, since the average widths found for transitions that could be reliably fitted was 0.17 V (FWHM 0.28 V), see Section 3.6 for more details.

The resulting fits are shown in Figure 3.20a and c and Figure 3.22. In general, the fits resemble the data well. The deviation between the fit and the data shown in Figure 3.20 between voltage (1) and (2) for $t_{sweep} = 3.3\,\mu s$ (yellow curve) is attributed to the effect of the cantilever oscillation (see Section 3.3.1), which is not taken into account in the fit. The fitting values are listed in Table 3.3. The large uncertainty of the $S_0 \rightarrow D_0^-$ transition is likely a result of the limited amount of data that was included for read-out at the D_0^- state (e.g. lack of data for initialization in T_1 and S_0).

The calibration of the lever arm was done at the S_1-S_0 transition of a pentacene molecule that was co-adsorbed on the same NaCl terrace as the PTCDA molecule under study (see Figure 3.19; pentacene 2 in Table 3.1), since the lever arm depends on the thickness of the

	PTCDA
Transition voltage (V)	
$D_0^+ \rightarrow S_0$	-3.66 ± 0.05
$D_0^+ \rightarrow T_1$	-1.86 ± 0.05
$D_0^+ \rightarrow S_1$	-0.29 ± 0.05
$D_0^+ \rightarrow T_2$	0.00 ± 0.05
$T_1 \rightarrow D_0^-$	-1.13 ± 0.05
$T_1 \rightarrow D_1^-$	0.76 ± 0.05
$D_0^- \rightarrow S_0$	-0.40 ± 0.05
$S_0 \rightarrow D_0^-$	0.65 ± 0.87
$T_1 \rightarrow D_0^+$	-3.05 ± 0.05
$S_0 \rightarrow D_0^+$	-4.97 ± 0.09
Other	
T_1 decay rate (μs^{-1})	0.0034 ± 0.0003
$f_{-\rightarrow+}$	0.031 ± 0.006
$f_{+\rightarrow-}$	0.79 ± 0.02
Initial T_1 population	0.791 ± 0.006
Lever arm α	0.71 ± 0.03
V_{CPD} (V)	-0.42 ± 0.02

Table 3.3.: Fitting results for a PTCDA molecule. The error bars are given by the uncertainty on the fit, with a minimal error bar on the transition voltages set to 0.05 V. The voltage of local contact potential difference (V_{CPD}) was determined as the maximum of a KPFS parabola measured above the molecule (see Section 2.3.3.3). The lever arm was determined as discussed in Sections 3.7 and 3.11.

NaCl layer. In this case, the uncertainty on α (see Section 3.7) was increased to account for possible slight variations in the lever arm for the two measurements, which could result from a slightly different tip height, or minor differences in the adsorption height of the molecules[58]. This additional uncertainty was estimated to be ± 0.02.

From the fits, the S_1-S_0, T_1-S_0, D_1^--D_0^- and T_2-S_0 energy differences were determined as: (2.39 ± 0.11) eV, (1.28 ± 0.07) eV, (1.34 ± 0.08) eV and (2.59 ± 0.12) eV, respectively. The reorganization energies were extracted as (0.93 ± 0.08) eV for $D_0^+ \leftrightarrow S_0$, (0.85 ± 0.06) eV for $D_0^+ \leftrightarrow T_1$ and (0.75 ± 0.62) eV for $S_0 \leftrightarrow D_0^-$. Thus, the reorganization energies are also in case of PTCDA similar. The widths of the transitions involved in the derivation of the energy differences are similar as well, in the range of 0.13 to 0.14 eV (FWHM 0.22 to 0.23 eV). These results are summarized in the many-body diagram shown in Figure 3.23a, where the relaxation energies are shown as half of the mean values of the reorganization energies listed above, excluding the value obtained for the S_0-D_0^- transition because of its large uncertainty.

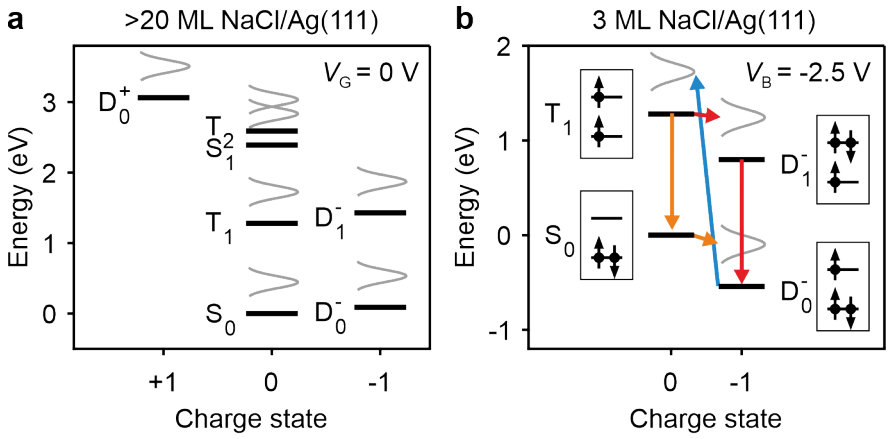

Figure 3.23.: Many-body energy diagrams of PTCDA. a, Many-body energy diagram of the electronic states of PTCDA in absence of gating, derived from fitting of excited-state spectroscopy measurements for one PTCDA molecule. As in Figure 3.5b, the rotated Gaussians (gray) indicate the broadening of the transitions due to electron-phonon coupling, although they are not a property of the state, but of the transition being made. Here all relaxation energies and widths are set to their averaged values derived from fitting the experimental data. The relaxation energies are set to half of the reorganization energies. The excited triplet state T_2 of PTCDA is assumed to have one electron in the HOMO and the other in a state higher in energy than the LUMO, that is, a higher-lying unoccupied orbital (T_2 may also entail further contributions of other configurations). **b**, Many-body energy diagram of PTCDA extrapolated to thin films (see Section 3.12.1 for details) showing two possible pathways (orange and red) that could lead to the STML signal with 1.33 eV photon energy for PTCDA[128,129] (both starting with the transition from the ground state D_0^- to T_1, blue arrow). This many-body energy diagram is drawn with respect to the chemical potential of the substrate and a bias voltage V_B of −2.5 V applied. That way, tunneling events to or from the substrate result in transitions that lower the energy. By tip-molecule tunneling charge transitions that increase the energy by maximally eV_B become possible, such as the $D_0^- \rightarrow T_1$ transition (involving molecule-tip tunneling, blue arrow) shown here (note that at this voltage also the $D_0^- \rightarrow S_0$ transition is possible (not shown)). On thin films the molecule will revert back to its ground state (here D_0^-) by molecule-substrate tunneling. Next to the direct transition from T_1 to D_0^- (not shown), pathways via S_0 (orange) and D_1^- (red) are possible. Here, the bias voltage also shifts (gates) the charged states with $-q(1-\alpha)V_B$, as explained in Section 2.3.3.4, which is taken into consideration in the level alignment displayed.

3.12. Origin of the STM-induced luminescence of PTCDA

3.12.1. Extrapolation to thin NaCl films

To compare our PTCDA results with the STML measurements on 3 ML NaCl/Ag(111), the many-body energy diagram we determined for >20 ML NaCl/Ag(111) was extrapolated to 3 ML NaCl/Ag(111) guided by the general considerations listed in Section 3.9.

First, the lever arm was estimated based on the STS and S_1-S_0 STML measurements from the work we compare with, ref. [128]. The lever arm was derived from the threshold voltage for LUMO imaging ($D_0^- \rightarrow S_0$) of −0.55 V and the threshold voltage for the observed S_1-S_0 STML (corresponding to the threshold for $D_0^- \rightarrow S_1$) of −3.3 V (ref. [128]). Comparing this S_1-S_0 voltage difference of 2.75 V to the observed S_1-S_0 luminescence of 2.45 eV (ref. [128]), a lever arm α of 0.89 results. In other words, 89% of the applied voltage drops

between molecule and tip, while $(1-\alpha) = 11\%$ of the voltage drops between molecule and substrate (see Figure 2.8a). Interestingly, this lever arm is the same as was found for 4 ML NaCl/Ag(100). This is in line with the expected similarity between lever arms for 3 and 4 ML NaCl.

Second, the three effects that change the relative energy alignment of the charged states with respect to the neutral states (screening due to polarization of the underlying metal substrate, changes in the work function and environmental variations, see Section 3.9) were taken into account for PTCDA by calibrating the S_0-D_0^- energy-degeneracy point using the measurements from the work we compare with, ref. [128]. From the conventional tunneling spectroscopy data of this reference[128], it follows that the maximum of the $D_0^- \rightarrow S_0$ transition is at V_B = -0.8 V. Taking the derived lever arm of 0.89 (see above) into account, this maximum lies at 0.71 eV above the D_0^- state (for $V_B = 0$ V). The relative energy alignment of the vibrational ground states of the S_0 and D_0^- states can then be derived by taking the relaxation energy into account. We estimate the relaxation energy as 0.45 eV, which corresponds to half of the average of the reorganization energies for PTCDA derived from our data. Thus, for this molecule on 3 ML NaCl/Ag(111), the D_0^- state is estimated to be 0.27 eV lower in energy than the S_0 state (for $V_B = 0$ V). Since the STML experiments were performed at $V_B = -2.5$ V, the lever arm further shifts the singly negative charge states down by 0.28 eV.

Taking this relative energy allignment and the shift due to the lever arm into account, the many-body energy diagram on 3 ML NaCl/Ag(111) was derived from the many-body diagram on >20 ML NaCl/Ag(111) (see Figure 3.23a), as shown in Figure 3.23b.

3.12.2. Interpretation of STM-induced luminescence

The PTCDA excited-state spectroscopy results obtained on thick insulating films (Section 3.11) and their extrapolation to thin insulating films (Section 3.12.1) allows us to shed some light on recent STML results[128,129].

The energy differences that we derived for PTCDA match closely those reported in the STML experiments. The S_1-S_0 STML signal was reported to have an energy of 2.45 eV, matching our obtained value of (2.39 ± 0.11) eV. The second STML signal at 1.33 eV was controversially assigned either as T_1-S_0 or D_1^--D_0^- (ref. [128, 129]). Our results indicate that both processes match in terms of energy the observed STML signal at 1.33 eV (the T_1-S_0 and D_1^--D_0^- energy differences were determined as (1.28 ± 0.07) eV and (1.34 ± 0.08) eV, respectively). The previous assignment of the STML signal as phosphorescence and, hence, to the T_1-S_0 transition was mainly based on comparing the photon energy to calculated energy differences of the two possible transitions[128]. Our data suggests that these two energies - extracted here experimentally - are too close to allow for an assignment of the transitions based on their energies.

In case of PTCDA on 3 ML NaCl films on Ag(111), the negative charge state is the ground state[128,156]. LUMO imaging at a threshold voltage of -0.55 V (ref. [128]) suggests that at this voltage an electron tunnels out of the LUMO resulting in the S_0 state. From our results we can infer that T_1 is (1.28 ± 0.07) eV higher in energy than S_0, which matches with the reported observation of a second peak in STS at a voltage of -2.05 V (ref. [128]), if a lever arm α of 0.89 is taken into account, see Section 3.12.1. The threshold voltage

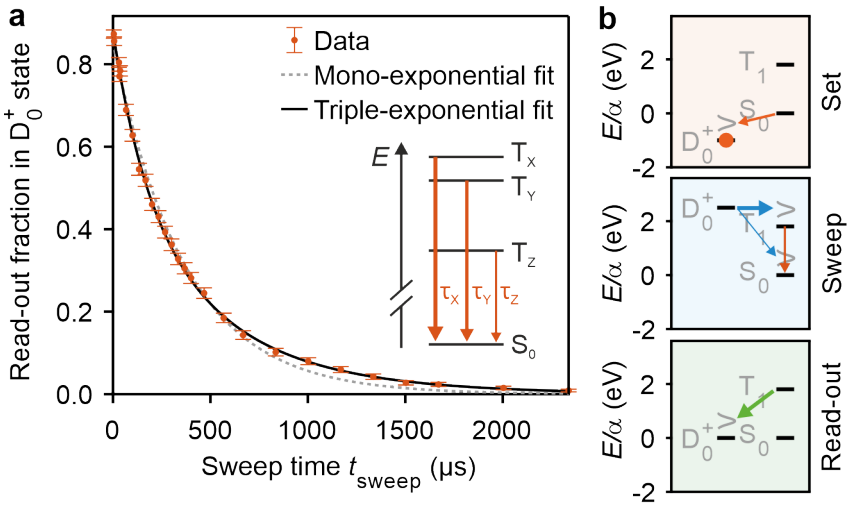

Figure 3.24.: Triplet decay of PTCDA. a, Plot of the measured read-out fraction in the D_0^+ state versus t_{sweep} for a PTCDA molecule on >20 ML NaCl/Au(111). Measurements were performed with a voltage pulse sequence similar to Figure 3.5b. At the end of the set pulse ($V_{set} = -4.54$ V), the D_0^+ state is populated. A sweep voltage of -1.04 V was chosen to populate the T_1 and S_0 states. The read-out was at the D_0^+-S_0 degeneracy ($V_{read\text{-}out} = -3.54$ V), mapping the T_1 state population onto the D_0^+ state. The voltage-pulse sequence was repeated 8 times per second for 160 seconds for every t_{sweep}, and the error bars were derived as the standard deviation of the binominal distribution[21], see Section 3.3.3. The resulting decay with increasing t_{sweep} reflects the decay of the T_1 state population, which can be well fitted with a triple-exponential decay (black). Averaging over three measurements (on two individual molecules) yields decay constants of (350 ± 43) µs, (170 ± 13) µs and (671 ± 62) µs. These three lifetimes are associated with the zero-field-split substates of T_1. This is confirmed by the zero-field triplet state ESR spectra which were measured for individual PTCDA molecules on the same substrate via AFM, see Section 4.10. **b**, Many-body energy diagrams of the transitions taking place during the set and sweep pulse and at the beginning of the read-out phase for the T_1-state lifetime measurement shown in **a**. The arrows and dots are analogous to Figure 3.8e.

of this $D_0^- \rightarrow T_1$ process corresponds to the threshold voltage for observing the STML signal with a photon energy of 1.33 eV (ref. [128]). This implies that the population of T_1 is important for the cycle leading to the luminescence signal. One interpretation of the observed STML is that it is due to phosphorescence from T_1 to S_0 (orange, Figure 3.23b). However, T_1 being part of the STML cycle does not necessarily imply that the observed luminescence occurs from this state. Alternatively, T_1 can decay to D_1^- by an electron tunneling from the substrate into the LUMO, opening the $D_1^- \rightarrow D_0^-$ luminescence transition (red, Figure 3.23b). Note that both pathways become accessible at the voltage where T_1 can be formed. Which pathway is dominating is given by the rates of the involved processes: phosphorescence from T_1 to S_0 versus tunneling from T_1 to D_1^-. Recently, the lifetimes of out-of-equilibrium charge states on 3 ML of NaCl were found to be on the timescale of 100 ps (ref. [35]). In contrast, we find a T_1 state lifetime on the order of 300 µs on >20 ML NaCl (see Figure 3.24) pointing toward a faster rate of T_1 decaying into D_1^- than into S_0. Note, however, that luminescence lifetimes can be strongly reduced on a few monolayers of NaCl. Based on our results, we can therefore not rule out the phosphorescence pathway. Note further that in case of a quinacridone molecule also both pathways were accessible,

but in this case, STML mapping allows to disentangle the two pathways and assign the signal to luminescence of the charged exciton instead of phosphoresence[121].

3.13. Conclusion and outlook

In conclusion, we introduce a single-molecule excited-state spectroscopy method using AFM. It relies on shuttling single-electrons between the tip of an AFM and a single molecule, placed on an insulating surface. Different electronic states (excited and charged states) can thereby be populated and subsequently read-out using the single-electron sensitivity of AFM. The elegance of the pump-probe sequence used to steer the electron tunneling is that it provides access to the temporal evolution of the populated states, and thereby allows discriminating short and long-lived excited states, giving access to the nature of these states. Furthermore, the interpretation of the transitions can be guided by repeating the experiments using different pump-probe pulses, which allows to assign the net charge of the molecule at the beginning and end of the different electronic transitions. From these insights into the individual electronic transitions of single molecules, the energy levels of the ground and excited states for different charges can be extracted. Further, the reorganization energies of redox transitions, and the electron-phonon broadened width of these transitions can be determined. Lastly, our method provides the relative rates of competing transitions.

We applied our method to pentacene and PTCDA, and demonstrated that the results obtained on thick insulating films can be used to interpret those on thin insulating films. Our method can thereby shed light on STM experiments, for instance on STML experiments. Since in such experiments only a small fraction of the involved transitions is experimentally accessible, their interpretation is often difficult, which led to controversial assignment of data in recent publications. Our spectroscopic method can not only directly access the energies of such optical transitions, but also extract which pathways are possible. Next to providing valuable insights regarding the interpretation of such data, we believe that these insights can also steer the engineering of phosphorescence and fluorescence of individual molecules.

As demonstrated for pentacene and PTCDA, our method can be used for the quantification of excitation energies that are difficult to access otherwise, for example those of triplet excitations. A review paper from this year, ref. [157], from the field of single-molecule photon emitters stated that the energies of such triplet states have been detected in the past but never from single molecules at low temperatures. Whereas the pioneering work by Fatayer et al.[20] paved the way to probe individual excited states of single molecules, the approach presented here goes far beyond that as discussed in the introduction. In particular, the unambiguous assignment of spectroscopic features to particular many-body states marks an important new achievement. We believe, therefore, that our newly developed method can fill this gap in the field of single-molecule photon emitters, and allows the determination of triplet energies of a variety of relevant molecules. The knowledge of the triplet energy in the field of single-molecule photon emitters could potentially allow the design of fast and high gain single-molecule all-optical transistors[157].

Next to the energetical mapping of ground and excited states, our spectroscopic method can also prepare the molecule in specific excited states and control the subsequent transi-

tions from such states. We envision the future use of this method to steer single-molecule chemical reactions and thereby guide the understanding and engineering of fundamental chemical reactions. For instance, reactions can be envisioned where dissociation of a molecule is steered by the population of a specific molecular state.

Finally, we demonstrated that by varying the lateral tip position the ratio of tunneling into different states can be modified, which revealed additional transitions in the excited-state spectra measured for pentacene. We anticipate that this spatial dependence of excited-state spectroscopy could be exploited for a spatial mapping of excited states.

4. Single-molecule electron spin resonance by means of atomic force microscopy

Most of the work presented in this chapter has been published in ref. [22]. Parts of the text and most of the figures in this chapter are reprinted and modified with permission from Springer Nature (2023). The results presented in this chapter have been obtained and interpreted in collaboration with Raffael Spachtholz within the framework of his master thesis[158], Sonja Bleher within the framework of her bachelor[159] and master thesis, Franziska Bruckmann[160], Maximilian Stahl[161], Jakob Eckrich[162] and Stefan Brinster[163] in the context of their bachelor theses, and Tobias Preis, Philipp Scheuerer and Jascha Repp.

4.1. Introduction

Electron spin resonance (ESR) is an indispensable tool in chemistry, biology, medicine, physics and material science. ESR is mainly used for the structural elucidation of radicals (molecules with unpaired electrons), but is also a promising tool to control qubits in quantum information processing. A drawback of conventional ESR is, however, that a large number of spins, typically at least 10^{10}, are required to get a detectable ESR signal[103]. This means that the resulting ESR signal reflects an average over a large ensemble of molecules and their environments.

Scaling ESR down to the sensitivity of a single molecule offers the prospect of truly locally probing the environment of this molecule, and thereby using the molecule as a quantum sensor[164]. Electron spins in single atoms[165] or molecules[166] can also act as qubits in quantum computing[167]. Next to a direct usage as qubits, ESR of single electron spins can be used to learn about properties key to quantum computers, such as the atomistic origins of decoherence[168].

In 1993, two groups succeeded simultaneously in the optical detection of an ESR signal for a single molecule embedded in a host crystal[169,170]. The optical sensitivity to a single molecule was demonstrated a few years earlier by Moerner and Orrit[171,172]. To this end, a molecule is optically excited from its S_0 ground state to its first excited singlet state S_1. For single molecules embedded in a host crystal, this $S_0 \rightarrow S_1$ transition is inhomogeneously broadened because of the slightly different environments that the molecules experience due to defects in the crystal[169,172]. Combining excitation in the wing of this inhomogeneously broadened transition with a narrow laser focus (approximately 5 µm)[169,172] on a thin crystal flake (typical thickness of 10 µm)[103] with a low concentration of embedded molecules (10^{-7}-10^{-9} mol/mol)[103], enabled the optical excitation of only one molecule. Subsequently, the emitted photon from the $S_1 \rightarrow S_0$ transition of this molecule can be detected. If the

molecule is back in its ground state, it will be re-excited, and the photon intensity resulting from many of these cycles is detected. A reduction in this photon intensity is observed when there is a significant probability to populate the dark T_1 state via intersystem crossing from S_1. The longer the molecule remains in the dark state, the more the luminescence signal is reduced. Since the three triplet substates have different lifetimes, driving transitions between them modifies the time that the triplet state is populated, and thereby the luminescence intensity[169,170]. Following this approach called optically-detected magnetic resonance (ODMR), zero-field triplet state ESR spectra of a single pentacene molecule could be measured[169,170]. This achievement was quickly followed by the demonstration of coherent spin manipulations[173] and nuclear spin detection[174–178].

A long-standing goal is to combine such single-molecule sensitivity of (electron) spin resonance with real-space spatial resolution on the atomic scale[179–181]. Here, we introduce a novel method that achieves this goal: we detect ESR signals of single molecules by means of AFM. To motivate the development of this method, the existing methods that combine real-space spatial resolution with electron spin resonance are reviewed.

In 1991, magnetic resonance force microscopy (MRFM) was proposed[179,182] with the vision of directly imaging biomolecules to unravel their three-dimensional structure, which is key to their function and possible roles in diseases[179,181]. Detecting them on the single-molecule scale would not only remove the ensemble averaging, but also broaden the applicability. For instance, proteins are often studied using X-ray crystallography, but that is typically only applicable if they can be crystallized[180,181]. In 1992, MRFM was demonstrated for the first time[183]. Thereby, a very small magnetic force was detected between a cantilever containing the spin-containing sample and a magnet[183]. Despite the tiny magnitude of the force, an ESR signal of a single spin with a spatial resolution of 25 nm was detected by Rugar et al. in 2004 (ref. [184]). Further developments pushed this resolution down to 4 nm to enable Magnetic Resonance Imaging (MRI) of tobacco mosaic virus particles[185], and even further to 0.9 nm (ref. [186]).

Another approach to measure ESR signals with nanometer spatial resolution relies on the measurement of triplet state ESR signals of NV centers in diamond (a substitutional nitrogen with an adjacent carbon atom vacancy) using ODMR[187]. Balasubramanian et al.[188] mounted diamond crystals with a single NV center to an AFM cantilever. They were thereby able to detect a change in the ESR signal of the NV center due to magnetic interactions with the surface with a 20 nm spatial resolution[188]. Although the coupling of NV centers to single electron spins in diamond could be detected with a spatial resolution of 1 nm (ref. [189]), NV centers mounted to AFM cantilevers are typically limited to a spatial resolution of 10 nm (ref. [190]). A better spatial resolution requires shallow NV centers (below 10 nm depth), which suffer from charge instability and spin dephasing, deteriorating their optical and spin properties[190].

These two approaches have in common that ESR with atomic-scale spatial resolution is (at least currently) out of reach. In 2015, Baumann et al. were the first to demonstrate ESR with subångström spatial resolution using STM[111,191]. As in conventional ESR, a large static magnetic field (typically 100 mT to a few T (ref. [111, 192])) was employed to split the spin states in energy (see Section 2.4). Combined with very low temperatures (typically sub-Kelvin), a significant population difference between the two spin-split states was induced. An RF magnetic field was generated by applying an RF electric field to the tip[111] or a separate antenna[192], which in combination with the used magnetic tip generated

an RF magnetic field in the tip-sample junction[193]. The ESR signal was detected employing the tunneling magnetoresistance effect[111,193]: the tunneling current depends on the relative orientation of the electron spin on the tip and the electron spin of the measured atom on the sample[193,194]. By driving RF transitions between the spin states of the electron spin of the studied atom, the orientation of its spin will change with respect to the fixed spin on the tip, generating a detectable ESR signal[111,193] (see for more details ref. [193]).

Similarly as for ODMR on single molecules, a demonstration of coherent spin oscillations[195,196] and access to nuclear spins[191] quickly followed this first demonstration of ESR-STM. Since atomic manipulation is possible with STM[5,8], the dipolar and exchange couplings could be tuned[197], and artificial atomic-scale quantum devices could be constructed[198,199]. Recently, it was shown that ESR-STM is applicable to a quickly growing number of systems, varying from different atomic species[111,197,200,201] to molecules[202,203].

Although these achievements demonstrate the great potential of ESR-STM for quantum sensing and computing applications, its energy resolution and the achievable coherence times are strongly limited by the decoherence sources that are intrinsically present. First of all, the sensing in ESR-STM is based on the tunneling current, which decoheres the spin being measured[193,195,198,204]. Specifically, it was shown that nearly every tunneling electron causes a decoherence event[204]. Secondly, the employed magnetic tip causes a fluctuating magnetic field at the measured atom, due to unintended fluctuations of the tip-sample distance[111] or thermally induced changes of the tip's magnetic moment[193,198,204]. Such a varying magnetic field leads to a substantial line broadening[111] and contributes to the decay of coherent spin oscillations[195,198]. It was found that this effect strongly depends on the used magnetic tip[193]. Third, decoherence is induced by scattering electrons from the required conductive substrate and the nearby tip[195,205]. For example, the spin lifetime T_1, which gives an upper limit to the spin-coherence time T_2 ($T_2 \leqslant 2 \cdot T_1$)[198] was found to almost increase by an order of magnitude upon increasing the thin decoupling layer used from 2 to 3 ML and from 3 to 4 ML of thickness[205].

If ESR is instead combined with AFM, a method could be developed that avoids these decoherence sources. AFM allows measuring on thick insulating films such as 20 ML of NaCl, and thereby allows to fully decouple the molecule from an underlying metal surface. This means that scattering with the electron bath of a conducting substrate is absent as a decoherence source. Note that there are also no electronic states available for scattering in a thick NaCl film close to the Fermi level. Although scattering with conduction electrons in the tip remains possible, decoherence owing to the latter is expected to be small because of the weak tunnel coupling. Secondly, a 20 ML thick NaCl film suppresses any tunneling to the underlying metal surface[19]. Tunneling processes between tip and molecule can be fully controlled and thereby also suppressed during the ESR measurement, ruling out decoherence owing to tunneling electrons. Lastly, an ESR-AFM method could be developed that does not use a magnetic tip and thereby avoids interaction between the spin system and the magnetic stray field of the tip.

Without a magnetic tip, a fundamentally different approach for the AFM detection of ESR signals is required. Here, we propose to measure zero-field triplet state ESR signals, which can be detected by a change in the T_1 state lifetime, similar as for the single-molecule ODMR mentioned above. Instead of optical detection, we propose to detect a change in triplet lifetime via AFM, relying on a pump-probe scheme that was introduced by Peng et al.[21]. Given this existing AFM technique, the main challenge to measure zero-field triplet

state ESR with AFM is to bring an RF magnetic field into the tip-sample junction, and preferably without the use of a magnetic tip.

We implement such an RF field and demonstrate for a single pentacene molecule that it can indeed modify the T_1 state lifetime. Upon sweeping the frequency of the RF field, ESR-AFM spectra can be measured. These spectra feature a sub-nanoelectronvolt energy resolution, allowing to distinguish molecules only differing in their isotopic configuration. Next to pentacene, we demonstrate that ESR-AFM can be applied to other molecules. Moreover, we show that the electron spins of pentacene can be coherently manipulated over tens of microseconds, likely not limited by the detection method but by the molecular properties. The signatures of these coherent manipulations depend on the orientation of the individual molecules, illustrating the selection rules at play.

4.2. Experimental setup and sample preparation

4.2.1. Radio-frequency magnetic field

To drive transitions between spin states of single molecules, a radio-frequency magnetic field $\boldsymbol{B}_{\mathrm{RF}}$ at their location is required. To detect these transitions with AFM, a $\boldsymbol{B}_{\mathrm{RF}}$ should be brought into the AFM setup (we use the same AFM/STM setup as described in Section 3.2.1). Importantly, the introduction of $\boldsymbol{B}_{\mathrm{RF}}$ should not impair the AFM measurements by raising the vibrational noise floor, by increasing the temperature substantially due to power dissipation or by affecting the electronic read-out of the AFM signals.

There are various approaches to bring a sufficiently strong $\boldsymbol{B}_{\mathrm{RF}}$ in a minimally perturbing way into a scanning probe setup. In the ESR-STM method mentioned in the previous section, a $\boldsymbol{B}_{\mathrm{RF}}$ was indirectly generated by applying an electric RF field to the tip-sample junction. In combination with a magnetic tip, locally a strong RF magnetic field was generated[193]. We choose to instead directly generate an RF magnetic field, to not rely on a magnetic tip. Such a $\boldsymbol{B}_{\mathrm{RF}}$ was introduced into a SPM setup in the context of MRFM via a microstrip[206], a small coil[183,207] or their combination[208]. We followed here a similar approach and combine a coil with a microstrip.

Our design is based on a coil consisting of a single loop. As follows from the Biot-Savart law, the magnetic field generated by running a current through a loop increases by reducing the size of the loop and the distance to the sample[209]. We choose to position our coil in the plane of the sample surface. A loop size of 10.5 mm was chosen such that the loop does not interfere with STM/AFM measurements on single crystals having a diameter of 6 mm (e.g. as used for the excited-state spectroscopy in Chapter 3).

To send an RF current through the coil, the generated RF current (see Section 4.2.1.1) was fed via a semi-rigid coaxial high-frequency cable (SC-033/50-AuSS-SS, Coax Japan Co. Ltd.) to the bottom of the liquid-helium bath cryostat. It was guided from there through a home-designed transmission line which ends in the single loop coil. The transmission line and coil were designed on a flexible kapton®/acrylic base material (Beta LAYOUT Ltd.). The flexibility of the material and the design of the transmission line were chosen such that mechanical perturbation of the free-hanging SPM scan head was avoided, in order to minimize the introduction of vibrational noise.

Furthermore, the capacitive coupling of the transmission line to metal parts of the SPM scan head was minimized by differential signaling and avoiding that the transmission line runs close to any metal parts of the scan head. The RF signal in the transmission line and loop could either directly or via ground couple into the electronic circuit of the AFM. This could, for example, lead to a modulation of the gate voltage of the sample, which could steer undesired tunneling events between the tip and the molecule. To avoid a significant modulation of the gate voltage, a frequency-dependent upper limit for the RF power was determined. This limit was set such that at a DC voltage corresponding to the charge degeneracy point no interconversion between the charge states was observed (at the tip-sample height used for the ESR-AFM measurements).

Finally, the RF power dissipation and concomitant heating were minimized by pulsing the RF field. Since our ESR-AFM method relies on measuring the T_1 state lifetime of a single molecule, which is performed in pump-probe cycles[21] (see e.g. Figure 3.24), the RF is only required during the time that the molecule is in its triplet state (the dwell time, see Figure 4.3), and is therefore only applied during this time. For a given RF pulse length and frequency the maximum used RF power was chosen such that the heating induced drift was negligible on the scale of the piezo creep present. More details about the design of the transmission line and its characterization can be found in the master thesis of Raffael Spachtholz[158] and the bachelor thesis of Franziska Bruckmann[160]; a manuscript for publication is in preparation.

At first glance, a metal sample, covered by a thick (>20 ML) NaCl film, seems to be a natural choice as a sample for measuring (the first) ESR-AFM signals. Such NaCl-covered metal samples were also used by Peng et al. for the T_1 state lifetime measurements[21]. However, in MRFM, typically either bulk insulators[184] or micrometer sized samples[183,185] were used. This choice was likely partly motivated by the fact that RF magnetic fields are suppressed by metallic samples because of the eddy currents that are generated. To be more specific, the RF magnetic field penetrates a few micrometers into metals such as gold, copper and silver at frequencies relevant to drive transitions between zero-field split triplet substates[210] (typically between 100 MHz and 4 GHz)[106,211]. In other words, for metallic samples with thicknesses of a few millimeters, the RF magnetic field at the surface is strongly suppressed.

Instead, we choose to deposit a thin gold film (300 nm thickness) in a loop structure onto a cleaved mica disc. Mica was chosen as an insulating substrate, since large flat terraces of gold in its (111) orientation can be grown onto mica[212]. The mica disc was glued onto a non-conducting spacer material, which was clamped onto the button heater (see for more details Section 4.2.2). Because of the 2.3 mm thickness of the spacer material, it is expected that the RF magnetic field is not significantly screened by the button heater.

This gold loop structure was designed such that it acts as a pick-up coil, to enhance the magnetic field at the surface, see Figure 4.1a. To this end, the diameter of the gold loop was chosen the same as the diameter of the coil: 10.5 mm. According to Lenz's law[209], the RF magnetic field in the coil induces an RF magnetic field in the pick-up coil which opposes the field produced by the coil. The ESR-AFM measurements were performed on molecules deposited on the gold pick-up coil, separated from it by a deposited thick (>20 ML) NaCl film (the sample preparation is described in more detail in Section 4.2.2). The part of the pick-up coil where we performed the ESR-AFM measurements was designed with a reduced width to locally enhance the RF magnetic field. We call this part the microstrip. From

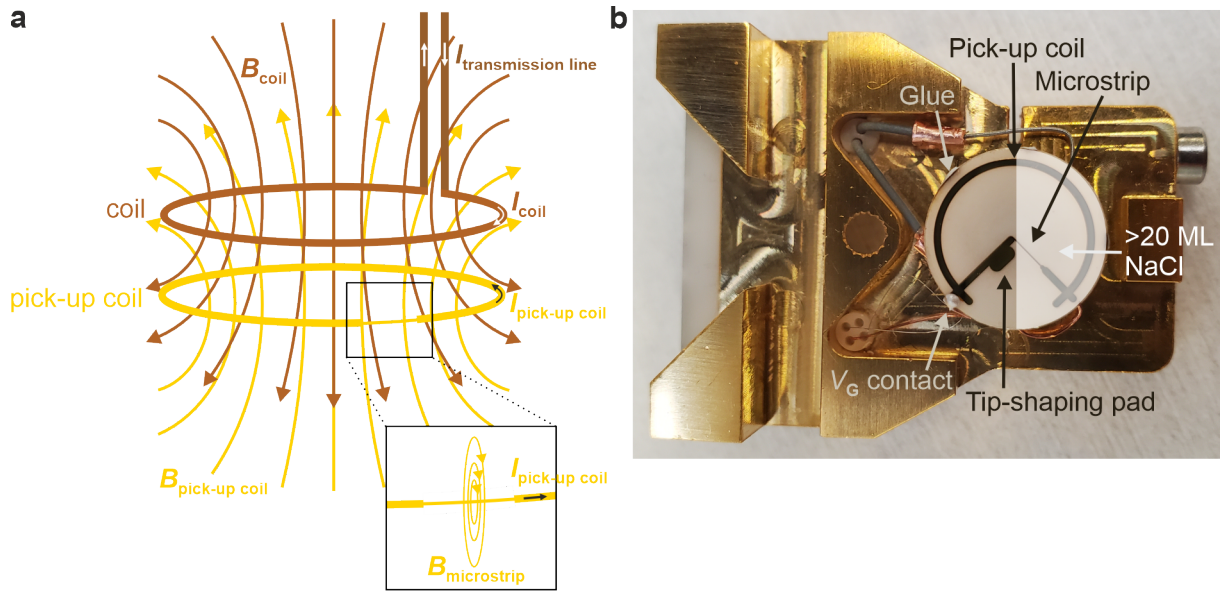

Figure 4.1.: RF generation and sample for ESR-AFM. a, An RF magnetic field $\boldsymbol{B}_{\mathrm{RF}}$ is generated at the sample surface by sending an RF current through a transmission line $\boldsymbol{I}_{\mathrm{transmission\ line}}$ which ends in a coil. The RF current in the coil $\boldsymbol{I}_{\mathrm{coil}}$ generates an RF magnetic field $\boldsymbol{B}_{\mathrm{coil}}$. This magnetic field induces a current in the pick-up coil $\boldsymbol{I}_{\mathrm{pick\text{-}up\ coil}}$ such that the magnetic field of the pick-up coil $\boldsymbol{B}_{\mathrm{pick\text{-}up\ coil}}$ has the opposite direction as $\boldsymbol{B}_{\mathrm{coil}}$. Part of the pick-up coil has a constriction (see inset) where the magnetic field $\boldsymbol{B}_{\mathrm{microstrip}}$ is locally enhanced. **b**, The pick-up coil is made of gold deposited onto a cleaved mica surface. This mica sample is mounted onto the button heater (not shown) of the sample holder (CreaTec Fischer & Co. GmbH) via a macor® spacer. The mica disk is glued onto the macor® spacer using small dots of silver epoxy. One of these dots serves as the contact to which a copper wire is attached such that a gate voltage V_{G} can be applied to the gold structure. The gold structure consists of a loop, which serves as the pick-up coil (see **a**). In the center of the mica disk within reach of our qPlus AFM sensor (having a range with a radius of approximately 4 mm from the center), the pick-up coil has a thin constriction to locally enhance the magnetic field (called microstrip). Furthermore, an additional gold pad for tip shaping is connected to the pick-up coil. On half of the sample a thick NaCl film (>20 ML) was evaporated covering the microstrip, but not the pad for tip shaping, as schematically indicated.

Ampère's law[209], it follows that the magnetic field strength is inversely proportional to the width of the microstrip (assuming that the thickness is small compared to the width). We, therefore, reduced the width of the microstrip to 100 µm. This microstrip was located within a distance of 4 mm from the center of the mica sample (see Figure 4.1b), which is approximately the range in which our qPlus AFM sensor (see Section 3.2.1) can move.

The resulting RF field from the microstrip is associated to field lines looping around the microstrip (Ampère's law, see Figure 4.1a). At the position of a molecule placed above the strip, the local magnetic field resulting from the microstrip is expected to be homogeneous, in the surface plane and perpendicular to the direction of the microstrip. We indeed find that the in-plane magnetic field component is perpendicular to the direction of the microstrip, as discussed in Section 4.12. Irrespectively, the coil and the pick-up coil are in the surface plane of the sample and add a vertical z component to the magnetic field.

The RF signal transmission of the cables including the attached coil was detected by a magnetic field probe and can be well approximated to be constant over intervals of tens of

megahertz around the T_X-T_Z transition, that is, wider than the spectral features observed in the experiments. Although the pick-up coil and microstrip will contribute to the overall transmission of the signal and thus affect the magnitude of the local magnetic field, they are expected to not introduce any resonances in the frequency range of interest. Note that the RF signal at a frequency of 1500 MHz (which is around the resonance frequency of the T_X-T_Z transition for pentacene) has a wavelength roughly three times the entire circumference of the loop of the pick-up coil.

4.2.1.1. RF generation

The RF signal was produced by a software-defined radio (bladeRF 2.0 micro xA4, Nuand) and low-pass filtered to eliminate higher-frequency components. A low-pass filter from the SLP series of Mini Circuits was chosen depending on the used frequency regime, such as SLP-2950+. Subsequently, the RF signal was amplified in two steps (ZX60-P103LN+, Mini Circuits; KU PA BB 005250-2 A, Kuhne electronic), with a maximum output power of 2 W continuous wave. The RF was pulsed using an RF switch (HMC190BMS8, Analog Devices), which was placed between the two amplifiers. This RF switch was gated by the AWG to allow synchronization with V_G and control over the pulse duration. To suppress the switching transients of the RF switch[213], the signal was high-pass filtered using a high-pass filter from the SHP series of Mini Circuits (e.g. SHP-800+), its frequency depending on the used frequency regime. The amplified RF signals were fed into the microscope head as described in the previous section.

4.2.2. Sample and tip preparation

As a sample substrate, we used a mica disc ($d = 12$ mm, Micro to Nano), which was cleaved using Scotch tape. On the mica disc, gold was deposited in a loop structure (Figure 4.1b; diameter, $d = 10.5$ mm; thickness, $t = 300$ nm) by means of electron-beam physical vapour deposition with a rate of 1.5 Å/s. This gold structure contained a 100-µm-wide constriction called microstrip (see Figure 4.1b), on which the measurements were performed. The mica disc was placed onto a macor® spacer and glued using small dots of silver epoxy adhesive (EPO-TEK® H20E). The macor® spacer was designed such that it can be clamped onto a button heater using three tungsten clamps (dimensions macor®: $t = 2.3$ mm, bottom $d = 8$ mm, middle $d = 6$ mm and top $d = 12$ mm). To apply the gate voltage to the surface, a copper wire was glued to the gold structure with another dot of the same silver epoxy adhesive (see contact V_G in Figure 4.1b).

To degas the glue and mica surface, the sample temperature was slowly increased to 600 °C (typically over a time interval of half an hour), holding the sample at this temperature for approximately 5 min. Subsequently, a similar procedure for sample preparation was followed for this gold on mica sample as for the Ag(111) sample (see Section 3.2.2). Importantly, the duration of the sputtering cycles was reduced to 4 minutes, because of the finite thickness of the Au film. The sample was sputtered and annealed in three cycles, annealing to $T = 600$ °C for the first two cycles, and to $T = 550$ °C for the final cycle. On half of the resulting Au(111) surface, a thick NaCl film (>20 ML) was grown at a sample temperature of approximately 60 °C (covering the microstrip, see Figure 4.1b); the

other half of the sample (containing the tip-shaping pad) was used for tip preparation (see Figure 4.1b), presumably resulting in the tip apex being covered with gold.

Part of the data was measured with a CO-functionalized tip. To this end, a sub-monolayer coverage of NaCl was also deposited on the entire surface at a sample temperature of approximately 35 °C, to grow two monolayer NaCl islands also on the half of the sample used for tip preparation. CO molecules were deposited in situ onto the sample in the scan head (T $\approx$ 8 K), by opening the shutter in the radiation shields (that is used for sample transfer) for approximately 5 s with a CO pressure of $1 \cdot 10^{-7}$ mbar in the preparation chamber. After preparing a tip by indentation into the remaining gold surface, a CO molecule was picked up from the two monolayer NaCl islands by scanning over a CO molecule with a setpoint of $I = 40$ pA and $V = 0.5$ V.

The measured molecules (pentacene-h_{14} and PTCDA-h_8, Sigma-Aldrich; pentacene-d_{14}, Toronto Research Chemicals) were deposited in situ onto the sample inside the scan head at a temperature of approximately 8 K.

4.2.3. Voltage pulses

The AC voltage pulses were generated by either a TGA12104, Aim-TTi AWG or a Pulse Streamer 8/2, Swabian Instruments. The rest of the setup was identical to the one described in Section 3.2.3 except for the following modifications. If the Aim-TTi was used, the pulses were not further amplified in contrast to the (tenfold) amplification required for the pulses generated with the Pulse Streamer (see Section 3.2.3). During the read-out of the charge states as described in Section 4.4, the voltage pulses were turned off using a gating signal generated by the control electronics of the microscope. This gating signal was outputted during the read-out of the charge states and fed from the control electronics of the microscope to the AWG. The voltage pulse output of the Aim-TTi was amplitude modulated using the gating signal to suppress the voltage pulses during the read-out of the charge states. In case of the Pulse Streamer, the gating signal was used to disable the used amplifier (ADA4870 evaluation board (Analog Devices, Inc), [a] in Figure 3.3) and, thereby, turn off the voltage pulses.

4.3. Effect of a radio-frequency magnetic field on the triplet-state lifetime

A schematic overview of the experimental set-up for ESR-AFM is shown in Figure 4.2. As described in the previous section, pentacene molecules were deposited onto NaCl (>20 ML) on a Au(111) microstrip on a mica disc such that RF magnetic fields can be applied. A gate voltage V_G was applied to the microstrip to control single-electron tunneling between the molecule and the conductive tip of the AFM[19]. The thick NaCl film prevents electron tunneling between the molecule and the microstrip[19]. The AFM was operated in frequency-modulation mode[43] with a cantilever oscillation amplitude of 0.55 Å (1.1 Å peak to peak), except if specified otherwise.

The ESR-AFM experiments were performed with a similar voltage-pulse sequence as used for the T_1 lifetime measurements[21] (as well as the excited-state spectroscopy measure-

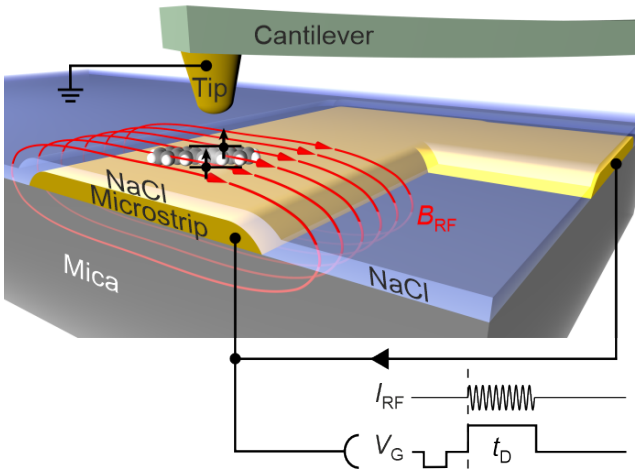

Figure 4.2.: Sketch of the experimental set-up for ESR-AFM. Individual pentacene molecules were adsorbed on a Au(111) microstrip on a mica disc, covered by a NaCl film (>20 ML), preventing electron tunneling between microstrip and molecule. A time-dependent gate voltage V_G was applied to the strip to repeatedly bring the molecule in the neutral triplet excited state T_1 (represented by the two arrows) by two subsequent tunneling events between molecule and conductive tip. During an experimentally controlled dwell time t_D, the neutral molecule can decay to the S_0 ground state. An RF current I_{RF} was run through the microstrip to generate an RF magnetic field. After t_D, the final state of the molecule was read out as described in Section 4.4.

ments, see Chapter 3), which is shown in Figure 4.3a. To drive and probe ESR transitions, we first bring the closed-shell pentacene molecule to the excited triplet state T_1 by driving two tunneling events with pulses of V_G (ref. [21]). During a set pulse, an electron is extracted from the HOMO, positively charging the molecule. The voltage of the second pulse, here called dwell pulse, was chosen such that it allows injecting an electron into the LUMO of the positively charged molecule[20,21]. This voltage was determined from excited-state spectroscopy measurements, see Figure 3.8. The two unpaired electrons in the HOMO and LUMO form the triplet. Note that the positively charged state (D_0^+) is only used to create the triplet state and facilitate the readout, whereas the ESR spectroscopy and spin manipulation described below occurs in the neutral triplet state.

The population in the T_1 state will decay over time into the S_0 state. This population decay can be measured (at a suitable gate voltage) by transferring the remaining population in T_1 after a controlled dwell time t_D to the positively charged state (D_0^+), whereas pentacene in S_0 remains in S_0 (see Figures 3.6 and 4.3)[21]. These two states have a different net charge and can thus be discriminated in the AFM signal[12] owing to their different electrostatic force acting on the tip during a read-out period. Upon repeating the pump-probe pulse sequence 8 times per second for typically 160 seconds, the population in the two charge states and, therefore, in the T_1 and S_0 state can be determined (see Figure 3.7 for an example of a data trace and Section 3.3.2 for a description of the data analysis). Varying the dwell pulse length t_D, the population decay of the T_1 state can be measured[21].

The red curve in Figure 4.4 shows such a population decay. The decay can be well-fitted with a triple-exponential decay. The three zero-field split triplet substates T_X, T_Y and T_Z (see Section 2.4.1 for the spin Hamiltonian) have different lifetimes, which we obtained from the fit as $\tau_X = 21\,\mu s$, $\tau_Y = 67\,\mu s$ and $\tau_Z = 136\,\mu s$. Driving an ESR transition

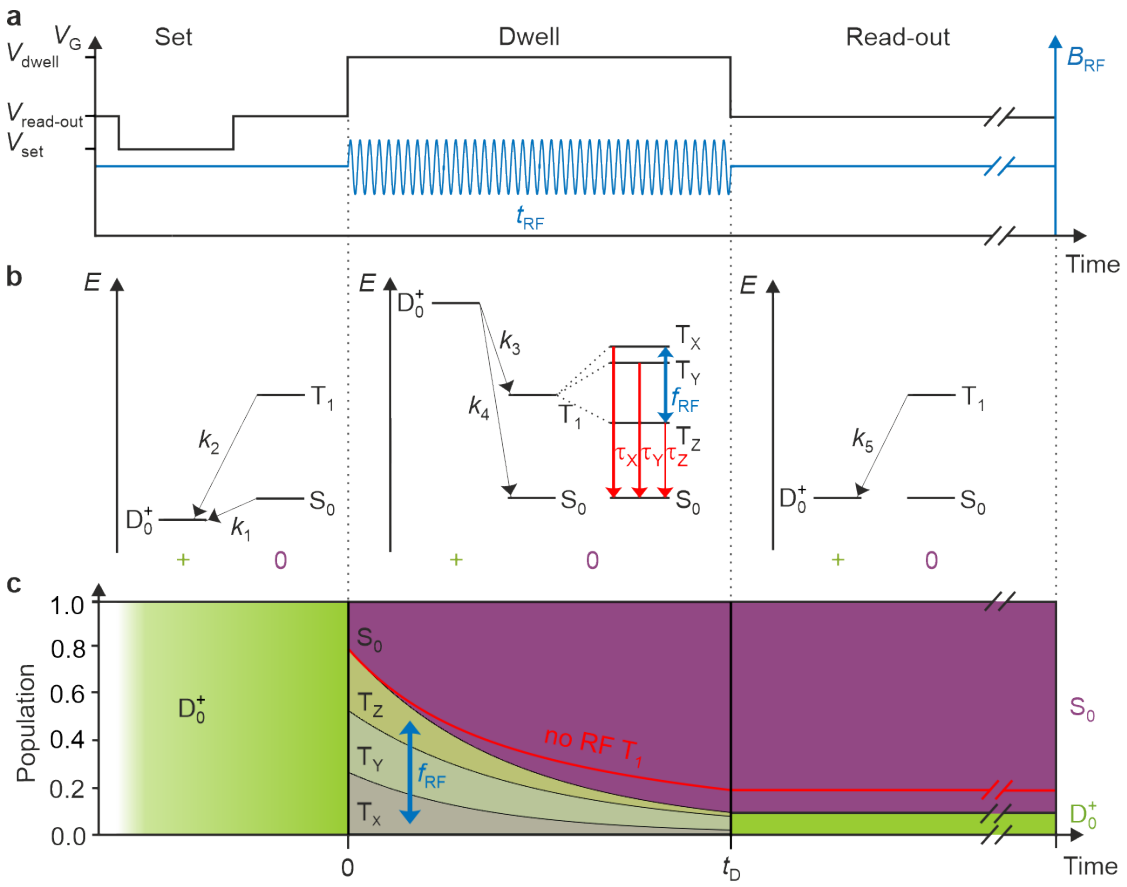

Figure 4.3.: Schematic of the pump-probe pulse sequence for the ESR-AFM measurements. a, Voltage-pulse sequence (black) containing the set pulse (typically $V_{set} = V_{read\text{-}out} - 1\,V$, $t_{set} = 33.4\,\mu s$) and dwell pulse ($V_{dwell} = V_{read\text{-}out} + 2.5\,V$, $t_D = 100.2\,\mu s$ for pentacene) applied as V_G to the sample. During the read-out interval, the voltage, $V_{read\text{-}out}$, was set to the middle of the charging hysteresis (see Figure 2.9) of S_0 and D_0^+ (typically -1.5 to $-2.1\,V$ for pentacene on NaCl(>20 ML)/Au(111)). An RF pulse (blue) was synchronized with the dwell pulse, having the same duration as the dwell pulse for the measurements of the triplet decay under resonant driving (Figure 4.4) and the ESR-AFM spectra. **b**, Many-body energy diagrams showing the mutual energetic alignment of D_0^+, S_0 and T_1 during the pump-probe sequence of **a** (the relaxation energies are not included for simplicity; the quantitative many-body energy diagram for pentacene can be found in Figure 3.18a). The charge-transfer rates (k_1-k_5) were chosen (by the tip height) to be much faster than the triplet decay, with $1/k_4$ set to around 4 µs for the ESR-AFM experiments (see Section 4.4) and 0.2 µs for the T_1 lifetime measurements. A closer tip-sample height for the T_1 lifetime measurements compared to the excited-state spectroscopy (see Chapter 3) and ESR-AFM measurements was chosen to prevent any influence of the tunneling rates on the measured T_1 lifetime decay[21]. During the set pulse, the molecule was brought to D_0^+. The dwell voltage pulse lifted the D_0^+ state above the T_1 and S_0 states; an electron can tunnel into the molecule, forming either the T_1 or the S_0 state, preferentially populating T_1 (see Figures 2.3 and 3.8), with rates k_3 and k_4, respectively. During the dwell pulse, the molecule in T_1 can decay into S_0. Two of the triplet substates (here T_X and T_Z) can be coupled during this time by the RF pulse. If the molecule was still in the triplet state after the dwell pulse, an electron can tunnel out of the molecule charging it, allowing a discrimination of the T_1 and S_0 states through the charged and neutral states, respectively (see Figure 3.6). **c**, Populations of the involved states during the pump-probe sequence, with (black lines and colored areas) and without (red line) RF. Note that, with RF, the T_X and T_Z substates both decay with the average decay rate of T_X and T_Z, assuming a sufficiently strong RF pulse.

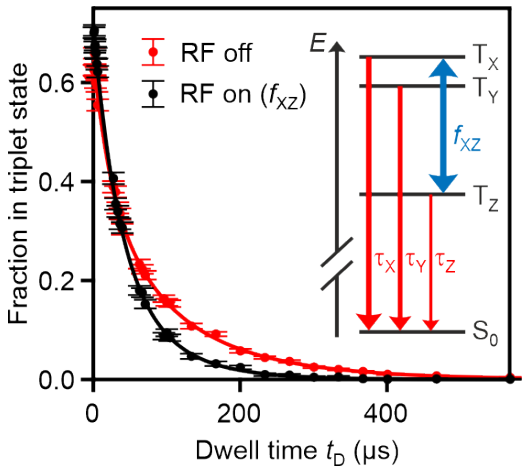

Figure 4.4.: Triplet decay under resonant driving. Decay of the T_1 state as measured without RF (red) and with a broadband RF pulse (black). The broadband RF pulse corresponded to a chirped pulse with a width of 12 MHz, a repetition time of 5 µs and a center frequency of 1544 MHz generated via I/Q (in-phase/quadrature-phase) modulation. T_1 is zero-field-split into three substates T_X, T_Y and T_Z having different lifetimes (inset), such that the RF pulse driving the T_X-T_Z transition changes the resulting overall decay. Solid lines represent fits to triple-exponential decays. Each data point corresponds to 1920 pump-probe cycles and the error bars were derived from the s.d. of the binomial distribution[21]; see Section 3.3.3. The difference in the fraction in the triplet state at $t_D = 0$ is attributed to a different ratio of tunneling into the HOMO and LUMO. Note that for a sharp metal tip (having an AC-STM contrast as shown in Figure 3.11) this ratio was found to be constant over the molecule and around 0.8 instead of the 0.6 found here (see Figure 3.11), indicating that the tip used for the measurement shown here was likely functionalized with an adsorbate.

between two of these substates by an RF magnetic field of matching frequency effectively equilibrates their populations and thereby strongly affects the overall population decay of the T_1 state[169,170,214]. For example, if the populations between T_X and T_Z were equilibrated, these substates would decay with the same (the average) decay rate: $k_X' = k_Z' = (k_X + k_Z)/2$ (ref. [103]). Using our decay constants, it is expected that $\tau_X' = \tau_Z' = 36$ µs, while the decay of T_Y is unaffected by driving with such an RF frequency ($\tau_Y' = \tau_Y = 67$ µs).

This was experimentally tested by measuring a triplet decay while driving the T_X-T_Z transition at 1540 MHz (see Section 4.5). The resulting decay is shown as the black curve in Figure 4.4. Fitting this curve yields $\tau_X = 35$ µs, $\tau_Y = 76$ µs and $\tau_Z = 35$ µs. Importantly, even with a tri-exponential fit, the fit yields two very similar decay constants. Furthermore, these experimentally found values are close to the predicted values, the differences are attributed to uncertainties on the experiments and fitting.

As seen in the data, there exist an optimal t_D at which the population difference between the two states (S_0 and T_1) is maximized: around 100 µs. This value can also be determined theoretically by comparing the triple-exponential decay without resonant driving with a decay where the two coupled substates (T_X and T_Y) decay with an uniform decay rate. This yields an optimal t_D of 92 µs, close to the experimentally found value. Since we choose the voltage pulses to be an integer multiple of cantilever periods (to prevent undesired excitation or damping of the cantilever), t_D was fixed to 100.2 µs. An ESR-AFM spectrum can then be measured by recording the triplet population at this fixed t_D as a function of

frequency f_{RF} of the driving field. This will be shown in Section 4.5; the next section will discuss the details of the data acquisition of these ESR-AFM spectra.

4.4. ESR-AFM spectra data acquisition

ESR-AFM spectra can be measured using the pump-probe pulse sequence shown in Figure 4.3, as explained in the previous section. To reduce the statistical uncertainty (see Section 4.6) for a given data-acquisition time, the pump-probe pulse sequence was repeated 160 or 320 times per second, instead of eight times per second used for the T_1 lifetime measurements (see previous section) and the excited-state spectroscopy (see Chapter 3). This repetition rate is too large to resolve the charge states during the read-out period individually for every pump-probe cycle. Instead, the frequency shift Δf was averaged over an interval of typically 20 s. This $\langle \Delta f \rangle$ is mainly determined by the read-out phases because they make up for approximately 95% of the total time (in case of parameters used for pentacene). $\langle \Delta f \rangle$ thus reflects the ratio of read-out in the charged and neutral states, corresponding to the ratio of T_1 and S_0 populations at the end of the dwell time, respectively.

Note that the change in Δf related to the different charge-state populations is very small. However, $\langle \Delta f \rangle$ is also sensitive to the tip-sample distance. These changes in the tip-sample distance are mainly attributed to creep of the piezo-electric actuator used to bring the tip in close contact to the sample. Creep is the time-dependent deformation of the piezo-electric material after a sudden change in the applied voltage[29]. To be more specific, the tip-sample height will reduce over time because of the extension of the piezo-electric material after the sudden application of a large voltage to bring the tip in close contact to the sample. Since the tip needs to be retracted from the surface before filling the cryogenics every three days (to prevent the tip from crashing into the surface during the filling process), there is always some residual creep of the piezo-electric actuators present. Next to creep, there can be other contributions to the fluctuations in the tip-sample distance, such as thermal drift. For simplification, the drift and piezo creep is abbreviated as drift in this chapter (although in our case typically the piezo creep is dominant). To minimize the effect of drift on the ESR-AFM spectra (which are measured in constant-height mode), ESR-AFM spectra were taken after at least a waiting time of four hours after approaching the sample. Secondly, the tip-sample distance was reset by shortly turning on the Δf feedback either after every sweep of the RF or after a fixed time (15 to 60 min). The length of this time interval was chosen depending on the size of the drift present at the start of the measurements.

Still, the remaining fluctuations due to the tip-sample height are very large; they are comparable in size to the detected signal, see the red curve in Figure 4.5. To quantify how small these remaining fluctuations should be to not dominate the uncertainty margins, we compare them to the size of the statistical uncertainty. The uncertainty on the average frequency shift due to the statistical uncertainty is typically around 0.2% for the parameters used, see Section 4.6. Since the size of the charging step for pentacene is typically around 0.3 Hz, an uncertainty of 0.2% corresponds to a frequency shift of less than 1 mHz. For a typical tip and a tip-sample distance at which our data is taken, a height change of only a few hundreds of femtometers results already in such a frequency shift.

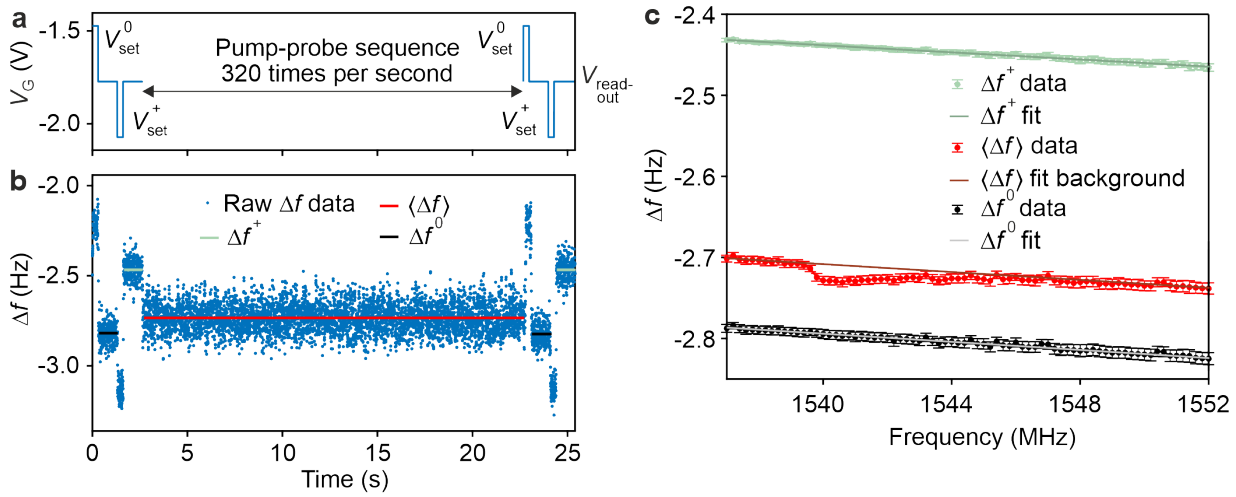

Figure 4.5.: Raw data and signal extraction toward an ESR-AFM spectrum. **a**, Voltage-pulse sequence for the acquisition of one data point. At the beginning and end, two voltage pulses were given to neutralize ($V^0_{\text{set}} = V_{\text{read-out}} + 0.3\,\text{V}$) and charge ($V^+_{\text{set}} = V_{\text{read-out}} - 0.3\,\text{V}$) the molecule, in between which the voltage was set to the center of the charging hysteresis ($V_{\text{read-out}}$); here a typical value for pentacene is shown. During the middle 20 s of the data trace, the pump-probe sequence shown in Figure 4.3 was repeated 320 times per second. **b**, One of the recorded Δf data traces with the pulse sequence shown in **a**. The frequency shifts of the neutral (Δf^0, black) and charged (Δf^+, green) molecule were extracted as the average over the 1-s intervals at the beginning and end of the trace. The averaged frequency shift ($\langle\Delta f\rangle$, red) was extracted from the interval during which the pump-probe sequence was turned on. **c**, ESR spectrum of pentacene-h_{14} without normalizing the frequency shift. The panel shows Δf^0, Δf^+ and $\langle\Delta f\rangle$ as a function of the RF (error bars are s.d. of seven repetitions). Owing to slight drift, all three signals show a similar overall trend line (fit curves). Around 1540 MHz, $\langle\Delta f\rangle$ shows clear deviations from this general trend, representing the ESR signal. Normalizing the frequency shift from these three values as $\Delta f_{\text{norm}} = \frac{\langle\Delta f\rangle - \Delta f^0}{\Delta f^+ - \Delta f^0}$ largely reduces the background trend owing to drift.

To minimize the influence of the remaining fluctuations in the tip-sample height, $\langle\Delta f\rangle$ was normalized using the frequency shifts of the positively charged Δf^+ and neutral Δf^0 molecule, as

$$\Delta f_{\text{norm}} = \frac{\langle\Delta f\rangle - \Delta f^0}{\Delta f^+ - \Delta f^0}. \tag{4.1}$$

This removes most of the remaining fluctuations, since $\langle\Delta f\rangle$ has a similar dependence on tip height as Δf^+ and Δf^0 (see Figure 4.5c) ($\langle\Delta f\rangle$ is mainly determined by the read-out phases, and thus by Δf^+ and Δf^0). Δf^+ and Δf^0 were determined at the beginning and end of every 20 s data trace (see Figure 4.5b). To this end, the charge state was changed by applying small voltage pulses ($V^0_{\text{set}} = V_{\text{read-out}} + 0.3\,\text{V}$, $V^+_{\text{set}} = V_{\text{read-out}} - 0.3\,\text{V}$). Tunneling events during the readout of these frequency shifts were minimized by using a tip-sample distance at which the decay constant for the decay of the D_0^+ state into the S_0 state during a pulse of $V_{\text{read-out}} + 1.2\,\text{V}$ was around 4 µs (note that this requirement restricts the possible distances to a small range, as the tip height should also be small enough such that the tunneling processes are considerably faster than the triplet decay). If still a charging event happened, the data trace was discarded. To maximize the rate of the

tunneling processes during the voltage-pulse sequence, the beginning and end of the voltage pulses were synchronized with the closest turnaround point of the cantilever movement. To prevent the excitation of the cantilever, the durations of the voltage pulses were set to an integer multiple of the cantilever period (33.4 µs).

The resulting Δf_{norm} signal typically deviates from the triplet population, since it is not only an average over the read-out periods, but also over the time during which the set and dwell voltage pulses are turned on. During this time, the frequency shift corresponds to the applied voltages and thus crucially depends on the exact shape of the KPFS[12]. In other words, the baseline of the Δf_{norm} signal (without RF or RF off-resonance) varies for different measurements - even for those above the same molecule - owing to differences in the position above the molecule. Still, for a given measurement, a linear relation exists between the Δf_{norm} signal and the triplet population. Quantitative results can be obtained from a calibration measurement in which the population is determined by counting the individual outcomes after each pulse sequence at a repetition rate of eight per second. Thereby, absolute information about the spin population can be obtained.

4.5. ESR-AFM spectra

Following the approach described in the previous sections, an ESR-AFM signal was measured for a single pentacene molecule. The resulting ESR-AFM signal, displayed in Figure 4.6a, has an asymmetric shape, which closely resembles the signal shape obtained with ODMR for single pentacene molecules[169,170]. This asymmetric shape entails information about the nuclear spin system of the molecule; it arises from the hyperfine coupling between the nuclei with non-zero spin and the electron spins. In case of protonated pentacene, these are the 14 proton nuclear spins. A detailed explanation of the hyperfine interaction and how it gives rise to the observed asymmetric lineshape at zero magnetic field can be found in Section 2.4.2.

It should be noted that although only a single molecule is being measured, the resulting asymmetric lineshape is very similar to those obtained for ensembles of molecules[169]. This lineshape reflects the different nuclear spin configurations that the molecule experiences (see Section 2.4.2). In an ensemble, this is a result of the different nuclear spin configurations every individual molecule has. In our case, only a single molecule is being measured. However, to obtain an ESR-AFM spectrum, the molecule is measured typically at least 20,000 times (the number of pump-probe cycles). Since the molecule can be in a different nuclear spin configuration during every pump-probe cycle[169], the large number of pump-probe cycles performed allow the mapping of the full asymmetric lineshape. In other words, instead of an ensemble average, we measure a time average, which is equivalent to an ensemble average over identical molecules (ergodic theory).

Next to the T_X-T_Z transition, the T_X-T_Y transition of pentacene can be probed with ESR-AFM. The resulting signal, shown in Figure 4.6b, has also an asymmetric shape, and resembles the shape of the T_X-T_Y signal measured for pentacene in a p-terphenyl matrix[103].

We can also compare the resonance frequencies of our ESR-AFM signals with those obtained for pentacene in different matrices. The measured T_X-T_Z transition frequency is shifted to higher frequencies by 60 to 120 MHz with respect to those measured for pentacene molecules in p-terphenyl[103,169,170], napthalene[215] and benzoic[216] host matrices. Although

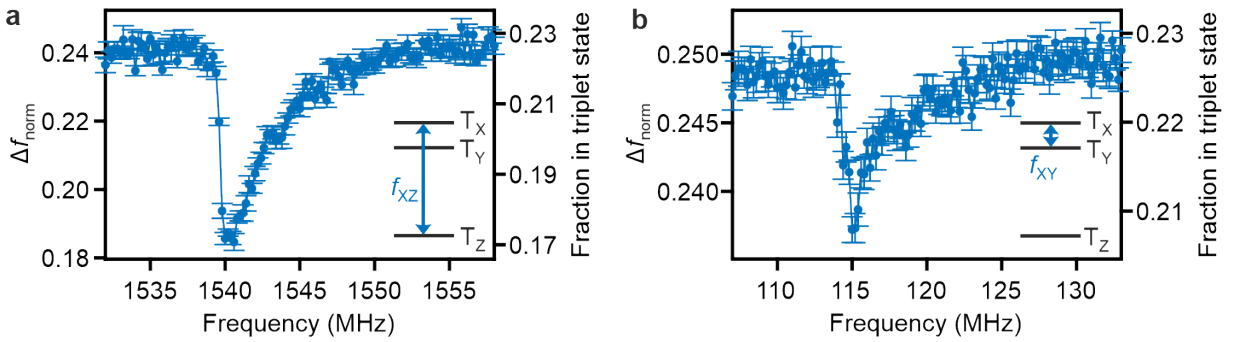

Figure 4.6.: ESR-AFM spectra of pentacene. **a**, **b**, ESR-AFM spectra of the T_X-T_Z and T_X-T_Y transitions of a single pentacene-h_{14} molecule, respectively. The RF was swept at a constant $t_D = 100.2\,\mu s$. The AFM signal Δf was normalized to Δf_{norm} as described in Section 4.4. The error bars were derived from the s.d. of seven and 38 measurements, respectively. Δf_{norm} can be calibrated against the triplet population[21] at t_D; see right axis. The calibration was performed for an RF corresponding to the maximum of the ESR signal, as well as an RF that was off-resonance. For this calibration, 7680 pump-probe cycles were recorded for both frequencies. Note that, because of the similar decay constants of the T_Y and T_Z substates, no ESR-AFM signal for the T_Y-T_Z transition of pentacene was detected.

our T_X-T_Y resonance frequency corresponds to the one found for two of the four lattice sites in p-terphenyl matrices[103], the resonance frequency is different by up to 30 MHz for pentacene in the two other lattice sites in p-terphenyl matrices[103], and in napthalene[215] and benzoic acid[216] matrices. These observed shifts can be rationalized by the different environments: the environment will affect the orbital densities of the two unpaired electrons, and thereby the zero-field splitting (see Section 2.4.1). The zero-field splitting is thus not only a fingerprint of the molecule but also of its environment, as demonstrated further in Section 4.8.

The ESR-AFM signal of the T_X-T_Y transition has a reduced signal magnitude compared to the one for the T_X-T_Z transition (see Figure 4.6). The magnitude of the ESR-AFM signal depends on the ratio of the decay constants of the involved substates. Since this ratio is for pentacene much smaller for the T_X-T_Y transition than the T_X-T_Z transition, a smaller signal is indeed expected for the T_X-T_Y transition. Using the decay constants for pentacene as determined in Section 4.3, a t_D of 100.2 µs and an initial triplet population of 80%, a theoretical maximum signal magnitude (difference in fraction in triplet population) of 0.1 and 0.04 results for the T_X-T_Z and T_X-T_Y transitions, respectively. The magnitudes of the measured signals are lower: 0.06 and 0.02, respectively. This discrepancy could be explained as follows. For the theoretical signal it is assumed that the RF driving constantly equilibrates the population of the two substates. However, relatively low RF powers were used here to prevent power broadening (see for more information Section 4.7 and Figure 4.9). Furthermore, because of the hyperfine interaction, the molecule is not always resonant with the RF radiation. Therefore, in our experiment, the populations are not constantly equilibrated, and the observed ESR-AFM signal is lower than the theoretical maximum.

The spatial resolution of the ESR-AFM signals is in first approximation determined by the spatial resolution for the formation of the triplet; the spin resonance itself is driven by an RF field, which is assumed to be constant over tens of micrometers (see Section 4.2.1).

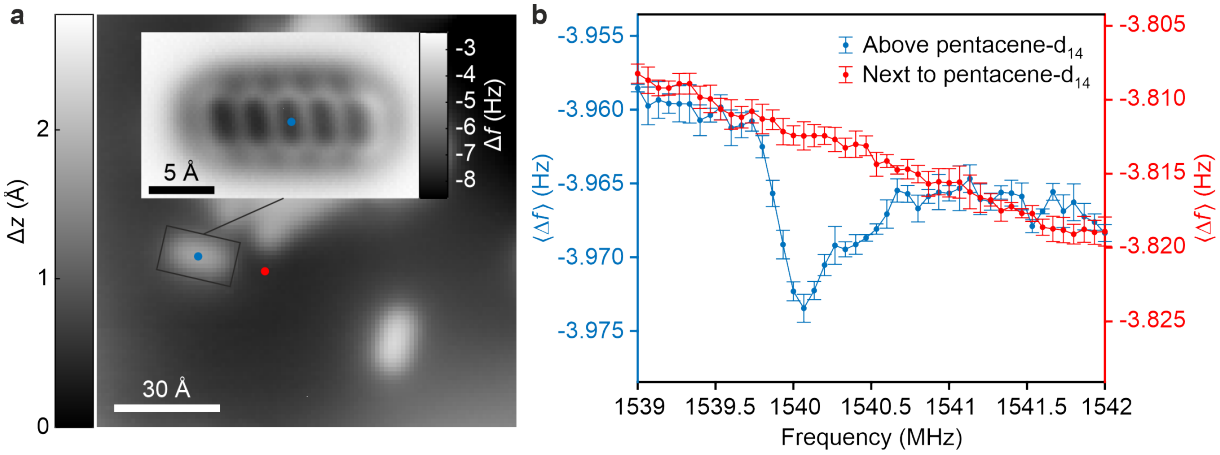

Figure 4.7.: Spectra above and next to a pentacene molecule. **a**, AFM topography image of a surface area with adsorbed pentacene molecules measured with a CO-terminated tip (setpoint: $\Delta f = -1.45\,\mathrm{Hz}$ at $V = 0\,\mathrm{V}$, $A = 1.65\,\mathrm{Å}$). The inset shows a constant-height AFM image as a zoom-in ($A = 0.3\,\mathrm{Å}$, $\Delta z = -4.76\,\mathrm{Å}$ with respect to the setpoint $\Delta f = -1.45\,\mathrm{Hz}$ at $V = 0\,\mathrm{V}$, $A = 0.3\,\mathrm{Å}$). **b**, ESR-AFM spectra above (blue) and next to (red) the pentacene-d_{14} molecule shown in **a** (error bars are s.d. of four repetitions). Although the former shows a clear feature around 1540 MHz, this feature is absent for the spectrum acquired next to the molecule. Note that the frequency shift was not normalized for these spectra.

The formation of the triplet relies on electron tunneling between the tip and the frontier orbitals of the molecule[21]. Therefore, the spatial resolution of the ESR-AFM signals is predominantly determined by the distance dependence of these tunneling processes[89] (see Section 3.4.1). Since the HOMO and LUMO are delocalized over the entire molecule for pentacene (see Figure 3.11), the signal can be measured at any location above these orbitals (typically the tip was positioned above the middle of the molecule). Outside the tunneling range between tip and frontier orbitals, no ESR-AFM signal can be detected, as shown in Figure 4.7. Therefore, ESR-AFM spectra can be unambiguously assigned to the individual molecule beneath the tip, as will be demonstrated in Figure 4.8 and Figure 4.13.

4.6. Sources of uncertainty

To determine the uncertainty on the ESR-AFM data points, the 20-s data traces were repeated several times and the error bars were extracted as the standard deviation of the mean of these repetitions. This way, any type of non-systematic uncertainty will be accounted for, irrespective of its source. To maximize the signal-to-noise ratio for a given measurement time, the measurement parameters were chosen by considering the main sources of uncertainty present, as will be discussed in this section.

The three main sources of uncertainty of Δf_{norm} are the statistical uncertainty from the finite number of repeats, the remaining drift of the tip height and the noise on the frequency shift Δf. The statistical uncertainty can be calculated with the formula presented in Section 3.3.3. We typically choose the number of repeats per data point such that the statistical uncertainty becomes comparable with the other two sources of uncertainty; depending on the exact experimental conditions, any of these three sources can dominate. For

example, the standard deviation on the datapoints in Figure 4.6a and b equals 0.20% and 0.16%, respectively (determined by taking the average of the standard deviation for every frequency). In case of Figure 4.6a, this standard deviation is dominated by the statistical uncertainty, which is 0.19% (seven repeats of the 20-s data trace were measured). In contrast, other uncertainty sources dominate in Figure 4.6b, since the statistical uncertainty was only 0.08% (38 repeats of the 20-s data trace were measured).

One of these sources is the remaining influence of the drift of the tip height and position. Although most of this drift is eliminated by our normalization process (see Section 4.4), in some cases a remaining minor influence of this drift was observed. For example, in case of the data shown in Figure 4.8c, the error bars appear to be larger than the noise that seems to be present given the distribution of the datapoints. Indeed the statistical uncertainty is around 0.18%, while the average standard deviation on the experimental data is 0.28%. In this case, the uncertainty due to drift is significantly increasing the error bars, since the Δf_{norm} changes by more than 0.01 from the first to the last repeat. Similarly, in the case of the data shown in Figure 4.21c (bottom) and Figure 4.21d (top), the drift was clearly dominating the uncertainty margins (not shown). Since this drift is on a slow timescale compared to one full frequency sweep, most of its effect can be easily removed from the data by adding an offset to every repetition, as we did for these three cases.

Since for most measurement we did not correct for lateral tip drift, as was done for the excited-state spectroscopy measurements (see Section 3.3.1), we believe that the minor drift observed in Δf_{norm} is, therefore, predominantly caused by lateral drift of the tip with respect to the molecule. To further minimize this lateral drift we implemented a lateral drift correction similar as for the excited-state spectroscopy measurements (see Section 3.3.1), which was used for the measurements of the Rabi oscillations in the context of the electric field dependence (see Section 4.9) and will be employed for future measurements.

The third factor that could dominate the error bars is the noise on the frequency shift Δf. Δf averaged over 1 s exhibits a typical uncertainty of 1 mHz for our used AFM/STM microscope (see Section 3.2.1). As Δf_{norm} is derived using the difference in Δf of the charged and neutral molecule, the size of the charging step will determine how much the Δf noise contributes to the uncertainty of Δf_{norm}. In other words, probe tips that give a strong response to charging (a large charging step in the KPFS) provide a better signal-to-noise ratio and, therefore, a smaller relative uncertainty. To minimize this contribution to the uncertainty, we only used tips for which the charging step was large compared with the noise in Δf (size of charging step typically 0.2-0.4 Hz for tips with a Δf setpoint around -1.5 Hz at zero bias). Note that the uncertainty due to the noise on the frequency shift can be reduced by increasing the intervals for determining the frequency shifts of the charged and neutral state, since these charge states were typically read-out for only 2 s, while $\langle \Delta f \rangle$ was typically measured for 20 s (see Figure 4.5a).

4.7. Isotope selective fingerprinting of molecules

As experimentally demonstrated in the previous section, the ESR-AFM signals of pentacene have an asymmetric lineshape due to the hyperfine interaction with the 14 proton nuclear spins. This hyperfine interaction strongly depends on the identity of the nuclear isotopes

(see Section 2.4.2) and thus allows us to distinguish molecules only differing in their isotopic composition.

To demonstrate the sensitivity to the nuclear isotopes, we measured an ESR-AFM spectrum for pentacene-d_{14}, which is shown in Figure 4.8a. Comparing with pentacene-h_{14}, the peak shape is similar but its high-frequency tail is reduced in width by a factor of approximately 14 (see Appendix A.1.1 for the fitting function). We attribute this reduction to the smaller hyperfine interaction of deuterium. As indicated in Section 2.4.2, the hyperfine interaction scales with the nuclear g-factor, which is 6.5 times smaller for ^{2}H compared to ^{1}H. The reported hyperfine coupling tensor elements for ^{2}H are indeed smaller by this factor[103]. Since the line broadening of the zero-field ESR spectra depends quadratically on the hyperfine interaction (see Equation (2.25)), the linewidth is expected to be reduced by a factor of 42 because of this difference in nuclear g-factor. Note that the possible magnetic quantum numbers m_I also differ for ^{2}H and ^{1}H ($m_I = -1,0,+1$ for ^{2}H, while it is $1/2,-1/2$ for ^{1}H). This will affect the resulting lineshape and linewidth according to Equation (2.25). ODMR measurements of pentacene-d_{14} embedded in a p-terphenyl matrix demonstrated a reduction in linewidth (FWHM of the signal) by a factor of 30. However, they only observed this large reduction for very low RF amplitudes[103,176]; for higher RF amplitudes broader ESR spectra were measured, which is in line with the ESR-AFM spectrum that we obtained for pentacene-d_{14}.

This additional broadening was attributed to the nuclear electric quadrupole interaction[103], which arises if nuclei are present that have a spin quantum number larger than 1/2, in this case ^{2}H, which has a spin quantum number of 1. Such nuclei have a non-spherical symmetric charge distribution and, therefore, a non-zero electric quadrupole moment, which interacts with the electric field gradients present in the molecular environment[217]. This interaction, called quadrupole interaction, causes an additional splitting of the spin states, in our case the triplet substates. In contrast to the hyperfine interaction, the first order quadrupole interaction does not vanish at zero-magnetic field and it splits every of the three triplet substates in the same way[218]. For example, for a spin-1 nucleus every triplet substate will be split in three substates, giving a total of 9 triplet substates (if the hyperfine interaction is neglected). In first approximation, this additional equal splitting does not affect the resulting zero-field ESR spectra, since transitions are being driven between the electronic spin states. However, because of the combination of the quadrupole and hyperfine interaction, there is a small probability to flip the nuclear spin in the process of driving the electron spin[218–220]: the hyperfine interaction mixes into electron-nuclear spin states small components of electron-nuclear spin states that differ in both their electronic and nuclear spin[218,219]. Since these components are small, the probability to drive electronic transitions in which also the nuclear spin flips is low, and, therefore, they are not observed at very low RF powers[103,218]. Upon increasing the RF power, all transitions are driven more strongly. While the allowed transitions are saturated already at relative low RF powers, these "forbidden" transitions are still increasing, leading to a change in lineshape with increasing RF power[218].

Depending on the size of the quadrupole interaction compared to the other interactions present (e.g. hyperfine interaction, lifetime broadening), the quadrupole interaction in zero-field ESR spectra was reported as an additional splitting of the lines[218,221] or as a broadening[103,220]. Given the expected magnitude of the quadrupole interaction of deuterium, we indeed expect an additional broadening of the zero-field ESR signals for pen-

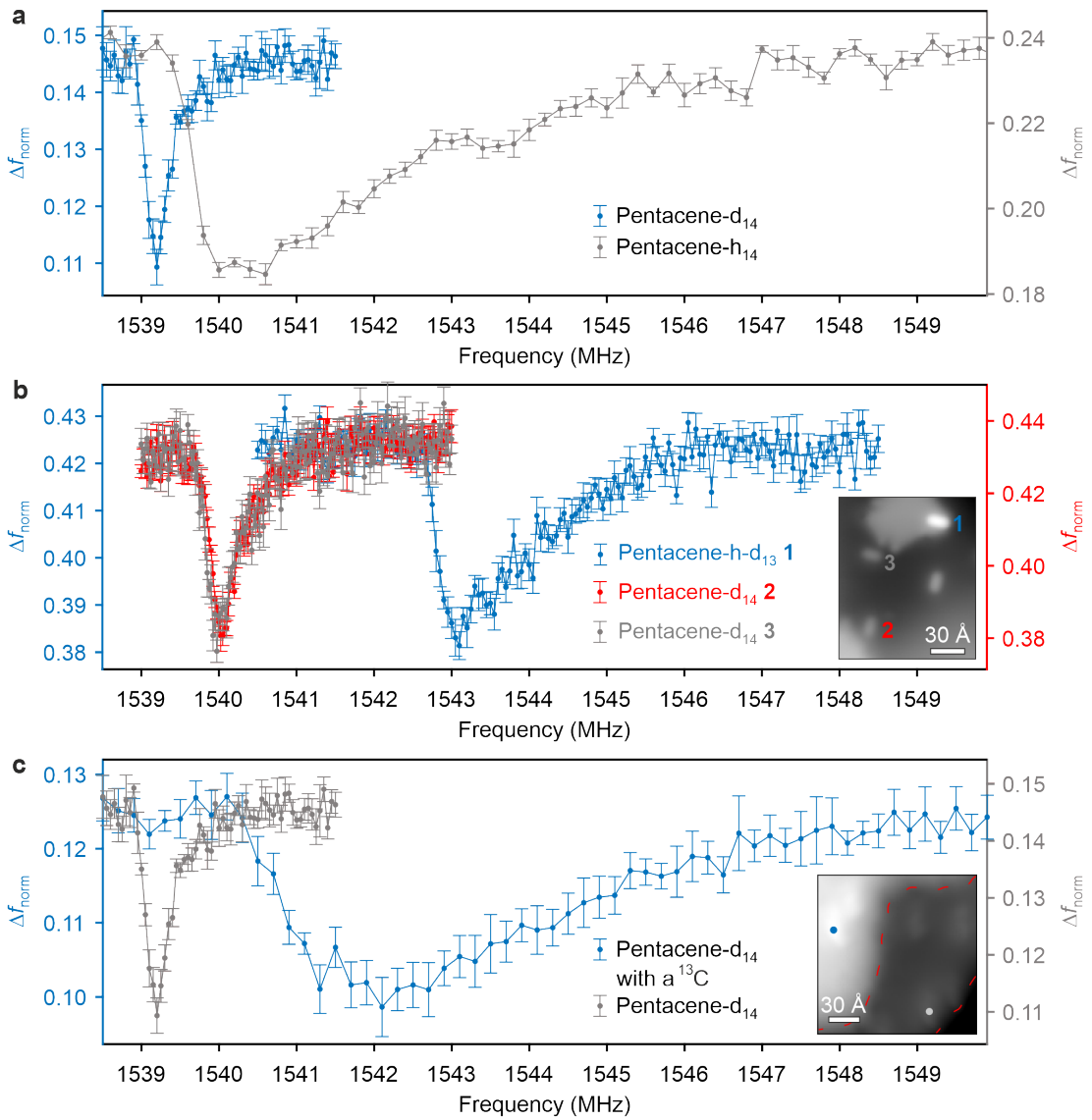

Figure 4.8.: ESR-AFM signals of different isotopomers of pentacene. **a**, ESR-AFM spectrum of pentacene-d_{14} (blue), exhibiting a much narrower resonance in comparison with pentacene-h_{14} (gray). The decreased hyperfine interaction leads to a reduced width of the high-frequency tail. The left flank of the signal corresponds to a width of only 0.12 MHz. The error bars result from the s.d. of eight (pentacene-d_{14}) and seven (pentacene-h_{14}) repetitions. **b**, ESR-AFM spectra of three individual deuterated pentacene molecules. Although the ESR-AFM spectra of two pentacene-d_{14} (red (denoted '2') and gray (denoted '3')) molecules are very similar, that of another isotopologue, pentacene-h-d_{13} (blue (denoted '1')) differs clearly (note that the gray dataset is offset by 0.19 with respect to the right (red) y-axis) (error bars are s.d. of four repetitions). AFM permits imaging these isotopologues in their unique environment (inset, AFM image with a CO-terminated tip at constant $\Delta f = -1.45$ Hz and $V_G = 0$ V, $A = 1.65$ Å) **c**, ESR-AFM spectra of two different isotopologues of pentacene (blue: pentacene-d_{14} containing a ^{13}C; gray: pentacene-d_{14} (same data as the pentacene-d_{14} data shown in **a**)). The error bars are s.d. of eight repetitions. The inset shows an AFM image at constant $\Delta f = -1.4$ Hz and $V_G = 0$ V, $A = 1.65$ Å, the red dashed lines mark the NaCl step edges (the limited spatial resolution of the image is attributed to tip imperfections). The different isotopomers were assigned by comparing their respective ESR spectra to measurements performed for pentacene molecules embedded in a p-terphenyl matrix[176,178]. Colors of the left/right Δf_{norm} scale correspond to data of the same respective color.

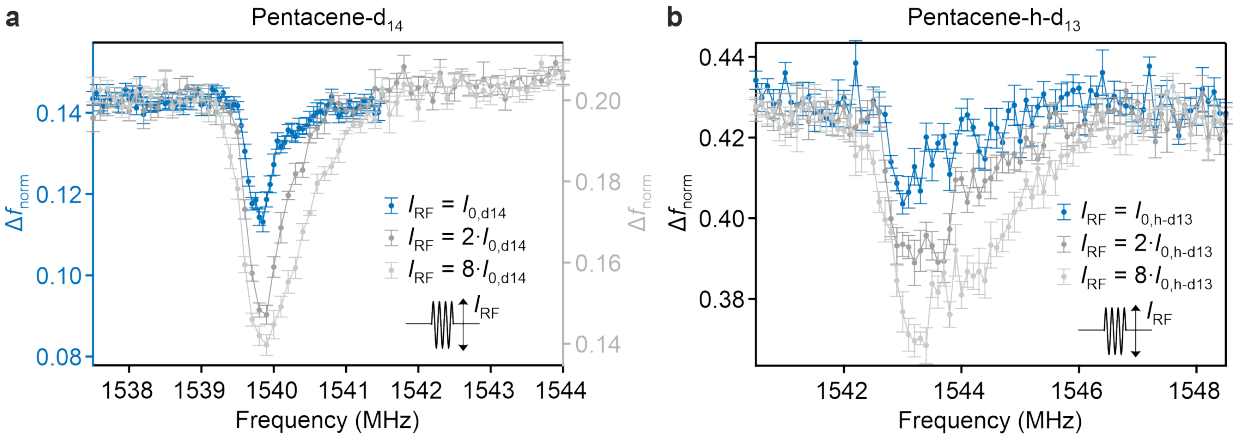

Figure 4.9.: Power broadening of ESR spectra. **a**, **b**, Spectra acquired at different RF amplitudes demonstrating the role of power broadening for pentacene-d_{14} and pentacene-h-d_{13}, respectively. For the spectra at medium and large amplitudes, the amplitude of the RF pulse was doubled and octuplicated, respectively. In case of **a**, the right axis corresponds to both gray datasets. In case of **b**, the (black) Δf_{norm} scale is for all datasets. The error bars were derived from the s.d. of 12 repetitions for the lowest power of pentacene-d_{14} and six repetitions for the other datasets.

tacene. In addition to the quadrupole moment, which depends on the nuclear isotope, the quadrupole interaction depends on the molecular environment. It has been shown for deuterocarbons that the quadrupole interaction depends predominantly on the nature of the deuterium-carbon bond. In case of deuteriums bound to sp^2 hybridized carbon atoms, the quadrupole interaction was found to be around 0.2 MHz (ref. [222]). This value is roughly twice as large as the broadening expected from the hyperfine interaction. We, therefore, expect for pentacene-d_{14} an additional broadening of the zero-field ESR signals due to the quadrupole interaction.

To experimentally test this hypothesized origin of the broadened ESR-AFM signals, ESR-AFM signals were recorded for different RF amplitudes. The resulting spectra in Figure 4.9a show that the signals broaden if a larger RF amplitude is used. Upon increasing the RF amplitude, the lifetimes of the involved substates reduce causing a power broadening. This effect alone would lead to a symmetric broadening; the resonance frequency for every nuclear spin configuration would broaden (see Section 3.6). However, the observed ESR-AFM signals broaden asymmetrically: the lineshape at the high-frequency side changes from a fast initial decay followed by a slow decay for the lowest RF amplitude to a more gradual intermediate decay for the higher RF amplitudes. We attribute this additional broadening to the effect of the quadrupole interaction. Note that in general for the measurements of ESR-AFM signals we adapted the RF amplitude such that power broadening was minimized.

As a next step, we measured ESR-AFM spectra for different deuterated pentacene molecules. Figure 4.8b shows the spectra measured for the three deuterated pentacene molecules indicated in the image in the inset. Molecules 2 and 3 show a very similar ESR-AFM signal, both in shape as well as resonance frequency, demonstrating the very high reproducibility of ESR-AFM (for a more detailed discussion of the reproducibility see Section 4.8). In contrast, molecule 1 shows a completely different ESR-AFM signal, which

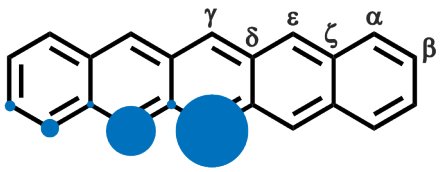

Figure 4.10.: Triplet spin density for pentacene. The spin density of the T_1 state of pentacene is shown at the carbon positions by the blue circles (for the bottom left quarter of the molecule). The diameter of the circles indicates the magnitude of the triplet spin density at the respective carbon positions, as based on data taken from ref. [223]. The carbons are labeled by Greek letters as indicated. At the equivalent carbons the spin density is the same. This figure is based on a figure from ref. [103].

is shifted to higher frequencies and strongly broadened. Comparing the width and shape of this signal to those for different isotopomers of pentacene embedded in p-terphenyl[178], we assign this signal to a pentacene-h-d_{13} molecule, where a proton replaces one of the six deuteriums bound to the inner three benzene rings of pentacene (bound to a γ or ϵ carbon, as defined in Figure 4.10). This comparison assumes that the hyperfine interaction is not significantly different for pentacene on a NaCl surface compared to pentacene embedded in a p-terphenyl matrix; an assumption well justified by the similar linewidths observed for both pentacene-h_{14} and pentacene-d_{14} on NaCl (Figure 4.8a) and in p-terphenyl matrices[103,178].

To understand how a single ^{1}H nucleus can cause such an extensive line broadening, we use Equation (2.25). The leading terms of the hyperfine interaction are proportional to $\left(\sum_i m_i \rho_i A^i_{zz}\right)^2$, assuming that the quantization axis of the nuclear spins is along the z axis. With a single ^{1}H nucleus (H) and thirteen deuteriums (D) this term can be written as

$$\left(\left(\sum_{i=1}^{13} m_{\mathrm{D},i}\rho_{\mathrm{D},i}A^{\mathrm{D}}_{zz}\right) + m_{\mathrm{H}}\rho_{\mathrm{H}}A^{\mathrm{H}}_{zz}\right)^2$$
$$= \left(\sum_{i=1}^{13} m_{\mathrm{D},i}\rho_{\mathrm{D},i}A^{\mathrm{D}}_{zz}\right)^2 + 2\left(\sum_{i=1}^{13} m_{\mathrm{D},i}\rho_{\mathrm{D},i}A^{\mathrm{D}}_{zz}\right)\cdot m_{\mathrm{H}}\rho_{\mathrm{H}}A^{\mathrm{H}}_{zz} + \left(m_{\mathrm{H}}\rho_{\mathrm{H}}A^{\mathrm{H}}_{zz}\right)^2. \quad (4.2)$$

Because the hyperfine interaction enters as a second-order term, the mere presence of one nucleus (here a proton) with strong hyperfine interaction also influences how strongly all the other nuclei (here deuterons) affect the line, thereby changing its overall shape, as expressed by the second term on the right hand side of Equation (4.2). Furthermore, this hyperfine interaction gives rise to a shift of the resonance frequency, as expressed by the last term in Equation (4.2) (although $m_{\mathrm{H}} = 1/2$ or $-1/2$, the $-$ sign drops out due to the square dependence).

The assignment of our ESR-AFM signal to a pentacene molecule where a single proton is bound to a γ or ϵ carbon of pentacene results from the much smaller linewidth observed with ODMR for a proton bound to the α or β carbon[178]. This is a direct consequence of the reduced spin density (ρ_{H}) at these carbons[223], as indicated in Figure 4.10.

In the assignment of zero-field ESR spectra to isotopomers, it is very important to rule out that an increased broadening is simply due to power broadening[178,224] instead of the presence of nuclei with a larger hyperfine coupling. To this end, we measured ESR-AFM spectra for pentacene-h-d_{13} at different RF amplitudes. The results are shown in

Figure 4.9b. Even at the lowest RF amplitude used, where the signal magnitude is significantly reduced, the ESR-AFM signal for pentacene-h-d_{13} is strongly broadened compared to the signals for pentacene-d_{14}. This confirms that the broadening is intrinsic, i.e. caused by the hyperfine interaction, and not induced by power broadening.

As a further demonstration of the combination of single-spin sensitivity and atomic-scale local information, we also locally identified a single pentacene-d_{14} molecule that contains a single ^{13}C nucleus, as shown in Figure 4.8c. Our observed signal matches both in terms of width and shape the signal reported for a pentacene-d_{14} molecule with a ^{13}C replacing one of the two ^{12}C atoms in the γ position[178]. Also in this case, the ESR-AFM signal was measured at different RF amplitudes (not shown, see the bachelor thesis of Sonja Bleher[159]), ruling out that the broadening is simply due to power broadening. Because of the natural abundance of 1.11% ^{13}C (ref. [106]), there is a very small likelihood (2.2%) of encountering a molecule with a ^{13}C in one of these two γ positions. Indeed, we observed only one molecule with a ^{13}C in a γ position out of the total number of 40 measured molecules (see Section 4.8). Note that the hyperfine interaction from a ^{13}C replacing one of the other carbons will be reduced in strength due to the lower spin density[223] (see Figure 4.10). For instance, a detectable broadening of the ESR signal of a pentacene-h_{14} molecule in a p-terphenyl matrix was only reported for a ^{13}C in the γ and ϵ positions[107].

The ESR-AFM spectrum for this pentacene-d_{14} with a single ^{13}C is even broader than the one for the molecule with a single ^{1}H, see Figure 4.8b and c. This is because of the approximately five times larger hyperfine tensor element A_{zz} for ^{13}C than for ^{1}H in case of pentacene[107,177]. At first glance, this seems counterintuitive, since the g-factor for ^{13}C is four times smaller than for ^{1}H (ref. [106]). However, both the Fermi contact and the dipole-dipole coupling term of the hyperfine interaction are observed to be larger for a ^{13}C than for a ^{1}H (bound to this carbon) in case of pentacene (see for a general discussion of these terms Section 2.4.2). The larger dipole-dipole interaction in the z direction arises from the closer distance of the ^{13}C to the π electrons and the different relative alignments of the spins[106]. In particular in case of pentacene, the relative spin alignment leads to an almost vanishing dipole-dipole interaction in the z direction for the ^{1}H nuclear spin, while it is maximized for the ^{13}C nuclear spin[103,106]. The explanation for the larger Fermi contact term is less straightforward. The Fermi contact term for ^{13}C has multiple contributions because of polarization of the electron spins in the C-H and C-C σ bonds and 1s inner shell orbital, which can have opposite signs[106]. In contrast, the Fermi contact term for ^{1}H arises only from the polarization of the electron spin in the C-H σ bond of ^{1}H (ref. [106]). The resulting Fermi contact term for ^{13}C is typically larger than for a ^{1}H bound to this carbon, as is observed for pentacene, although this is not always the case[106]. Thus, the Fermi contact and dipole-dipole coupling terms for ^{13}C are larger than for ^{1}H (bound to this carbon), explaining the broader ESR-AFM spectrum observed for a molecule with a single ^{13}C than the one for a molecule with a single ^{1}H.

The demonstrated ability to distinguish molecules only differing in a single nuclear isotope is provided by the very high energy resolution of ESR-AFM. We define our spectral resolution using the left flank of the signal, since the right flank is dominated by broadening because of the hyperfine interaction. The left flank of the pentacene-d_{14} ESR-AFM signal exhibits a width of 0.12 MHz (FWHM; see Appendix A.1.1), corresponding to less than a nanoelectronvolt in spectral resolution.

Tip	Pentacene-d_{14}	T_X-T_Y transition	T_X-T_Z transition	$V_{\text{read-out}}$
a (metal tip)	1	118.1 MHz	1538.2 MHz	−2.07 V
	2	118.2 MHz	1538.5 MHz	−2.01 V
	3	118.0 MHz	1539.1 MHz	−1.91 V
	4	117.4 MHz	1539.9 MHz	−1.63 V
	5	116.4 MHz	1540.2 MHz	−1.72 V
b (CO tip)	6	116.9 MHz	1540.1 MHz	−1.52 V
	7	116.8 MHz	1540.0 MHz	−1.70 V
	8	118.6 MHz	1539.6 MHz	−1.77 V
	9	117.1 MHz	1540.1 MHz	−1.92 V
	10	117.0 MHz	1539.9 MHz	−1.65 V
	11	116.6 MHz	1540.3 MHz	−2.04 V

Table 4.1.: Molecule-to-molecule variations of the resonance frequencies. List of the T_X-T_Y and T_X-T_Z transition frequencies for 11 different individual molecules including the read-out voltage used for these ESR-AFM measurements, showing small but appreciable molecule-to-molecule variations. For data acquisition, two different tips were used, as indicated, one of which was terminated with a CO molecule. Note that the atomic structure of the tip apex was not altered between the different datasets corresponding to the same tip.

4.8. Reproducibility of the ESR-AFM signals

To demonstrate the reproducibility of ESR-AFM, we repeated the ESR-AFM measurements for many individual pentacene molecules using many different microtips. Specifically, the T_X-T_Z transition was measured for 19 individual pentacene-h_{14} molecules, 20 pentacene-d_{14} (of which one contained a ^{13}C) and 1 pentacene-h-d_{13}; for 18 of these molecules, we also measured the T_X-T_Y transition. In total, 16 different tips were used for these measurements.

We find that the observed ESR-AFM signals for a certain isotopologue are very reproducible both in shape as well as resonance frequency, as is demonstrated in Figure 4.8b and Table 4.1. The measurement technique itself seems thus to not strongly influence the measurements. Even upon chemically changing the tip apex from metallic to terminated by a CO molecule, no strong changes in the observed resonance frequencies are observed, see Table 4.1.

Still, we observe some variations in the resonance frequencies of the measured molecules. We attribute these small differences to variations of the local environment. Note that the voltage applied during the spin manipulations also varies from molecule to molecule. This dwell voltage was always set to $V_{\text{read-out}} + 2.5\,\text{V}$. Variations of up to 0.5 V were observed for the degeneracy point of the neutral and positively charged state, the voltage to which $V_{\text{read-out}}$ was set. Although the T_X-T_Z transition frequency for the metal tip in Table 4.1 seems to reduce with increasing voltages, no clear trends are observed for the T_X-T_Y transition and the transition frequencies measured using the CO tip (see Table 4.1). The change in dwell voltage, attributed to a change in environment, could thus contribute to the observed shifts (see next section), but other effects also seem to play a role. The atomistic environment can, for instance, influence the triplet state density and thereby change the zero-field splitting and thus the ESR transition frequencies.

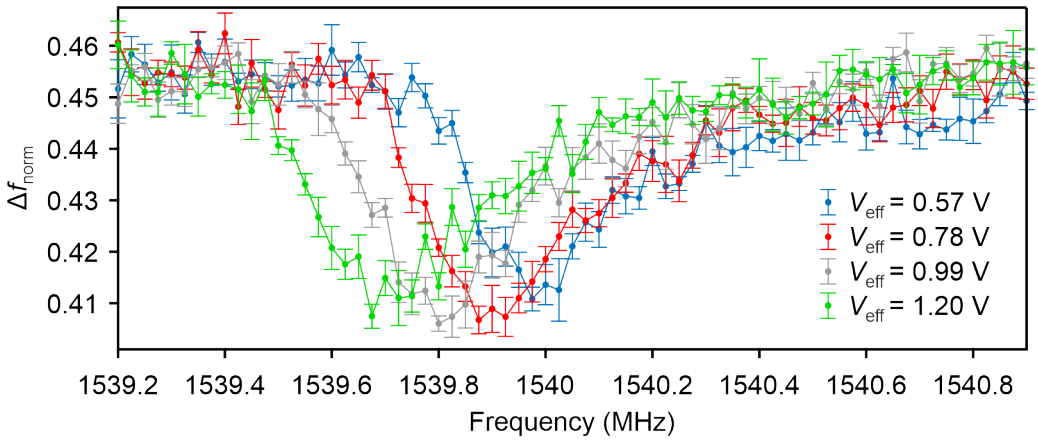

Figure 4.11.: ESR-AFM spectra for different applied electric fields. ESR-AFM spectra measured of the T_X-T_Z transition of a pentacene-d_{14} molecule for four different voltages V_{eff} in the tip-sample junction (error bars are s.d. of six repetitions). A shift of the resonance frequency of the ESR-AFM signals of around −0.4 MHz/V is observed with increasing V_{eff}. The datasets were offset in Δf_{norm} by 0.038 (red), 0.143 (gray) and 0.29 (green) with respect to the blue dataset.

4.9. Effect of the electric field on ESR-AFM

As noted in the previous section, the dwell voltage used might cause shifts in the observed resonance frequency. Varying the dwell voltage means a change in electric field present during the spin manipulations. Shifts of zero-field triplet state ESR signals were reported when an electric field was applied to p-benzoquinone embedded in a 1,4-dibromobenzene host crystal[225]. Therefore, we investigated the influence of the applied electric field on the ESR-AFM signals of pentacene-d_{14} by varying V_{dwell} for single pentacene-d_{14} molecules.

The range in which V_{dwell} can be chosen for the molecule under study can be determined by measuring an excited-state spectrum (see e.g. Figure 3.8a). The lower boundary is given by the voltage required to form the T_1 state, while the upper boundary is determined by the voltage at which the T_1 state can decay via D_0^- into S_0 (see Figure 3.8e, (3B)). Importantly, the electric field in the junction scales with V_{dwell} as $V_{eff} = (V_{dwell} - V_{CPD})\alpha$. Here, V_{CPD} is the voltage of local contact potential difference, which is the constant offset of the gate voltage due to the difference in work function of the tip and sample and can be derived from KPFS (see Section 2.3.3.3). V_{dwell} is further scaled by the lever arm α, since the electric field is proportional to the voltage dropping in the vacuum between the tip and the molecule (see Figure 2.8b). For the data reported in this section, V_{CPD} was determined for the used microtip above the measured molecule and α was set to a reasonable estimate of 0.70 (see Table 3.1) (α can in principle be derived from a full excited-state spectroscopy dataset (see Section 3.7), however, such datasets were not measured for the molecules under investigation in this section).

The ESR-AFM spectra of the T_X-T_Z transition of pentacene-d_{14} measured for four different electric field strengths are shown in Figure 4.11a. The spectra show that the ESR-AFM resonance frequency shifts to lower frequencies with increasing V_{eff} by approximately −0.4 MHz/V. For two different microtips and pentacene-d_{14} molecules, we observe similar shifts on the order of −0.4 and −0.6 MHz/V. The difference in the observed shifts is attributed to different tip geometries, such that for the same V_{eff}, a different electric field is

present in the tip-sample junction (the tip-sample junction acts like a capacitor and can be roughly modeled as a plate capacitor[58,93], the latter is justified by the tip curvature being typically very large compared to the size of a molecule). Using a plate capacitor model, we can roughly estimate the size of the electric field present in the tip-sample junction: $E = V_{\text{eff}}/d$, which gives an electric field on the order of 1 GV/m for a V_{eff} of around 1 V and a tip-sample distance d of around 9 Å. More details about the dependence of the resonance frequency on the applied voltage can be found in the bachelor thesis of Stefan Brinster[163].

Note further that the spin manipulations occur over multiple cantilever periods. Thus, the tip-sample distance and, therefore, the electric field in the tip-sample junction varies during the spin manipulations. The resulting ESR-AFM signal is a weighted average of the ESR-AFM signals sampled at the different electric field strengths present during a cantilever period. We thus expect a finite broadening of the ESR-AFM signal due to this mechanism. However, this effect is expected to be small, because of the relatively small shifts observed with varying electric field. As a rough estimate, assuming a change in electric field of approximately 10% (the cantilever oscillates over approximately 10% of the tip-sample height), a V_{eff} of 1 V and a shift of −0.5 MHz/V, an additional broadening on the order of 25 kHz is expected. Since we found a width of the left flank of the ESR-AFM signals of pentacene-d_{14} of around 120 kHz (if power broadening was minimized), the width is likely dominated by the finite lifetimes of the states and hardly broadened by the fluctuating electric field. Indeed, no appreciable broadening is observed upon increasing the electric field, see Figure 4.11.

4.10. Applicability of ESR-AFM

So far, we demonstrated ESR-AFM by applying it on single pentacene molecules. The applicability of ESR-AFM is certainly not restricted to pentacene, as demonstrated in this section.

To be suitable for ESR-AFM, three requirements need to be met. First, the molecule needs to be stably adsorbed onto an insulating film (here NaCl), both in its neutral as well as in its cationic charge state and under the application of a few volts voltage pulses. This means that the molecule should not change its adsorption site, adsorption geometry or conformation in the time during which the ESR-AFM spectra are measured (the charged and neutral molecule can have a difference in adsorption site, adsorption geometry[227] or conformation[228], as long as the molecule in a certain charge state does not change its adsorption site, adsorption geometry or conformation). Such changes were, for instance, observed for acridine, phenazine and acridine orange (see for more details the bachelor thesis of Jakob Eckrich[162]). The second requirement is that at least two of the three triplet substates should have sufficiently different lifetimes. To be more quantitative, the decay constants of the connected states should differ by approximately (at least) a factor 2. This factor depends on the RF power used (here assumed to be large such that the signal is saturated), on the T_1 state population at $t_D = 0$ (here assumed to be 0.8) and on the detection limit, which is estimated to be around 1% of the total population. The third requirement for ESR-AFM is that the fundamental gap of the molecule needs to be larger than twice the S_0-T_1 energy difference (see Figure 4.12). Otherwise, the molecule can decay to the D_0^- state via a tunneling event, as is shown in Figure 4.12a. At the used tip-sample

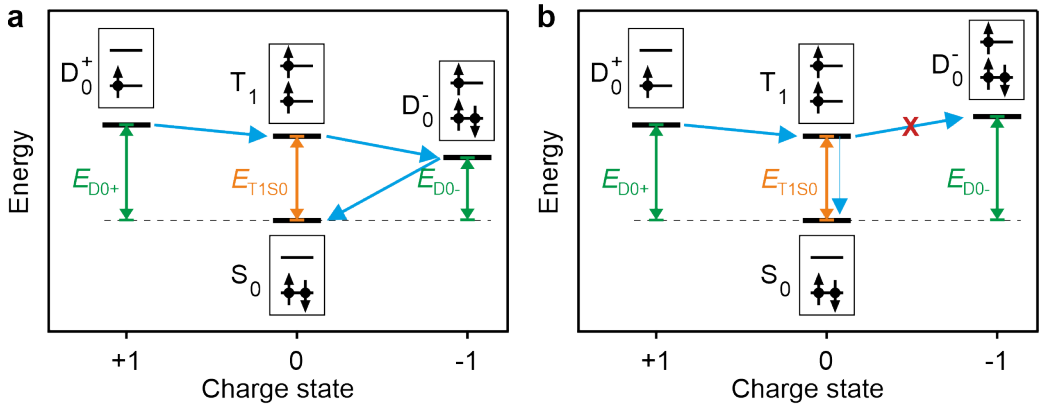

Figure 4.12.: Energy level alignment requirement for ESR-AFM. One condition for ESR-AFM is that during the dwell time both D_0^+ and D_0^- must be higher in energy than the T_1 state (D_0^+ is necessarily higher than T_1 at the used gate voltage to be able to form T_1; D_0^- should also be higher than T_1 to prevent a decay of T_1 into D_0^- (here we neglect for simplicity the relaxation energies)). **a**, Many-body energy diagram showing an example of a hypothetical molecule for which the energetic alignment of the states is such that an ESR-AFM spectrum cannot be measured. In this case, the fundamental gap[226] ($E_{D0+} + E_{D0-}$) is smaller than twice the T_1-S_0 energy difference (E_{T1S0}). The fundamental gap is given by $E_{D0+} + E_{D0-}$ (green arrows): at a bias voltage where the D_0^+ state is lower in energy than S_0, an electron can be tunneled out of the HOMO, while at a bias voltage where D_0^- is lower in energy than S_0 an electron can tunnel into the LUMO (note that although E_{D0+} and E_{D0-} depend on the bias voltage, $E_{D0+} + E_{D0-}$ stays constant). Because of this energetic allignment, the T_1 state can decay via the D_0^- state into the S_0 state during the dwell time. **b**, An example in which $E_{D0+} + E_{D0-} > 2E_{T1S0}$ and thus ESR-AFM can be performed. If the fundamental gap is larger than twice the T_1-S_0 energy difference, the T_1 state cannot decay via tunneling events back to the S_0 state. Note that for simplicity the relaxation energies are not drawn in this figure; if the relaxation energies are assumed to be equal for the different transitions, the same requirement for ESR-AFM results (fundamental gap > twice T_1-S_0 energy difference).

distance, this tunneling process is much faster than the triplet decay, and the same for the three triplet substates (since no magnetic tip is used). In other words, the lifetime of the three triplet substates will be the same, such that according to the second requirement, the ESR-AFM signal will not be detectable. It was found that this requirement is, for instance, not met for p-sexiphenyl.

Perylenetetracarboxylic dianhydride (PTCDA) is one of the molecules that fulfills all three requirements. It stably adsorbs on NaCl (ref. [137, 229]), and its fundamental gap is 2.5 times the T_1-S_0 energy difference, as derived from the excited-state spectroscopy measurements presented in Section 3.10 (see Table 3.3). Furthermore, the lifetimes of the three triplet substates were determined by us as (350 ± 43) µs, (170 ± 13) µs and (671 ± 62) µs, see Figure 3.24 (error bars on the lifetimes are derived from the s.d. of three measurements).

The pulse sequence presented in Figure 4.3 works in general for any molecule fulfilling the requirements for ESR-AFM, provided that the parameters of the pulses are adapted according to the molecular properties. Specifically, next to the $V_{\text{read-out}}$, which differs for every molecule because of its individual environment, V_{dwell} and t_D should be determined. The dwell voltage should be chosen high enough such that the T_1 state can be accessed, but low enough to prevent the decay of the T_1 state by a tunneling event (forming D_0^-,

see Figure 3.8e, (3B)). According to the excited-state spectroscopy data (Figure 3.20a), a V_{dwell} set to $V_{\text{read-out}}$ + 2.35 V fulfills these requirements. t_{D} can be determined from the T_1 lifetimes, and depends on the transition being probed. The largest ESR-AFM signal is expected for the two substates differing most in their lifetimes, in case of PTCDA: (170 ± 13) µs and (671 ± 62) µs. The optimal t_{D} can be theoretically derived by comparing the triple-exponential decay with a decay where the two coupled substates decay with an uniform decay rate (the average of the two rates). This results in a t_{D} of 501 µs for coupling the shortest- and longest-lived substates of PTCDA.

Using these pulse parameters, the RF frequency was swept over a large frequency range. One of such measurements is shown in Figure 4.13b. Around a frequency of 1252 MHz, a clear reduction in Δf_{norm} is observed. In comparison, a pentacene-d_{14} molecule on the same island (Figure 4.13a) shows a reduction around 1540 MHz. Figure 4.13c shows a spectral zoom-in around 1252 MHz, which shows that there is an asymmetric ESR-AFM signal at this frequency. Analogously to pentacene, the hyperfine interaction of the eight proton nuclear spins in PTCDA gives rise to its asymmetric lineshape. Note that the flank with the larger width appears here at the low-frequency side. Such a lineshape is expected for a T_Y-T_Z signal[103], as becomes clear from Figure 2.12b (when considering the T_Y-T_Z transition instead of the T_X-T_Z transition that is explicitly illustrated).

The magnitude of the T_Y-T_Z ESR-AFM signal indicates that the T_Y and T_Z substates are the shortest- and longest-lived substates. Assuming that the change in triplet population is similar to the observed change in Δf_{norm}, a drop of signal of approximately 0.06 is found. Assuming an initial triplet population of 90% (see Figures 3.20 and 3.24), the triplet lifetimes of PTCDA as derived above and a t_{D} of 501 µs, signal magnitudes of 0.01, 0.02 and 0.06 are expected, where the 0.06 is between the substates with the shortest and longest lifetime. We attribute the observed signal, thus, to the shortest- and longest-lived substates. The longest-lived substate is assigned to the T_Z substate, as it is typically found to have the longest lifetime[211], such that the lifetimes of PTCDA can be assigned as: $\tau_X = (350 \pm 43)$ µs, $\tau_Y = (170 \pm 13)$ µs and $\tau_Z = (671 \pm 62)$ µs.

Next to the T_Y-T_Z transition, also the T_X-T_Z and T_X-T_Y transitions of PTCDA can be observed. The T_X-T_Z transition is - per definition[104] - at higher resonance frequencies (see Section 2.4.1). Given the above-mentioned τ_X and τ_Z, a t_{D} of 801.6 µs was chosen for a sensitive detection of the T_X-T_Z transition. Sweeping the RF frequency at this t_{D} resulted in the ESR-AFM signal at 1501 MHz shown in Figure 4.13d. The flank with the larger width appears here at the high-frequency side, as expected for the T_X-T_Z transition (see Figure 2.12). Similarly, a small signal was detected for the T_X-T_Y transition at 252 MHz at a t_{D} of 501 µs (not shown, see the bachelor thesis of Jakob Eckrich[162]). The smaller signals observed for these two transitions compared to the T_Y-T_Z transition reflect the smaller ratio of the lifetimes of the involved substates.

The width of the asymmetric shoulder of the T_X-T_Z signal of PTCDA was found to be approximately three times smaller than the one for the T_X-T_Z signal of pentacene-h_{14} (from fitting the signals shown in Figure 4.13d and Figure 4.6a, respectively, as explained in Appendix A.1.1). The difference in energy splitting of the T_X-T_Y transition contributes to this difference in observed width; the dominating contribution to the asymmetric broadening is inversely proportional to the energy splitting of T_X-T_Y (see Equation (2.25)). With only this contribution, the width of the ESR-AFM signal of PTCDA is expected to be slightly more than a factor of two smaller than for pentacene-h_{14}. An intuitive explanation of the

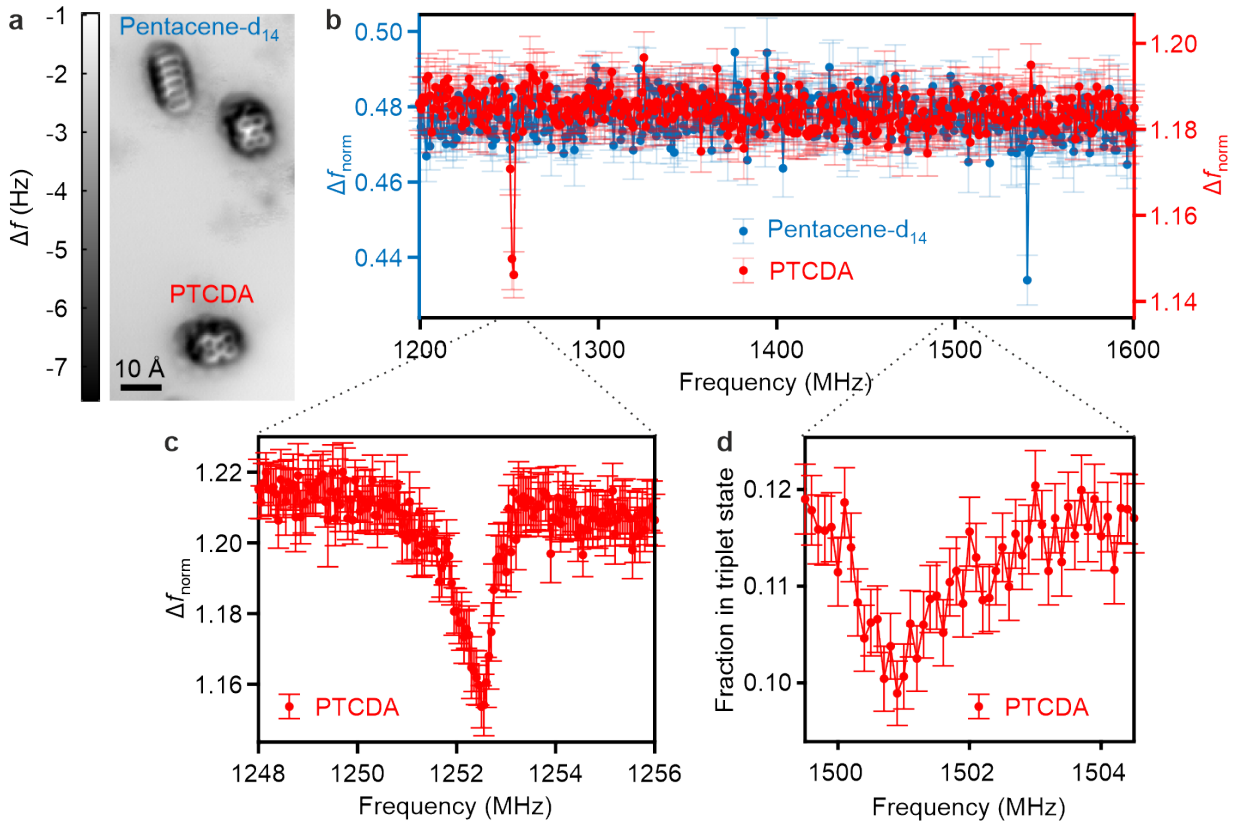

Figure 4.13.: ESR-AFM spectra of PTCDA. a, Constant-height AFM image atomically resolving two PTCDA and a pentacene molecule, measured with a CO-functionalized tip (z-offset $\Delta z = -3.1\,\text{Å}$ with respect to the setpoint: $\Delta f = -1.05\,\text{Hz}$ at $V = 0\,\text{V}$, oscillation amplitude $A = 0.55\,\text{Å}$). The two molecules, above which the spectra were taken, are labelled with pentacene-d_{14} and PTCDA. The weaker features seen around the molecules are due to tip imperfections. **b**, ESR-AFM spectra of pentacene-d_{14} and PTCDA over a broad frequency range. Each molecule shows a sharp line at a characteristic frequency corresponding to its intrinsic zero-field splitting. Note that, for PTCDA, there is a very small signal at 1501 MHz (see **d**) that is too small to be observed at the parameters used for the spectrum shown in **b**. The molecules were measured under identical parameters (error bars are s.d. of twelve repetitions for PTCDA and seven repetitions for pentacene-d_{14}), except for the read-out voltage (which is specific to the molecule) and the dwell pulse parameters: $V_{\text{dwell}} = V_{\text{read-out}} + 2.50\,\text{V}$, $t_{\text{D}} = 100.2\,\mu\text{s}$, $V_{\text{read-out}} = -1.907\,\text{V}$ for pentacene-d_{14}, $V_{\text{dwell}} = V_{\text{read-out}} + 2.35\,\text{V}$, $t_{\text{D}} = 501\,\mu\text{s}$, $V_{\text{read-out}} = -3.19\,\text{V}$ for PTCDA. **c**, Spectral zoom-in of the feature around 1250 MHz of the PTCDA molecule, revealing its asymmetric lineshape (error bars are s.d. of eight repetitions). Note that the flank with the larger width appears here at the low-frequency side, indicative of the T_Y-T_Z transition. **d**, ESR-AFM spectrum of the T_X-T_Z transition of PTCDA, measured using a repetition rate of the pump-probe pulse sequence of eight per s. The dwell time was set to be 801.6 µs.

larger observed reduction in width is the lower number of contributing protons (8 instead of 14). However, the spin density at the carbon to which these protons are bound should also be taken into account (see Section 2.4.2 and Equation (2.25)); a lower spin density at these carbons in case of PTCDA compared to pentacene would also explain the observed reduction in linewidth.

4.11. Coherent spin manipulations

If instead of the RF frequency, the RF pulse length is swept, Rabi oscillations can be measured[173,230]. In general, Rabi oscillations are the oscillations of population between two energy levels driven by an oscillatory driving field. The frequency of the driving field, in our case the frequency of the RF field, should be chosen resonant with the transition between the two states, in our case two spin substates. If a population difference between the two substates exists, this population difference can be coherently driven from the most populated substate to the other and back. In case of ESR-AFM, the three triplet substates are initially populated equally, since the probability to tunnel in the three substates is equal (same spatial distribution and tunneling barrier, as their energy differences are negligibly small). After initialization with equal populations, a population difference will naturally develop over time, since the triplet substates have different decay times. The RF pulse can then drive this population difference between two of the triplet substates. To be able to differentiate how this population difference is divided over the two triplet substrates at the end of the RF pulse, the triplet substates are again let to decay independently during the rest of the dwell voltage pulse. This allows to distinguish the population in the longer and shorter-lived triplet states. There exists thus an optimal delay time t_S between the start of the dwell voltage pulse (when the triplet is formed) and the start of the RF pulse.

To experimentally determine the optimal delay time to measure Rabi oscillations of the T_X-T_Z transition of pentacene, the timing of a π RF pulse resonant with this transition was swept over the range of the dwell pulse, as shown in Figure 4.14. A π RF pulse drives the population difference of the T_X and T_Z substates from the (more populated) T_Z to the (less populated) T_X substate. Figure 4.14 shows that if $t_S = 0$ (meaning the pulse starts at the start of the dwell pulse), the observed Δf_{norm} is within uncertainty margins equal to the measurement without RF pulse, confirming the expectation that these two triplet substates are initially equally populated in our experiment. For larger t_S, the triplet substates will decay during t_S with their corresponding decay times, building up a population difference between the T_X and the T_Z substate. The π pulse subsequently transfers this population difference from T_Z to T_X, after which it decays with the fast decay constant of T_X during the rest of the dwell pulse, reducing the fraction in the triplet state and thus Δf_{norm}. If the RF pulse gets close to the end of the dwell pulse, Δf_{norm} increases again because the remaining time in the triplet state is too short for the population in the T_X substate to decay.

The optimal delay time for the Rabi oscillations is, therefore, shortly before the middle of the dwell voltage pulse, such that the initial population difference is maximized, while simultaneously after the end of the RF pulse still enough time is left to differentiate between the T_X and T_Z substates. Furthermore, it is important that, on increasing the duration of the RF pulse, the sensitivity for differentiating T_X and T_Z does not greatly reduce,

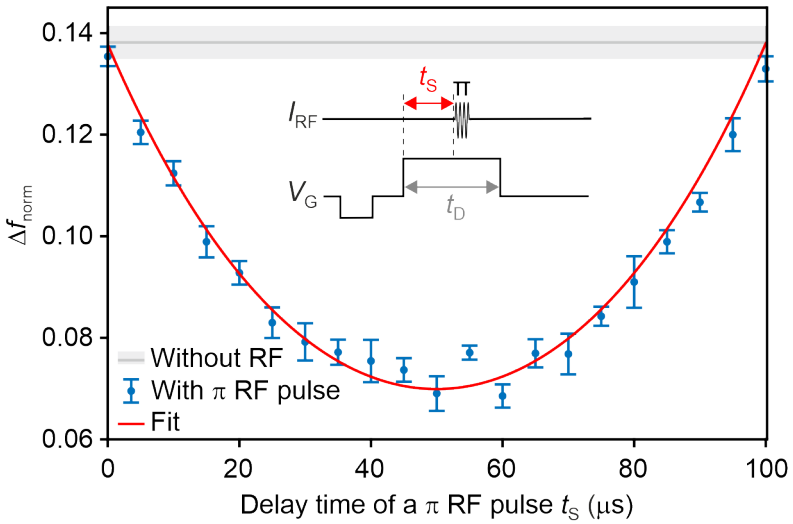

Figure 4.14.: The effect of the delay time of a π RF pulse. A π RF pulse (duration: 0.29 µs, determined from the measured Rabi oscillations on the same pentacene-d_{14} molecule, as shown in Figure 4.16c) resonant with the T_X-T_Z transition is applied after a variable delay time (t_S) with respect to the start of the dwell voltage pulse (duration: t_D = 100.2 µs), see inset for the used pump-probe scheme. This π RF pulse drives the population difference of the T_X and T_Z substates from the (more populated) T_Z to the (less populated) T_X substate, after which this population can decay with the fast decay rate of the T_X substate. At short delay times, only a small signal (difference between with RF and without RF) is observed, due to the equal initial population of the three triplet substates. The population difference increases with delay time, initially increasing the detected signal. In case of long delay times, the signal reduces again (Δf_{norm} rises), because the remaining time during the dwell voltage pulse becomes too short for the additional T_X population to decay. Error bars are s.d. of six repetitions.

otherwise a decay of the observed Rabi oscillations is induced by the readout. This is easiest to understand from an example: suppose we would like to measure the T_X-T_Z Rabi oscillations for a pentacene-d_{14} molecule using a pump-probe sequence with a dwell time of 100.2 µs and a delay time t_S of either 40 or 60 µs. The initial population difference will be slightly larger for t_S = 60 than 40 µs, while the sensitivity for read-out of the population difference after an RF pulse with a duration of a few µs would be slightly larger for t_S = 40 than 60 µs. Thus, the amplitude of the observed Rabi oscillations will be similar for both cases (which is in agreement with the observation that a π RF pulse at t_S = 40 or 60 µs gives a similarly large signal, see Figure 4.14). However, if a long RF pulse is used, e.g. 30 µs, the observed Rabi oscillation signal would be much smaller for t_S = 60 µs than 40 µs, since the time to differentiate the T_X and T_Z population at the end of the pulse is too short for t_S = 60 µs (only 10 µs). This is also apparent from the data in Figure 4.14, where the π RF pulse results in a much smaller signal (larger Δf_{norm}) when the time after the RF pulse is only 10 µs, compared to the case where this time is 30 µs.

To this end, a delay time of t_S = 45.1 µs was chosen for the measurements of the Rabi oscillations of pentacene. After this time, the longest-lived T_Z substate is predominantly populated. Subsequently, an RF pulse of variable duration (t_{RF} = 0 to 7 µs) at resonance with the T_X-T_Z transition was applied, driving the population to oscillate between T_Z and T_X. During the remaining roughly 50 µs of a fixed total t_D = 100.2 µs, the triplet substates again decayed independently from each other, such that - after each pulse sequence - pre-

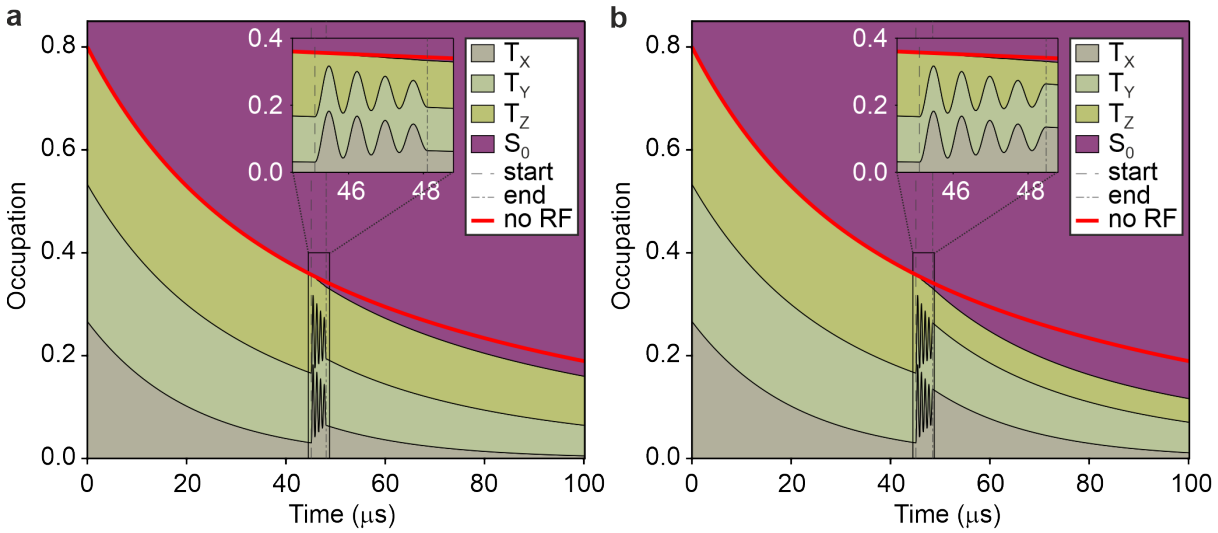

Figure 4.15.: Maxwell-Bloch simulations of two data points of the Rabi oscillations. The populations of the three triplet substates and the S_0 state during the dwell voltage pulse ($t_D = 100.2\,\mu s$) are shown. The simulation parameters were chosen similar to those of the measured Rabi oscillations for pentacene-h_{14} (see Figure 4.16a). At time zero, the beginning of the dwell voltage pulse, it is assumed that the three triplet substates are equally populated; their population summing to 80% of the total population (see Figure 3.8). During the dwell time, the three triplet substates decay with $\tau_X = 21\,\mu s$, $\tau_Y = 67\,\mu s$ and $\tau_Z = 136\,\mu s$ back to S_0. At the starting time t_S, an RF pulse is turned on with a frequency matching the T_X-T_Z energy splitting. This RF pulse causes coherent oscillations between these two triplet substates, as clearly visible in the inset. The populations in the T_X and T_Z substates at the end of the RF pulse depend, thus, on the duration of the RF pulse. The larger the population in the fastest-decaying T_X substate, the lower the triplet population at the end of the dwell pulse. This is exemplified by the simulations shown in **a** and **b** with RF pulse durations corresponding to 4 and 4.5 Rabi oscillation periods, respectively (Rabi frequency: 1.33 MHz, decay constant of the oscillations: 2.2 µs).

dominantly the T_Z population remained and was detected. This is visualized in Figure 4.15 by Maxwell-Bloch simulations (see Appendix A.1.2) for two different durations of the RF pulse.

The measured Rabi oscillations are shown in Figure 4.16. Multiple oscillations of the population between T_Z and T_X can be observed, spanning a timescale of multiple microseconds. The data can be fitted with an exponentially decaying sinusoidal on top of a decaying baseline. The decay of the baseline arises from the decay of the T_X and T_Z substates into the S_0 state during the RF pulse, as discussed in more detail in Appendix A.1.3. Other effects (for example, RF-induced heating) may also add to the temporal evolution of the baseline. These contributions were not separately accounted for but they were fitted as part of the decay of the baseline.

A decay constant of the oscillation amplitude of $(2.2 \pm 0.3)\,\mu s$ was extracted from the fit in Figure 4.16a (error bar 95% CI on the fit). Our results can be compared with those obtained with ODMR for a single pentacene molecule embedded in a p-terphenyl matrix, where a decay constant of 5 µs was obtained[173]. They attributed their decay to fluctuations of the nuclear spin configuration for every measurement cycle, which gives rise to the peculiar lineshape reflecting all different nuclear spin configurations (as explained in

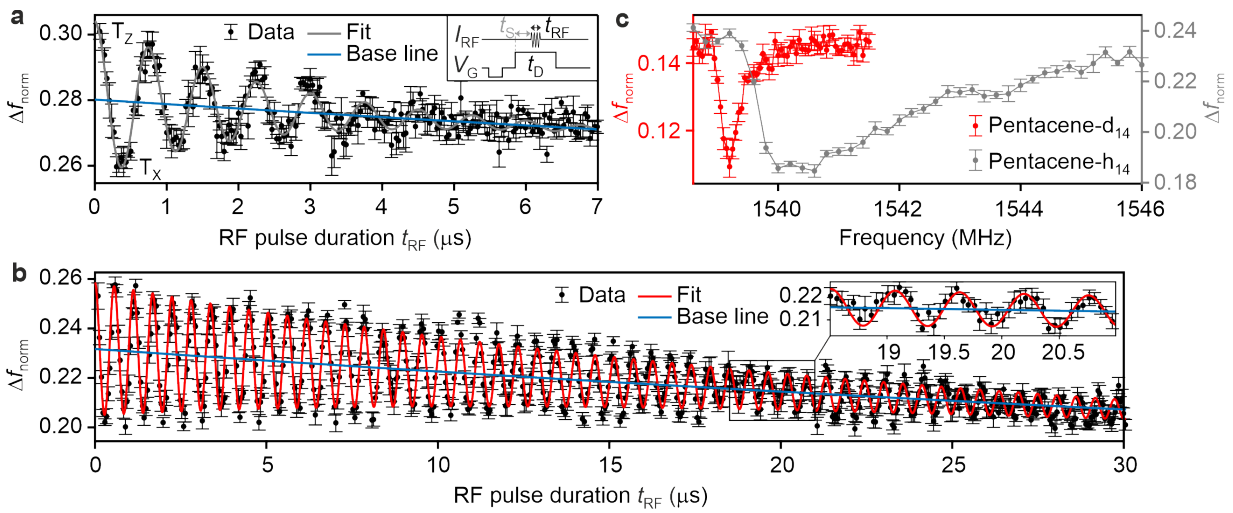

Figure 4.16.: Rabi oscillations of a protonated and perdeuterated pentacene molecule. **a**, Rabi oscillations from driving the T_X-T_Z transition ($f_{RF} = 1540.5\,\text{MHz}$) showing coherent spin manipulation. The pump-probe pulse scheme is shown in the inset ($t_D = 100.2\,\mu\text{s}$, $t_S = 45.1\,\mu\text{s}$, t_{RF} variable) and described in Section 4.11 (error bars are s.d. of four repetitions). The predominant contribution to T_1 is T_Z at $t_{RF} = 0$, then starting to oscillate toward a predominant contribution of T_X and back, as indicated for the first oscillation. A fit (gray line) yields a decay constant of the Rabi oscillations of $(2.2 \pm 0.3)\,\mu\text{s}$ (see Appendix A.1.3 for details on the fit of the baseline (blue line)). **b**, The Rabi oscillations of pentacene-d_{14} have a longer decay time of $(16 \pm 4)\,\mu\text{s}$. The pump-probe pulse scheme was the same as that used for **a** (error bars are s.d. of eight repetitions) but with $t_S = 30\,\mu\text{s}$. **c**, For reference the ESR-AFM spectrum of pentacene-d_{14} (red) and pentacene-h_{14} (gray) are shown. This subfigure displays the same data as Figure 4.8a.

Section 2.4.2). The measured oscillations represent thus an average over finding the single pentacene molecule in different nuclear spin configurations and, consequently, of a resonance frequency differing for every individual measurement cycle. Since the Rabi frequency depends on the resonance frequency with respect to the fixed driving frequency[195], the Rabi frequency will also differ for every measurement cycle. Hence, they attributed the decay of their Rabi oscillations solely to the dephasing from the fluctuating Rabi frequency[231]. Similarly, we expect our observed decay to be dominated by this effect.

Interestingly, the decay constant we observe is two times lower than the one measured with ODMR[170]. In contrast, our observed ESR-AFM linewidth (FWHM 2.7 MHz (sum of the FWHM of the asymmetric shoulder and the Lorentzian broadening, see Appendix A.1.1)) is quite similar to what was reported with ODMR (FWHM 3.7 MHz (ref. [103])) (Note that the RF power induced broadening (see Figure 4.9) is likely slightly different for both cases due to the likely different RF powers used). Therefore, at first glance more similar decay constants would be expected. However, the RF power and thus Rabi frequency is different for the ODMR measurements compared to our measurements: a Rabi frequency of 4.6 MHz compared to 1.3 MHz, respectively. A fast driving of the spins at their resonance frequency can indeed enhance the coherence time[232], as discussed in Section 4.11.2. It is, therefore, likely that a large part of the difference in coherence time is due to the difference in Rabi frequencies.

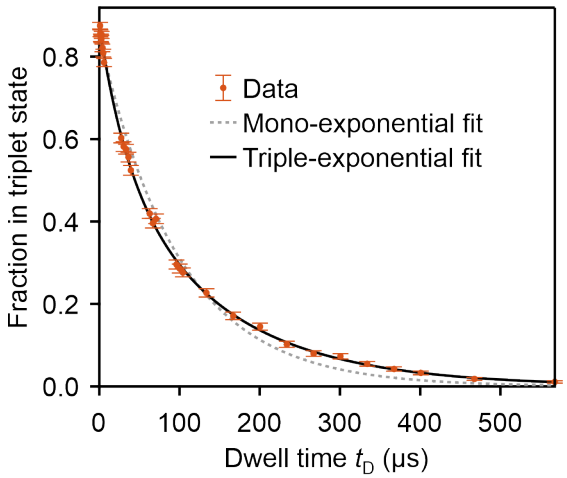

Figure 4.17.: Triplet decay of pentacene-d_{14}. Decay of the T_1 state of pentacene-d_{14}. The data can be well-fitted with a triple-exponential decay (solid line). Each data point corresponds to 1920 pump-probe cycles and the error bars were derived from the s.d. of the binomial distribution[21]; see Section 3.3.3.

4.11.1. Rabi oscillations on pentacene-d_{14}

The explanation of the decay of the Rabi oscillation amplitude due to the hyperfine coupling to the nuclear spins inside the molecule mentioned in the previous section can be tested by measuring Rabi oscillations for a molecule with a reduced hyperfine interaction (see Section 4.7, Figure 4.16c), such as pentacene-d_{14}. The Rabi oscillations on pentacene-d_{14} are shown in Figure 4.16b and exhibit a much longer decay time of (16 ± 4) µs. This shows that, in the experiments on protonated pentacene, the coherence was indeed limited by the molecule itself and not by the detection method.

In the study of excited triplet states, there is a limit on the attainable coherence time due to the lifetimes of the involved triplet substates. To be more exact, during the RF pulse the population difference between the triplet substates decays with the average decay rate of the two involved triplet substates. The triplet state decay of pentacene-d_{14} is shown in Figure 4.17. The decay times found from three measurements are $\tau_X = (33.6 \pm 0.8)$ µs, $\tau_Y = (118 \pm 8)$ µs and $\tau_Z = (158 \pm 9)$ µs.

Note that this decay of the T_1 state is slower than the decay for pentacene-h_{14} (from ref. [21]: $\tau_X = (11 \pm 5)$ µs, $\tau_X = (75 \pm 12)$ µs, $\tau_X = (135 \pm 11)$ µs). Similarly, an increase of the triplet lifetimes was found for pentacene-d_{14} compared to pentacene-h_{14} embedded in p-terphenyl matrices[216,233]. Since the radiative decay rate was found to be independent of deuteration, it was concluded that the non-radiative decay rate was increased[216,233]. This non-radiative decay caused by spin-orbit coupling depends apart from the electronic also on the nuclear wavefunction overlap between the ground state of T_1 and vibrationally excited states of S_0 with similar energies as the T_1 ground state[233–235]. This Franck-Condon overlap factor is expected to be smaller for the deuterated molecule, since the vibrational quanta of C-D modes are smaller than that of C-H modes[233,235]. Thus, the non-radiative decay constant and therefore the lifetime of the T_1 state is expected to be longer for deuterated pentacene, as we also observe here.

From the pentacene-d_{14} decay constants, the decay constant of the T_X-T_Z coherence due to the finite lifetimes can be derived as (28 ± 1) µs. This is slower than the observed decay of the coherences ((16 ± 4) µs). Thus, other mechanisms are dominating the decay. The decay of the Rabi oscillations of pentacene-d_{14} can be (partly) due to the same mechanism as the decay for pentacene-h_{14}: dephasing due to the fluctuating Rabi frequency by the fluctuating nuclear spin configurations. Since the linewidth of the pentacene-d_{14} ESR-AFM signal is much smaller than the one of pentacene-h_{14} (see Figure 4.16b), the dephasing due to this effect is expected on a slower timescale. It is challenging to make more quantitative predictions about the decay of the Rabi oscillations of pentacene-d_{14} and pentacene-h_{14} from the existing data, since the Rabi oscillations for these two molecules have a different Rabi frequency and the decay of the Rabi oscillations is also dependent on the Rabi frequency (see next section). Instead, we could compare the Rabi oscillations measured for pentacene-d_{14} molecules (Figure 4.21c) with those measured for a pentacene-h-d_{13} molecule (Rabi oscillations not shown). The observed decay constant for pentacene-h-d_{13} is approximately three times smaller than those of pentacene-d_{14} molecules, while the Rabi frequencies are very similar. Interestingly, the line widths of the ESR-AFM signals for these different isotopologues also differ by approximately a factor of 3 (see Figure 4.8b). This observation indicates that the coherence time for deuterated pentacene is likely still limited by the smaller but nonzero interaction with the nuclear spins and the resulting fluctuating Rabi frequency.

The observed decay could also have other origins, due to the different interactions the electron spins can have with their environment. Importantly, such interactions do not all necessarily lead to additional decoherence. Next to the interaction, a fluctuation of this interaction from pump-probe cycle to pump-probe cycle or on the timescale of the measured Rabi oscillations (tens of µs) is required. Note that fluctuations on both of these timescales can lead to a decay of the Rabi oscillations, while only the latter would contribute to the decay measured via a spin echo, see e.g. ref. [236] for more details.

A second expected decoherence source of the Rabi oscillations measured via ESR-AFM is due to the flip flops of the nuclear spins in the environment, which couple through the hyperfine interaction with the electron spins[231,236,237]. In case of molecules embedded in a matrix, it was found that the hyperfine coupling to the proton spins of the neigboring molecules causes a substantial dephasing. This was confirmed by the increased coherence time found upon deuteration of the host matrix[237,238]. In contrast to these measurements performed in host matrices, we typically studied molecules for which no other molecules were lying close-by (further away than 30 Å), such that the hyperfine coupling to nuclear spins in neighboring molecules is typically negligibly small. Instead the electron spins could be dephased by coupling to the nuclei of the NaCl film, which all have a spin quantum number of 3/2 (^{23}Na (100% natural abundance), ^{35}Cl (76% natural abundance) and ^{37}Cl (24% natural abundance))[106].

We believe that ESR-AFM can give access to such interactions of the electron spins with the environment. To this end, it is important to rule out dephasing induced by the intramolecular hyperfine interaction. This can be achieved by choosing a molecule with an even further reduced hyperfine interaction, preferably a molecule without any nuclear spins. Furthermore, decoherence due to the ESR-AFM measurement technique itself should be ruled out. For instance, in case of ESR-STM, the technique itself gives rise to a strong decoherence, limiting the coherence times (typically on the 100 ns timescale[198,204,239]). As

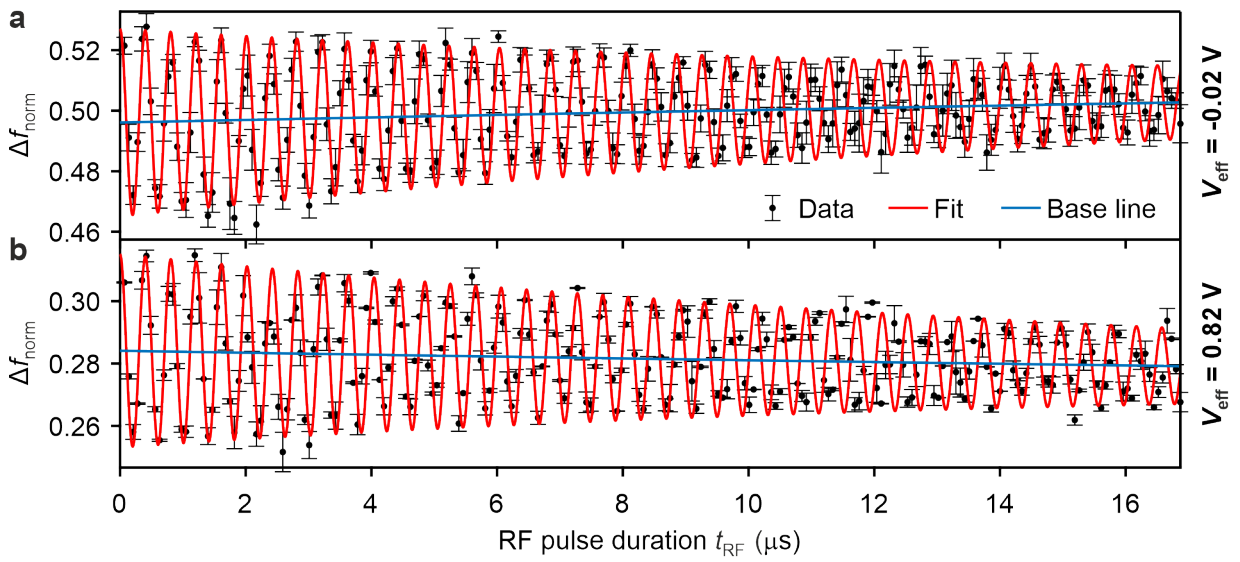

Figure 4.18.: Rabi oscillations for different applied electric fields. a, **b**, Rabi oscillations of the T_X-T_Z transition of one pentacene-d_{14} molecule for two different voltages V_{eff} in the tip-sample junction (error bars are s.d. of two repetitions for **a** and six repetitions for **b**, averaging for every repetition 30 s over $\langle \Delta f \rangle$ instead of 20 s (see Section 4.4)). A cantilever oscillation amplitude of 1 Å (2 Å peak to peak) was used. A delay time of $t_S = 50\,\mu s$ was chosen, such that the Rabi oscillations start at the top turnaround point and end for the longest RF pulse durations at the bottom turnaround point. For this molecule and microtip, a shift of the resonance frequency due to the electric field of −0.4 MHz/V was observed. Because of the varying phase of the oscillations, the data could not be adequately fitted by an exponentially decaying sinusoidal of fixed frequency. Since only the decay of the envelope function of the oscillations is relevant for the determination of the coherence time, the Rabi oscillations were fit manually to reproduce the decaying envelope function. This resulted in a decay constant of $(18 \pm 4)\,\mu s$ for both datasets.

discussed in the introduction (Section 4.1), decoherence due to tunneling electrons, scattering electrons from the surface and a varying stray magnetic field are present in ESR-STM. These decoherence sources are eliminated for ESR-AFM. Although scattering with conduction electrons in the tip remains possible, decoherence owing to the latter is expected to be small because of the weak tunnel coupling.

To further confirm that the ESR-AFM technique itself is minimally invasive (on the timescale of tens of µs), we studied the effect of the measurement technique on the coherence times of pentacene-d_{14}. First, we investigated the effect of the electric field present in the tip-sample junction, which shifts the resonance frequency of the ESR-AFM signals (see Section 4.9). Since this electric field will vary during a cantilever oscillation period (the tip-sample junction can be described as a capacitor, and the tip-sample distance is varying), the effect of this varying electric field on the Rabi oscillations was studied. To this end, Rabi oscillations were measured for a pentacene-d_{14} molecule for two different electric field strengths, by using two different dwell voltages. The resulting oscillations are shown in Figure 4.18 and show no appreciable difference in their coherence times ($(18 \pm 4)\,\mu s$).

The influence of the oscillating tip was in addition tested by measuring Rabi oscillations for different tip heights and cantilever oscillation amplitudes. The results are shown in Figure 4.19. Very similar fitting parameters were obtained for these three datasets with decay constants of 10.6 µs (a), 10.9 µs (b) and 11.1 µs (c), equal within uncertainty margins

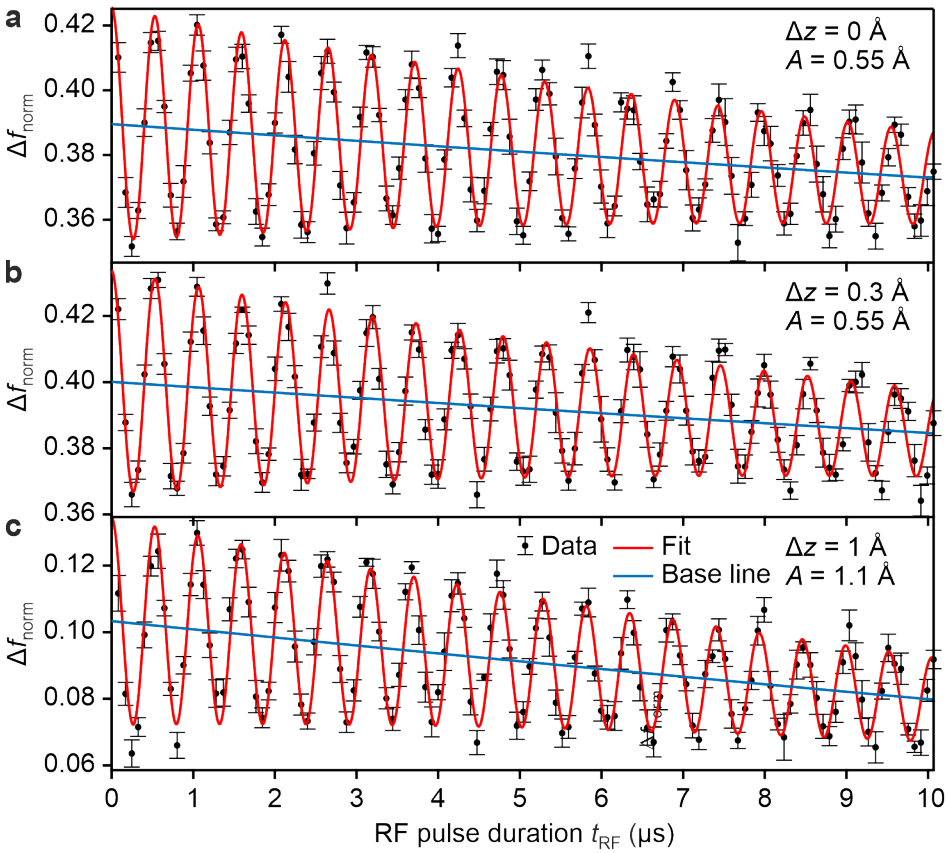

Figure 4.19.: Role of tip height and cantilever oscillation amplitude on Rabi oscillations. a-c, Rabi oscillations acquired on pentacene-d_{14} with a CO-terminated tip for different relative tip heights Δz (referring to the zero crossing from the setpoint of the cantilever: $\Delta f = -1.42\,\mathrm{Hz}$ at $V = 0\,\mathrm{V}$, $A = 1.65\,\mathrm{Å}$; positive Δz values are further away from the surface) and cantilever oscillation amplitudes A, as indicated in the panels (error bars are s.d. of eight repetitions). The Rabi oscillations show no appreciable differences.

of ± 3 (95% CI). We, therefore, conclude that the presence of the tip as well as its oscillation were not limiting the coherence times.

4.11.2. RF amplitude dependence

The RF amplitude dependence of the Rabi oscillations is a basic control and characterization test, since it is very characteristic of Rabi oscillations that their frequency depends linearly on the driving amplitude. Figure 4.20a to c shows the Rabi oscillations measured for three different RF amplitudes. From a fitting of these Rabi oscillations (see previous section and Appendix A.1.3 for details), the Rabi frequencies and decay constants can be extracted. These are plotted versus the RF amplitude in Figure 4.20d and e, respectively.

The Rabi frequency increases linearly with the RF amplitude, as expected. This proofs that the observed oscillations can indeed be attributed to Rabi oscillations, instead of some other oscillatory property, such as an electronic oscillation or mechanical mode of the cantilever.

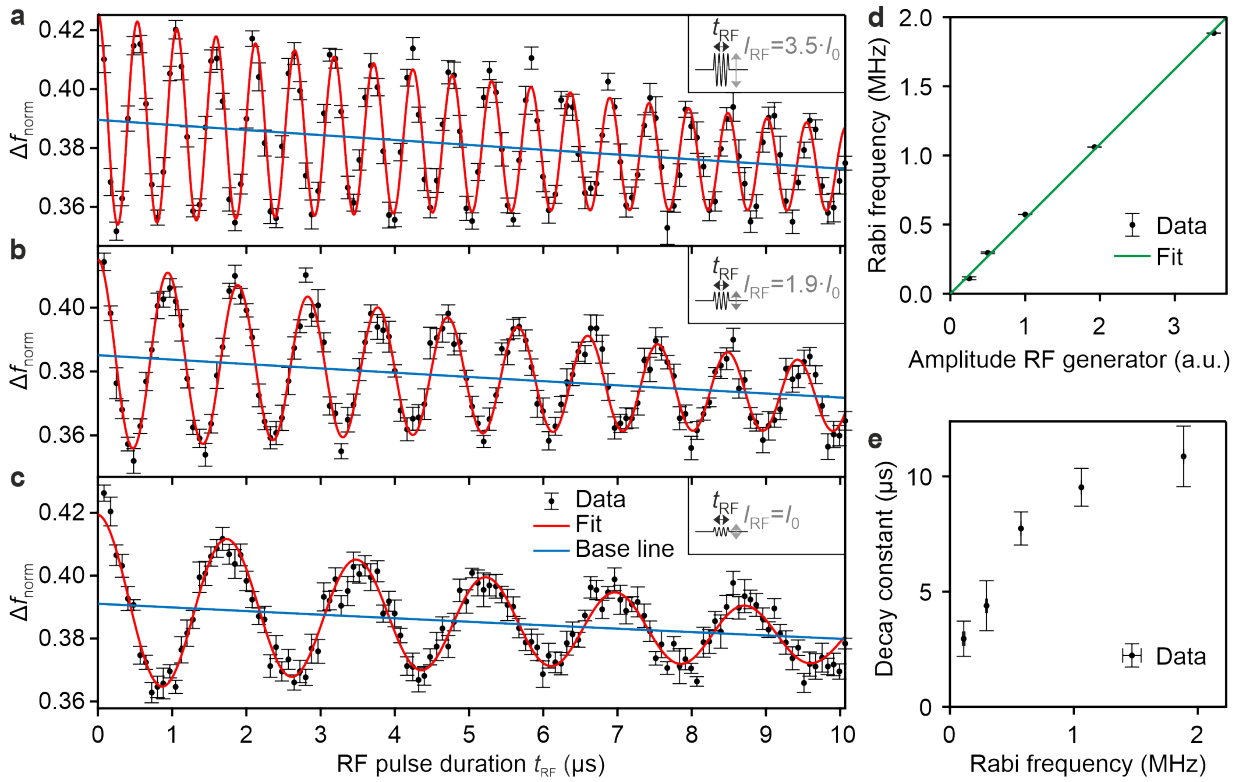

Figure 4.20.: Power dependence of Rabi oscillations. **a-c**, Rabi oscillations acquired on pentacene-d_{14} with a CO-terminated tip for different RF amplitudes demonstrating the increase of Rabi frequency with increasing RF amplitude (error bars are s.d. of eight repetitions). **d**, Rabi frequency versus the RF amplitude, determined before entering the microscope. The Rabi frequency increases linearly with the amplitude, which is characteristic for Rabi oscillations. **e**, Fitted decay constants of the Rabi oscillations plotted versus the frequencies of the Rabi oscillations.

The fitted decay constants of the Rabi oscillations, Figure 4.20e, show that the Rabi oscillations decay faster for lower RF amplitudes. In other words, the decay of the Rabi oscillations is suppressed if a stronger RF field is applied at the resonance frequency. This behavior was described already in 1955 by Redfield[232]. He showed that the decay of transverse magnetization (given by the spin-spin relaxation time T_2) is partially forbidden by energy and entropy considerations when a large resonant RF field is applied[232]. The effective dephasing time becomes power dependent with limiting values of T_2 at weak RF fields and spin-lattice relaxation time T_1 at strong RF fields[232,240]. Translated to our situation: if the Rabi frequency is larger than the frequency of the fluctuations of the resonance frequency (fluctuations caused by for example flip flops of the nuclear spins in the environment[231,237]), the decay of the Rabi oscillations is partially forbidden[232], and the Rabi oscillations decay slower than predicted from the T_2 that enters in the Bloch equations (see Appendix A.1.2)[231]. This suppression of dephasing due to strong driving, often called spin locking, not only (partly) decouples the electron spins from fluctuations from the environment, but also reduces the decay due to the fluctuations of the nuclear spin configuration of the molecule itself[241].

As mentioned in the previous section, in our case the decay of the Rabi oscillations is ultimately limited by the lifetimes of the involved substates. The spin-lattice relaxation

time is likely longer than this lifetime limit of 28 µs (ref. [215, 216]). We thus expect that in the limit of infinite RF amplitudes the coherence time will be limited by this lifetime limit. Note that for other molecules, e.g. PTCDA, this lifetime is longer (see Figure 3.24), possibly allowing access to even longer coherence times.

4.12. Selection rules and the orientation of the RF field

As already eluded to in the introduction, the main advantage that ESR-AFM brings is to combine the atomic-scale local information provided by AFM with the capabilities offered by ESR. As a proof of principle, we studied the interplay of the ESR selection rules and the molecular orientation.

In 1964, Brandon et al. experimentally demonstrated the selection rules for zero-field triplet state ESR for phenanthrene molecules oriented in diphenyl host crystals. To this end, they rotated the crystal with respect to the direction of the RF field[242]. It was found that any two of the three zero-field split substates are coupled by means of the magnetic field component pointing in the remaining third real-space dimension. For example, T_X and T_Z are only coupled through B_y, such that only the latter can drive the T_X-T_Z transition. These selection rules also follow from the Hamiltonian in Equation (2.23).

These selection rules can be demonstrated with ESR-AFM by measuring the frequency of the Rabi oscillations for different orientations of the molecules with respect to the RF field. The Rabi frequency depends linearly on the RF amplitude, see Figure 4.20d. As explained in Section 4.2.1, the RF field will have a component in the z direction, as well as an in-plane component perpendicular to the microstrip.

The pentacene-d_{14} molecules under study adsorb on NaCl in two different orientations, as shown in Figure 4.21a. The two orientations differ from each other by 90°, in line with the reported observation that pentacene adsorbs centered above a Cl^- with the long molecular axis aligned with one of the two $\langle 001 \rangle$ polar directions of the NaCl (ref. [3]). Because the x, y and z axes are in case of pentacene along the high-symmetry axes of the molecule (see Figure 2.11), the direction of the x and y axes for molecules in these two orientations differ, but their z axes coincide.

Figure 4.21b shows the Rabi oscillations of the T_X-T_Z transition for two molecules with the same orientation. As expected, their Rabi frequencies are equal within their uncertainty margins. The average of the Rabi frequencies of four molecules is (1.90 ± 0.02) MHz (error bars represent s.d.). In contrast, the Rabi frequency found for three molecules in the 90° rotated adsorption geometry is (0.60 ± 0.02) MHz, as shown for two molecules in Figure 4.21c. Apparently, the RF magnetic field component that drives the T_X-T_Z transition (the component along the short molecular axis of the molecule)[242], is smaller for the 90° rotated molecules.

Next to the T_X-T_Z transition, also the Rabi oscillations of the T_X-T_Y transition can be measured. To this end, the RF frequency was set to the maximum of the ESR signal of this transition. The T_X-T_Y transition is driven only by the RF-field component perpendicular to the molecular plane. As the latter always coincides with the surface plane, the corresponding Rabi frequency should be the same for all molecules. Indeed, very similar Rabi frequencies were found for the T_X-T_Y transition for molecules with different orienta-

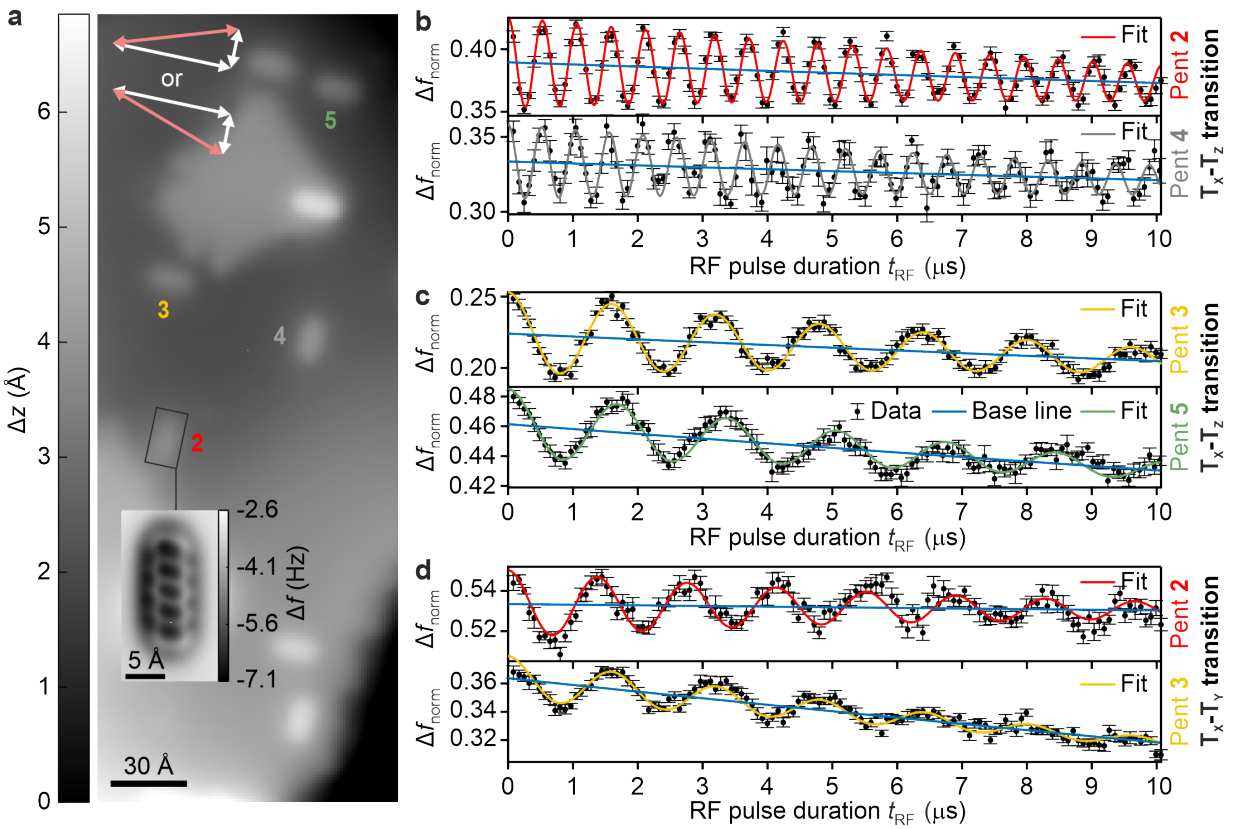

Figure 4.21.: Demonstration of the orientational dependence of Rabi oscillations. a, AFM topography image of the NaCl-covered surface with several individual pentacene molecules measured with a CO-functionalized tip (setpoint: $\Delta f = -1.45\,\mathrm{Hz}$ at $V = 0\,\mathrm{V}$, $A = 1.65\,\mathrm{Å}$). The length of the white arrows indicates the strength of the RF field in that direction, with their sum indicated by the pink arrows. Note that this overview image is rotated by $-8°$ and flipped along the y axis compared to the real-space directions. The inset shows a constant-height AFM image as a close-up of molecule 2 resolving its structure ($A = 0.3$ Å, $\Delta z = -5.08\,\mathrm{Å}$ with respect to the set point $\Delta f = -1.45\,\mathrm{Hz}$ at $V = 0\,\mathrm{V}$, $A = 0.3\,\mathrm{Å}$). **b**, **c**, Rabi oscillations of the $\mathrm{T_X}$-$\mathrm{T_Z}$ transition of four pentacene-$\mathrm{d_{14}}$ molecules, two per orientation, to demonstrate the orientational dependence of the Rabi frequencies (error bars are s.d. of eight repetitions). The averaged values of the Rabi frequencies are $(1.90 \pm 0.02)\,\mathrm{MHz}$ and $(0.60 \pm 0.02)\,\mathrm{MHz}$, derived for four and three molecules, respectively (error bars represent s.d.). **d**, Rabi oscillations of the $\mathrm{T_X}$-$\mathrm{T_Y}$ transition of the two individual molecules 2 and 3 (error bars are s.d. of ten repetitions). For the same RF power the Rabi frequency of the $\mathrm{T_X}$-$\mathrm{T_Y}$ transition for the two molecules is comparable.

tions (see Figure 4.21d). Together with the different Rabi frequencies found for the $\mathrm{T_X}$-$\mathrm{T_Z}$ transition, this experimentally demonstrates the selection rules at play.

Still, there is a small but notable difference observed between the Rabi frequencies of the $\mathrm{T_X}$-$\mathrm{T_Y}$ transition for the two different orientations (see Figure 4.21d). Rabi oscillations of this transition were measured for three molecules, of which two have the same orientation. For the molecules with the same orientation, a Rabi frequency of 0.72 MHz was determined, while for the molecule with the other orientation, the Rabi frequency equals 0.62 MHz. We hypothesize that this difference in driving by the z component of the RF magnetic field is due to the asymmetry of the metal tip. The metal tip is believed to influence the RF field in its proximity because of induced eddy currents in the tip, which likely depend crucially

on the exact shape of the metal tip. To test this hypothesis, the measurements could be repeated with another tip.

Next to a demonstration of the selection rules, these measurements allow us to experimentally derive the direction of the in-plane magnetic field based on the selection rules. To this end, bond-resolved AFM images were taken of the molecules for which the Rabi oscillations were measured. Thereby, the exact orientation of these molecules could be determined. From the orientations of the molecules and their corresponding Rabi frequencies, it follows that the magnetic RF field could either be orientated with a real-space angle of $(1 \pm 2)^\circ$ or $(36 \pm 2)^\circ$ with respect to the axis of the sample holder (error bars represent s.d.), as shown in the inset in Figure 4.21a. The expected orientation of the in-plane RF field is perpendicular to the long axis of the microstrip, which was for the used sample $(37 \pm 1)^\circ$. This is in excellent agreement with the determined angle of $(36 \pm 2)^\circ$.

4.13. Conclusion and outlook

In conclusion, we introduced a novel approach to detect single-molecule electron spin resonance, making use - for the first time - of an atomic force microscope. This ESR-AFM method relies on driving electron spin transitions between the non-equilibrium triplet substates of a single molecule. First, the molecule is brought to its triplet excited state. Since the triplet substates are split up in energy by the zero-field splitting, transitions between these substates can be driven at zero magnetic field. Driving such transitions modifies the decay of the triplet state, because of the different lifetimes of the triplet substates. The triplet decay and thus the ESR signal can be read-out using spin-to-charge conversion and single-electron charge detection by AFM.

We demonstrated our ESR-AFM method by applying it on single pentacene molecules. The resulting ESR-AFM signals exhibit sub-nanoelectronvolt energy resolution - unprecedented in scanning probe microscopy. Because of this very high energy resolution and the absence of a static magnetic field, the signals can provide a fingerprint of the molecule and its surroundings. On the one hand, minor differences in the zero-field splitting could be observed for different individual pentacene molecules, which we attributed to differences in the environment. On the other hand, some molecules showed a completely different lineshape, attributed to the presence of a single ^{1}H or ^{13}C nuclear spin, which couples via the hyperfine interaction to the electron spins being measured. ESR-AFM can thus serve as a tool to straightforwardly identify the isotopic composition of individual molecules adsorbed on an insulating surface. Whereas different STM-based approaches have been developed with which molecules differing in their isotopic composition can be distinguished[114,243–245], we are not aware of any AFM-based approach with which isotopomers can be identified.

The broader applicability of ESR-AFM was illustrated by the ESR-AFM signals that were measured for a second molecule, PTCDA. Comparing the ESR-AFM signals for pentacene and PTCDA demonstrates that the ESR-AFM signals provide a clear fingerprint, since the zero-field splitting depends crucially on the spatial distribution of the unpaired electrons, and thus on the molecular species under study. In general, ESR-AFM can be applied to molecules that stably adsorb on an insulating surface, can be brought to a long-lived triplet state (that does not decay via a charged state), and have a difference in

lifetimes of the triplet substates. We believe that these requirements are fulfilled for a large class of molecules.

Furthermore, we demonstrated that ESR-AFM can be used to coherently manipulate the spins in a single molecule. We reported coherent manipulations on a few microsconds timescale for a pentacene-h_{14} and tens of microseconds timescale for a pentacene-d_{14} molecule. Differing only in their isotopic composition, we attributed the difference in observed coherence time to the intramolecular hyperfine interaction, which is strongly reduced upon deuteration. The much longer coherence time found for pentacene-d_{14} indicates that the detection method did not limit the observed coherence for pentacene-h_{14}. This is in contrast to existing methods such as ESR-STM, for which the coherence time is typically limited by decoherence caused by tunneling electrons, the presence of a magnetic tip and the conductive substrate. Eliminating these decoherence sources by using ESR-AFM gives, therefore, access to tens of microseconds coherence time for pentacene-d_{14}, two orders of magnitude longer than typically observed for atoms and molecules measured with ESR-STM[198,204,239]. The decay of the coherence for pentacene-d_{14} may also be limited by the residual hyperfine interaction, but could also have a different origin. We excluded that the varying electric field in the tip-sample junction limits the observed coherence, although we observed that the electric field can induce shifts of the resonance frequency of the ESR-AFM signals.

The strength of ESR-AFM lies in its ability to directly resolve the atomic-scale geometry in relation to minute differences in observed ESR properties, such as the zero-field splitting, hyperfine coupling, spin decoherence and spin-spin coupling. We believe that such measurements will boost our atomistic understanding of the underlying mechanisms, such as the origins of decoherence, relevant for applications in quantum computing. As an example of combining spatial information with ESR, we measured the Rabi oscillations for molecules in different orientations. The frequency of these oscillations is directly related to the molecular orientation, because of the selection rules that are at play. These measurements also allowed us to experimentally derive the orientation of the in-plane magnetic RF field, which exactly matched the expected orientation from the experimental setup.

Furthermore, ESR-AFM could also be combined with the toolset of atomic and molecular manipulation. For instance, new directions for fundamental studies can be opened by combining it with spin[246] and charge-state[12] control and with controlled positioning of atoms[6,247].

Finally, we plan to use the SPM tip to locally perturb the molecule under study and measure this perturbance using ESR-AFM. Spatial resolution due to a perturbing tip is called scanning-gate microscopy[248] and was used in ESR-STM to measure MRI images[249]. Combined with our high-energy resolution and, therefore, sensitivity to individual isotopes in molecules, we envision to localize these isotopes inside molecules. The ability to localize isotopes could potentially be used to further enhance the understanding of on-surface chemical reactions, by following such reactions using isotopic labeling.

5. Summary and outlook

5.1. Summary

In this thesis, two novel single-molecule AFM spectroscopic methods were introduced. These methods allow studying non-equilibrium electronic and spin states of individual molecules, and can be combined with the atomic-scale spatial resolution and manipulation capabilities offered by AFM.

Essential to these methods is the use of a thick insulating film (>20 ML NaCl), which electronically decouples the molecules from the underlying metal substrate. In other words, no electron tunneling is taking place between the molecules and the underlying metal substrate, thereby stabilizing non-equilibrium charges and excited states. Electron tunneling can be steered between the conductive tip of the AFM cantilever and the molecule, by applying a voltage to the sample. Common to both developed methods is that a pump-probe voltage pulse scheme is used: The molecule is first initialized in a specific state, after which it is brought to a variety of states. As a third and last step, the population of the states is read-out by mapping the populated states onto two states differing in their net charge. Because of the single-electron charge sensitivity of AFM, these charge states can be distinguished in the AFM signal (the frequency shift) during a read-out interval.

In Chapter 3, we demonstrated that such an electronic pump-probe pulse scheme provides access to many transitions of different types, including radiative, non-radiative and redox (charge-related) transitions. In other words, we introduced an excited-state spectroscopy method by applying it on the well-studied pentacene molecule. Many features were resolved in the resulting spectra, which we could assign to specific transitions between different electronic states. The use of different pulse durations allows even to access the temporal evolution of the populations. This way, transitions into (and out of) long-lived states could be discriminated from those into short-lived states. Furthermore, the pump-probe pulse scheme allows to prepare the molecule in different initial states and read it out in different pairs of final states, providing additional information about the nature of the populated states. Further control over the possible transitions and their relative rates was obtained by varying the lateral position of the AFM tip above the molecule. Taking all these variations of the pump-probe voltage pulse scheme together, an unambiguous assignment of the observed spectral features to transitions between electronic states of pentacene could be made. From a fit of the excited-state spectra, we obtained the energy levels of ground and excited states for different charges of the molecule, as well as the reorganization energies of redox transitions. These results can complement other scanning probe experiments, as we demonstrated for STM-induced luminescence results found in literature. A controversy exists for such STML experiments performed for PTCDA. That is why we also applied our excited-state spectroscopy on PTCDA. The resulting spectral features were qualitatively similar as for pentacene, and a straightforward assignment was possible. The

quantitative energy level alignment of the low-lying electronic states could be obtained from a fit of the data, allowing us to shed light on the possible transition pathways in the reported STML experiments on PTCDA.

In Chapter 4, we used a similar electronic pump-probe scheme to access the spin properties of the first excited triplet state of single molecules. Importantly, this triplet state consists of three substates, which differ in their spin state, their energy (because of the zero-field splitting) as well as their decay times into the ground state. Because of the different lifetimes of the triplet substates, the overall triplet state lifetime will be modified upon driving transitions between the substates, using a sufficiently strong resonant radio-frequency magnetic field, generated here via a microstrip that was prepared as part of the sample structure. We could, thereby, drive transitions between the triplet substates of pentacene molecules and detect the resulting reduction in triplet lifetime with an electronic pump-probe scheme.

ESR-AFM spectra were measured for individual molecules by sweeping the frequency of the RF field. The asymmetric shape of the resulting signals was attributed to the hyperfine interaction: the coupling of the electron spins to the nuclear spins in the molecule. Because of the strong dependence of the hyperfine interaction on the identity of the nuclear spins, we could distinguish protonated and deuterated pentacene molecules, as well as locally identify deuterated pentacene molecules that contained a single ^{1}H or ^{13}C nucleus. Comparing different individual fully deuterated pentacene molecules against each other, small differences in the ESR resonance frequency were observed, which could be detected because of the very high spectral resolution (less than a nanoelectronvolt). These changes were attributed to variations in the local environment, partly due to the resulting difference in applied voltage during the ESR-AFM measurements. Because of the latter a different electric field is present in the tip-sample junction, causing a shift of the resonance frequency via the Stark effect. Next to pentacene, we believe that ESR-AFM can be applied to a wide class of molecules, as we demonstrated by applying it to PTCDA. In general, ESR-AFM is applicable to molecules that stably adsorb on an insulating film, have a long-lived excited triplet state (which cannot decay via a charged state) and have different lifetimes of the triplet substates.

We could coherently manipulate the spins by sweeping the RF pulse duration, at a fixed RF frequency. We measured the resulting Rabi oscillations for protonated and deuterated pentacene molecules. While a coherence time of a few µs was found for protonated pentacene, a coherence time of tens of µs was found for deuterated pentacene. We, therefore, concluded that the decay of the Rabi oscillations for protonated pentacene is dominated by the dephasing due to the fluctuating proton nuclear spins in pentacene. For deuterated pentacene, the decay could similarly be dominated by the (smaller) dephasing caused by the deuterium nuclear spins in the molecule. Other possible decoherence sources are the nuclear spins in the surface, and interference from the measurement technique itself. For the latter we ruled out that the presence of the tip and its oscillation (including the resulting varying electric field) had a strong effect on the decay of the Rabi oscillations. On the other hand, the decay of the Rabi oscillations was found to strongly depend on the RF amplitude, which we attributed to the well-known suppression of dephasing due to strong resonant driving. Finally, we demonstrated the selection rules in triplet-state ESR in real-space by measuring Rabi oscillations for molecules with different orientations. From these measurements, the orientation of the RF magnetic field in the surface plane could

be derived, which was found to match the expected orientation of the RF field due to our microstrip design.

5.2. Outlook

The novel AFM spectroscopic methods introduced in the context of this thesis, excited-state spectroscopy and ESR-AFM, have a wide range of applications, of which some are mentioned here.

One exciting application is to combine these methods with on-surface chemical reactions. First, the use of an electronic pump-probe sequence may expand the so far limited number of chemical reactions that can be performed on thick insulating films. To be more specific, chemical reactions could be induced by selective population of different excited states. Thereby, valuable insights into reaction mechanisms may be obtained. Second, we hope to expand ESR-AFM to be able to localize single isotopes inside single molecules. Such an extension might be used to follow isotopes during an on-surface chemical reaction.

The combination of ESR-AFM and excited-state spectroscopy with the already existing AC-STM method offers a toolbox to characterize individual molecules on thick insulating films. We, for instance, recently applied excited-state spectroscopy to copper phthalocyanine molecules, which have a much more complex electronic structure, including a localized unpaired electron and a long-lived quadruplet state. As demonstrated for PTCDA, excited-state spectroscopy can also be applied to molecules studied with other SPM methods, for which an understanding of the energy level alignment is crucial for the interpretation of the data (e.g. in STML). Excited-state spectroscopy can further be applied to molecules for which information on the excited states (such as the first excited triplet state) is lacking and crucial for applications, for instance in the field of single-molecule photon emitters. Spin properties can be accessed via ESR-AFM, such as zero-field splitting, hyperfine coupling, spin decoherence and spin-spin coupling. Next to molecular characterization, we believe that studying these properties could give atomistic insights into the underlying mechanisms, relevant for applications such as quantum computing.

Finally, we hope to extend both excited-state spectroscopy and ESR-AFM to generate intramolecular spatial resolution. Spatially mapping the excited-state spectroscopy signals could provide maps of excited states, analogously to the mapping of the charge transitions in AC-STM. In ESR-AFM, we could potentially use the tip to locally perturb the triplet-state spin density, which may allow the above-mentioned localization of individual isotopes inside individual molecules.

A. Appendix

A.1. Fitting and simulations of ESR-AFM

Most of the text and equations presented in this appendix have been published in ref. [22].

A.1.1. Fitting of the ESR-AFM lineshapes

A formula to fit the ESR-AFM lineshapes can be derived considering the hyperfine interaction as well as lifetime broadening.

As explained in Section 2.4.2, the hyperfine interaction is the origin of the asymmetric lineshape of the ESR signals. The lineshape of the T_X-T_Z transition can be well approximated by a sudden onset at a frequency f_{onset} followed by an exponential decay of width f_{decay} (FWHM: $f_{\text{decay}} \cdot \ln(2)$) (ref. [224]) as

$$\theta(f - f_{\text{onset}}) \exp(-\frac{f - f_{\text{onset}}}{f_{\text{decay}}}), \tag{A.1}$$

in which $\theta(x)$ denotes the Heaviside function.

A second contribution to the overall lineshape results from the finite lifetimes of the involved substates. This leads to a lifetime broadening, resulting in a Lorentzian of the form

$$\frac{\pi^{-1}\Gamma}{(f - f_{\text{res}})^2 + \Gamma^2} \tag{A.2}$$

centred around each resonance frequency f_{res} with a FWHM of 2Γ.

Accordingly, the experimental resonances are fit to a convolution of the above two functions, allowing us to extract the broadening owing to the hyperfine interaction and the finite lifetimes separately. We note that non-Markovian processes[224,231] may lead to a deviation from the idealized Lorentzian and that power broadening was avoided in the measurements of the ESR-AFM signals. The effect of power broadening is illustrated in Figure 4.9.

A.1.2. Maxwell-Bloch simulations of the Rabi oscillations

To guide the understanding of the Rabi oscillations measured using ESR-AFM (see Section 4.11), we performed simulations using the Maxwell-Bloch equations[250], analogous to the model used for ODMR[251]. The Rabi oscillation data are a temporal average of a single molecule, which - according to the ergodic assumption - is the same as an ensemble average. Therefore, we can use the density-matrix formalism[252] to simulate our data.

To illustrate the effect of an RF pulse with a frequency corresponding to the maximum of the T_X-T_Z ESR signal, the evolution of the populations of the three triplet substates and the singlet state during the dwell voltage pulse were simulated, as shown in Figure 4.15. Note that, on driving the T_X-T_Z transition, T_Y is decoupled from the T_X and T_Z dynamics and simply decays independently. The Bloch equations in the density-matrix formalism can therefore be restricted to the two coupled substates[253], here T_X and T_Z, whereas the population of the third triplet substate is treated separately as a simple exponential decay function. With respect to the two coupled substates, the system is described by the density matrix[252]

$$\boldsymbol{\rho} = \begin{pmatrix} \rho_{ZZ} & \rho_{ZX} \\ \rho_{XZ} & \rho_{XX} \end{pmatrix} \tag{A.3}$$

and evolves according to the Liouville equation[252]

$$\frac{\mathrm{d}\boldsymbol{\rho}}{\mathrm{d}t} = -\frac{i}{\hbar}[\boldsymbol{\mathcal{H}}, \boldsymbol{\rho}]. \tag{A.4}$$

The Hamiltonian of the molecule interacting with the RF field (with Rabi rate Ω) at resonance with the T_X-T_Z transition (with resonance frequency $\omega_Z - \omega_X$) can be written as[251]

$$\boldsymbol{\mathcal{H}} = \begin{pmatrix} \hbar\omega_X & -\hbar\Omega\cos(\omega_Z - \omega_X) \\ -\hbar\Omega\cos(\omega_Z - \omega_X) & \hbar\omega_Z \end{pmatrix}. \tag{A.5}$$

According to this Hamiltonian, the time evolution of the density operator in the rotating-frame approximation (see for more details e.g. ref. [217, 251]), with phenomenologically added relaxation and dephasing terms, can be described as[251]

$$\frac{\mathrm{d}\rho_{XX}}{\mathrm{d}t} = \frac{i\Omega}{2}(\rho_{ZX} - \rho_{XZ}) - \frac{\rho_{XX}}{\tau_X}, \tag{A.6}$$

$$\frac{\mathrm{d}\rho_{ZZ}}{\mathrm{d}t} = \frac{i\Omega}{2}(\rho_{XZ} - \rho_{ZX}) - \frac{\rho_{ZZ}}{\tau_Z}, \tag{A.7}$$

$$\frac{\mathrm{d}\rho_{XZ}}{\mathrm{d}t} = \frac{i\Omega}{2}(\rho_{ZZ} - \rho_{XX}) - \rho_{XZ}\left(\frac{1}{T_2} + \frac{1}{2\tau_X} + \frac{1}{2\tau_Z}\right), \tag{A.8}$$

$$\frac{\mathrm{d}\rho_{ZX}}{\mathrm{d}t} = \frac{i\Omega}{2}(\rho_{XX} - \rho_{ZZ}) - \rho_{ZX}\left(\frac{1}{T_2} + \frac{1}{2\tau_X} + \frac{1}{2\tau_Z}\right), \tag{A.9}$$

while the time evolution of T_Y is simply given by

$$\frac{\mathrm{d}\rho_{YY}}{\mathrm{d}t} = -\frac{\rho_{YY}}{\tau_Y}. \tag{A.10}$$

These last five equations were used for the simulation for Figure 4.15. As input parameters for the simulation, we used the parameters that were experimentally derived for pentacene-h_{14}: the decay constants of the triplet substates: $\tau_X = 20.8\,\mu s$, $\tau_Y = 66.6\,\mu s$ and $\tau_Z = 136.1\,\mu s$; the decay constant of the Rabi oscillations: $T_2 = 2.2\,\mu s$; the initial populations $\rho_{XX} = \rho_{YY} = \rho_{ZZ} = 0.8/3$ and coherences $\rho_{XZ} = \rho_{ZX} = 0$; the starting time of the RF pulse $t_S = 45.1\,\mu s$ and its duration of 4 and 4.5 Rabi-oscillation periods, respectively. Note that interconversion between T_X and T_Z resulting from spin-lattice relaxation is assumed to be negligible compared with τ_X and τ_Z. Here the initial populations of the T_X,

T_Y and T_Z substates are assumed to be all equal to 0.8/3. The data in Figure 3.8 and ref. [21] show that the triplet state is initially approximately 80% populated. We assume that the probability to tunnel in the three substates is equal (same spatial distribution and tunneling barrier, as their energy differences are negligibly small).

The Maxwell-Bloch simulations were performed to guide the understanding of our Rabi-oscillation measurements. For this purpose, we disregarded non-Markovian effects[224,231] and modelled the relaxation with a single phenomenological time constant T_2. In other words, we neglected the RF power dependence of the relaxation time that we observed (see Figure 4.20e).

A.1.3. Fitting of the Rabi oscillations

As discussed in Section 4.11, the Rabi oscillations were fitted using an exponentially decaying sinusoidal with a decaying baseline. In this section, the decay of the baseline of the Rabi oscillations between the T_X and T_Z substates is described (analogous for the measured Rabi oscillations between the T_X and T_Y substates). This baseline represents the situation of equal populations in the coupled substates T_X and T_Z during the pulse; even if the Rabi signal is not yet decayed, it is oscillating around the baseline. The decay of the baseline arises from the decay of the (on average) equally populated T_X and T_Z substates into the singlet state during the RF pulse. As the final population of T_Y is independent of the RF signal, it will only give rise to a constant background and will be disregarded in the following.

Hence, the baseline is defined by the following: in the initial phase $0 < t < t_S$, all three triplet substates decay independently from each other. At the beginning of the RF pulse, that is, at $t = t_S$, the sum of populations in T_X and T_Z is

$$P_{XZ}(t_S) = \frac{P_0}{3}(\exp(-k_X t_S) + \exp(-k_Z t_S)), \tag{A.11}$$

in which $k_X = \tau_X^{-1}$ and $k_Z = \tau_Z^{-1}$ are the decay rates of T_X and T_Z, respectively, and P_0 is the initial total population in the triplet state, such that $P_0/3$ is the initial population in each T_X, T_Y and T_Z. During the RF pulse, that is, for $t_S < t < t_E$ (with t_E being the end of the RF pulse), the RF signal equilibrates (on average) the populations of two of the substates, thus at the end of the RF pulse

$$P_{XZ}(t_E) = P_{XZ}(t_S) \exp\left(-\frac{(k_X + k_Z)(t_E - t_S)}{2}\right). \tag{A.12}$$

Finally, for $t_E < t < t_D$, the substates decay again independently, giving at the end of the dwell time

$$P_{XZ}(t_D) = P_{XZ}(t_S) \exp\left(-\frac{(k_X + k_Z)(t_E - t_S)}{2}\right) \frac{\exp(-k_X(t_D - t_E)) + \exp(-k_Z(t_D - t_E))}{2}, \tag{A.13}$$

which can be rearranged to

$$P_{\mathrm{XZ}}(t_{\mathrm{D}}) = \frac{P_{\mathrm{XZ}}(t_{\mathrm{S}})}{2}\left[\exp(-(k_{\mathrm{X}}(t_{\mathrm{D}}-t_{\mathrm{S}}))\exp\left(t_{\mathrm{RF}}\frac{k_{\mathrm{X}}-k_{\mathrm{Z}}}{2}\right)+ \right.$$
$$\left. \exp(-k_{\mathrm{Z}}(t_{\mathrm{D}}-t_{\mathrm{S}}))\exp\left(-t_{\mathrm{RF}}\frac{k_{\mathrm{X}}-k_{\mathrm{Z}}}{2}\right)\right]. \quad \text{(A.14)}$$

Note that $P_{\mathrm{XZ}}(t_{\mathrm{S}})$ does not depend on $t_{\mathrm{RF}} = t_{\mathrm{E}} - t_{\mathrm{S}}$ and therefore just represents a constant prefactor. The two terms provide contributions to the baseline that rise and fall exponentially with t_{RF}, respectively. For the specific case and parameters considered here, the prefactor of the rising term is much smaller than that of the falling term and is therefore neglected. Because the decay rates were determined (see Figure 4.4) for the pentacene-h_{14} molecule, for which the Rabi oscillations were measured, these rates were used for the fitting of the Rabi oscillations of the pentacene-h_{14} molecule (Figure 4.16a). In case of pentacene-d_{14} (Figure 4.16c), we set $(k_{\mathrm{X}} - k_{\mathrm{Z}})/2 = 0.012\,\mu\mathrm{s}^{-1}$ based on the measured decay rates of other individual pentacene-d_{14} molecules (see Figure 4.17). The experimental data show a variation in the slope of the baseline (see e.g. Figure 4.21d). Next to the decay of the baseline due to the decay of the populations, other effects may add to the temporal evolution of the baseline, such as a thermal expansion owing to RF-induced heating. These contributions were not separately accounted for; they were fitted as part of the falling term described above.

Bibliography

1. Binnig, G., Rohrer, H., Gerber, C. & Weibel, E. Surface studies by scanning tunneling microscopy. *Physical Review Letters* **49,** 57 (1982).
2. Binnig, G., Quate, C. F. & Gerber, C. Atomic force microscope. *Physical Review Letters* **56,** 930 (1986).
3. Repp, J., Meyer, G., Stojković, S. M., Gourdon, A. & Joachim, C. Molecules on insulating films: scanning-tunneling microscopy imaging of individual molecular orbitals. *Physical Review Letters* **94,** 026803 (2005).
4. Gross, L., Mohn, F., Moll, N., Liljeroth, P. & Meyer, G. The chemical structure of a molecule resolved by atomic force microscopy. *Science* **325,** 1110–1114 (2009).
5. Eigler, D. M. & Schweizer, E. K. Positioning single atoms with a scanning tunnelling microscope. *Nature* **344,** 524–526 (1990).
6. Sugimoto, Y. *et al.* Atom inlays performed at room temperature using atomic force microscopy. *Nature Materials* **4,** 156–159 (2005).
7. Crommie, M. F., Lutz, C. P. & Eigler, D. M. Confinement of electrons to quantum corrals on a metal surface. *Science* **262,** 218–220 (1993).
8. Hla, S.-W., Bartels, L., Meyer, G. & Rieder, K.-H. Inducing all steps of a chemical reaction with the scanning tunneling microscope tip: towards single molecule engineering. *Physical Review Letters* **85,** 2777 (2000).
9. Albrecht, F. *et al.* Selectivity in single-molecule reactions by tip-induced redox chemistry. *Science* **377,** 298–301 (2022).
10. Kaiser, K. *et al.* An sp-hybridized molecular carbon allotrope, cyclo[18]carbon. *Science* **365,** 1299–1301 (2019).
11. Pavliček, N. *et al.* Synthesis and characterization of triangulene. *Nature Nanotechnology* **12,** 308–311 (2017).
12. Gross, L. *et al.* Measuring the charge state of an adatom with noncontact atomic force microscopy. *Science* **324,** 1428–1431 (2009).
13. Leoni, T. *et al.* Controlling the charge state of a single redox molecular switch. *Physical Review Letters* **106,** 216103 (2011).
14. Lambert, N. *et al.* Quantum biology. *Nature Physics* **9,** 10–18 (2013).
15. Qiu, X., Nazin, G. & Ho, W. Vibrationally resolved fluorescence excited with submolecular precision. *Science* **299,** 542–546 (2003).
16. Imada, H. *et al.* Real-space investigation of energy transfer in heterogeneous molecular dimers. *Nature* **538,** 364–367 (2016).

17. Doppagne, B. *et al.* Electrofluorochromism at the single-molecule level. *Science* **361,** 251–255 (2018).

18. Steurer, W., Fatayer, S., Gross, L. & Meyer, G. Probe-based measurement of lateral single-electron transfer between individual molecules. *Nature Communications* **6,** 8353 (2015).

19. Steurer, W. *et al.* Manipulation of the charge state of single Au atoms on insulating multilayer films. *Physical Review Letters* **114,** 036801 (2015).

20. Fatayer, S. *et al.* Probing molecular excited states by atomic force microscopy. *Physical Review Letters* **126,** 176801 (2021).

21. Peng, J. *et al.* Atomically resolved single-molecule triplet quenching. *Science* **373,** 452–456 (2021).

22. Sellies, L. *et al.* Single-molecule electron spin resonance by means of atomic force microscopy. *Nature* **624,** 64–68 (2023).

23. Pan, Y. *et al.* Computational investigation on the large energy gap between the triplet excited-states in acenes. *RSC Advances* **7,** 26697–26703 (2017).

24. Coto, P. B., Sharifzadeh, S., Neaton, J. B. & Thoss, M. Low-lying electronic excited states of pentacene oligomers: A comparative electronic structure study in the context of singlet fission. *Journal of Chemical Theory and Computation* **11,** 147–156 (2015).

25. Roos, B. O. *et al.* in *Advances in Chemical Physics* 219–331 (John Wiley & Sons, 1996).

26. Fazekas, P. *Lecture Notes on Electron Correlation and Magnetism* (World Scientific, 1999).

27. Feng, Q. & Oppeneer, P. M. Investigation of on-site interorbital single-electron hoppings in general multiorbital systems. *Physical Review B* **86,** 035107 (2012).

28. Chen, C. J. *Introduction to Scanning Tunneling Microscopy* 2nd ed. (Oxford University Press on Demand, 2008).

29. Voigtländer, B. *Scanning Probe Microscopy* (Springer, 2015).

30. Pauli, W. Über den Zusammenhang des Abschlusses der Elektronengruppen im Atom mit der Komplexstruktur der Spektren. *Zeitschrift für Physik* **229,** 765–783 (1925).

31. Hagelstein, P. L., Senturia, S. D. & Orlando, T. P. *Introductory Applied Quantum and Statistical Mechanics* (John Wiley & Sons, 2004).

32. Tersoff, J. & Hamann, D. Theory and application for the scanning tunneling microscope. *Physical Review Letters* **50,** 1998 (1983).

33. Tersoff, J. & Hamann, D. R. Theory of the scanning tunneling microscope. *Physical Review B* **31,** 805 (1985).

34. Bardeen, J. Tunnelling from a many-particle point of view. *Physical Review Letters* **6,** 57 (1961).

35. Kaiser, K., Lieske, L.-A., Repp, J. & Gross, L. Charge-state lifetimes of single molecules on few monolayers of NaCl. *Nature Communications* **14,** 4988 (2023).

36. Giessibl, F. J. & Binnig, G. Investigation of the (001) cleavage plane of potassium bromide with an atomic force microscope at 4.2 K in ultra-high vacuum. *Ultramicroscopy* **42,** 281–289 (1992).

37. Ohnesorge, F. & Binnig, G. True atomic resolution by atomic force microscopy through repulsive and attractive forces. *Science* **260,** 1451–1456 (1993).

38. Giessibl, F. J. Advances in atomic force microscopy. *Reviews of Modern Physics* **75,** 949 (2003).

39. McClelland, G. M., Erlandsson, R. & Chiang, S. in *Review of Progress in Quantitative Nondestructive Evaluation* 1307–1314 (Springer, 1987).

40. Giessibl, F. J. Forces and frequency shifts in atomic-resolution dynamic-force microscopy. *Physical Review B* **56,** 16010 (1997).

41. Giessibl, F. J. The qPlus sensor, a powerful core for the atomic force microscope. *Review of Scientific Instruments* **90,** 011101 (2019).

42. García, R. & Pérez, R. Dynamic atomic force microscopy methods. *Surface Science Reports* **47,** 197–301 (2002).

43. Albrecht, T., Grütter, P., Horne, D. & Rugar, D. Frequency modulation detection using high-Q cantilevers for enhanced force microscope sensitivity. *Journal of Applied Physics* **69,** 668–673 (1991).

44. Martin, Y., Williams, C. C. & Wickramasinghe, H. K. Atomic force microscope–force mapping and profiling on a sub 100-Å scale. *Journal of Applied Physics* **61,** 4723–4729 (1987).

45. Rugar, D. & Hansma, P. Atomic force microscopy. *Physics Today* **43,** 23–30 (1990).

46. Giessibl, F. J. Atomic resolution on Si(111)-(7×7) by noncontact atomic force microscopy with a force sensor based on a quartz tuning fork. *Applied Physics Letters* **76,** 1470–1472 (2000).

47. Giessibl, F. J. Atomic resolution of the silicon (111)-(7×7) surface by atomic force microscopy. *Science* **267,** 68–71 (1995).

48. Sugawara, Y., Ohta, M., Ueyama, H. & Morita, S. Defect motion on an InP(110) surface observed with noncontact atomic force microscopy. *Science* **270,** 1646–1648 (1995).

49. Gross, L. *et al.* in *Noncontact Atomic Force Microscopy* 223–246 (Springer, 2015).

50. Bartels, L., Meyer, G. & Rieder, K.-H. Controlled vertical manipulation of single CO molecules with the scanning tunneling microscope: A route to chemical contrast. *Applied Physics Letters* **71,** 213–215 (1997).

51. Moll, N., Gross, L., Mohn, F., Curioni, A. & Meyer, G. The mechanisms underlying the enhanced resolution of atomic force microscopy with functionalized tips. *New Journal of Physics* **12,** 125020 (2010).

52. Giessibl, F. J. High-speed force sensor for force microscopy and profilometry utilizing a quartz tuning fork. *Applied Physics Letters* **73,** 3956–3958 (1998).

53. Repp, J., Meyer, G., Olsson, F. E. & Persson, M. Controlling the charge state of individual gold adatoms. *Science* **305,** 493–495 (2004).

54. Olsson, F. E., Paavilainen, S., Persson, M., Repp, J. & Meyer, G. Multiple charge states of Ag atoms on ultrathin NaCl films. *Physical Review Letters* **98,** 176803 (2007).

55. Wu, S., Ogawa, N. & Ho, W. Atomic-scale coupling of photons to single-molecule junctions. *Science* **312,** 1362–1365 (2006).

56. Nilius, N., Ernst, N. & Freund, H.-J. Photon emission spectroscopy of individual oxide-supported silver clusters in a scanning tunneling microscope. *Physical Review Letters* **84,** 3994 (2000).

57. Marcus, R. A. Electron transfer reactions in chemistry. Theory and experiment. *Reviews of Modern Physics* **65,** 599 (1993).

58. Fatayer, S. *et al.* Reorganization energy upon charging a single molecule on an insulator measured by atomic force microscopy. *Nature Nanotechnology* **13,** 376 (2018).

59. Hernangómez-Pérez, D. *et al.* Reorganization energy and polaronic effects of pentacene on NaCl films. *Physical Review B* **102,** 115419 (2020).

60. Marcus, R. A. Electrostatic free energy and other properties of states having nonequilibrium polarization. I. *The Journal of Chemical Physics* **24,** 979–989 (1956).

61. Condon, E. U. The Franck-Condon principle and related topics. *American Journal of Physics* **15,** 365–374 (1947).

62. Franck, J. & Dymond, E. Elementary processes of photochemical reactions. *Transactions of the Faraday Society* **21,** 536–542 (1926).

63. Condon, E. U. Nuclear motions associated with electron transitions in diatomic molecules. *Physical Review* **32,** 858 (1928).

64. Atkins, P. & de Paula, J. *Physical Chemistry* 9th ed. (OUP Oxford, 2010).

65. Barbara, P. F., Meyer, T. J. & Ratner, M. A. Contemporary issues in electron transfer research. *The Journal of Physical Chemistry* **100,** 13148–13168 (1996).

66. Jortner, J. Temperature dependent activation energy for electron transfer between biological molecules. *The Journal of Chemical Physics* **64,** 4860–4867 (1976).

67. Condon, E. A theory of intensity distribution in band systems. *Physical Review* **28,** 1182 (1926).

68. Verhoeven, J. Glossary of terms used in photochemistry (IUPAC Recommendations 1996). *Pure and Applied Chemistry* **68,** 2223–2286 (1996).

69. Henriksen, N. E. & Hansen, F. Y. *Theories of Molecular Reaction Dynamics: the Microscopic Foundation of Chemical Kinetics* (Oxford University Press, 2018).

70. Repp, J., Meyer, G., Paavilainen, S., Olsson, F. E. & Persson, M. Scanning tunneling spectroscopy of Cl vacancies in NaCl films: strong electron-phonon coupling in double-barrier tunneling junctions. *Physical Review Letters* **95,** 225503 (2005).

71. Wingreen, N. S., Jacobsen, K. W. & Wilkins, J. W. Inelastic scattering in resonant tunneling. *Physical Review B* **40,** 11834 (1989).

72. Dow, J. D. & Redfield, D. Toward a unified theory of Urbach's rule and exponential absorption edges. *Physical Review B* **5,** 594 (1972).

73. Wu, S., Ogawa, N., Nazin, G. & Ho, W. Conductance hysteresis and switching in a single-molecule junction. *The Journal of Physical Chemistry C* **112,** 5241–5244 (2008).

74. Gadzuk, J. Inelastic resonance scattering, tunneling, and desorption. *Physical Review B* **44,** 13466 (1991).

75. Fatayer, S. *et al.* Molecular structure elucidation with charge-state control. *Science* **365,** 142–145 (2019).

76. Gross, L. *et al.* Investigating atomic contrast in atomic force microscopy and Kelvin probe force microscopy on ionic systems using functionalized tips. *Physical Review B* **90,** 155455 (2014).

77. Stoneham, A. & Tasker, P. Metal-non-metal and other interfaces: the role of image interactions. *Journal of Physics C: Solid State Physics* **18,** L543 (1985).

78. Leung, T.-C., Kao, C., Su, W., Feng, Y. & Chan, C. T. Relationship between surface dipole, work function and charge transfer: Some exceptions to an established rule. *Physical Review B* **68,** 195408 (2003).

79. Onishi, H. & Sasahara, A. in *Kelvin Probe Force Microscopy: Measuring and Compensating Electrostatic Forces* 201–219 (Springer, 2011).

80. Smoluchowski, R. Anisotropy of the electronic work function of metals. *Physical Review* **60,** 661 (1941).

81. Stern, J., Terris, B., Mamin, H. & Rugar, D. Deposition and imaging of localized charge on insulator surfaces using a force microscope. *Applied Physics Letters* **53,** 2717–2719 (1988).

82. Schönenberger, C. & Alvarado, S. Observation of single charge carriers by force microscopy. *Physical Review Letters* **65,** 3162 (1990).

83. Bussmann, E., Kim, D. J. & Williams, C. Single-electron tunneling to insulator surfaces measured by frequency detection electrostatic force microscopy. *Applied Physics Letters* **85,** 2538–2540 (2004).

84. Bussmann, E., Zheng, N. & Williams, C. Single-electron manipulation to and from a SiO_2 surface by electrostatic force microscopy. *Applied Physics Letters* **86** (2005).

85. Bussmann, E. & Williams, C. Single-electron tunneling force spectroscopy of an individual electronic state in a nonconducting surface. *Applied Physics Letters* **88** (2006).

86. Stomp, R. *et al.* Detection of single-electron charging in an individual InAs quantum dot by noncontact atomic-force microscopy. *Physical Review Letters* **94,** 056802 (2005).

87. Zhu, J., Brink, M. & McEuen, P. Frequency shift imaging of quantum dots with single-electron resolution. *Applied Physics Letters* **87** (2005).

88. Azuma, Y., Kanehara, M., Teranishi, T. & Majima, Y. Single electron on a nanodot in a double-barrier tunneling structure observed by noncontact atomic-force spectroscopy. *Physical Review Letters* **96,** 016108 (2006).

89. Patera, L. L., Queck, F., Scheuerer, P. & Repp, J. Mapping orbital changes upon electron transfer with tunnelling microscopy on insulators. *Nature* **566,** 245 (2019).

90. Ardhuin, T., Guillermet, O., Gourdon, A. & Gauthier, S. Measurement and control of the charge occupation of single adsorbed molecules levels by STM and nc-AFM. *The Journal of Physical Chemistry C* **123,** 26218–26225 (2019).

91. Berger, J. *et al.* Quantum dissipation driven by electron transfer within a single molecule investigated with atomic force microscopy. *Nature Communications* **11,** 1337 (2020).

92. Datta, S. *et al.* Current-voltage characteristics of self-assembled monolayers by scanning tunneling microscopy. *Physical Review Letters* **79,** 2530 (1997).

93. Wu, S., Nazin, G., Chen, X., Qiu, X. & Ho, W. Control of relative tunneling rates in single molecule bipolar electron transport. *Physical Review Letters* **93,** 236802 (2004).

94. Ihn, T. *Semiconductor Nanostructures: Quantum States and Electronic Transport* (OUP Oxford, 2009).

95. Koch, J. & Von Oppen, F. Franck-Condon blockade and giant Fano factors in transport through single molecules. *Physical Review Letters* **94,** 206804 (2005).

96. Zavoisky, E. Paramagnetic relaxation of liquid solutions for perpendicular fields. *Journal of Physics* **9,** 211 (1945).

97. Roessler, M. M. & Salvadori, E. Principles and applications of EPR spectroscopy in the chemical sciences. *Chemical Society Reviews* **47,** 2534–2553 (2018).

98. Rieger, P. H. *Electron Spin Resonance: Analysis and Interpretation* (Royal Society of Chemistry, 2007).

99. Poole, C. P. *ESR: A Comprehensive Treatise on Experimental Techniques* 2nd ed. (Dover Publications, Inc., 1996).

100. Hutchison Jr, C. A. & Mangum, B. W. Paramagnetic resonance absorption in naphthalene in its phosphorescent state. *The Journal of Chemical Physics* **29,** 952–953 (1958).

101. Vahtras, O., Loboda, O., Minaev, B., Ågren, H. & Ruud, K. Ab initio calculations of zero-field splitting parameters. *Chemical Physics* **279,** 133–142 (2002).

102. Weil, J. A. & Bolton, J. R. *Electron Paramagnetic Resonance: Elementary Theory and Practical Applications* (John Wiley & Sons, 2007).

103. Köhler, J. Magnetic resonance of a single molecular spin. *Physics Reports* **310,** 261–339 (1999).

104. Poole Jr, C. P., Farach, H. A. & Jackson, W. K. Standardization of convention for zero field splitting parameters. *The Journal of Chemical Physics* **61,** 2220–2221 (1974).

105. Richert, S., Tait, C. E. & Timmel, C. R. Delocalisation of photoexcited triplet states probed by transient EPR and hyperfine spectroscopy. *Journal of Magnetic Resonance* **280,** 103–116 (2017).

106. Gerson, F. & Huber, W. *Electron Spin Resonance Spectroscopy of Organic Radicals* (John Wiley & Sons, 2003).

107. Brouwer, A., Köhler, J., Groenen, E. J. & Schmidt, J. ^{13}C isotope effects for pentacene in p-terphenyl: High-resolution spectroscopy and single-spin detection. *The Journal of Chemical Physics* **105,** 2212–2222 (1996).

108. McConnell, H. M. & Strathdee, J. Theory of anisotropic hyperfine interactions in π-electron radicals. *Molecular Physics* **2,** 129–138 (1959).

109. Hutchison Jr, C. A., Nicholas, J. V. & Scott, G. W. Magnetic Resonance Spectroscopy of Triplet-State Organic Molecules in Zero External Magnetic Field. *The Journal of Chemical Physics* **53,** 1906–1917 (1970).

110. Cocker, T. L., Peller, D., Yu, P., Repp, J. & Huber, R. Tracking the ultrafast motion of a single molecule by femtosecond orbital imaging. *Nature* **539,** 263–267 (2016).

111. Baumann, S. *et al.* Electron paramagnetic resonance of individual atoms on a surface. *Science* **350,** 417–420 (2015).

112. Zhang, R. *et al.* Chemical mapping of a single molecule by plasmon-enhanced Raman scattering. *Nature* **498,** 82–86 (2013).

113. Chen, C., Chu, P., Bobisch, C., Mills, D. & Ho, W. Viewing the interior of a single molecule: vibronically resolved photon imaging at submolecular resolution. *Physical Review Letters* **105,** 217402 (2010).

114. Imada, H. *et al.* Single-molecule laser nanospectroscopy with micro–electron volt energy resolution. *Science* **373,** 95–98 (2021).

115. Yang, B. *et al.* Sub-nanometre resolution in single-molecule photoluminescence imaging. *Nature Photonics,* 1–7 (2020).

116. Imai-Imada, M. *et al.* Orbital-resolved visualization of single-molecule photocurrent channels. *Nature* **603,** 829–834 (2022).

117. Gutzler, R., Garg, M., Ast, C. R., Kuhnke, K. & Kern, K. Light–matter interaction at atomic scales. *Nature Reviews Physics* **3,** 441–453 (2021).

118. Zhang, Y. *et al.* Visualizing coherent intermolecular dipole–dipole coupling in real space. *Nature* **531,** 623–627 (2016).

119. Luo, Y. *et al.* Electrically driven single-photon superradiance from molecular chains in a plasmonic nanocavity. *Physical Review Letters* **122,** 233901 (2019).

120. Cao, S. *et al.* Energy funnelling within multichromophore architectures monitored with subnanometre resolution. *Nature Chemistry* **13,** 766–770 (2021).

121. Jiang, S. *et al.* Many-body description of STM-induced fluorescence of charged molecules. *Physical Review Letters* **130,** 126202 (2023).

122. Kaiser, K. *et al.* Electrically driven cascaded photon-emission in a single molecule. *arXiv preprint arXiv:2402.17536* (2024).

123. Hung, T.-C. *et al.* Bipolar single-molecule electroluminescence and electrofluorochromism. *Physical Review Research* **5,** 033027 (2023).

124. Kaiser, K., Gross, L. & Schulz, F. A single-molecule chemical reaction studied by high-resolution atomic force microscopy and scanning tunneling microscopy induced light emission. *ACS Nano* **13,** 6947–6954 (2019).

125. Vasilev, K. *et al.* Internal Stark effect of single-molecule fluorescence. *Nature Communications* **13,** 677 (2022).

126. Doležal, J. *et al.* Mechano-Optical Switching of a Single Molecule with Doublet Emission. *ACS Nano* **14,** 8931–8938 (2020).

127. Friedrich, N. *et al.* Fluorescent single-molecule STM probe. *arXiv preprint arXiv:2311.16805* (2023).

128. Kimura, K. *et al.* Selective triplet exciton formation in a single molecule. *Nature* **570,** 210–213 (2019).

129. Dolezal, J. *et al.* Real space visualization of entangled excitonic states in charged molecular assemblies. *ACS Nano* **16,** 1082–1088 (2022).

130. Klein, L. J. & Williams, C. C. Single electron tunneling detected by electrostatic force. *Applied Physics Letters* **79,** 1828–1830 (2001).

131. Bussmann, E. B., Zheng, N. & Williams, C. C. Imaging of localized electronic states at a nonconducting surface by single-electron tunneling force microscopy. *Nano Letters* **6,** 2577–2580 (2006).

132. Johnson, J., Zheng, N. & Williams, C. Atomic scale imaging and spectroscopy of individual electron trap states using force detected dynamic tunnelling. *Nanotechnology* **20,** 055701 (2009).

133. Münnich, G. *Cross-sectional scanning probe microscopy on GaAs: Tip-induced band bending, buried acceptors and adsorbed molecules* PhD thesis (2014).

134. Buchner, T. *Atomic scale light-matter interaction: From ultrafast physics to photoexcitation phenomena* PhD thesis (2023).

135. Zöphel, S. *Der Aufbau eines Tieftemperatur-Rastertunnelmikroskops und Strukturuntersuchungen auf vicinalen Kupferoberflächen* PhD thesis (2000).

136. Szabo, A. & Ostlund, N. S. *Modern Quantum Chemistry: Introduction to Advanced Electronic Structure Theory* (Courier Corporation, 2012).

137. Scheuerer, P., Patera, L. L. & Repp, J. Manipulating and Probing the Distribution of Excess Electrons in an Electrically Isolated Self-Assembled Molecular Structure. *Nano Letters* **20,** 1839–1845 (2020).

138. Queck-Scharrer, F. *Implementierung der Rastertunnelmikroskopie auf Isolatoren* PhD thesis (2019).

139. Lakowicz, J. R. *Principles of Fluorescence Spectroscopy* (Springer, 2006).

140. Kasha, M. Characterization of electronic transitions in complex molecules. *Discussions of the Faraday Society* **9,** 14–19 (1950).

141. Kuhnke, K., Grosse, C., Merino, P. & Kern, K. Atomic-scale imaging and spectroscopy of electroluminescence at molecular interfaces. *Chemical Reviews* **117,** 5174–5222 (2017).

142. Williams, J. O., Jones, A. C. & Davies, M. J. Radiationless transitions in p-terphenyl crystals doped with anthracene, tetracene and pentacene. *Journal of the Chemical Society, Faraday Transactions 2: Molecular and Chemical Physics* **79,** 263–269 (1983).

143. Köhler, J., Brouwer, A., Groenen, E. J. & Schmidt, J. On the intersystem crossing of pentacene in p-terphenyl. *Chemical Physics Letters* **250,** 137–144 (1996).

144. Patterson, F., Lee, H., Wilson, W. L. & Fayer, M. Intersystem crossing from singlet states of molecular dimers and monomers in mixed molecular crystals: picosecond stimulated photon echo experiments. *Chemical Physics* **84,** 51–60 (1984).

145. Kong, F.-F. *et al.* Probing intramolecular vibronic coupling through vibronic-state imaging. *Nature Communications* **12,** 1280 (2021).

146. Fowler, R. H. & Nordheim, L. Electron emission in intense electric fields. *Proceedings of the Royal Society of London. Series A, Containing Papers of a Mathematical and Physical Character* **119,** 173–181 (1928).

147. Gös, W. *Hole trapping and the negative bias temperature instability* PhD thesis (Technische Universität Wien, 2011).

148. Dweydari, A. & Mee, C. Oxygen adsorption on the (111) face of silver. *physica status solidi (a)* **17,** 247–250 (1973).

149. Bennewitz, R. *et al.* Aspects of dynamic force microscopy on NaCl/Cu(111): resolution, tip–sample interactions and cantilever oscillation characteristics. *Surface and Interface Analysis* **27,** 462–466 (1999).

150. Ploigt, H.-C., Brun, C., Pivetta, M., Patthey, F. & Schneider, W.-D. Local work function changes determined by field emission resonances: NaCl/Ag(100). *Physical Review B* **76,** 195404 (2007).

151. Zhang, L. *et al.* Electrically driven single-photon emission from an isolated single molecule. *Nature Communications* **8,** 580 (2017).

152. Burgos, J., Pope, M., Swenberg, C. E. & Alfano, R. Heterofission in pentacene-doped tetracene single crystals. *physica status solidi (b)* **83,** 249–256 (1977).

153. Imai-Imada, M. *et al.* Energy-level alignment of a single molecule on ultrathin insulating film. *Physical Review B* **98,** 201403 (2018).

154. Scivetti, I. & Persson, M. Frontier molecular orbitals of a single molecule adsorbed on thin insulating films supported by a metal substrate: electron and hole attachment energies. *Journal of Physics: Condensed Matter* **29,** 355002 (2017).

155. Dweydari, A. & Mee, C. Work function measurements on (100) and (110) surfaces of silver. *physica status solidi (a)* **27,** 223–230 (1975).

156. Cochrane, K. A., Schiffrin, A., Roussy, T. S., Capsoni, M. & Burke, S. A. Pronounced polarization-induced energy level shifts at boundaries of organic semiconductor nanostructures. *Nature Communications* **6,** 8312 (2015).

157. Adhikari, S., Smit, R. & Orrit, M. Future Paths in Cryogenic Single-Molecule Fluorescence Spectroscopy. *The Journal of Physical Chemistry C* **128,** 3–18 (2024).

158. Spachtholz, R. *Exciton transitions of a single molecule on a surface* Master thesis (University of Regensburg, 2021).

159. Bleher, S. *Unterscheidung von Isotopologen mittels Elektronenspinresonanz-Rastersondenmikroskopie* Bachelor thesis (University of Regensburg, 2022).

160. Bruckmann, F. *Introducing radio frequency radiation into a scanning probe microscope via a coil* Bachelor thesis (University of Regensburg, 2021).

161. Stahl, M. *Simulation zur Triplettaufspaltung von Pentacen im Einfluss der Spitze eines Rastersondenmikroskops* Thesis (University of Regensburg, 2022).

162. Eckrich, J. *Expanding force-detection electron spin resonance to multiple compounds* Bachelor thesis (University of Regensburg, 2023).

163. Brinster, S. *Investigating the Stark shift in electron spin resonance of single molecules measured with atomic force microscopy* Bachelor thesis (University of Regensburg, 2024).

164. Yu, C.-J., Von Kugelgen, S., Laorenza, D. W. & Freedman, D. E. A molecular approach to quantum sensing. *ACS Central Science* **7,** 712–723 (2021).

165. Monroe, C. & Kim, J. Scaling the ion trap quantum processor. *Science* **339,** 1164–1169 (2013).

166. Gaita-Ariño, A., Luis, F., Hill, S. & Coronado, E. Molecular spins for quantum computation. *Nature Chemistry* **11,** 301–309 (2019).

167. Ladd, T. D. *et al.* Quantum computers. *Nature* **464,** 45–53 (2010).

168. DiVincenzo, D. P. The physical implementation of quantum computation. *Fortschritte der Physik: Progress of Physics* **48,** 771–783 (2000).

169. Köhler, J. *et al.* Magnetic resonance of a single molecular spin. *Nature* **363,** 242–244 (1993).

170. Wrachtrup, J., Von Borczyskowski, C., Bernard, J., Orrit, M. & Brown, R. Optical detection of magnetic resonance in a single molecule. *Nature* **363,** 244–245 (1993).

171. Moerner, W. E. & Kador, L. Optical detection and spectroscopy of single molecules in a solid. *Physical Review Letters* **62,** 2535 (1989).

172. Orrit, M. & Bernard, J. Single pentacene molecules detected by fluorescence excitation in a p-terphenyl crystal. *Physical Review Letters* **65,** 2716 (1990).

173. Wrachtrup, J., Von Borczyskowski, C., Bernard, J., Orrit, M. & Brown, R. Optically detected spin coherence of single molecules. *Physical Review Letters* **71,** 3565 (1993).

174. Wrachtrup, J., Gruber, A., Fleury, L. & Von Borczyskowski, C. Magnetic resonance on single nuclei. *Chemical Physics Letters* **267,** 179–185 (1997).

175. Köhler, J., Brouwer, A., Groenen, E. J. & Schmidt, J. Fluorescence detection of single molecule magnetic resonance for pentacene in p-terphenyl. The hyperfine interaction of a single triplet spin with a single ^{13}C nuclear spin. *Chemical Physics Letters* **228,** 47–52 (1994).

176. Köhler, J., Brouwer, A., Groenen, E. J. & Schmidt, J. Single molecule electron paramagnetic resonance spectroscopy: hyperfine splitting owing to a single nucleus. *Science* **268,** 1457–1460 (1995).

177. Köhler, J., Brouwer, A.-J. C., Groenen, E. J. & Schmidt, J. Isotopomer selective spectroscopy on pentacene. *Journal of the American Chemical Society* **120,** 1900–1905 (1998).

178. Brouwer, A., Köhler, J., van Oijen, A. M., Groenen, E. J. & Schmidt, J. Single-molecule fluorescence autocorrelation experiments on pentacene: The dependence of intersystem crossing on isotopic composition. *The Journal of Chemical Physics* **110,** 9151–9159 (1999).

179. Sidles, J. Noninductive detection of single-proton magnetic resonance. *Applied Physics Letters* **58,** 2854–2856 (1991).

180. Christensen, D. V. *et al.* 2024 Roadmap on Magnetic Microscopy Techniques and Their Applications in Materials Science. *Journal of Physics: Materials* (2024).

181. Sidles, J. A. *et al.* Magnetic resonance force microscopy. *Reviews of Modern Physics* **67,** 249 (1995).

182. Sidles, J. Folded Stern-Gerlach experiment as a means for detecting nuclear magnetic resonance in individual nuclei. *Physical Review Letters* **68,** 1124 (1992).

183. Rugar, D., Yannoni, C. & Sidles, J. Mechanical detection of magnetic resonance. *Nature* **360,** 563–566 (1992).

184. Rugar, D., Budakian, R., Mamin, H. & Chui, B. Single spin detection by magnetic resonance force microscopy. *Nature* **430,** 329–332 (2004).

185. Degen, C., Poggio, M., Mamin, H., Rettner, C. & Rugar, D. Nanoscale magnetic resonance imaging. *Proceedings of the National Academy of Sciences* **106,** 1313–1317 (2009).

186. Grob, U. *et al.* Magnetic resonance force microscopy with a one-dimensional resolution of 0.9 nanometers. *Nano Letters* **19,** 7935–7940 (2019).

187. Van Oort, E., Manson, N. & Glasbeek, M. Optically detected spin coherence of the diamond NV centre in its triplet ground state. *Journal of Physics C: Solid State Physics* **21,** 4385 (1988).

188. Balasubramanian, G. *et al.* Nanoscale imaging magnetometry with diamond spins under ambient conditions. *Nature* **455,** 648–651 (2008).

189. Grinolds, M. *et al.* Subnanometre resolution in three-dimensional magnetic resonance imaging of individual dark spins. *Nature Nanotechnology* **9,** 279–284 (2014).

190. Janitz, E. *et al.* Diamond surface engineering for molecular sensing with nitrogen-vacancy centers. *Journal of Materials Chemistry C* **10,** 13533–13569 (2022).

191. Willke, P. *et al.* Hyperfine interaction of individual atoms on a surface. *Science* **362,** 336–339 (2018).

192. Seifert, T. S. *et al.* Single-atom electron paramagnetic resonance in a scanning tunneling microscope driven by a radio-frequency antenna at 4 K. *Physical Review Research* **2,** 013032 (2020).

193. Chen, Y., Bae, Y. & Heinrich, A. J. Harnessing the quantum behavior of spins on surfaces. *Advanced Materials* **35,** 2107534 (2023).

194. Wiesendanger, R. Spin mapping at the nanoscale and atomic scale. *Reviews of Modern Physics* **81,** 1495 (2009).

195. Yang, K. *et al.* Coherent spin manipulation of individual atoms on a surface. *Science* **366,** 509–512 (2019).

196. Veldman, L. M. *et al.* Free coherent evolution of a coupled atomic spin system initialized by electron scattering. *Science* **372,** 964–968 (2021).

197. Yang, K. *et al.* Engineering the eigenstates of coupled spin-1/2 atoms on a surface. *Physical Review Letters* **119,** 227206 (2017).

198. Wang, Y. *et al.* An atomic-scale multi-qubit platform. *Science* **382,** 87–92 (2023).

199. Yang, K. *et al.* Probing resonating valence bond states in artificial quantum magnets. *Nature Communications* **12,** 993 (2021).

200. Yang, K. *et al.* Electrically controlled nuclear polarization of individual atoms. *Nature Nanotechnology* **13,** 1120–1125 (2018).

201. Reale, S. *et al.* Electrically Driven Spin Resonance of 4f Electrons in a Single Atom on a Surface. *arXiv preprint arXiv:2309.02348* (2023).

202. Zhang, X. *et al.* Electron spin resonance of single iron phthalocyanine molecules and role of their non-localized spins in magnetic interactions. *Nature Chemistry* **14,** 59–65 (2022).

203. Kawaguchi, R. *et al.* Spatially Resolving Electron Spin Resonance of π-Radical in Single-molecule Magnet. *Nano Letters* **23,** 213–219 (2022).

204. Willke, P. *et al.* Probing quantum coherence in single-atom electron spin resonance. *Science Advances* **4,** eaaq1543 (2018).

205. Paul, W. *et al.* Control of the millisecond spin lifetime of an electrically probed atom. *Nature Physics* **13,** 403–407 (2017).

206. Poggio, M., Degen, C., Rettner, C., Mamin, H. & Rugar, D. Nuclear magnetic resonance force microscopy with a microwire rf source. *Applied Physics Letters* **90** (2007).

207. Stipe, B. *et al.* Electron spin relaxation near a micron-size ferromagnet. *Physical Review Letters* **87,** 277602 (2001).

208. Mamin, H., Budakian, R. & Rugar, D. Superconducting microwave resonator for millikelvin magnetic resonance force microscopy. *Review of Scientific Instruments* **74,** 2749–2753 (2003).

209. Serway, R. & Jewett, J. *Physics for Scientists and Engineers with Modern Physics* 9th ed. (Cengage Learning, 2014).

210. Mottl, Z. The quantitative relations between true and standard depth of penetration for air-cored probe coils in eddy current testing. *NDT International* **23,** 11–18 (1990).

211. Sixl, H. & Schwoerer, M. Optische Elektronenspin-Polarisation (OEP) in Triplett-Zuständen organischer Moleküle. *Zeitschrift für Naturforschung A* **25,** 1383–1394 (1970).

212. Chidsey, C. E., Loiacono, D. N., Sleator, T. & Nakahara, S. STM study of the surface morphology of gold on mica. *Surface Science* **200,** 45–66 (1988).

213. Blair, E., Farrington, K. & Tubbs, K. Selecting the right RF switch. *Microwave Journal* **32,** 161–166 (1989).

214. Brouwer, A., Groenen, E. & Schmidt, J. Detecting magnetic resonance through quantum jumps of single molecules. *Physical Review Letters* **80,** 3944 (1998).

215. Van Strien, A. & Schmidt, J. An EPR study of the triplet state of pentacene by electron spin-echo techniques and laser flash excitation. *Chemical Physics Letters* **70,** 513–517 (1980).

216. Yu, H.-L., Lin, T.-S., Weissman, S. & Sloop, D. J. Time resolved studies of pentacene triplets by electron spin echo spectroscopy. *The Journal of Chemical Physics* **80,** 102–107 (1984).

217. Levitt, M. H. *Spin Dynamics: Basics of Nuclear Magnetic Resonance* (John Wiley & Sons, 2013).

218. Schmidt, J. & Van der Waals, J. The structure of the zero-field transitions of phosphorescent quinoxaline. *Chemical Physics Letters* **3,** 546–549 (1969).

219. Chan, I.-Y., Schmidt, J. & van der Walls, J. Optical detection of endor in a zero-field transition of phosphorescent quinoxaline. *Chemical Physics Letters* **4,** 269–274 (1969).

220. Gotberg, K. & Tinti, D. Determination of the complete ^{14}N quadrupole interaction tensor in a photoexcited triplet state by zero and low field optically detected ENDOR Application to $NaNO_2$/Ag. *Molecular Physics* **47,** 97–120 (1982).

221. Kothandaraman, G., Pratt, D. & Tinti, D. Optically detected magnetic resonance spectra of the lowest triplet state of 1-iodonaphthalene in durene at zero and high magnetic fields. *The Journal of Chemical Physics* **63,** 3337–3348 (1975).

222. Olympia Jr, P., Wei, I. & Fung, B. Deuteron quadrupole coupling constants in deuterocarbons. *The Journal of Chemical Physics* **51,** 1610–1614 (1969).

223. Lin, T., Ong, J.-L., Sloop, D. & Yu, H.-L. in *Pulsed EPR: A New Field of Applications* 191 (North-Holland, Amsterdam, 1989).

224. Kilin, S. Y., Nizovtsev, A., Berman, P., Von Borczyskowski, C. & Wrachtrup, J. Theory of non-Markovian relaxation of single triplet electron spins using time-and frequency-domain magnetic resonance spectroscopy measured via optical fluorescence: Application to single pentacene molecules in crystalline p-terphenyl. *Physical Review B* **58,** 8997 (1998).

225. Sheng, S. & El-Sayed, M. Second order Stark effect on the optically detected signals of the zero-field transitions of the triplet state. *Chemical Physics Letters* **34,** 216–221 (1975).

226. Bredas, J.-L. Mind the gap! *Materials Horizons* **1,** 17–19 (2014).

227. Patera, L. L., Queck, F., Scheuerer, P., Moll, N. & Repp, J. Accessing a Charged Intermediate State Involved in the Excitation of Single Molecules. *Physical Review Letters* **123,** 016001 (2019).

228. Scheuerer, P. *et al.* Charge-induced structural changes in a single molecule investigated by atomic force microscopy. *Physical Review Letters* **123,** 066001 (2019).

229. Mohn, F. *et al.* Reversible bond formation in a gold-atom–organic-molecule complex as a molecular switch. *Physical Review Letters* **105,** 266102 (2010).

230. Schmidt, J., Van Dorp, W. & Van der Waals, J. Phosphorescence modulation by coherent coupling to a microwave field. *Chemical Physics Letters* **8,** 345–348 (1971).

231. Kilin, S. Y., Nizovtsev, A., Berman, P., Wrachtrup, J. & Von Borczyskowski, C. Stochastic theory of optically detected single-spin coherent phenomena: Evidence for non-Markovian dephasing of pentacene in p-terphenyl. *Physical Review B* **56,** 24 (1997).

232. Redfield, A. G. Nuclear magnetic resonance saturation and rotary saturation in solids. *Physical Review* **98,** 1787 (1955).

233. Ong, J.-L., Sloop, D. J. & Lin, T.-S. Deuteration effect on the spin dynamics of the photo-excited triplet state of pentacene in p-terphenyl crystals. *Chemical Physics Letters* **241,** 540–546 (1995).

234. Robinson, G. W. & Frosch, R. Electronic excitation transfer and relaxation. *The Journal of Chemical Physics* **38,** 1187–1203 (1963).

235. Robinson, G. W. Spectra and energy transfer phenomena in crystalline rare gas solvents. *Journal of Molecular Spectroscopy* **6,** 58–83 (1961).

236. Wrachtrup, J., Von Borczyskowski, C., Bernard, J., Brown, R. & Orrit, M. Hahn echo experiments on a single triplet electron spin. *Chemical Physics Letters* **245,** 262–267 (1995).

237. Van 't Hof, C. & Schmidt, J. The effect of spectral diffusion on the phase coherence of phosphorescent triplet spins. *Molecular Physics* **38,** 309–320 (1979).

238. Schmidt, J. Electron spin echoes in photo-excited triplet states of organic molecules in zero magnetic field. *Chemical Physics Letters* **14,** 411–414 (1972).

239. Willke, P. *et al.* Coherent spin control of single molecules on a surface. *ACS Nano* **15,** 17959–17965 (2021).

240. DeVoe, R. G. & Brewer, R. G. Experimental test of the optical Bloch equations for solids. *Physical Review Letters* **50,** 1269 (1983).

241. Bodey, J. *et al.* Optical spin locking of a solid-state qubit. *npj Quantum Information* **5,** 95 (2019).

242. Brandon, R. W., Gerkin, R. E. & Hutchison Jr, C. A. Paramagnetic resonance absorption in phenanthrene in its phosphorescent state. *The Journal of Chemical Physics* **41,** 3717–3726 (1964).

243. Stipe, B. C., Rezaei, M. A. & Ho, W. Single-molecule vibrational spectroscopy and microscopy. *Science* **280,** 1732–1735 (1998).

244. Heinrich, A., Lutz, C., Gupta, J. & Eigler, D. Molecule cascades. *Science* **298,** 1381–1387 (2002).

245. Natterer, F. D., Patthey, F. & Brune, H. Distinction of nuclear spin states with the scanning tunneling microscope. *Physical Review Letters* **111,** 175303 (2013).

246. Kahn, O. & Martinez, C. J. Spin-transition polymers: from molecular materials toward memory devices. *Science* **279,** 44–48 (1998).

247. Custance, O., Perez, R. & Morita, S. Atomic force microscopy as a tool for atom manipulation. *Nature Nanotechnology* **4,** 803–810 (2009).

248. Topinka, M. *et al.* Imaging coherent electron flow from a quantum point contact. *Science* **289,** 2323–2326 (2000).

249. Willke, P., Yang, K., Bae, Y., Heinrich, A. J. & Lutz, C. P. Magnetic resonance imaging of single atoms on a surface. *Nature Physics* **15,** 1005–1010 (2019).

250. Berman, P. R. & Malinovsky, V. S. *Principles of Laser Spectroscopy and Quantum Optics* (Princeton University Press, 2011).

251. Brown, R., Wrachtrup, J., Orrit, M., Bernard, J. & Von Borczyskowski, C. Kinetics of optically detected magnetic resonance of single molecules. *The Journal of Chemical Physics* **100,** 7182–7191 (1994).

252. Blum, K. *Density Matrix Theory and Applications* (Springer Science & Business Media, 2012).

253. Likharev, K. K. *Quantum Mechanics: Lecture notes* (IOP Publishing, 2019).

Acronyms

AC	Alternating current
AC-STM	Alternate-charging scanning tunneling microscopy
AFM	Atomic force microscopy/microscope
AWG	Arbitrary waveform generator
CI	Confidence interval
CPD	Contact potential difference
CW	Continuous wave
DC	Direct current
ESR	Electron spin/paramagnetic resonance
FM-AFM	Frequency-modulated atomic force microscopy
FWHM	Full width at half maximum
HFI	Hyperfine interaction
HOMO	Highest occupied molecular orbital
I/Q modulation	In-phase/quadrature-phase modulation
KPFS	Kelvin probe force spectroscopy/spectrum
LUMO	Lowest unoccupied molecular orbital
ML	Monolayers
MRFM	Magnetic resonance force microscopy
MRI	Magnetic resonance imaging
NV	Nitrogen vacancy
ODMR	Optically-detected magnetic resonance
OpAmp	Operational amplifier
pp	peak-to-peak
PTCDA	Perylenetetracarboxylic dianhydride
Q-factor	Quality factor
RF	Radio frequency
s.d.	standard deviation
SOMO	Singly occupied molecular orbital
SPM	Scanning probe microscopy/microscope
STM	Scanning tunneling microscopy/microscope
STML	Scanning tunneling microscopy-induced luminescence
STS	Scanning tunneling spectroscopy
UHV	Ultra-high vacuum
WKB	Wentzel–Kramers–Brillouin

Acknowledgments

This thesis as well as the time I spent in Regensburg would not have been so great without the involvement of the following people.

First and foremost, I would like to thank Jascha Repp for being the best PhD supervisor I could have wished for. It was really great to work together due to your kindness, extensive knowledge of physics, mechanical and electronic engineering insights and programming skills. But especially since you combine this with your great explanation talent and willingness to help, as well as the freedom you offer to develop and pursue own ideas. I really would like to thank you for all the in-depth and enjoyable scientific discussions we had, and all the things you taught me ranging from physics and electronics to general scientific skills. Although all the work presented in this thesis could not have resulted as such without our close collaboration, I want to especially thank you for scheduling two meetings to convince us to try to combine ESR with AFM (hard to imagine that I was once skeptic about this great idea ;)), all your input and practical help related to the coil and sample design as well as the other electronics, all the help you offered in repairing the machine every time it broke, the very useful idea of the normalized frequency shift, the nice schematic explanation of the hyperfine interaction, your already long-existing idea to try some excited-state spectroscopy, your indispensable help in programming and modeling of the data (especially for the excited-state spectroscopy), and the valuable input you gave on my thesis. It was a very great pleasure to work together on these exciting projects!

Second, I would like to thank all the Bachelor and Master students I was allowed to supervise on a daily basis. It was a great pleasure to be able to collaborate with you (doing research together is much more fun than alone!), and thank you very much for all the time spent in performing the measurements. I am also very grateful for all the exercise I got in explaining things, and reversibly, for everything I could learn from everyone of you! In particular, I would like to thank Raffael Spachtholz for our collaboration during the beginning of my PhD, when you did your master thesis, as well as afterwards when you started your PhD. It was really great to start the ESR-AFM project together. I am especially very grateful for all your work on the built-up of the experimental setup and for all the experimental skills I could learn from you (such that you brought me to the practical course room and explained me some basics :)). I would like to thank Franziska Bruckmann for joining the project as the first Bachelor student that I was allowed to supervise and the great time we spent together in trying to test the implementation of the RF field; it was also great that you afterwards now and then came by for a visit! A special thanks goes out to Sonja Bleher, who was my longest experimental coworker on these projects, both as Bachelor, SHK and Master student. I really enjoyed working together, and want to especially thank you for all the work you did so that I could focus on other things! I would like to thank Maximilian Stahl for the DFT calculations he did for a future possible project, and the enjoyable discussions we had in which we could develop some insights related to the triplet substates. Many thanks goes out to Jakob Eckrick; you worked yourself so

quickly into the project that you certainly deserved an authorship to both works presented in this thesis! Thank you especially for your commitment in finishing the excited-state spectroscopy measurements during your SHK time. I would like to thank Stefan Brinster for joining the ESR-AFM project, the many hours spent on tip shaping and the interesting discussions about the electric field dependence. And finally I would like to thank Clea Ruth for joining at the end of my PhD and continuing doing interesting experiments; you provided a nice distraction during writing my thesis.

Third, I would like to thank the other group members of the Atomic-Scale Science on Insulators group. Philipp Scheuerer, my first and at the end even my longest room mate, thank you for our collaboration on the ESR-AFM project at beginning of my PhD; it was really great to have someone involved with many years of experience! Tobias Preis, although we only worked together for a few months, I enjoyed it very much and would like to thank you for your ideas on the gold on mica sample and the help you offered in the clean room. I would like to thank Christoph Rohrer for all the support he offered over all the years, especially with the many openings and closing of our machine. I would like to thank Thomas Buchner, especially for introducing me to the field of scanning probe microscopy during my second master internship, and making me so enthusiastic that I decided to stay; a special thanks for all the physics you taught me. Andreas Rank, I really enjoyed having you as a colleague over the last years; a special thanks for reading over parts of my thesis. Tzu-Chao Hung, thank you for the interesting discussions and literature insights you gave me, as well as your feedback on parts of my thesis. Sophia Sokolov, it was great to start in a physics group where already another chemist was doing her PhD, thank you for the nice conversations we had! Carmen Roelcke, although we didn't had so many interactions, I always really enjoyed talking to you. I also would like to thank all the other former and current group members for the enjoyable time and nice conversations.

This leaves me to thank the people outside of Jascha's research group. A great thanks goes out to Leo Gross, for all the very nice discussions we had during conferences and project meetings (mostly at beautiful locations ;)) about science and everything around it. A special thanks for the very insightful feedback you provided on the excited-state spectroscopy manuscript and parts of my thesis! I am looking forward to join your group as a postdoc! I am also very grateful for all the interesting discussions and the theoretical input on the excited-state spectroscopy project from Andrea Donarini, thank you also for agreeing to co-referee this thesis. I would like to thank Shadi Fatayer for the very enjoyable time during the weeks you spent in the lab; a special thanks for all the interesting discussions we had during that time and at conferences! I would also like to thank Laerte Patera for very interesting discussions; it is really great to discuss science with you! I would also like to thank the large number of great people I met at conferences; you made the conferences very enjoyable, and I am very grateful for everything I could learn from you! I especially would like to thank Fabian Paschke and Nicolaj Betz for great and insightful discussions and the enjoyable time we could spent traveling together between conferences. Furthermore, I would like to thank the Gießibl group, especially Franz Gießibl and Jay Weymouth, for interesting discussions over the last years. I would like to thank Cornelia Linz and Dieter Weiss for providing access to the clean room facility. I would like to thank Rupert Huber and Isabella Gierz for agreeing to be on the board of examiners and conduct the oral examination. Finally, I would like to thank Alexander Khajetoorians for giving me advice on where to do my second master internship; at that time I did not realize that

I would end up in one of the best scanning probe microscopy groups, thank you for your great advice!

Meine Zeit in Regensburg wäre nicht so schön gewesen, ohne meine Freunde, von denen ich die meisten bei der SMD kennengelernt habe. Ich hätte mich keine bessere Freizeitgestaltung wünschen können! Vielen Dank für alle Zeit, die wir gemeinsam verbringen konnten, für alles, was wir zusammen machen und gestalten konnten, und für alles was ich durch euch lernen durfte!

Ik wil ook mijn familie en vrienden in Nederland bedanken voor de ondersteuning en voortdurende en zelfs nieuw onstane vriendschappen, ondanks de grote afstand.

Mijn grootste dank gaat uit aan God, de schepper van dit universum (inclusief de moleculen die ik mocht onderzoeken :)), en mijn liefdevolle vader en trouwe vriend.